Cross Shore Sediment Transport and Beach Profile Change

by

Lauren Schmied, Nobuhisa Kobayashi,
Andres Payo and Jack Puleo

RESEARCH REPORT NO. CACR-06-03
July, 2006

Center for Applied Coastal Research
Ocean Engineering Laboratory
University of Delaware
Newark, DE 19716

ACKNOWLEDGEMENTS

This study was supported by the NOAA Office of Sea Grant, Department of Commerce, under Grant No. NA85AA-D-SG033 (Project SG0507 R/ETE-4) and by the U.S. Army Corps of Engineers, Coastal and Hydraulics Laboratory (MORPHOS-3D Project). The third author was supported by the Spanish Postdoctoral Scholarship, MEC/FULBRIGHT.

TABLE OF CONTENTS

LIST OF FIGURES

LIST OF TABLES

ABSTRACT

The investigation of cross-shore sediment transport is complex due to the variability of factors contributing to sediment motion. It has been an increasingly important topic as coastlines around the world continue to change. The knowledge of cross-shore sediment transport is important to be able to predict shoreline change. In this study, the objective was to develop a numerical model that could robustly predict beach profile change under varying conditions. The model contains a new formulation for calculating bedload transport. Two laboratory experiments were conducted with the goal of reproducing on a small scale, erosive and accretive events similar to those found in nature. These experimental results as well as results obtained in a large scale laboratory experiment, were used to test the validity of the new transport model. One additional experiment was conducted to analyze the temporal and spatial variability of suspension events under breaking waves.

Chapter 1

INTRODUCTION

Cross-shore sediment transport on beaches has been investigated extensively, however the prediction of beach erosion and accretion accurately even for the idealized case of alongshore uniformity, normally-incident waves, and uniform sediment is still not possible. In order to improve our predictive capabilities, sediment transport models are getting more sophisticated but less transparent. Many are employing sophisticated and computationally intensive wave and hydrodynamic components while still relying on simple empirical formulations for sediment transport. Moreover, the roles of bedload and suspended load are not clear judging from the successful prediction of the onshore bar migration at Duck, North Carolina by Hoefel and Elgar (2003) using the skewed acceleration effect on bedload and by Henderson *et al.* (2004) using a suspended sediment model. An attempt is made here to synthesize and simplify existing cross-shore sediment transport models with the aim of developing a simple and robust model that is suited for engineering applications.

The experimental and numerical work presented here is a continuation of Kobayashi *et al.* (2005) who conducted small-scale tests on a fine sand beach and developed a numerical model for cross-shore suspended sediment transport. They obtained simple formulas for the offshore and onshore suspended sediment transport rates due to the undertow current and the correlation between the horizontal fluid velocity and suspended sediment concentration, respectively. The formulas are combined here to obtain a formula for the net rate of the suspended sediment transport

which is directed offshore. This formula includes the probability of sediment suspension so that it may be applied to coarser sediments for which sediment suspension may be limited by their large settling velocities.

The net bedload transport rate is predicted by a new formula. The probability of sediment movement is included so that this bedload formula may be applied to sediments that do not move continuously under wave action. This formula is similar to the sheet flow model by Trowbridge and Young (1989) which predicted the onshore movement of a bar observed during low-energy wave conditions at Duck, North Carolina. This formula is also shown to be consistent with the energetics-based bedload formula of Bagnold (1966) if the net bedload transport is assumed to be in the direction of wave propagation. The net cross-shore sediment transport rate is the sum of the net suspended sediment and bedload transport rates. The predicted net transport rate is shown to be in reasonable (within a factor of about 2) agreement with the water tunnel data of Ribberink and Al-Salem (1994) and Dohmen-Janssen *et al.* (2002) and the large-scale wave flume data of Dohmen-Janssen and Hanes (2002). Furthermore, the proposed simple sediment model predicts the existence of equilibrium profiles (Dean, 1991) with additional assumptions.

The proposed sediment model coupled with the conservation equation of bottom sediment is used to predict the beach profile evolution. The predicted profile changes on the three equilibrium beaches in the small-scale experiment by Kobayashi *et al.* (2005) are shown to be fairly small. Erosion and accretion tests conducted in the same wave flume in this study are used to examine whether the sediment model can predict both beach erosion and accretion. Finally, the sediment model is compared with the three profile evolution tests in a large wave flume reported by Roelvink and Reniers (1995).

The measure of cross-shore sediment transport and beach profile change is dependent on the understanding of the mechanisms of sediment movement and

suspension. Suspended sand concentration measured on natural beaches have been shown to have intermittently intense suspension events inside the surf zone (e.g. Cox and Kobayashi, 2000; Brenninkmeyer, 1976). A number of mechanisms have been suggested as possible explanations for these large events, however a lack of experimental data has made it difficult to formulate the definite mechanism behind these events. In addition, measurement of sediment concentration in laboratory models is traditionally performed with point source collectors such as optical transmitting, optical and acoustic backscattering, laser diffraction particle analyzing, among others (Okayasu *et al.*, 2004). As in field measurements, point measurements in the laboratory are not sufficient to understand suspension events, which are extremely variable in space and time. In addition, much laboratory instrumentation is intrusive to the flow field, and could significantly alter the flow. It is therefore advantageous to utilize a measurement technique that can at least encompass two spatial dimensions of the flow (Okayasu *et al.*, 2004). The rise in accessibility to imaging and processing techniques has made digital visualization of intense suspension events possible. Image analysis of sediment suspension over ripples has been attempted with success (Crawford and Hay, 1998). However the spatial and temporal study of cross-shore suspension events is still elusive.

In this study, images were collected over the bar region under irregular breaking waves in an attempt to quantify spatial and temporal quantities related to suspension events. An simple algorithm was developed to separate suspension events from collected images. A total of 48 events of both plunging and spilling breaking wave events were analyzed for spatial and temporal structure.

Chapter 2 outlines the experimental methods employed in the two small scale profile evolution tests, and the one suspension imaging test. Chapter 3 provides the background into the analysis of the data that were collected for the two small scale profile evolution tests. It also gives an introduction to the data collected and analysis

for the three large scale profile evolution tests conducted by Roelvink and Reniers (1995). Chapter 4 gives an overview of the wave model, the suspended sediment model developed by Kobayashi *et al.* (2005), and the new bedload formula. Chapter 5 reviews the results of the computations for the 5 small scale tests, and 3 large scale tests. Chapter 6 discusses the results from the image analysis of sediment suspension events under breaking waves, and Chapter 7 concludes the study and discusses extensions and the possibility of future work in the problems presented here. Five appendices follow the main text, that display experimental and comparison data. Appendices A and B are associated with the small scale erosive and accretive tests respectively. Appendices C through E are associated with the large scale tests 1a through 1c respectively.

It is noted that the results in this study will be presented concisely by Schmied *et al.* (2006) and Kobayashi *et al.* (2006).

Chapter 2

EXPERIMENTAL METHODS

A clear understanding of cross-shore suspension events and the underlying hydrodynamic processes is essential in predicting profile evolution accurately. Cross-shore profile change is a complex problem involving many interactions between the dynamics of suspended sediment load, bed load, hydrodynamics and wave motion. Physical modeling on various scales is imperative in the determination of these physical processes. In this chapter, three laboratory experiments will be described. Two experiments were conducted to evaluate accretional and erosional profile change under irregular breaking waves. Another experiment used imaging techniques to qualitatively and quantitatively evaluate sediment suspension events during individual, irregular breaking wave events.

2.1 Profile change experiments

All the experiments were conducted in a wave tank 30 m long, 2.4 m wide, and 1.5 m deep. For the two profile change experiments, the still water level was kept constant at an offshore depth of 90 cm. A 1:30 slope plywood beach was constructed in the tank to reduce the quantity of sand required to build the beach. An artificial wall was constructed along the centreline of the tank, and sand was placed only on the left side of the constructed wall (looking shoreward). A rock slope at the far end of the tank acted as an absorbing beach in order to reduce wave reflection. The set up of the wave tank is shown in Figure 2.1.

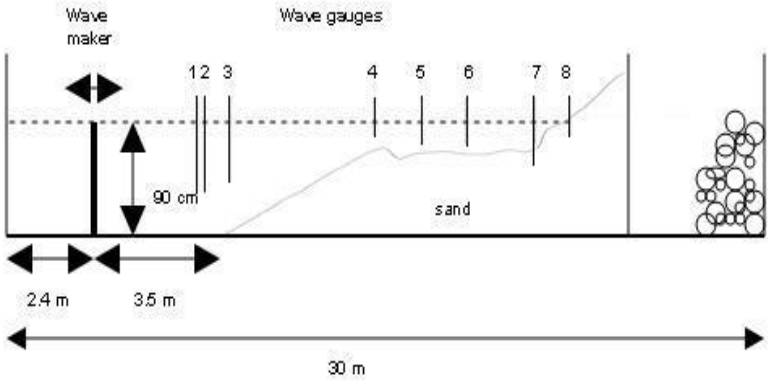

Figure 2.1: Experimental conditions for the small scale laboratory experiments.

The experiments were performed to simulate erosive and accretive events on a natural beach. Repeatable irregular waves based on a TMA spectrum were generated using a piston-type wave paddle. The peak period, T_p, was set to be 2.6 s for both tests. The root mean squared wave height, H_{rms}, was set at 12 cm for the erosional case, and reduced to 8 cm for the accretional case. These target values turned out to be very close to the measured values used in the data analysis in Chapter 3. Waves were propagated in bursts of 400 s throughout both tests. This duration was chosen to prevent seiching in the tank and behind the wave paddle. The sand used for the tests had a median diameter, d_{50}, of 0.18 mm, a specific gravity, s, of 2.6 and a fall velocity, w_f, of 2.0 cm/s. These small scale tests display the difficulties maintaining the similitude in sediment transport experiments. The diameter of the sand is not able to be reduced to the appropriate scaling of the rest of the experiment. Therefore the sand behaves more like coarse sediment on a natural beach.

2.1.1 Erosion Test

The initial geometry of the sand beach was constructed based on the equilibrium profile for a peak period, $T_p = 2.6s$, produced by Zhao and Kobayashi (2005).

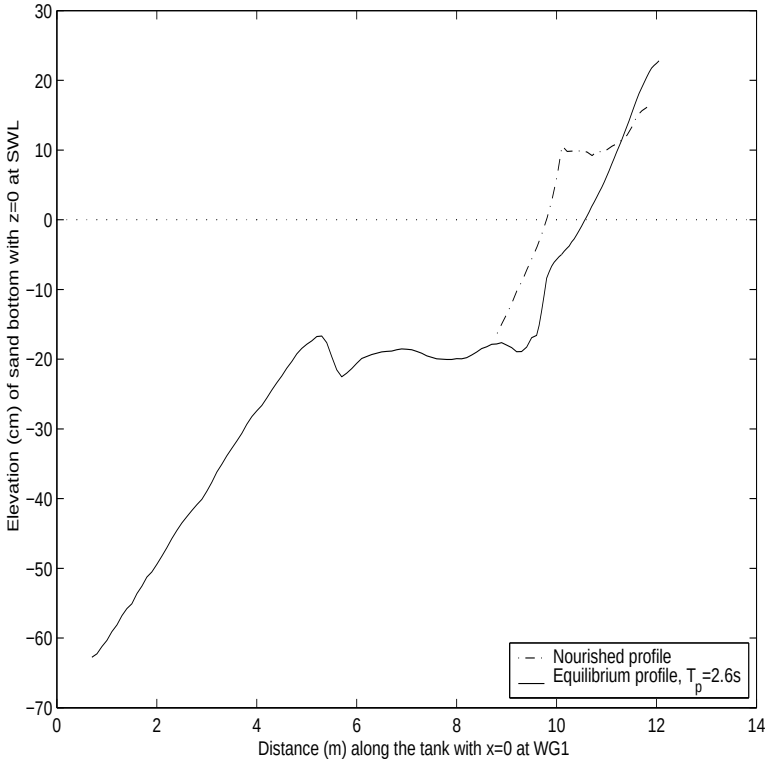

Figure 2.2: Profile built at the start to the erosion test. The nourished part of the profile (dash-dot), was built on top of the equilibrium profile (solid line) for a peak period, $T_p = 2.6s$. The dotted line indicates the still water level at z=0, 90 cm water depth near the wavemaker.

A nourished beach was built in the swash zone as shown in Figure 2.2. The nourished beach was subject to 1 burst of 400 s of waves before the start of the test in order to decrease the artificial effects that were anticipated with the unnatural slope of the nourishment area. The resulting profile is subsequently referred to as the initial profile for the erosion test. This profile is shown in Figure 2.3. A total of 43 bursts of waves, 400 s each, were propagated under the conditions specified above. 23 of these tests were conducted as the erosion test. The final 20 tests were conducted under the same wave conditions, but were used in the image test which

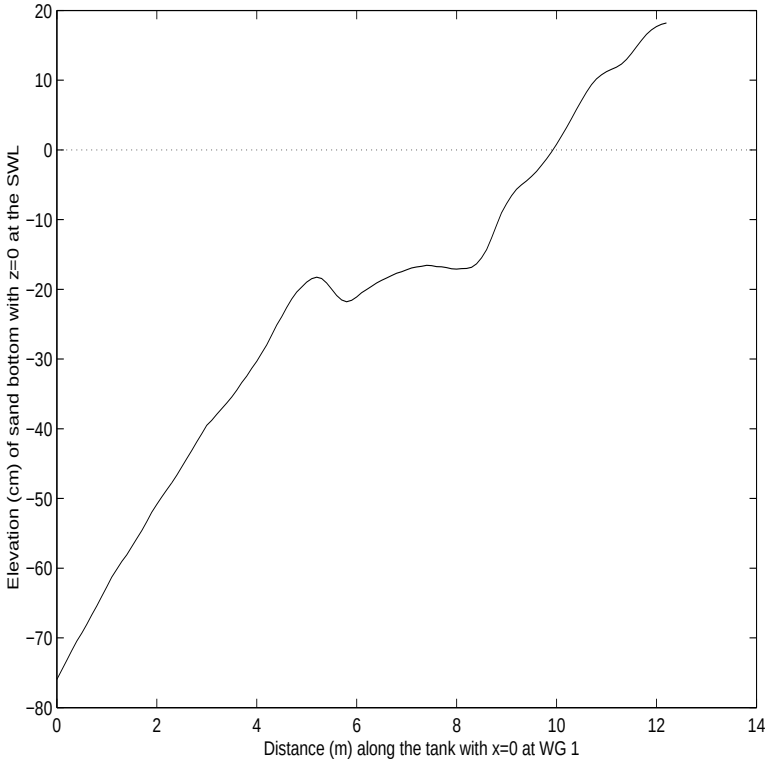

Figure 2.3: Initial profile taken before the start of the erosion test (after 400s of waves on the nourished profile). The still water level, z=0, is 90 cm from the base of the wave tank for the duration of the erosion test. x=0 at the position of wave gauge 1. The dotted line indicates the still water level, z=0.

is discussed in section 2.2. The following sections describe the measurements conducted for the erosion test (bursts 1 through 23). Profiles were measured throughout the experiment with a spacing, $\Delta x = 10$ cm. A final profile was taken at the end of the image experiment, after 43 bursts of waves.

2.1.2 Accretion Test

The accretion tests were performed with no addition of sand. The accretion tests were started using the equilibrium profile obtained at the end of the image experiment, following 43 bursts of erosional waves (shown in Figure 2.4). The root mean squared wave height was reduced in order to induce accretive conditions, however, the peak period remains the same as in the erosion test. A total of 20 bursts were run under these wave conditions. Similar to the erosion test, profiles were measured with a Δx spacing of 10 cm throughout the test, and a final profile was taken after 20 bursts of waves. Measurements collected during the course of the test are described in the following sections.

2.1.3 Experimental configuration

The configuration of wave gauges is shown in Figure 2.7. The position of the wave gauges remained unchanged for both the accretion and erosion tests. The initial x coordinate location, $x = 0$ is located at the position of wave gauge 1. Three offshore wave gauges were used to separate incident and reflected waves and test the repeatability of the generated waves. Table 2.1 shows the position of the wave gauges used in both the erosion and accretion test.

Velocity and concentration measurements were taken synchronously at several vertical elevations, z_m, above the local bottom. Instrumentation was attached to a movable cart. The vertical and horizontal locations of the velocity and concentration measurements is found in Table 2.2. At the position of wave gauge 6, $z_m =$, 2, 4, 6 and 8 cm from the local bed. The lowest elevation, 2 cm, was found to be the

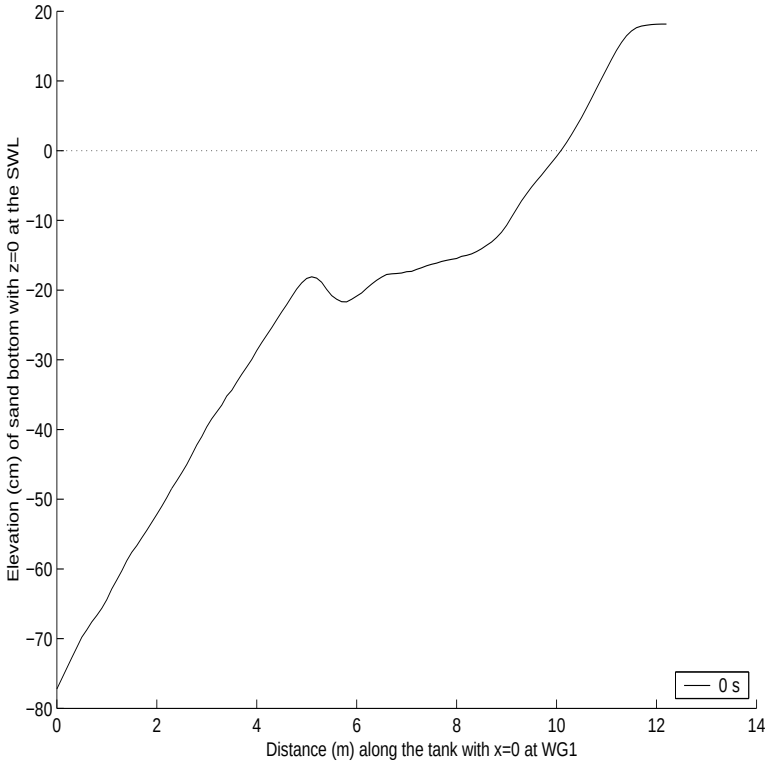

Figure 2.4: Initial profile taken before the start of the accretion test (after 17,200 seconds of waves under erosive conditions). The still water level, z=0, is set at 90 cm from the base of the wave tank for the entire duration of the accretion test. x=0 at the position of wave gauge 1. The dotted line indicates the still water level, z=0

Table 2.1: Position of wave gauges for the erosion and accretion tests.

Gauge	x **(m)**
1	0
2	0.22
3	0.92
4	5
5	6.35
6	7.6
7	9.5
8	10.5

lowest point at which the rippled bed had minimal effects. The height and length of ripples were approximately 0.7 cm and 8 cm between wave gauges 4 and 7. At the position of wave gauge 4, z_m= 2 and 4 cm from the local bed due to intense wave breaking at this location. Instrument exposure from the water column was problematic at higher elevations. Velocity and concentration measurements were not taken during erosion tests 24 through 43 (image experiment).

Table 2.2: x position and elevation of velocity and concentration measurements for both the erosion and accretion tests.

Erosion Test			Accretion Test		
test	x(m)	z_m (cm)	test	x(m)	z_m (cm)
E1	7.6	8	A1	7.6	4
E2	7.6	8	A2	7.6	6
E3	7.6	6	A3	7.6	4
E4	7.6	6	A4	7.6	4
E5	7.6	6	A5	7.6	4
E6	7.6	6	A6	7.6	6
E7	7.6	6	A7	7.6	6
E8	7.6	6	A8	7.6	8
E9	7.6	6	A9	7.6	8
E10	7.6	6	A10	7.6	8
E11	5	4	A11	7.6	8
E12	5	4	A12	7.6	2
E13	5	2	A13	7.6	2
E14	5	2	A14	7.6	2
E15	7.6	4	A15	7.6	2
E16	7.6	4	A16	7.6	4
E17	7.6	4	A17	7.6	4
E18	7.6	4	A18	7.6	6
E19	7.6	2	A19	7.6	6
E20	7.6	2	A20	7.6	6
E21	7.6	2			
E22	7.6	2			
E23	7.6	2			

2.1.4 Sand characteristics

The sand beach was constructed with approximately eight to nine tons of fine quarry sand. A sand size distribution was obtained through a sieve analysis using nine different sieve sizes (Lawrence and Kobayashi, 2003). The sand sample, weighing 293.9 g, was agitated for 20 minutes. Results from this analysis are found in Figure 2.5 and Table 2.3. The median diameter, d_{50} was found to be 0.18 mm. The sand density, fall velocity, and specific gravity were also measured.

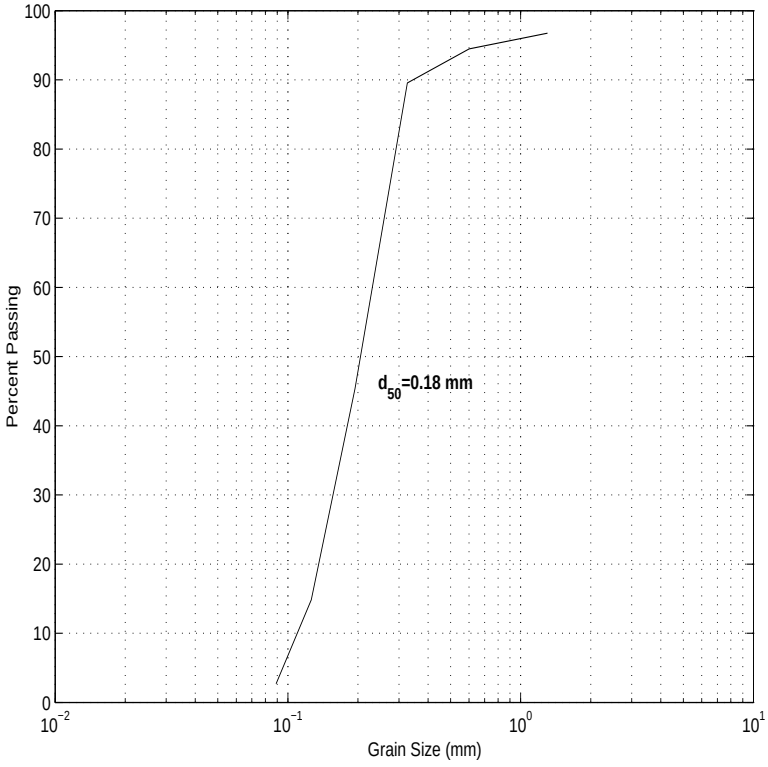

Figure 2.5: Sand grain size distribution.

To determine the sand density, a known mass of sand was placed in a graduated cylinder with a known volume of water. The displaced volume of water gave the volume of sand. The specific gravity of the sand, defined as $s = \rho_s/\rho_w$ was 2.6, where ρ_s is the sand density, and ρ_w is the density of fresh water. The porosity was

Table 2.3: Summary of sieve test

Sieve Size (mm)	**Geometric Mean Diameter (mm)**	**Mass (g)**	**Percent of M_{total}**	**Percent Passing**
2.0		0	0	100
0.850	1.300	2.3	0.77	99.2
0.425	0.601	0.8	0.27	99.0
0.250	0.326	6.5	2.20	96.8
0.212	0.230	10.1	3.44	93.3
0.150	0.178	132.6	45.12	48.2
0.125	0.137	65.7	22.34	25.9
0.106	0.115	48.3	16.42	9.4
0.075	0.089	26.8	9.13	0.3
Pan		0.9	0.3	0.0
TOTAL		293.9	100	

found from the measured dry mass and combined volume of sand and void, together with the specific gravity, giving a value of $n_p = 0.4$.

The fall velocity of the sediment was determined by dropping several grains from each of the nine size groups into a clear glass cylinder filled with fresh water. The motion was timed for a distance of one meter. Ten falls were measured for each of the size groups. This velocity was multiplied by a proportional weighting factor, which was related to the percent of the total mass, M_{total} that the size group represented. The mean fall velocity was then determined to be 2.0 cm/s.

2.1.5 Profile measurements

Beach profiles were measured along three cross-shore transects using a manual veriner pointer in the swash zone and two Panametrics 25DLHP ultrasonic depth gauges in deeper water. One transect was taken along the centreline, while the other two were taken 23.5 cm on either side. The cross-shore sample spacing for the profiles was 10 cm. There was a four point overlap in the transition between electronic and manual profiling. Figure 2.6 shows an example of the three transects

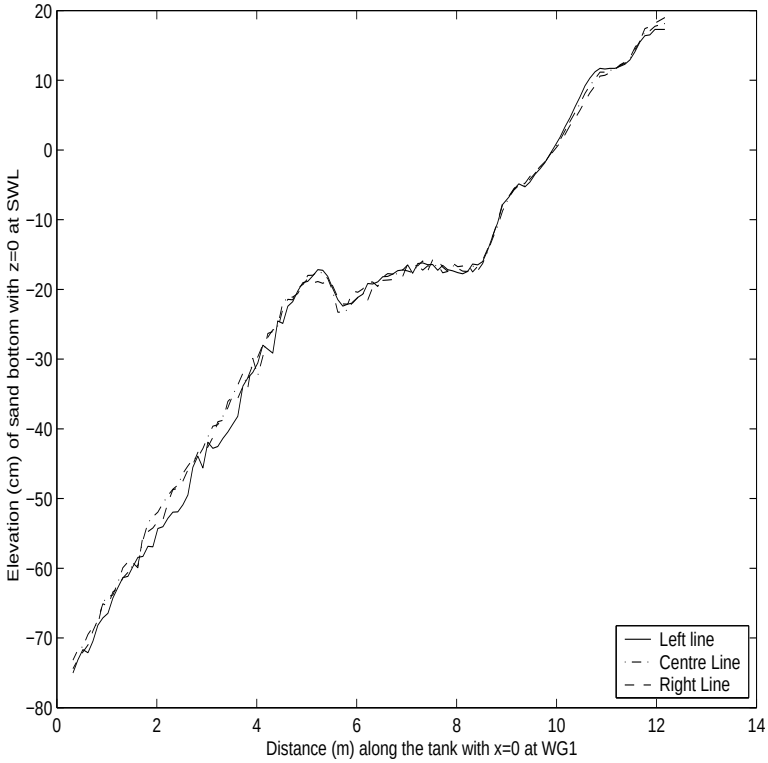

Figure 2.6: 3 transects taken at the centreline and 23.5 cm on either side.

that were taken. These transects were averaged and smoothed using a 5-point running average and extrapolated to x=0, since the measurements were limited to a minimum cross-shore location of 0.35 m, due to the finite length of the depth gauges. Each smoothed cross-shore profile is hereafter designated as PN, where N signifies the number of 400 second wave bursts that occurred prior to the measured profile. The smoothed measured profiles are displayed in chapter 5 where they are compared to model results.

2.1.6 Wave gauges

Eight capacitance wave gauges were placed in the configuration shown in Figure 2.7. The cross shore coordinate system in this and all following experiments

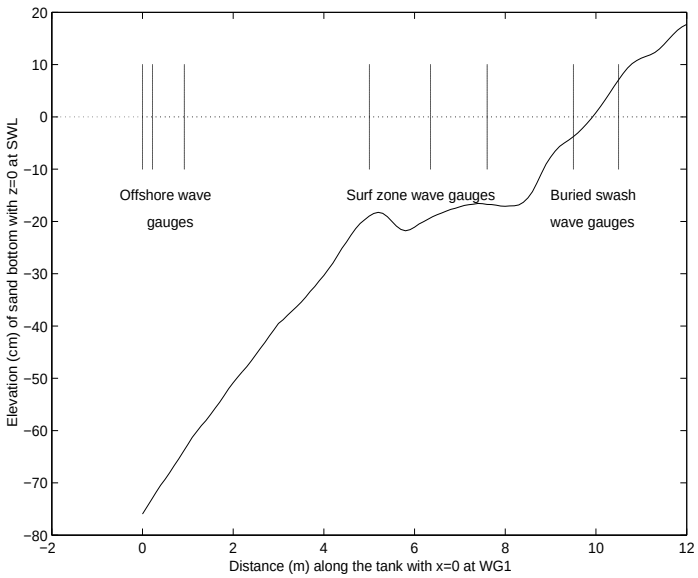

Figure 2.7: Wave gauge set up for both the erosion and the accretion tests.

is set at x=0 at the position of wave gauge 1. Wave gauges 1, 2, and 3 are placed offshore to separate the incident and reflected waves and check the repeatability of the generated waves. Gauges 4, 5, and 6 are placed in the breaking surf zone; gauges

4 and 6 are the positions of velocity and concentration measurements. Wave gauges 7 and 8 are buried in the sand to measure swash on the beach.

Wave gauges were calibrated before each run to ensure the accuracy of the experimental data. Calibrations were conducted by raising the water level 15 cm above the still water level and then draining the tank while recording the gauge readings for every 1 cm change of the water level. This was done until the water level dropped 10 cm below the still water level. The calibration data for each gauge followed a linear relation, and a typical calibration curve is shown in Figure 2.8. For gauges 7 and 8, which were buried in the sand, the calibration followed a linear

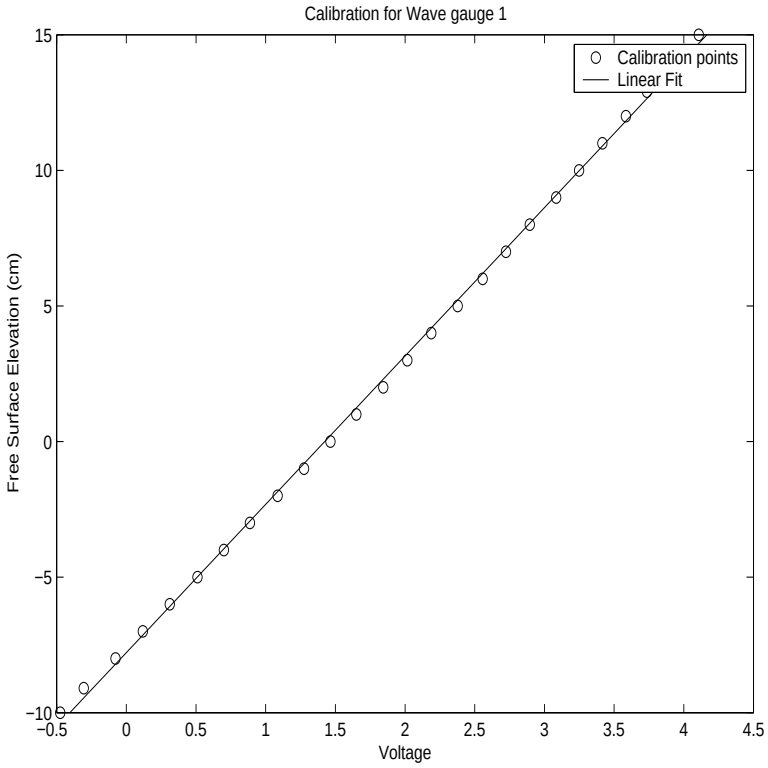

Figure 2.8: Sample calibration curve for wave gauge 1

relationship until the point where the water level dropped below the sand line. An example calibration is shown in Figure 2.9.

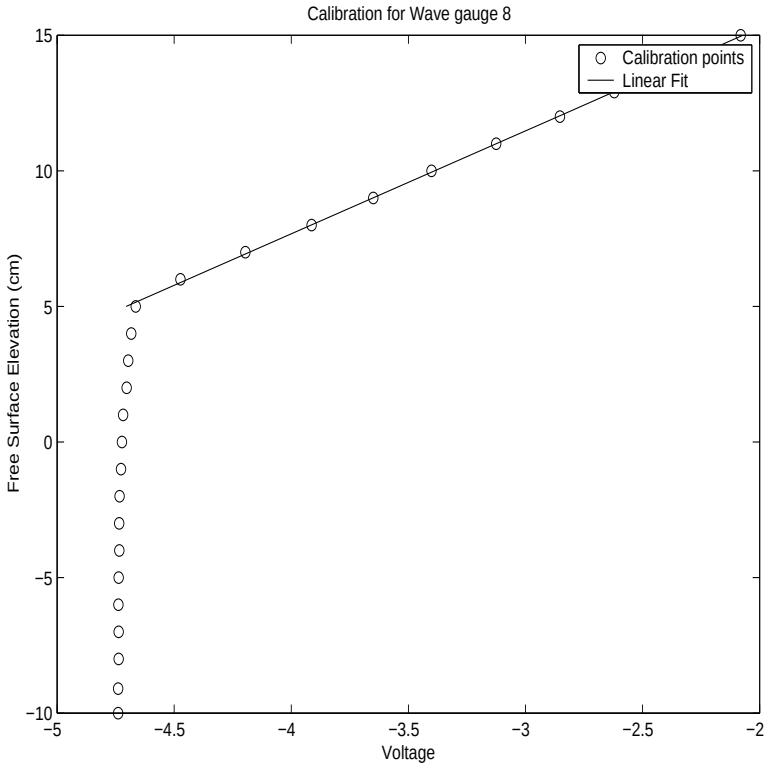

Figure 2.9: Sample calibration curve for a wave gauge buried in the sand bed

2.1.7 Acousitc-Doppler Velocimeters

Two Acoustic-Doppler Velocimeters (ADVs) were used to measure the fluid velocities in the water column. One was equipped with a downward looking probe measuring the cross-shore, alongshore, and vertical velocities at 5 cm from the probe tip. The other ADV had a sideward looking probe measuring the cross-shore and alongshore velocities at 5 cm from the probe tip. The sampling volumes for both ADVs was approximately 0.1 cm^3. The velocities were measured at four different elevations for each cross-shore position, with the exception of the location for wave gauge 4, where intense breaking did not permit accurate measurements at elevations above 4 cm.

Figure 2.10 depicts the alongshore setup of the ADVs. They were fixed to

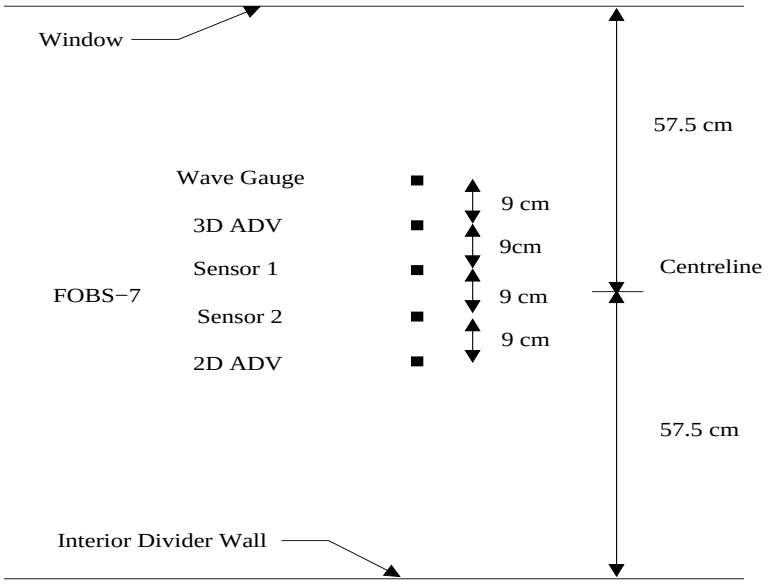

Figure 2.10: Configuration of cart mounted ADVs and FOBS.

adjustable mounts and repositioned with respect to the local bed before every test. The 3D ADV's sampling volume was determined by the software supplied by the manufacturer and has a positioning accuracy within ± 0.5 mm. The elevation of the

2D ADV was measured with a tape measure within ±1 mm, originally positioning the ADV with the probe touching the local bottom. The software provided by the manufacturer converts the ADV voltage values into velocities, so no calibration was required.

2.1.8 Fiber Optic Sediment Monitors (FOBS-7)

Two Fiber Optic Sediment Monitors (FOBS-7) were used to measure the suspended sediment concentrations synchronously at the same vertical elevation at the two alongshore positions shown in Figure 2.10. The FOBS-7's were positioned symmetrically about the centreline. The FOBS-7 is a laboratory version of the optical backscatter sensors (OBS-3) used in field measurement (Downing *et al.*, 1981). It measures sediment concentration by detecting infrared radiation (IR) backscattered from the particles. The measurement volume is approximately 10 mm^3 and is approximately 1.0 cm from the sensor tip as shown in Figure 2.11.

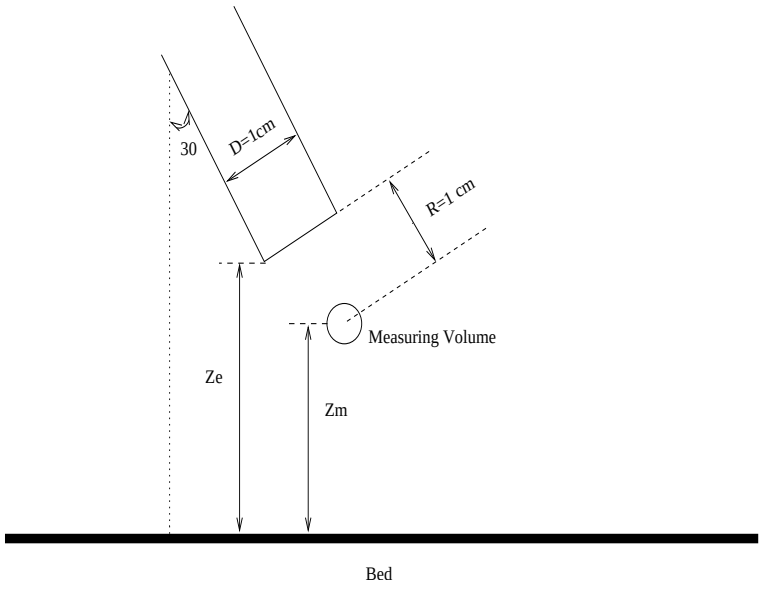

Figure 2.11: Diagram of Fiber Optic Sediment Monitor and its position with respect to the local bed.

The FOBS-7 elevation from the bed, z_m was determined by moving the instruments down until they reached their maximum voltage value of approximately 2.6 V at $z_e = 0$ as shown in Figure 2.11. They were then raised slowly until the voltage dropped suddenly. This is the $z_m = 0$ value. The sensors were then raised to the desired z_m position. As shown, the sensors were mounted at a 30 degree angle, θ. Therefore, the sampling volume elevation was determined to be $z_m = \left(z_e - R\cos\theta + \frac{D}{2}\sin\theta\right)$ where R is the distance of 1 cm from the sensor tip to the sampling volume. The diameter of the sensor, D is 1 cm.

Each FOBS-7 was calibrated in the same procedure developed in previous studies (Lawrence and Kobayashi, 2003) before the start of both the erosion and the accretion tests using a low speed blender to mix the sediment in 1 l of water and measuring the time series of the voltage sampled at 20 Hz for 60 s. For each of FOBS 1 and FOBS 2, 24 time series were collected at 4 g increments to a total of 28 g/L. Each concentration was measured at 5, 6, and 7 cm from the base of the blender to assure uniform vertical mixing. A total of 24 one minute time series were used to determine the time averaged voltage, which was used to develop a calibration curve. The fluctuating voltage was used to assess the error, which was less than 20%, due to the variability caused by the small sampling volume. The calibration curves for both FOBS are shown in Figures 2.12 and 2.13.

The FOBS-7's were determined to be susceptible to entrained air when the blender speed was high. The presence of bubbles in the water column has been found to increase the voltage readings by 25% or more (Puleo *et al.*, 2006). This problem was solved by using a variable speed blender, which allowed the blender to be placed on a lower speed, but allowed for uniform mixing of sediment without significant bubble entrainment.

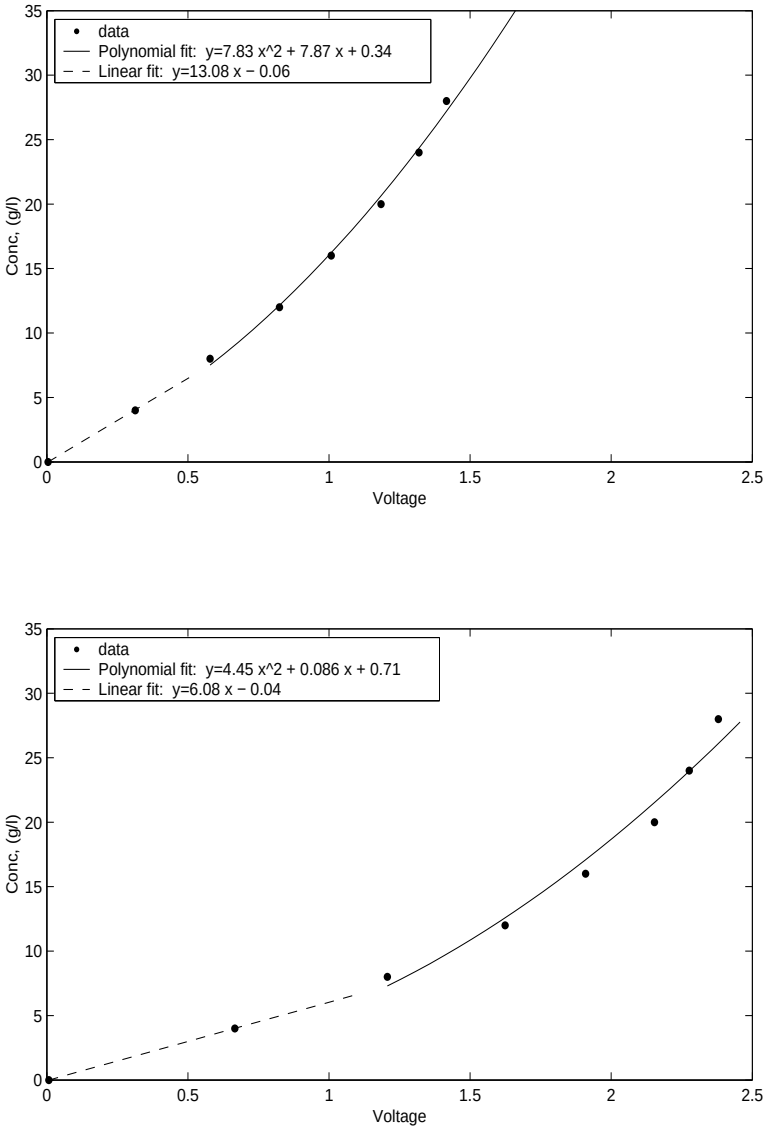

Figure 2.12: FOBS 1 and 2 calibration before the start of the erosion test.

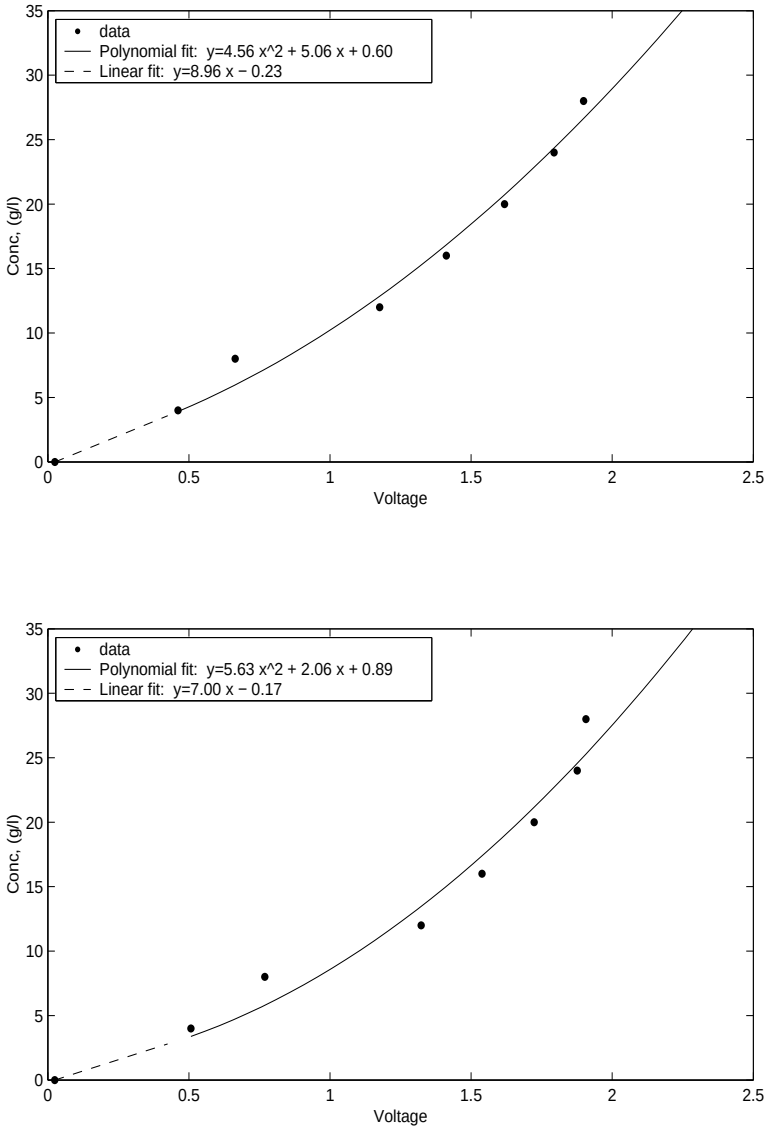

Figure 2.13: FOBS 1 and 2 calibration before the start of the accretion test.

Table 2.4: Average incident and reflected spectral and time series parameters for tests 1 through 23, 24 through 43, and all tests.

mean	$\bar{\eta}$(cm)	$\sigma_\eta(cm)$	Incident spectral		Reflection	Incident Time Series	
			H_{mo} (cm)	T_p (s)	coefficient	H_s (cm)	T_s (s)
1 to 23	-0.16	4.45	17.5	2.57	0.171	17.2	2.24
24 to 43	-0.16	4.61	18.1	2.57	0.158	17.9	2.25
all tests	-0.16	4.53	17.8	2.57	0.165	17.5	2.24

2.1.9 Data collection

Data from all instruments was synchronously collected using a 16 channel National Instruments data acquisition board. The wave maker was also wired to the data acquisition board. The wave maker voltage signal was transmitted at 20 Hz. All data was sampled at 20 Hz for the 400 s burst duration. The initial transition period of 20 s starting from the point of no wave action at time $t = 0$ was removed from each time series for all subsequent statistical and spectral analyses.

2.1.10 Incident and reflected waves

The repeatability of the wave conditions was checked by separating the incident and reflected waves for each of the 43 runs for the erosion test. The separated incident and reflected wave spectra were plotted together for the first 23 runs as is shown in Figure 2.14. The spectra were smoothed using band averaging with 16 degrees of freedom. The spectra were virtually identical, proving the repeatability of the tests. Table 2.4 shows the average values of the incident and reflected wave spectral and time series parameters, where H_{mo} is the spectral significant wave height, and H_s and T_s are the significant wave height and period based on a zero-upcrossing method. The reflection coefficient is estimated using the method described by Kobayashi *et al.* (1990)

Wave conditions for the last 20 bursts (imaging experiment) did not change

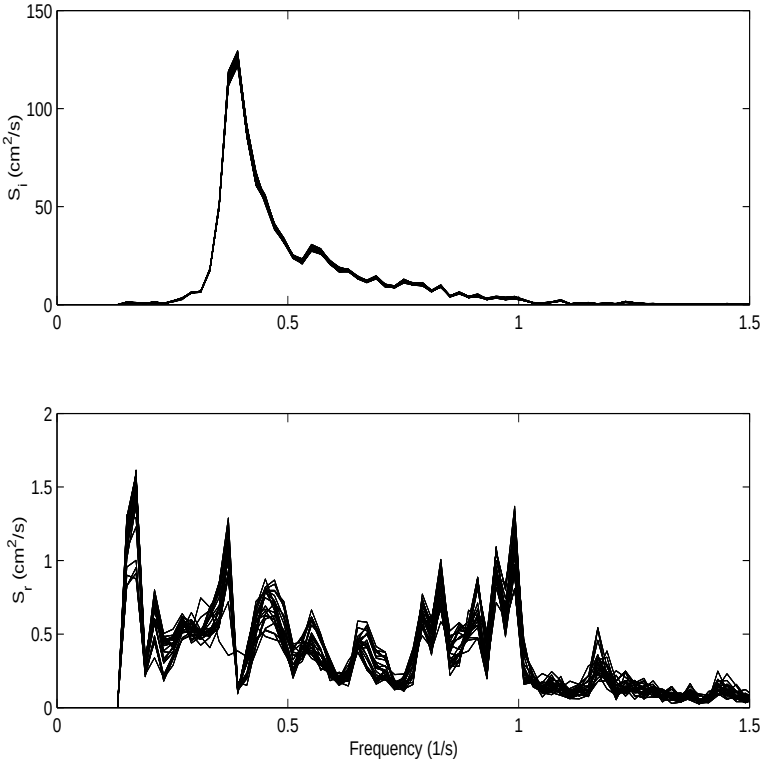

Figure 2.14: Incident and reflected wave spectra for the erosion test.

significantly, and will be considered only in a mean sense for the evaluation of profile change. A similar analysis was performed for the accretion test, and the results are shown in Figure 2.15 and Table 2.5

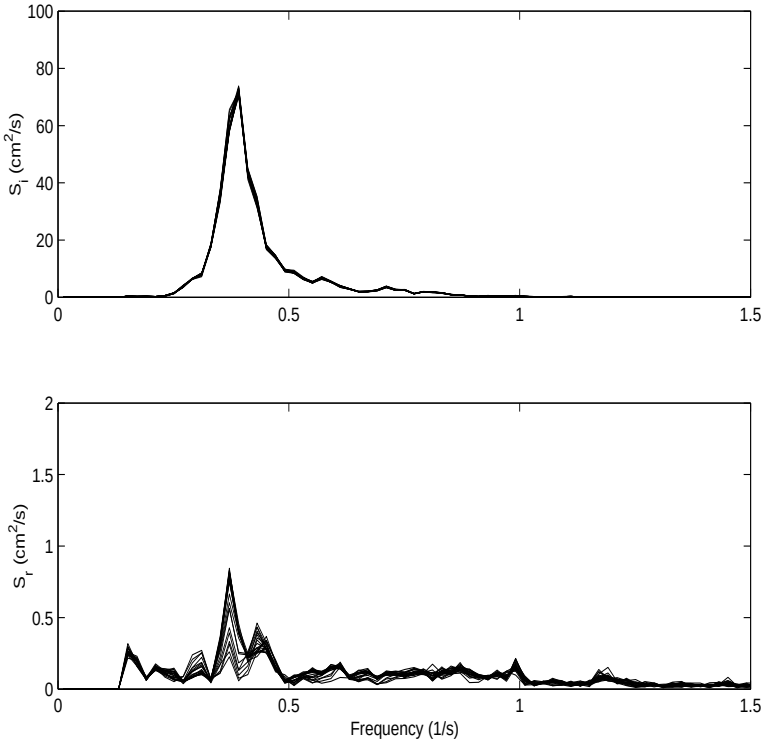

Figure 2.15: Incident and reflected wave spectra for the accretion test.

Table 2.5: Average incident and reflected spectral and time series parameters for all accretion tests.

mean	$\bar{\eta}$(cm)	$\sigma_\eta(cm)$	Incident spectral		Reflection coefficient	Incident Time Series	
			H_{mo} (cm)	T_p (s)		H_s (cm)	T_s (s)
all tests	-0.067	2.87	11.16	2.68	0.14	10.99	2.47

2.2 Experimental imaging techniques used to evaluate sediment suspension

Measurements of sediment concentration in laboratory physical models is traditionally performed with point source collectors and involve optical transmitting, optical and acoustic backscattering, and laser diffraction particle analyzing among others (Okayasu *et al.*, 2004). As in field measurements, point measurements in the lab are not sufficient to understand the significant spatial and temporal variability of suspension events. It is therefore necessary to develop a non-intrusive measurement technique, that can in addition encompass two dimensions of the flow.

For quantifying sediment motion, the technique, Particle Image Velocimitry, has been used in moderate effectiveness to actually track each individual sediment particle through a spatial image, usually in an $x - z$ plane. Ahmed and Sato (2001) discuss this technique in the bottom boundary under sheet flow conditions. Limitations arise from the need for uniform seeding, fairly large particles that may not act as they would in the field. Acoustic methods have also been employed to analyze sediment suspension in the lab with partial success (Adams *et al.*, 1998). Okayasu et al. (2004) developed a method that is not intrusive to the flow field and two dimensional in nature. Computed Tomography consists of laser and photo diodes that measure the distribution of concentration and transmit this information through the side walls of the flume. They found a linear relationship of light attenuation with sediment concentration, and the method works well to quantitatively evaluate sediment concentration. Investigations have also been made into sand suspension at the crest of bed ripples using a laser-illuminated technology (Crawford and Hay, 1998). This technique produced images of sediments shedded from ripples that are similar to those produced in this study, however in this study, the area under examination was a large area encompassing the entire water column over an offshore sandbar.

This experiment attempted to quantify the sediment suspension in the water

column using imaging techniques. The use of satellite imagery in the quantification of surface sediment concentration has proven effective within 20% error of in situ OBS measurements (Ruhl *et al.*, 2001). In a similar vein, but on a laboratory scale, the present method attempted to correlate in situ FOBS measurements with brightness values in addition to determining several pseudo quantitative values with relation to length and time scales of suspension events. Similarly to field based remote sensing, a spatial map of sediment concentrations could do much to understand the evolution and nature of suspension events. Much of what happens near the bed in the sheet flow layer is unknown. Imagery techniques can also help to narrow the range of empirical coefficients used in existing models.

2.2.1 Experimental configuration

This experiment was conducted in the same experimental environment that was described in 2.1. Repeatable irregular waves, based on the TMA spectrum with the spectral peak period, T_p, of 2.6 were propagated at an offshore water depth of 90 cm in 400 s bursts. These waves have the same period and wave height as those used in the erosion test of the previous section.

A SONY DFW-X710 camera and a Pentex 6.0 mm lens were used to collect image data at 10 Hz. The coordinate system for the experiment was set with x=0 at the position of wave gauge 1, which remains unchanged from the profile change experiments. y=0 at the interior side of the double-paned glass on the exterior of the tank with negative values inside the tank to ensure a left-handed coordinate system. z=0 at the still water level, which was kept at 90 cm throughout the experiment. The camera was positioned at x=5.3 m, y=1.24 m, and z=3.7 cm. Uniform lighting conditions were available since all ambient light was blocked out of the basement, where the experiments were run. Immediately above the experimental section, three halogen lights were placed equidistant from each other at 30 cm intervals. They

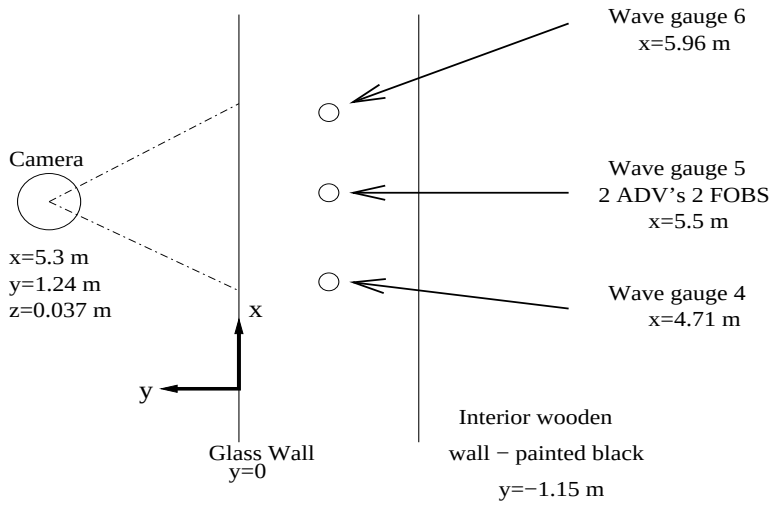

Figure 2.16: Configuration for the imaging experiment. The camera had a field of view encompassing the three gauges. ADVs and FOBS were placed at the position of wave gauge 5.

encompassed the entire camera's field of view. Figure 2.16 shows the image field of view and camera position.

In addition, three offshore gauges were placed in the same positions as stated in section 2.1.6. The three offshore wave gauges were used to separate the incident and reflective waves, and to test the repeatability of the generated waves. Suspended sediment concentrations were taken in 1 cm increments from 1 cm above the bed to 8 cm above the bed. Two Acousitc Doppler Veolcimeters (ADV) were used to measure the fluid velocities at two alongshore locations at the same cross shore and vertical location as the two FOBS sensors. The sampling rate for all in situ instrumentation was 20 Hz. The instrumentation was calibrated in the same way as described in Section 2.1.8.

2.2.2 Image collection

A total of 4500 images were collected over each 400 s burst. Each image was collected at a resolution of 1024 by 768 pixel length. Figure 2.17(1) displays an example of a collected image. The images were collected using the Fire-I software, which was set to collect at a 5 μs exposure time, with a temporal sampling rate of 10 Hz. The temporal sampling rate was determined to actually be between 9 and 9.2 Hz. The image files contain a time stamp in milliseconds, and when it was examined, it turned out that the time between images was approximately 110 ms. An interpolation scheme is used to synchronize the time signals between the in situ data and the camera data. This is discussed further in section 2.2.4.1.

When using imaging techniques to obtain quantitative data, the system must be understood. Three important components to an image collection technique are the lens, sensor, and collection mechanism (Erikson and Hanson, 2005). Light is transmitted through the lens to the camera sensor, or CCD, which measures the transmitted energy. This is then passed to the collection mechanism which calibrates and records the resulting image signal. Distortion due to the lens used is an important parameter in image collection, the curved nature of the lens, and imperfections in its curvature, cause straight lines to appear curved in an image. This distortion is almost always radially symmetric (Erikson and Hanson, 2005)and must be accounted for if spatial accuracy is needed in the analysis. The CCD "collects" the amount of light passed through the lens, and concerts this to a digital form, which is then collected and written to a file that appears as an image file, such as a JPEG file. When loaded into a processing software such as MATLAB, the image appears as a three dimensional matrix, containing layers related to three colours, red, green, and blue.

2.2.3 Image rectification

In order to analyze the data from the collected images, it was necessary to transform the images into a Cartesian coordinate system from the image coordinate system based on the resolution of the image. Stable and proven transformation schemes use a two-step process, where the transformation is dependent on two types of parameters, intrinsic and extrinsic (Holland *et al.*, 1997). Extrinsic parameters consist of the camera position and orientation relative to the coordinate system. Intrinsic parameters are dependent on the equipment used such as the lens distortion, the camera, and the acquisition system. The two-step method here uses a closed-form solution for the external parameters and focal length and an iterative process to compute the remaining parameters (Holland *et al.*, 1997).

Before the camera system was used in the laboratory experiments described above, the intrinsic parameters of the camera and lens were determined. These included the horizontal and vertical scaling factors, the lens distortion coefficients, and the coordinates of the plane center of the image. They were determined using a fixed grid of black background and white dots of known spacing and diameter. These parameters were fixed for the resulting rectification scheme. The parameters were found to be unchanging for the same combination of lens and camera, and thus the one time determination of these parameters is acceptable (Holland *et al.*, 1997).

Knowing the intrinsic parameter values reduces the unknown parameters from 11 to 7. Given control points with known Cartesian coordinates, and the corresponding image coordinates, the unknown parameters can be determined using an iterative minimization technique. For the purposes of this experiment, 6 control points were used. Figure 2.17 is used to explain the steps of the algorithm employed to extract suspension data from the raw images. The flowchart starts at the top left corner, and ends in the bottom left corner. Each figure displayed from step 2 through step 5 is displayed in Cartesian, x and z, coordinates with a range of x from

4.8 m (right) to 5.9 m, (left) and z from -0.4 m (bottom) to 0.4 (top). Each step, starting with rectification is displayed. The control points used in the rectification are displayed in Figure 2.17(1a). Three of these points were placed in the plane y=0. The other points were in the plane z=0, at the points where the instruments intersect with the still water level. As can be seen in Figure 2.17, there were more points with determined coordinates, o's, than were used in the iterative scheme. This is due to the fact that over-specification of the system leads to unreasonable geometries. The calculated camera position was within 2 cm of the measured position, which is reasonable given the measurement margin of error. It is seen from the image, that the algorithm predicts the control points within a 4 pixel, or approximately 4 mm accuracy, which is acceptable for the purposes of this analysis since conventional wave gauges have a maximum accuracy of within 4.5 mm (Erikson and Hanson, 2005). With the final seven parameters solved for, the total geometry of the image could be determined, and using these parameters could be translated into xyz coordinates using the method described in Holland *et al.* (1997).

4500 images were collected for each time series of waves. Not all of the time series were used in the analysis to follow. However, all 4500 images were rectified for the two time series that were analyzed. It took approximately 2.3 seconds per image, for a computational time of approximately 3 hours per image set. An example of one grayscale version of the raw images collected is shown in Figure 2.17(1). The rectified images is shown in Figure 2.17(2). It can be seen in this example, that the rectified image is flattened in comparison to the raw image, with the corners stretched out to account for the lens distortion. The rectified images are the images that will hereafter be used for the analysis of the images. The rectified image and all subsequent images will be discussed in terms of the real world Cartesian coordinate system, x and z, rather than the image coordinate system of u and v, which is determined by the resolution.

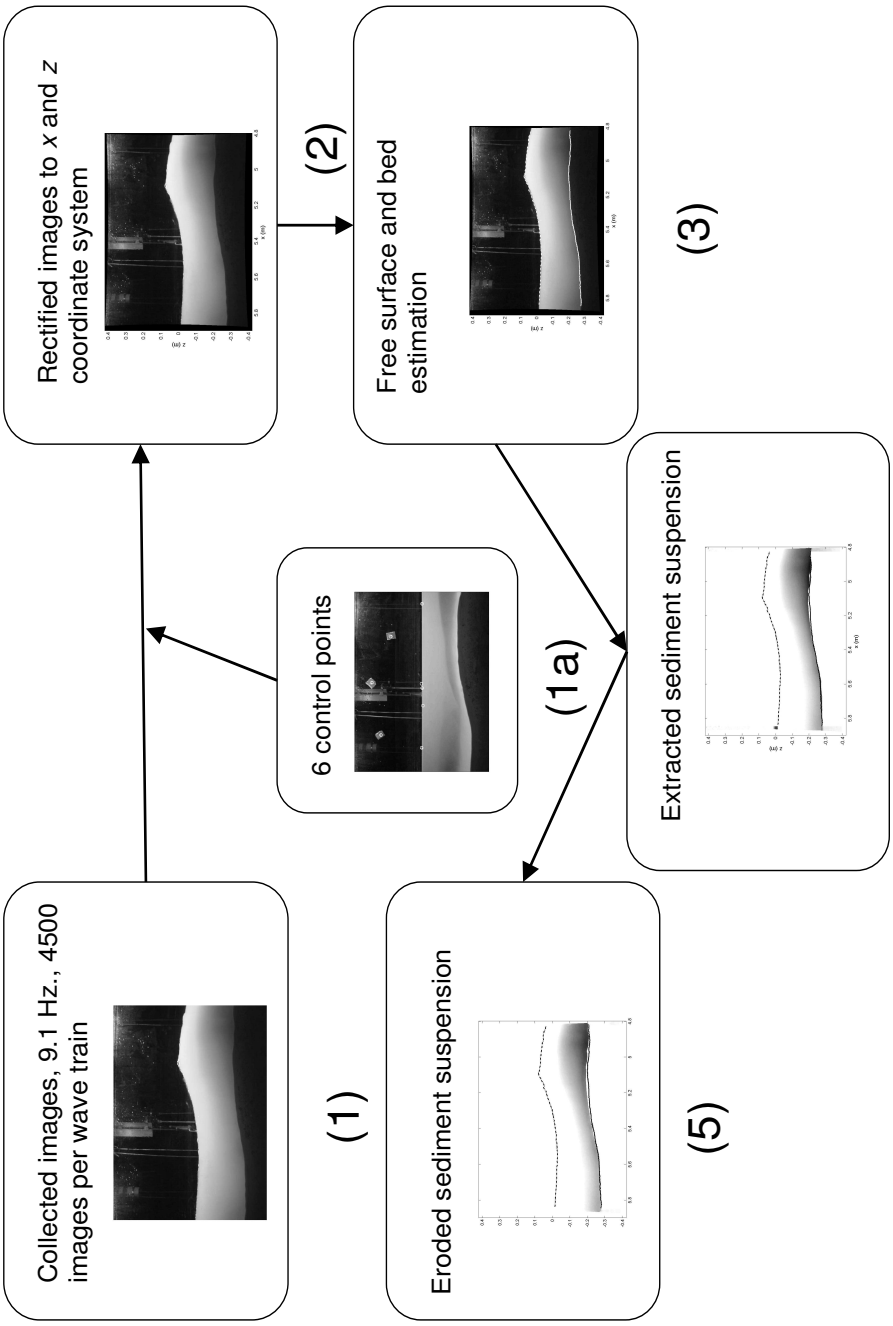

Figure 2.17: Flowchart of pre-processing techniques

2.2.4 Algorithm development

There were three major stages of processing. First, the instantaneous free surface and bed were estimated. Second, to isolate suspension events, the ensemble averaged mean pixel values were subtracted from the instantaneous water column values. Third, post-processing morphological filtering techniques were used to eliminate computational noise. Following these steps, it was possible to visualize the isolated suspension events throughout a sequence of snapshots of irregular waves.

2.2.4.1 Free surface and bed tracking

Free surface tracking mechanisms are not new in the field of imaging analysis (Erikson and Hanson, 2005; Jiang *et al.*, 1998; Foote *et al.*, 2002). For the purposes of this analysis, we did not require a high degree of accuracy, as more important is the trend of the data. Suspension events are a large feature within the water column, and the estimation of the free surface and bed were used as a rough boundary for the analysis. Therefore, a simple gradient method was implemented to find the highest change between neighboring pixels in the grayscale image. Due to the high contrast between the air-water interface, and the water sand interface, the gradient algorithm worked without the need to laser illumination or seeding particles which are often used to extract the free surface (Jiang *et al.*, 1998).

The algorithm is implemented within MATLAB 7.1 R14. A MATLAB function was written to return the pixel values of the tracked surface and bed, given the following inputs: condition of tracking bed or surface, name of the image file, starting low and high pixel value - range in which the first point of the free surface or bed can be found, a threshold for distance between two points, and a gradient threshold. The algorithm was created to be entirely automated and modular.

While the detection algorithm was based on a gradient method such as those found in the MATLAB edge detection function such as the Canny or Roberts methods, it was given an initial range of values to search for the highest gradient so as

to reduce computational time and to further specify the edge. The distance and gradient thresholds were used to ensure that the function did not recognize edges not related to the free surface and the bed, such as image noise, or equipment placed in the field of view. Typical results of the free surface detection and bed detection for one image are shown in Figure 2.17(3).

All of the cases cited above used instrumentation in addition to extracting the free surface from the image. However the air-water interface in their studies was well-defined. Erikson and Hanson (2005) concentrated their efforts in the swash zone, while Crawford and Hay (1998) used a laser to investigate ripple suspension. The tracking of the free surface under intense breaking waves is more difficult due to the significant region of air entrainment. Observations have shown that as much as 20% of the volume of a plunging breaker can be made up of air (Miller, 1972). In this study, the free surface was secondary to the determination of sediment suspension and computational effort was not expended to demand perfect accuracy for the free surface. Figure 2.18 shows one minute of free surface measurements from both a wave gauge in the field of view, and the time series extracted from the image at the same location. The R^2 value was 0.77 with a linear regression coefficient of 0.81. This deficiency is due to the choice of the image free surface boundary as the highest gradient highest gradient. Since there is air entrained in the plume, the wave gauge finds the surface somewhere in the middle of this plume, and not at the top, where the image finds the highest gradient. The free surface boundary between air and water is questionable. This was not a problem for Erikson and Hanson (2005) due to the fact that their free surface was stable, with a solid boundary between air and water.

In order to analyze the effect of this, k is set to be the relationship of the wave amplitude to the water depth, where the amplitude is assumed to be the distance between the crest of the wave and the still water level for simplicity, $k = a/h$.

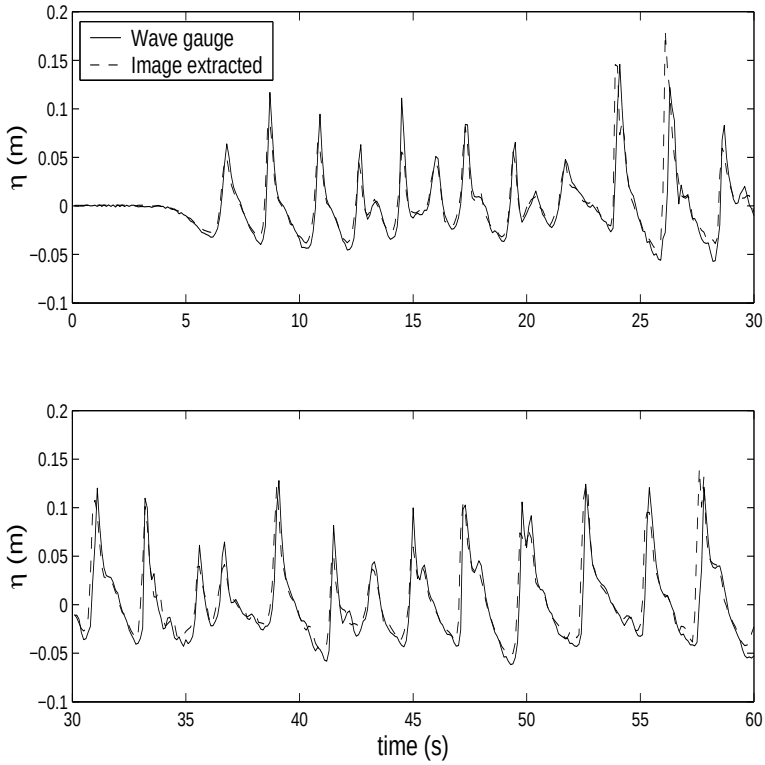

Figure 2.18: Comparison of wave gauge and extracted free surface from the image for one minute of waves. Solid line indicates wave gauge data, and slashed line shows free surface extracted from the image.

Boundary values for k were chosen as 0.4 and 0.5. All time series points with k values greater than these points were eliminated from the analysis. With $k = 0.5$, the R^2 value between the instantaneous wave gauge measurements and the extracted image value of the free surface was 0.75 and the regression coefficient was 0.95. With $k = 0.4$, the regression coefficient increased to 0.98, and $R^2 = 0.78$. This shows good correlation and an virtually linear relationship between the extracted time series and the wave gauge values. Therefore, this method was determined to be adequate for estimating the free surface in this analysis.

The free surface and bed detected using this algorithm are used in separating the suspended sediment from the rest of the image. Since the area above the free surface and below the bed are not used to analyze suspension events, these areas are set to zero for the remainder of the analysis.

2.2.4.2 Sediment plume extraction

The goal of the algorithm is to isolate sediment suspension events from the water column as they occur under breaking waves. In digital intensity images, such as a grayscale image, there is a discrete range of values from 0 (black) to 255 (white). Due to gradation, sediment plumes appear darker, or have a lower intensity value in the image matrix than the surrounding water column. In order to isolate the suspension events from background wash-load or fines suspension, a base image was created. This base image is an average of the last 20 images in the 4500 image series. The wash load, or fines suspension remains in suspension through this time period. Ensemble averaging the last 20 images gives an average of the wash load in the water column. This assumes that the bed did not change significantly during the course of 400 seconds. This was in fact the case, since the profile was almost at equilibrium. This averaged, base image was subtracted from each instantaneous image. Each image was inverted such that sediment plumes becomes positive. All negative pixel values are then set to zero to isolate the sediment plume.

The above process results in an intensity image that displays the sediment plume shown in Figure 2.17. The values were inverted to a white background for visual effect, however the analysis continues with zero values (black) indicating no suspension. This method tends to leave computational artifacts near the free surface, especially in the wave trough region which is lower than the free surface in the base image and also appears as regions of extremely high intensity in comparison to the sediment plume. Therefore, additional methods need to be employed to eliminate these image artifacts.

2.2.4.3 Morphological filtering

In order to compensate for the image processing artifacts that are found near the free surface, morphological operators found within MATLAB's image processing toolbox were employed. Morphological filtering in image analysis compares individual pixel values to their neighboring pixels. They use a structuring element to define the neighborhood of comparison using binary elements of 0 and 1. Erosion of the neighborhood removes pixels on the boundary of the neighborhood, while dilation adds pixels to the boundaries. Morphological filters are commonly employed in remote sensing applications to reduce noise in SAR images and to extract ocean features (Simhadri *et al.*, 1998; Soille and Pesaresi, 2002).

The images were first eroded six using a disk operator structuring element of radius two. The images were eroded 6 times to ensure the elimination of free surface noise. An example of the morphologically altered suspension event is shown in Figure 2.17(5). This image has also been inverted for visual effect so that white areas indicate no suspension, and dark areas indicate areas of sediment suspension, however computationally, areas of no suspension still retain zero pixel values (black). Note that the computational noise at the free surface was removed, making the sediment suspension easy to analyze throughout the entire image. The pixels of sediment suspension events have positive matrix values, giving it brightness, whereas

background suspension, fines, water, the regions above the free surface and below the bed have values of zero. The images throughout this section and chapter 6 are all inverted for visual effect, but were analyzed as discussed.

Chapter 3

DATA ANALYSIS

As described in Chapter 2, two tests were conducted demonstrating erosive and accretive conditions. The data analysis for these two tests is described in section 3.1. In addition, three tests from the LIP 11D Delta Flume Experiments (Roelvink and Reniers, 1995) were used in the model comparisons in Chapter 5, and the analysis for these tests is also described in section 3.2.

3.1 Small-scale laboratory tests

The experimental setup and procedures for the small scale laboratory experiments are described in Chapter 2. The collected data were analyzed to determine the quantities used in evaluating model performance. The following sections describe the extraction of free surface elevation,η, velocity, U, concentration, C, suspended sediment volume,V_s and the suspended sediment transport rate, q_s.

3.1.1 Free surface

As shown in Figure 2.7, wave gauges were positioned at 8 locations for each of the two tests conducted in the 30 m wave flume. Samples were taken at 20 Hz for 400 second wave bursts. The first 20 seconds of data were removed from all time series, since it encompassed the initial transition to the wave bursts. Overbars will designate time-averaging for the remaining 380 s. In Table 3.1 the average wave conditions at the most offshore wave gauge, at x=0 are shown for both the

erosion and accretion tests where the wave conditions for each burst are presented in Appendices A and B.

Table 3.1: Average wave conditions at wave gauge 1 for accretion and erosion tests

test (s)	**Burst Duration (s)**	**d (cm)**	$\overline{\eta}$ **(cm)**	$\mathbf{H_{rms}}$ **(cm)**	$(\mathbf{H_{rms}})_\mathbf{i}$ **(cm)**	**Reflection Coefficient**
Erosion	400	76.0	-0.16	12.8	12.6	0.17
Accretion	400	77.2	-0.067	8.12	7.9	0.14

The mean water depth, $\overline{h}$ is defined as the sum of $\overline{\eta}$ and d, the water depth in still water, while the root-mean square wave height, H_{rms} is $H_{rms} = \sqrt{8}\sigma_\eta$. The values of the total and incident root-mean square wave height are also shown in Table 3.1. It can be seen that H_{rms} was significantly lower for the accretion test. This height was intentionally decreased to induce onshore bar movement. Three wave gauges offshore were used to separate the incident and reflected waves using linear wave theory (Kobayashi *et al.*, 1990). The reflection coefficient, $R = (H_{rms})_r/(H_{rms})_i$, where the total, H_{rms}, includes both the incident and reflected components, and is approximately the same as $(H_{rms})_i$.

Free surface measurements were made at the 8 cross-shore locations. The time-averaged mean of the free surface, or wave setup, $\overline{\eta}$, standard deviation of the free surface, σ_η, and depth, d, for each test and their cross-shore location are displayed in Appendices A and B.

Wave breaking for both tests was concentrated in the bar region, at wave gauge 4, x=5 m. The intensity of the breaking was much greater, with larger plunging breakers for the erosion test than for the accretion test. The waves became bores through wave gauges 5 and 6, and then all waves broke on the steep face at wave gauge 8. The ripples for both tests, which were present in a three dimensional pattern offshore, and in a two dimensional pattern past the bar region, were about 0.7 cm in height and 8 cm in length.

3.1.2 Velocity measurements

Velocity measurements were taken at two cross shore locations for the erosion test, x=5.0 m and x=7.6 m. For the accretion test, velocity measurements were only taken at one cross-shore location, x=7.6 m. Measured velocities were collected using two sensors, giving two horizontal velocity time series, U_1 and U_2. These two velocities were in phase apart from high frequency perturbations due to turbulence. The average horizontal velocity,

$$U = (U_1 + U_2)/2 \tag{3.1}$$

is used to calculate the time-averaged mean, $\overline{U}$, and standard deviation, σ_U, of the horizontal velocity at each elevation from the bottom, z_m, and horizontal location, x. Measured values of $\overline{U}$ and σ_U are tabulated in Appendices A and B.

The mean horizontal velocity, $\overline{U}$, is negative for both cross-shore locations, representing an offshore undertow current. The variation in $\overline{U}$ did not display enough of a discernable vertical trend to fit a curve to the data, and therefore, the vertically-averaged values are used as a representation of the undertow current in these tests. The vertical variation of σ_U is negligible which is consistent with previous observations (e.g Guza and Thornton, 1980).

In order to estimate the time-averaged turbulent velocity, the method introduced by Trowbridge (1998), is used, expressing the measured velocities in the form,

$$U_1 = \overline{U_1} + u_w + u_1\prime \quad ; \quad U_2 = \overline{U_2} + u_w + u_2\prime \tag{3.2}$$

The wave component is assumed to be the same for both measured quantities, and the turbulent component is indicated by $u_i\prime$. If it is assumed that $\overline{u_1\prime^2} \simeq \overline{u_2\prime^2} \simeq \overline{u\prime^2}$ and $\overline{u_1\prime u_2\prime} \simeq 0$, then the turbulent velocity variance, $\overline{u\prime^2}$, can be approximated to be

$$\overline{u\prime^2} \simeq \frac{1}{2}\overline{[(U_1 - \overline{U_1}) - (U_2 - \overline{U_2})]^2}. \tag{3.3}$$

Using equation (3.2) in (3.1) gives

$$\overline{U} = (\overline{U_1} + \overline{U_2})/2 \quad ; \quad \sigma_U^2 = \overline{(U - \overline{U})^2} \simeq \overline{u_w^2} \ , \tag{3.4}$$

where u_w is much larger than the turbulent velocities. Alongshore velocities, V_1 and V_2, did not contain a wave component, so the turbulent velocity variance was estimated as the average of the two individual variances.

$$\overline{v\prime^2} \simeq \frac{1}{2}[\overline{(V_1 - \overline{V_1})^2} + \overline{(V_2 - \overline{V_2})^2}]. \tag{3.5}$$

The measured time-averaged velocities, $\overline{V_1}$ and $\overline{V_2}$ are nearly zero since there are no net alongshore currents. Therefore, the fluctuating or turbulent component of the alongshore velocity is what is of importance.

Contrary to the horizontal and alongshore velocities, the vertical velocity was only measured with one instrument. The intention of the two probes was mainly to compare horizontal and alongshore velocities near the bed. The measured vertical velocity was fairly small and with low sand concentrations, corresponds to the fluid velocities. With large concentrations, the vertical velocities are more affected by sand velocities, and is an intermediary between fluid velocities and sand velocities (Kobayashi *et al.*, 2005).

Assuming there is no correlation between the wave and turbulent components, the turbulent variance of the vertical velocity is estimated to be

$$\overline{w\prime^2} \simeq \sigma_W^2 - \left(\frac{2\pi\sigma_\eta}{T_p}\frac{z_m}{\overline{h}}\right)^2 . \tag{3.6}$$

The terms within the parentheses represent the wave velocity variance, which is estimated using linear long wave theory (Dean and Dalrymple, 1984) with measured values of σ_η and $\overline{h}$ at every cross shore location. The wave period is represented by the peak period. The turbulent velocity variances are tabulated in Appendices A and B.

The turbulent kinetic energy per unit mass can be calculated from the turbulent velocity variances.

$$k = \frac{1}{2}\overline{u\prime^2} + \overline{v\prime^2} + \overline{w\prime^2}. \tag{3.7}$$

Figures 3.1 and 3.2 show the comparison between the turbulent velocity variances and the turbulent kinetic energy. The following approximate relationships between the variances and the kinetic energy for the three tests by Kobayashi *et al.* (2005) turn out to hold for the erosion (E) and accretion (A) tests.

$$\begin{aligned} \overline{u\prime^2}/(2k) &\simeq 0.6, \\ \overline{v\prime^2}/(2k) &\simeq 0.3, \text{ and} \\ \overline{w\prime^2}/(2k) &\simeq 0.1, \end{aligned} \tag{3.8}$$

which are similar to the relationships associated with boundary layer flow (Svendsen, 1987).

3.1.3 Concentration analysis

Concentration was measured at two cross-shore locations in the erosion test, 5 m, and 7.6 m, and one cross-shore location in the accretion test, 7.6 m. It was measured at the same cross-shore and elevation position as the velocity measurements. Thus, the velocity and concentration can be correlated to be used to determine cross-shore transport. Measured volumetric values of concentration from each of two FOBS-7 sensors are designated, C_1 and C_2, where the volumetric concentration is equal to the measured concentration (g/l) divided by 2600 for the sand with a specific gravity of 2.6 in fresh water. High concentration events occurred simultaneously in both sensor time series. The average, $C = (C_1 + C_2)/2$ is used to calculate the time averaged mean concentration, $\overline{C}$ and the standard deviation, σ_C. The mean and standard deviation of the measured values for each test and their

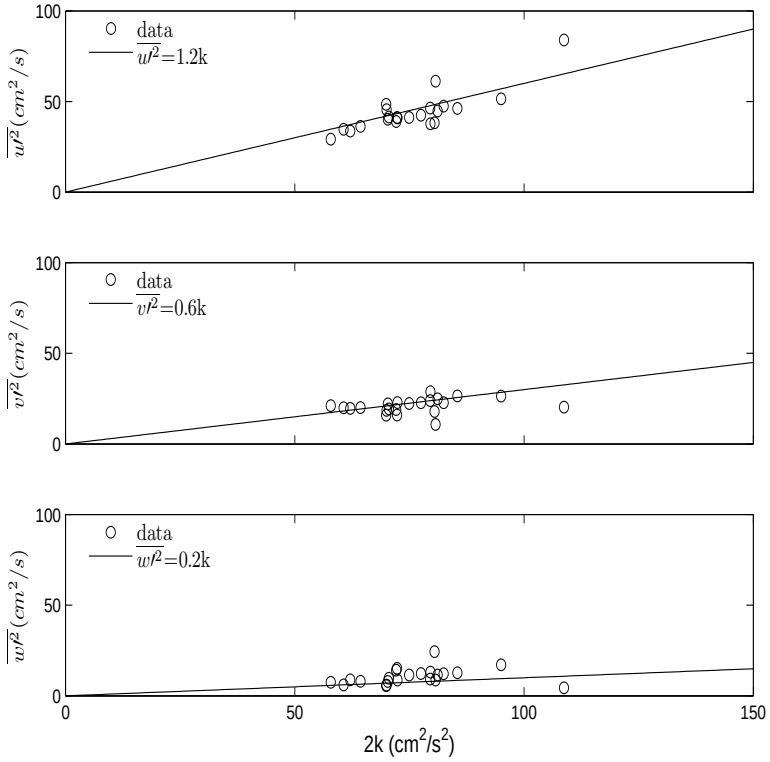

Figure 3.1: Test E: Turbulent velocities, $\overline{u\prime^2}$, $\overline{v\prime^2}$, and $\overline{w\prime^2}$, as compared to the turbulent kinetic energy per unit mass, 2k.

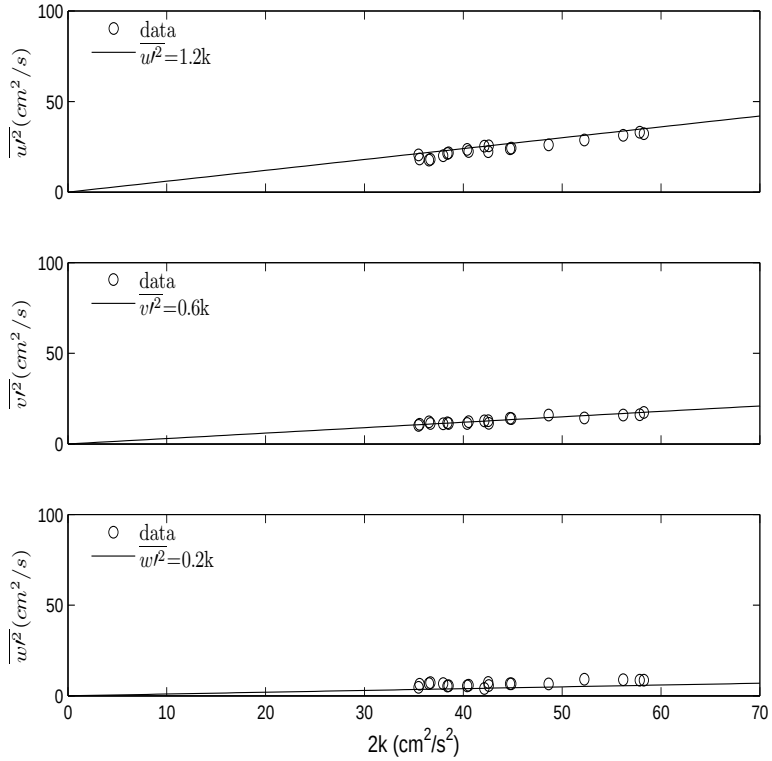

Figure 3.2: Test A: Turbulent velocities, $\overline{u\prime^2}$, $\overline{v\prime^2}$, and $\overline{w\prime^2}$, as compared to the turbulent kinetic energy per unit mass, 2k.

cross-shore location are found in Appendices A and B The correlation coefficient, γ_{UC} is calculated using equation (3.9),

$$\gamma_{UC} = \frac{\overline{(C-\overline{C})(U-\overline{U})}}{\sigma_C \sigma_U}. \tag{3.9}$$

The vertical distribution of $\overline{C}$ is evaluated using the standard diffusion approach (Nielsen, 1992). The vertical mixing coefficient, ϵ_v is assumed to be constant and includes both the wave-induced and turbulence effects. This gives the following vertical structure of $\overline{C}$,

$$\overline{C} = \overline{C_b}\exp(-z_m/l_c) \quad ; \quad l_c = \epsilon_v/w_f \tag{3.10}$$

where $\overline{C_b}$ is the extrapolated concentration at the local bed, $z_m = 0$. This exponential distribution of concentration has been shown to predict concentration profiles in the surf zone, (Peters and Dette, 1999) and over rippled beds (Ribberink and Al-Salem, 1994). However, assuming that $\epsilon_v = z_m v_C$, with v_C as the velocity scale of ϵ_v gives a power form distribution

$$\overline{C} = \overline{C_a}(z_a/z_m)^n \quad ; \quad n = w_f/v_c, \tag{3.11}$$

where $\overline{C_a}$ is the concentration at a reference elevation, z_a. In the tests used for this analysis, z_a was taken to be 1 cm from the local bed. The power form vertical distribution of sediment concentration has been shown to represent concentration profiles under sheet flow conditions in a water tunnel (Ribberink and Al-Salem, 1994). Both the exponential and power form distributions were fitted to concentration data for the accretion and erosion tests. These fits are shown in Figures 3.3 and 3.4, where n, l_c, $\overline{C_a}$, and $\overline{C_b}$ were fitted for each test and cross-shore location. Empirical fits for concentration can only predict the order of magnitude of the reference concentration (Dunkley *et al.*, 1999), and we can see from Figures 3.3 and 3.4 that the exponential

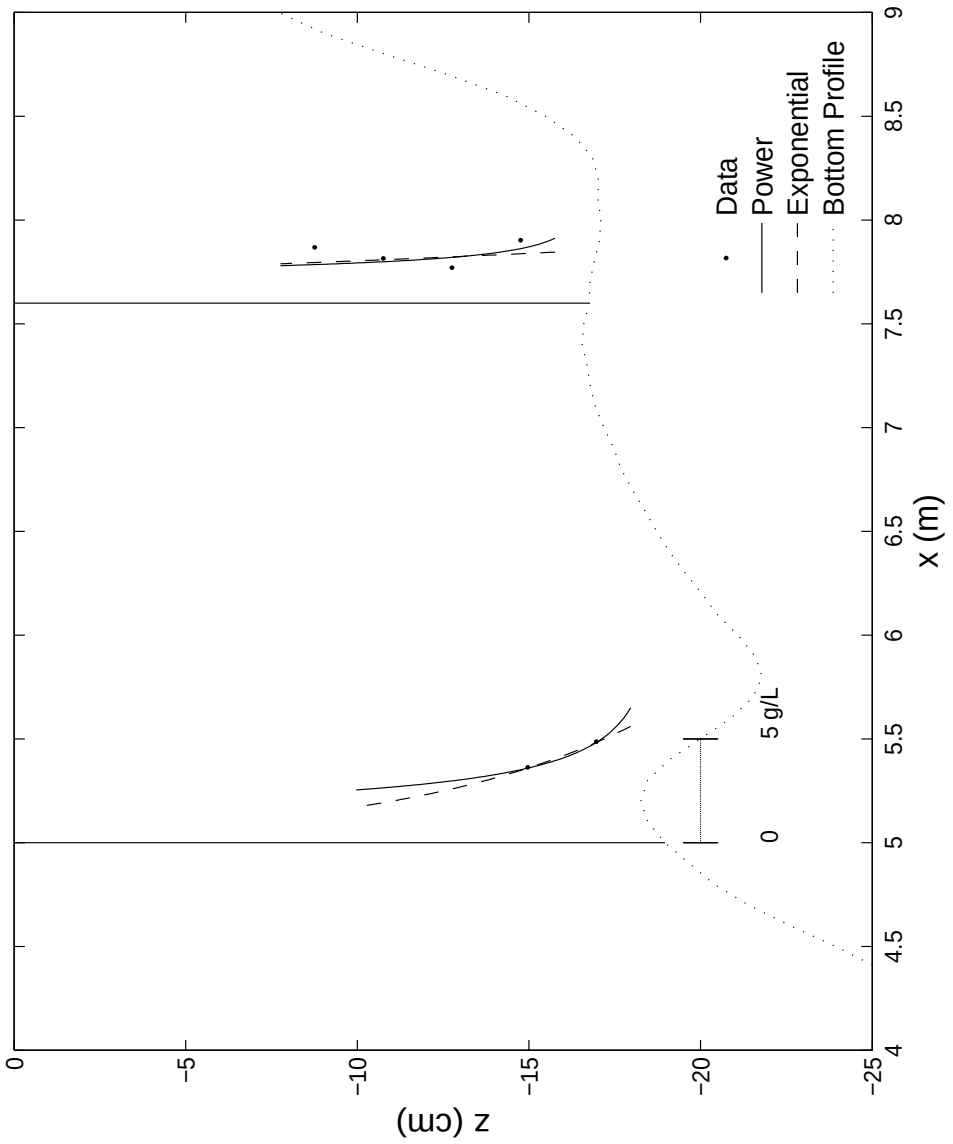

Figure 3.3: Test E: Measured and fitted exponential and power form profiles of mean concentration, $\overline{C}$, for cross shore locations $x = 5$ and 7.6 m.

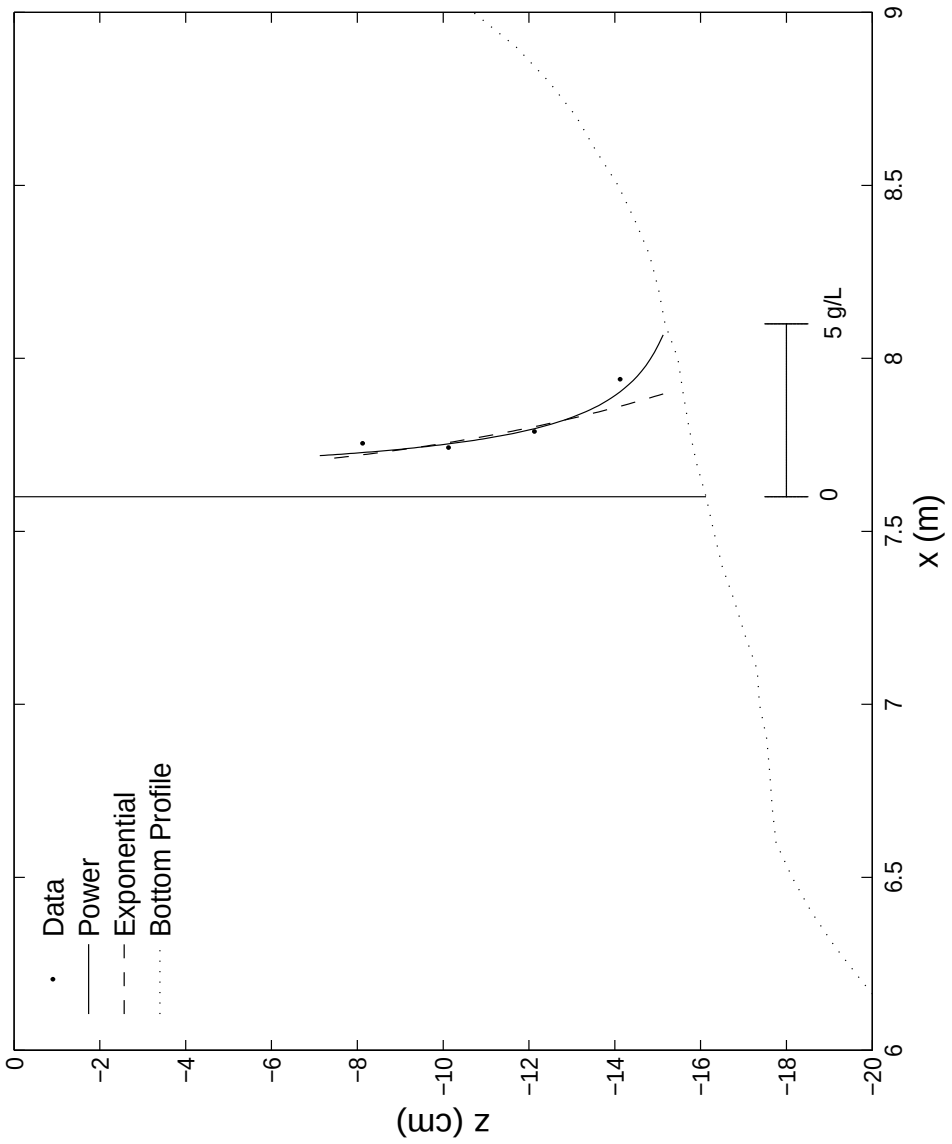

Figure 3.4: Test A: Measured and fitted exponential and power form profiles of mean concentration, $\overline{C}$, for cross shore locations $x = 7.6$ m.

fit loses significant concentration near the bed, therefore, the reference concentration of $\overline{C_a}$ and the power form fit are used to estimate the suspended sediment volume per unit area for comparisons with model results. The time-averaged suspended sediment volume per unit horizontal area can be predicted by integrating equations (3.10) and (3.11) from $z_m = 0$ or z_a to $\overline{h}$, the time-averaged water depth. Note that the power form fit cannot be extrapolated to $z_m = 0$, so the reference location, z_a is used.

$$\overline{V_b} = \overline{C_b} l_c [1 - exp(-\frac{\overline{h}}{l_c})] \quad ; \quad \overline{V_a} = \frac{\overline{C_a} z_a}{1-n} [(\frac{\overline{h}}{z_a})^{1-n} - 1] \tag{3.12}$$

The difference between $\overline{V_a}$ and $\overline{V_b}$ is less than 19% with the erosion test at wave gauge 4 having the worst agreement. Values related to the calculation of $\overline{V_a}$ and $\overline{V_b}$ are shown in Table 3.2 along with fitted parameters and the correlation coefficients (C.C.). The values of $\overline{V_a}$ are to compare to the computed V_s values in Chapter 5 and will subsequently be referred to as V_s.

Table 3.2: Fitted distribution of suspended sediment concentration and calculated volume for small scale erosion and accretion tests. Erosion 4 indicates FOBS-7 sensors at position of wave gauge 4, while Erosion 6 indicates FOBS-7 sensors at position of wave gauge 6.

test	$\overline{\mathbf{C_a}}$	**n**	$\overline{\mathbf{V_a}}$ (cm)	**C.C.** (power)	$\overline{\mathbf{C_b}}$	$\mathbf{l_c}$ (cm)	$\overline{\mathbf{V_b}}$ (cm)	**C.C.** (exp.)
Accretion	0.0018	0.6248	0.0088	0.80	0.0013	7.81	0.0089	0.79
Erosion 4	0.0025	0.4275	0.0183	0.95	0.0025	6.75	0.015	0.95
Erosion 6	0.0012	0.2520	0.0115	0.59	0.00098	30.46	0.012	0.34

In order to calculate suspended load quantities, of interest is the relationship between volumetric concentration, C, and horizontal velocity, U. The cross-shore

suspended sediment transport is analyzed using the $\overline{UC}$ quantity, which is defined by the following relationship

$$\overline{UC} = \overline{U}\,\overline{C} + \overline{(U-\overline{U})(C-\overline{C})} \tag{3.13}$$

Table 3.3 and 3.4 show the quantities related to the suspended sediment flux. NR designates unreliable experimental data where $\overline{U}\ \overline{C}$ is negative (offshore) due to $\overline{U} < 0$, and the last term related to the correlation between U and C is positive (onshore).

The vertical variation of $\overline{UC}$ was not apparent, so a vertically-averaged value of this quantity was used to determine the cross shore suspended sediment transport rate.

$$q_s = \overline{UC}\,\overline{h}. \tag{3.14}$$

Tabulated values of q_s are shown in Table 3.5, where the measured $\overline{q_s}$ was negative (offshore).

3.2 Large scale data

Large scale data obtained from the Delft LIP Delta Flume experiments was also analyzed for comparison with the numerical model developed in Chapter 4. This data is available in full form in Roelvink and Reniers (1995). The three tests analyzed included (Test 1a) with minimal profile change, (Test 1b) with erosional change, and (Test 1c) with accretional change. The median diameter of the sand was d_{50}=0.2 mm. The specific gravity and porosity are assumed as s=2.65 and n_p=0.4. The estimated fall velocity for the corresponding sphere is w_f=2.3 cm/s.

Waves were run for one-hour bursts for the duration of each test, with Test 1a lasting 12 hours, Test 1b lasting 18 hours, and Test 1c lasting 13 hours. Profiles were taken almost hourly during the course of each experiment. Cross shore profiles were taken in three lines, z_1, z_3, and z_5, and parabolically fitted using equation (3.15)

$$z_b = 0.407z_1 + 0.186z_3 + 0.407z_5 \tag{3.15}$$

Table 3.3: Suspended sediment fluxes for erosion test

test	x	z_m	$\bar{U}$	$\bar{C}$	$\bar{U}\bar{C}$	$\overline{(U-\bar{U})(C-\bar{C})}$	$\overline{UC}$
	(m)	(cm)	(cm/s)		(cm/s)	(cm/s)	(cm/s)
E1	7.6	8	-6.43	0.0017	-0.0111	0.0011	-0.0101
E2	7.6	8	-6.01	0.0010	-0.0062	0.0005	-0.0057
E3	7.6	6	-6.36	NR	NR	NR	NR
E4	7.6	6	-7.01	0.00068	-0.0048	0.0009	-0.0039
E5	7.6	6	-6.86	0.00085	-0.0058	0.0007	-0.0051
E6	7.6	6	-6.56	0.00085	-0.0056	0.0008	-0.0047
E7	7.6	6	-6.24	0.00084	-0.0052	0.0009	-0.0043
E8	7.6	6	-5.90	0.00088	-0.0052	0.0006	-0.0046
E9	7.6	6	-5.93	0.00084	-0.0050	0.0007	-0.0043
E10	7.6	6	-6.32	0.00086	-0.0054	0.0008	-0.0046
E11	5.0	4	-8.44	0.00132	-0.0111	0.0069	-0.0042
E12	5.0	4	-8.40	0.00147	-0.0123	0.0076	-0.0048
E13	5.0	2	-7.13	0.00196	-0.0140	0.0113	-0.0027
E14	5.0	2	-5.91	0.00179	-0.0106	0.0110	0.0004
E15	7.6	4	-6.76	0.00048	-0.0032	0.0009	-0.0024
E16	7.6	4	-6.78	0.00056	-0.0038	0.0010	-0.0028
E17	7.6	4	-6.39	0.00070	-0.0045	0.0010	-0.0035
E18	7.6	4	-6.75	0.00071	-0.0048	0.0013	-0.0035
E19	7.6	2	-6.93	0.00103	-0.0071	0.0025	-0.0046
E20	7.6	2	-5.80	0.00098	-0.0057	0.0025	-0.0032
E21	7.6	2	-6.30	0.00117	-0.0074	0.0032	-0.0042
E22	7.6	2	NR	0.00127	NR	NR	NR
E23	7.6	2	-5.77	0.00138	-0.0080	0.0036	-0.0044

Table 3.4: Suspended sediment fluxes for accretion test

test	x	z_m	$\bar{U}$	$\bar{C}$	$\bar{U}\bar{C}$	$\overline{(U-\bar{U})(C-\bar{C})}$	$\overline{UC}$
	(m)	(cm)	(cm/s)		(cm/s)	(cm/s)	(cm/s)
A1	7.6	4	-4.07	0.00093	-0.0038	0.0008	-0.0029
A2	7.6	4	-4.89	0.00094	-0.0046	0.0007	-0.0039
A3	7.6	4	-4.15	0.00068	-0.0028	0.0007	-0.0021
A4	7.6	4	-4.67	0.00084	-0.0039	0.0008	-0.0031
A5	7.6	6	-3.76	0.00055	-0.0021	0.0006	-0.0015
A6	7.6	6	-3.81	0.00055	-0.0021	0.0005	-0.0016
A7	7.6	6	-4.15	0.00057	-0.0024	0.0006	-0.0018
A8	7.6	8	-2.79	0.00047	-0.0013	0.0004	-0.0009
A9	7.6	8	-3.76	0.00058	-0.0022	0.0004	-0.0018
A10	7.6	8	-3.14	0.00064	-0.0020	0.0004	-0.0016
A11	7.6	8	-3.31	0.00069	-0.0023	0.0004	-0.0019
A12	7.6	2	NR	0.0011	NR	NR	NR
A13	7.6	2	-5.01	0.0016	-0.0080	0.0021	-0.0059
A14	7.6	2	-4.50	0.0013	-0.0057	0.0014	-0.0043
A15	7.6	2	-4.28	0.0013	-0.0054	0.0011	-0.0043
A16	7.6	4	-4.58	0.00049	-0.0022	0.0006	-0.0016
A17	7.6	4	-4.02	0.00048	-0.0019	0.0005	-0.0014
A18	7.6	6	-3.62	0.00044	-0.0016	0.0003	-0.0013
A19	7.6	6	-3.81	0.00056	-0.0021	0.0005	-0.0016
A20	7.6	6	-4.07	0.00061	-0.0025	0.0004	-0.0021

Table 3.5: Suspended sediment transport rate for small scale erosion and accretion tests. Erosion 4 indicates FOBS-7 sensors at position of wave gauge 4, while Erosion 6 indicates FOBS-7 sensors at position of wave gauge 6.

test	$\overline{\mathbf{UC}}$ (cm/s)	$\overline{\mathbf{h}}$ (cm)	$\overline{\mathbf{q_s}}$ (cm^2/s)
Accretion	-0.0024	16.24	-0.039
Erosion 4	-0.0028	16.33	-0.046
Erosion 6	-0.0045	16.23	-0.074

Measured profiles for the three tests are displayed in comparison to the model results in Chapter 5. During Test 1a, profiles were taken at 0, 2, 3, 4, 5, 6, 7, and 12 hours. During Test 1b, profiles were taken at 0, 1, 2, 3, 4, 5, 6, 7, 8, 9, 12, and 18 hours. During Test 1c, profiles were taken at 0, 1, 2, 3, 4, 7, 10, and 13 hours.

For comparison with the model, the free surface measurements obtained with the offshore wave gauges were used. 5 current meters, and 10 suction samplers were placed on a movable cart to measure velocities and mean concentrations respectively, and were fixed in one position for each hour of waves. The positions of the cart for tests 1a, 1b, and 1c are shown in Table 3.6. NaN indicates that data was not provided for this wave hour. For each test, one wave gauge was placed 20 m from

Table 3.6: Location of instrument carriage for all tests

test	**x(m)**	**test**	**x(m)**	**test**	**x(m)**
1a.1	45	1b.1	45	1c.1	45
1a.2	80	1b.2	82	1c.2	95
1a.3	95	1b.3	95	1c.3	82
1a.4	110	1b.4	110	1c.4	110
1a.5	118	1b.5	118	1c.5	105
1a.6	125	1b.6	NaN	1c.6	114
1a.7	132	1b.7	125	1c.7	118
1a.8	140	1b.8	132	1c.8	125
1a.9	136	1b.9	140	1c.9	152
1a.10	121	1b.10	150	1c.10	140
1a.11	82	1b.11	45	1c.11	150
1a.12	NaN	1b.12	82	1c.12	NaN
		1b.13	NaN	1c.13	NaN
		1b.14	NaN		
		1b.15	95		
		1b.16	110		
		1b.17	118		
		1b.18	NaN		

the wavemaker. For the purposes of comparison, this is defined to be x=0. z=0 is

defined at the still water level, with 4.1 meters of offshore water depth for all three tests.

The sand used in this experiment had a d_{50} of 0.2 mm. Using the standard specific gravity for sand of 2.65, the fall velocity was calculated to be 2.3 cm/s by using the relationship of Madsen and Grant (1976)

$$\frac{w_f}{\sqrt{(s-1)gd_{50}}} \text{ as a function of } S_* = \frac{d_{50}}{4\nu}\sqrt{(s-1)gd_{50}} \tag{3.16}$$

which is valid for spherical particles. This value was checked with fall velocity curves for sand particles in fresh water of 10 and 18 degrees Celcius.

3.2.1 Wave gauge data

Measurements were taken with three wave gauges for each test. One wave gauge was always located offshore at 20 m from the wave maker, taken to be x=0. The values of the mean free surface elevation and the standard deviation of the free surface are presented in Roelvink and Reniers (1995) and are displayed in Appendices C through E.

3.2.2 Velocity data

Velocity measurements were taken by five current meters measuring horizontal and alongshore velocities at varying elevations from the bed. The cross shore position of the velocity measurements are shown in Table 3.6. Velocity measurements were collected at 10, 20, 40, 70 and 110 cm from the local bed.

No vertical velocity, w, measurements were taken, and therefore the cross-shore momentum equation cannot be used to predict the mean cross-shore velocity (Deigaard and Fredsœ, 1989). Instead, the measured $\overline{U}$ was fitted to a parabolic profile (Svendsen, 1984).

$$\overline{U} = a_U z_m^2 + b_U z_m + c_U, \tag{3.17}$$

where the coefficients, a_U, b_U, and c_U are fitted to minimize the mean square error. Figures 3.5 through 3.7 show the cross shore variations in horizontal velocity as well as the comparison of the parabolic fit to the data. In total, the correlation coefficient between the fitted cross-shore velocities and the measured velocities for all three large scale tests was 0.9987. During Test 1b, velocity measurements were repeated at 4 cross-shore positions: 82, 95, 110, and 118 m. So there are two parabolic fits shown in Figure 3.6 at each of these locations. There are several lines in Test 1a and Test 1c in which the parabolic fit did not approximate the data well. In these cases, a vertically-averaged value was used to estimate the horizontal velocity. In order to find the average offshore velocity, equation (3.17) can be extrapolated within the region of 0 to h_0, where $\overline{U} = 0$ at $z = h_0$. Then the time-averaged offshore volume flux, q_0 and corresponding velocity are

$$q_0 = \int_0^{h_0} \overline{U} dz_m \quad ; \quad \overline{U_0} = q_0/h_0 \tag{3.18}$$

The offshore vertically-averaged velocity then is calculated for each hour of waves at a different cross-shore location. Table 3.7 shows the average velocity, $\overline{U_0}$, for all three tests. NaN continues to indicate no reliable data provided. The standard deviation of the velocity measurements, σ_U was tabulated in Roelvink and Reniers (1995). Due to the negligible vertical variation of σ_U, the values were averaged over depth. These values are displayed in Table 3.8 for all three large scale tests. The values of $\overline{U_0}$ and σ_U are compared to model results in Chapter 5.

3.2.3 Concentration data

Concentration measurements were taken by suction samples measuring mean concentration. Measurements were all located at the same cross-shore location, tabulated for the three tests in Table 3.6. Concentration samples were taken at 10 elevations from the local bed, 5, 7.5, 10, 13, 18, 25.5, 40, 65, 105, and 155 cm. 5 cm was the lowest elevation at which concentration was collected. This is still far

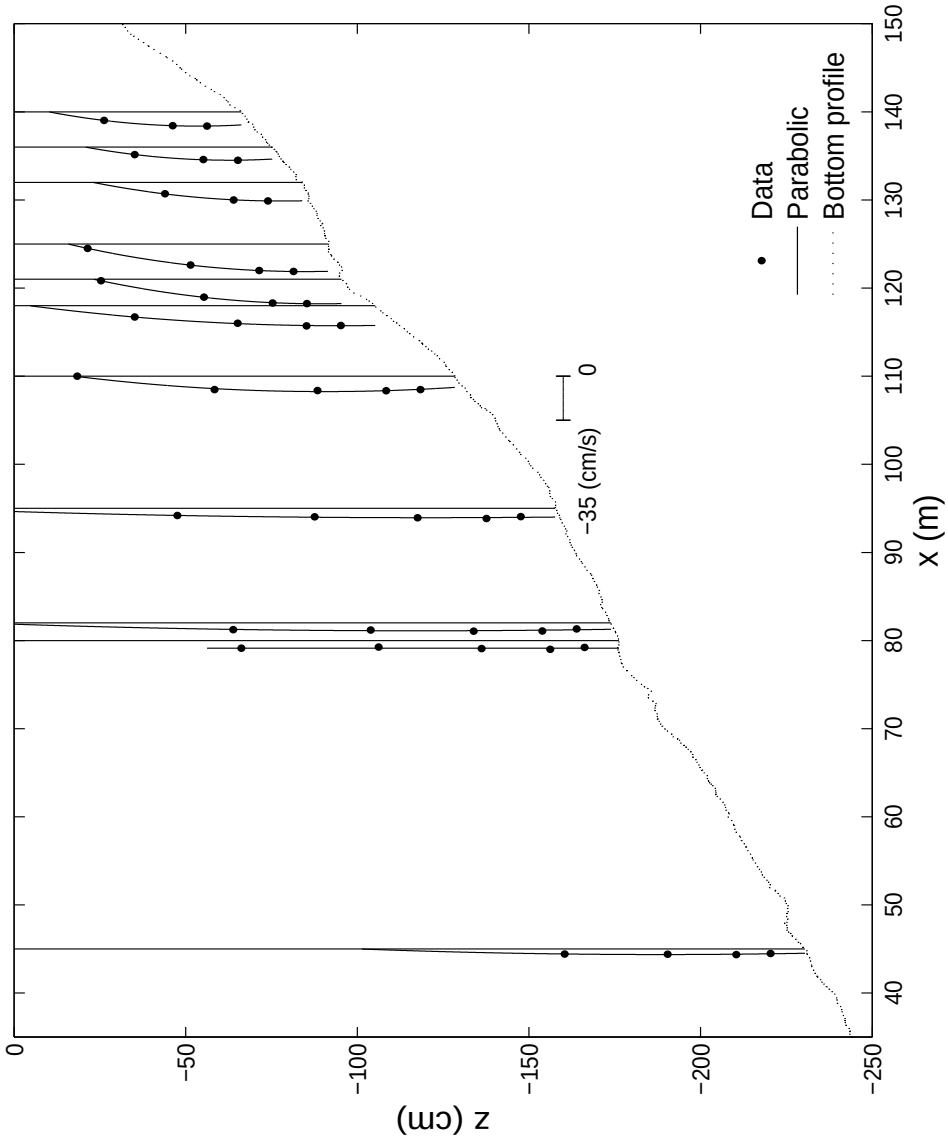

Figure 3.5: Test 1a: Measured and fitted parabolic profiles of mean horizontal velocity, $\overline{U}$, at cross-shore measurement locations shown in Table 3.6.

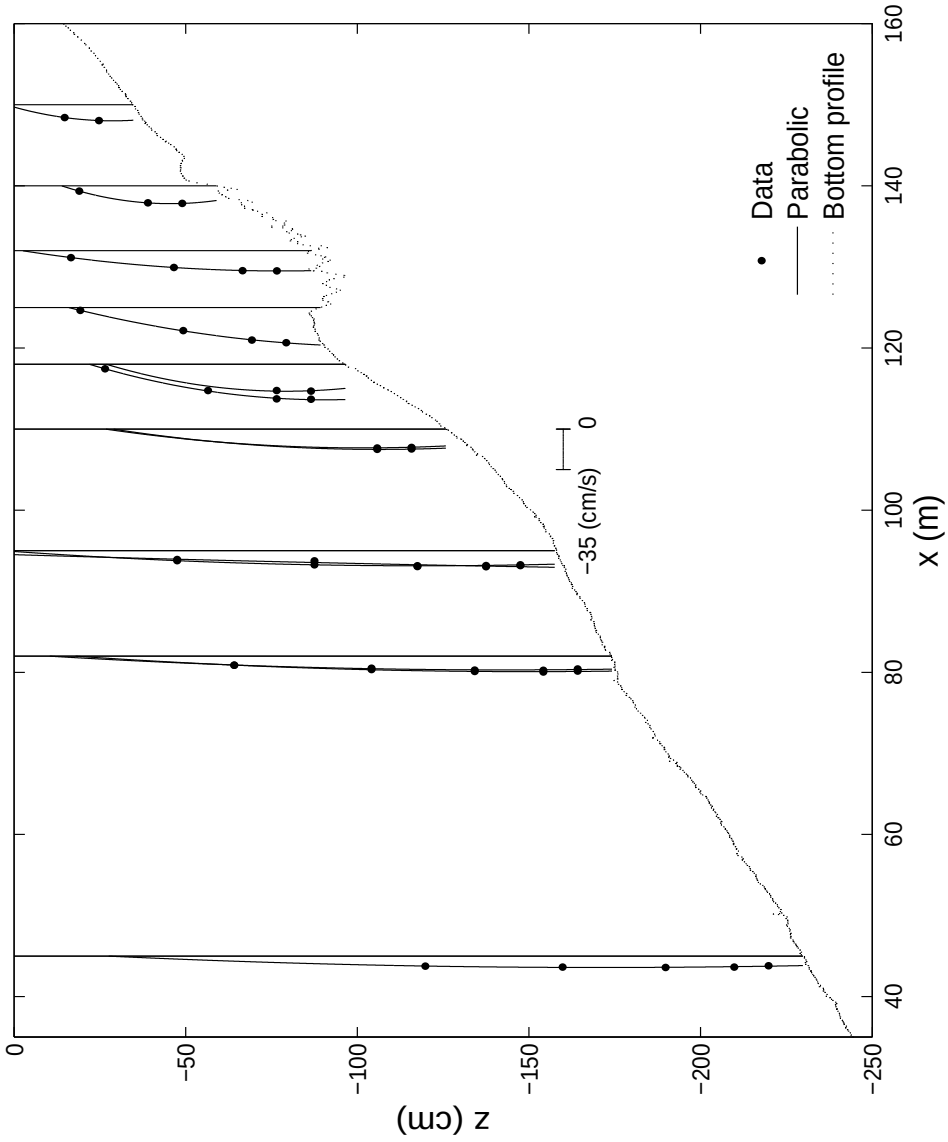

Figure 3.6: Test 1b: Measured and fitted parabolic profiles of mean horizontal velocity, $\overline{U}$, at cross-shore measurement locations shown in Table 3.6

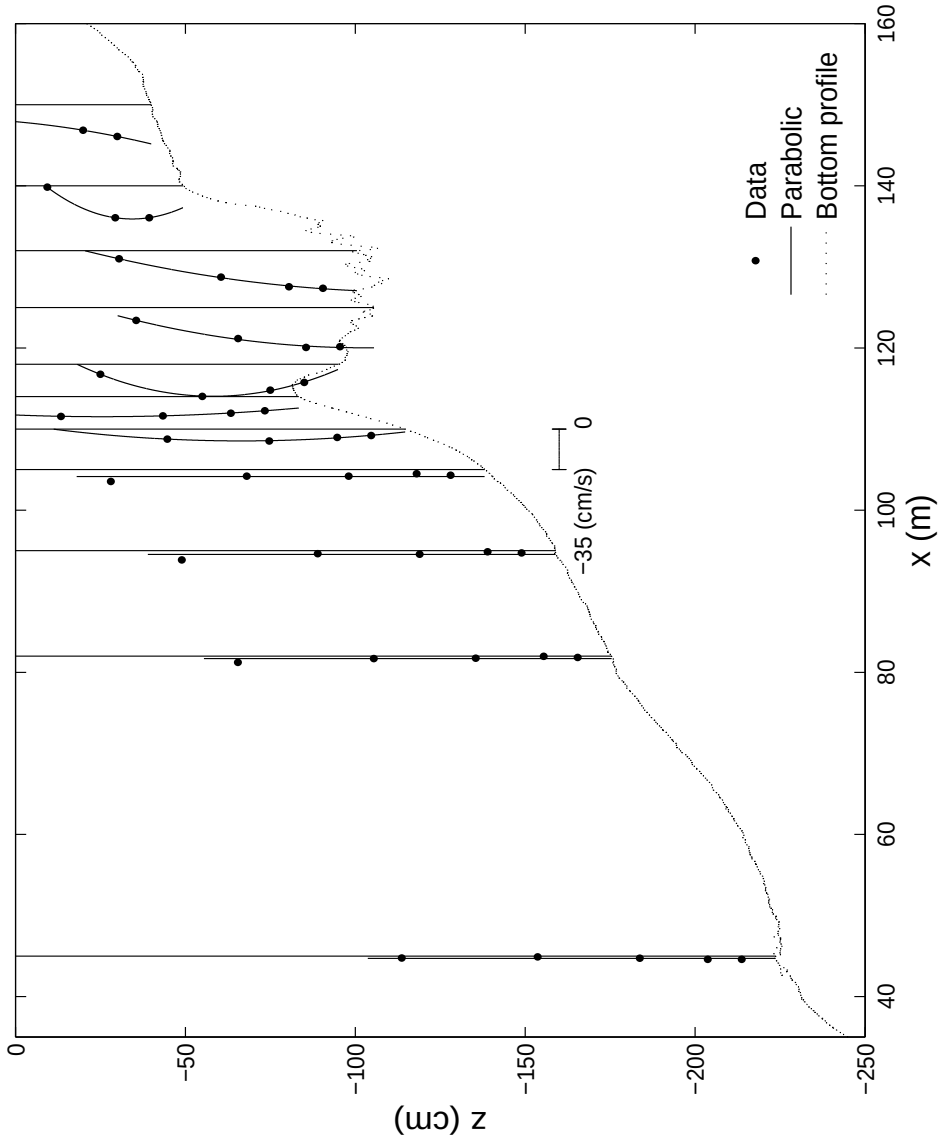

Figure 3.7: Test 1c: Measured and fitted parabolic profiles of mean horizontal velocity, $\overline{U}$, at cross-shore measurement locations shown in Table 3.6.

Table 3.7: Calculated values of $\overline{U_0}$ for the LIP Delta Flume tests based on parabolic fit

Test 1a		**Test 1b**		**Test 1c**	
x **(m)**	$\overline{U_0}$ **(cm/s)**	x **(m)**	$\overline{U_0}$ **(cm/s)**	x **(m)**	$\overline{U_0}$ **(cm/s)**
45	-3.31	45	-7.39	45	-0.84
80	-6.02	82	-8.65	95	-1.40
95	-5.90	95	-9.81	82	-0.92
110	-9.18	110	-12.01	110	-3.10
118	-11.16	118	-17.26	105	-2.56
125	-15.21	NaN	NaN	114	-6.10
132	-10.38	125	-19.84	118	-8.22
140	-8.33	132	-12.25	125	-11.10
136	-7.68	140	-11.50	132	-9.10
121	-13.52	150	-10.51	140	-9.17
82	-4.73	45	NaN	150	-9.1
NaN	NaN	82	-9.62	NaN	NaN
		NaN	NaN	NaN	NaN
		NaN	NaN		
		95	-9.35		
		110	-12.82		
		118	-21.25		
		NaN	NaN		

Table 3.8: Depth-averaged standard deviation of the velocity, for three large scale tests, 1a, 1b, 1c

Test 1a		**Test 1b**		**Test 1c**	
x **(m)**	$\sigma_{\mathbf{U}}$ (cm/s)	x **(m)**	$\sigma_{\mathbf{U}}$ (cm/s)	x **(m)**	$\sigma_{\mathbf{U}}$ (cm/s)
45	30.30	45	45.56	45	26.72
80	40.96	82	47.10	95	31.22
95	39.86	95	46.60	82	30.02
110	45.26	110	48.74	110	36.27
118	46.35	118	54.38	105	36.00
125	42.05	NaN	NaN	114	44.12
132	35.73	125	42.20	118	49.88
140	37.33	132	32.92	125	31.40
136	38.35	140	52.50	132	32.60
121	46.85	150	47.83	140	50.20
82	41.68	45	NaN	150	40.00
NaN	NaN	82	47.58	NaN	NaN
		NaN	NaN	NaN	NaN
		NaN	NaN		
		95	44.14		
		110	49.92		
		118	47.97		
		NaN	NaN		

away from the local bed, which means that a large volume of suspended sediment may not be accounted for.

The vertical variation of concentration was approximated using the power form approximation described in section 3.1.3. Figures 3.8 through 3.10 show the fitted curves and the collected data for each of the large scale tests. Concentration values for each wave hour were fitted with the power form fit described in section 3.1.3 and $\overline{V_a}$ was calculated using equation (3.12) with $\overline{V_a}$ now being taken to be V_s. The exponential fit was not considered given the large elevation from the local bed, and the exponential fit's tendency to underpredict volume near the bed. The reference elevation, z_a used for these calculations was taken to be 1 cm. The values of the volume of suspended sediment are shown in Tables 3.9 through 3.11. Since concentration measurements were taken at multiple elevations for each wave hour, the power form was fitted for each wave hour. Therefore, suspended sediment volume could be calculated for many cross-shore locations.

Table 3.9: Test 1a: Quantities related to the calculation of the volume of suspended sediment.

x (m)	$\overline{\mathbf{h}}$**(cm)**	$\overline{\mathbf{C_a}}$	**n**	**C.C.**	$\mathbf{V_s}$**(cm)**
45	243	0.000224	1.22	0.95	0.000707
80	188	0.000154	1.04	0.93	0.000721
95	166	0.000477	1.30	0.99	0.001255
110	140	0.000450	0.63	0.92	0.006365
118	122	0.000617	0.46	0.92	0.014009
125	97	0.000478	0.44	0.98	0.010355
132	89	0.000641	0.65	0.99	0.006952
140	80	NaN	NaN	NaN	NaN
136	89	0.000307	0.48	0.98	0.005506
121	112	0.001084	0.54	0.98	0.018003
82	182	0.002441	1.33	1.00	0.006124
NaN	NaN	NaN	NaN	NaN	NaN

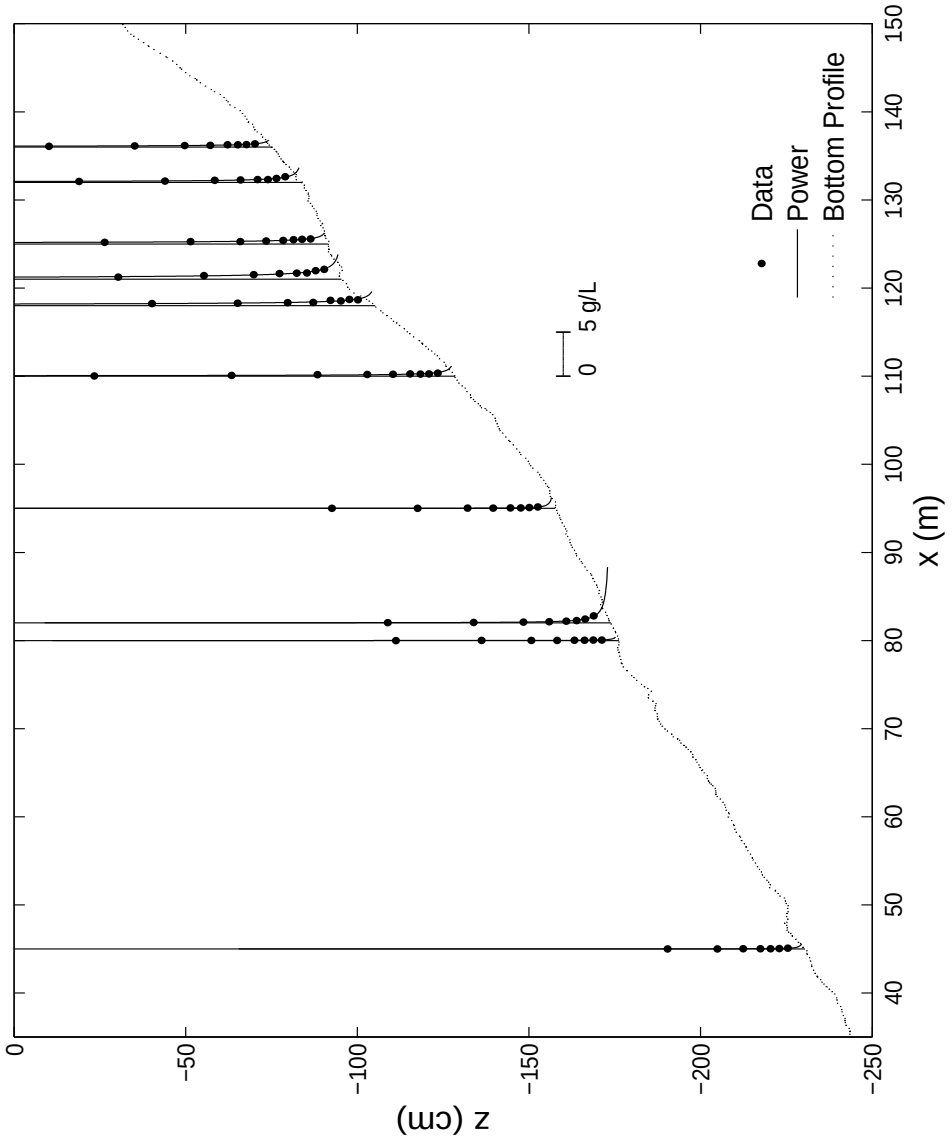

Figure 3.8: Test 1a: Measured and fitted power form profiles of mean concentration, $\overline{C}$, at cross-shore measurement locations.

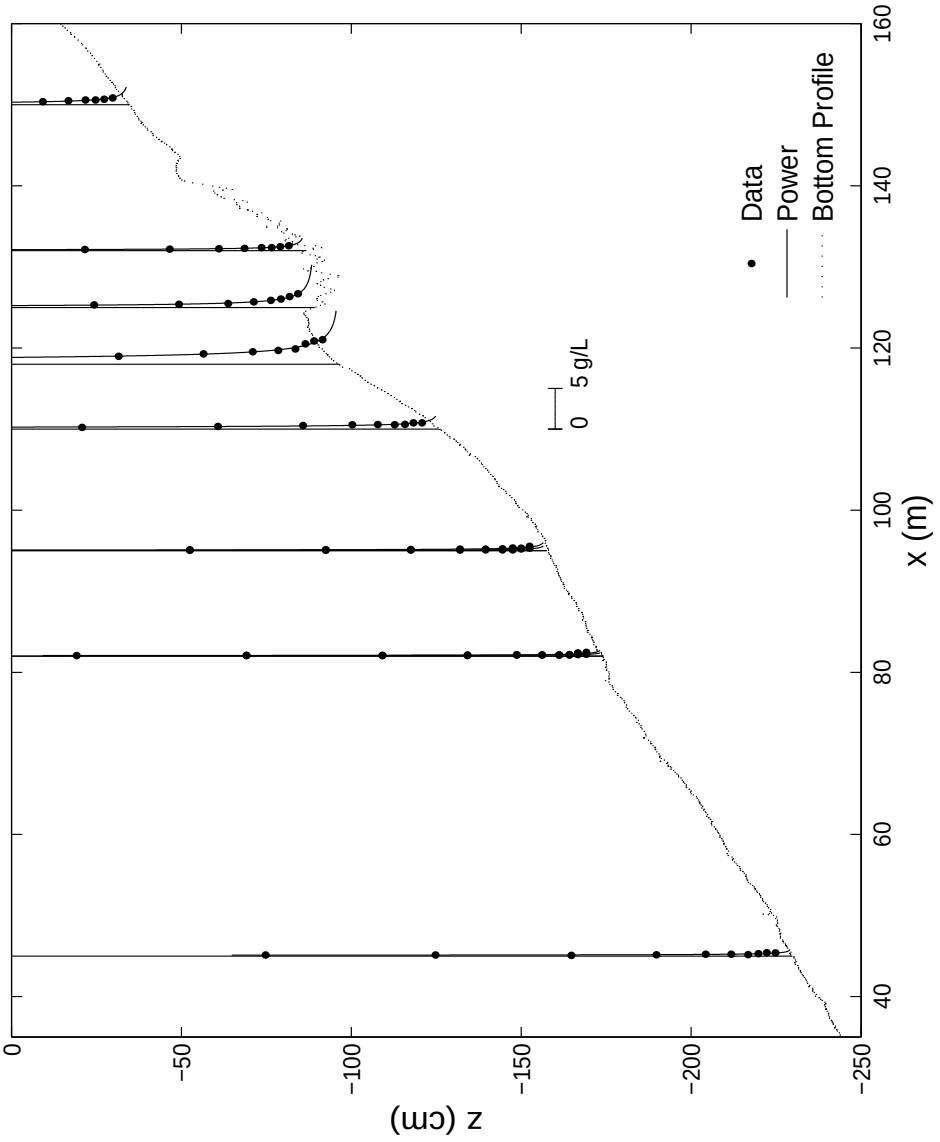

Figure 3.9: Test 1b: Measured and fitted power form profiles of mean concentration, $\overline{C}$, at cross-shore measurement locations.

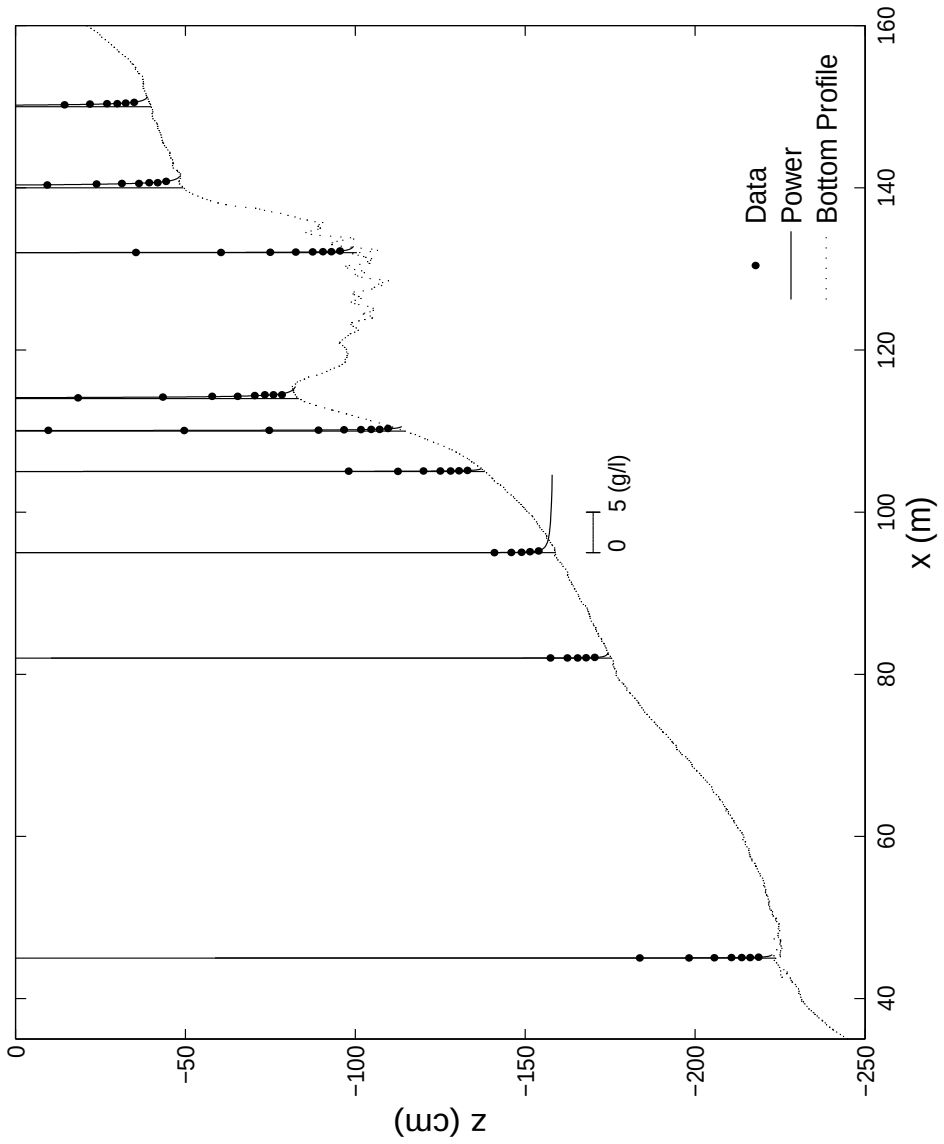

Figure 3.10: Test 1c: Measured and fitted power form profiles of mean concentration, $\overline{C}$, at cross-shore measurement locations.

Table 3.10: Test 1b: Quantities related to the calculation of the volume of suspended sediment.

x (m)	$\overline{\mathbf{h}}$**(cm)**	$\overline{\mathbf{C_a}}$	**n**	**C.C.**	$\mathbf{V_s}$**(cm)**
45	230	0.000255	0.37	0.92	0.011959
82	174	0.000271	0.49	0.89	0.006952
95	158	0.000391	0.52	0.97	0.008462
110	126	0.000369	0.38	0.98	0.011341
118	97	1.000000	0.00	NaN	NaN
NaN	NaN	NaN	NaN	NaN	NaN
125	89	0.001990	0.70	1.00	0.019050
132	87	0.000596	0.57	1.00	0.008039
140	59	NaN	NaN	NaN	NaN
150	35	0.000843	0.55	0.97	0.007329
45	230	NaN	NaN	NaN	NaN
82	174	0.000152	0.40	0.94	0.005391
NaN	NaN	NaN	NaN	NaN	NaN
NaN	NaN	NaN	NaN	NaN	NaN
95	158	0.000225	0.59	0.94	0.003786
110	126	0.000617	0.40	0.93	0.017969
118	97	0.002534	0.45	0.98	0.051818
NaN	NaN	NaN	NaN	NaN	NaN

Table 3.11: Test 1c: Quantities related to the calculation of the volume of suspended sediment.

x (m)	$\overline{\mathbf{h}}$**(cm)**	$\overline{\mathbf{C_a}}$	**n**	**C.C.**	$\mathbf{V_s}$**(cm)**
45	232	0.000159	0.86	0.99	0.001286
95	166	0.003696	2.27	0.97	0.002899
82	183	0.000269	1.45	0.98	0.000539
110	141	0.000218	0.46	0.98	0.005494
105	149	0.000135	0.60	0.95	0.002125
114	128	0.000578	0.57	0.91	0.009524
118	102	NaN	NaN	NaN	NaN
125	95	NaN	NaN	NaN	NaN
132	103	0.000311	0.84	0.98	0.002143
140	93	0.000547	0.36	0.97	0.014528
150	45	0.000477	0.49	0.98	0.005563
NaN	NaN	NaN	NaN	NaN	NaN
NaN	NaN	NaN	NaN	NaN	NaN

Chapter 4

NUMERICAL MODEL DEVELOPMENT

4.1 Time-averaged wave model

The time-averaged model described by Kobayashi *et al.* (2005) was used to predict the cross-shore variations of the variables involved in the sediment model developed in sections 4.2 and 4.3. This model is an extension of the models developed by Battjes and Stive (1985), Stive and DeVriend (1994), and Ruessink et al. (2001). The model extends to the lower swash zone. The governing cross-shore momentum and energy equations for normally-incident random waves are expressed as

$$\frac{dS_{xx}}{dx} = -\rho g \overline{h} \frac{d\overline{\eta}}{dx} - \tau_b \quad ; \quad \frac{dF}{dx} = -D_B - D_f, \tag{4.1}$$

where x represents the cross-shore coordinate, with positive x onshore, S_{xx} representing the cross-shore component of the radiation stress, ρ is the fluid density, g is the acceleration due to gravity, and $\overline{h}$ is the mean water depth given by $\overline{h} = \overline{\eta} - z_b$. z_b represents the elevation of the local bed and $\overline{\eta}$ is the mean free surface elevation. τ_b is the bottom shear stress, F is the wave energy flux, and D_B and D_f are the energy dissipation rates due to wave breaking and bottom friction respectively. Linear wave theory is used to estimate the radiation stress and the wave energy flux given respectively by

$$S_{xx} = \rho g \sigma_\eta^2 \left(\frac{2C_g}{C_p} - \frac{1}{2} \right) + \rho C_p q_r \quad ; \quad F = \rho g C_g \sigma_\eta^2. \tag{4.2}$$

C_g and C_p are respectively the group and phase velocity in the mean water depth corresponding to the spectral peak period, T_p. σ_η is the standard deviation of the

free surface, η, and q_r is the volume flux due to the roller that occurs on the front of a breaking wave.

The roller effect is often represented by its energy and area (Svendsen, 1984), however here, the volume and momentum fluxes are used due to the effect in the increase of undertow current. The term $\rho C_p q_r$ in equation (4.2) represents the roller momentum flux due to the roller propagation at C_p and causes a landward shift of the peak of $\overline{\eta}$ in the breaker zone. Models developed by Battjes and Stive (1985), Stive and DeVriend (1994), and Ruessink et al. (2001) do not include the roller effect in F. Svendsen et al. (2003) did include it and related it to the square of the wave height. The differences in these models have to do with the interpretation of the wave energy flux and dissipation due to wave breaking. The approach used by Battjes and Stive (1985), Stive and DeVriend (1994), and Ruessink et al. (2001) predicts the cross-shore H_{rms} well as long as the breaker ratio parameter, γ, is calibrated. In this case, the dissipated wave energy is converted to the roller energy, which is governed by (Stive and DeVriend, 1994)

$$\frac{d}{dx}\left(\rho C_p^2 q_r\right) = D_B - D_r \quad ; \quad D_r = \rho g \beta_r q_r \tag{4.3}$$

where the roller dissipation rate, D_r, is assumed to be equal to the rate of work required to maintain the roller on the front slope of the wave,β_r.

Linear shallow-water wave theory was used to determine the local relationship between η and U according to Guza and Thornton (1980). The standard deviation of the depth averaged horizontal velocity, U, can be estimated as

$$\sigma_U = \sigma_* \sqrt{g\overline{h}} \quad ; \quad \sigma_* = \sigma_\eta / \overline{h} \tag{4.4}$$

The depth-integrated continuity equation for water on an impermeable beach can then be expressed as

$$\sigma_\eta \sigma_U + \overline{U}\ \overline{h} + q_r = 0 \tag{4.5}$$

where $\sigma_\eta \sigma_U$ is the onshore flux due to linear shallow water waves (Kobayashi *et al.*, 1998) and $\overline{U}$ is the depth-averaged return current. $\overline{U}$ can be expressed as

$$\overline{U} = -\sigma_*^2 \sqrt{g\overline{h}} - q_r/\overline{h} \tag{4.6}$$

The time averaged bottom shear stress and dissipation rate can be defined as

$$\tau_b = \frac{1}{2}\rho f_b \overline{|U|U} \quad ; \quad D_f = \frac{1}{2}\rho f_b \overline{|U|^3}, \tag{4.7}$$

where the overbar indicates time-averaging and f_b is the bottom friction factor taken as 0.015. In order to express τ_b and D_f in terms of $\overline{U}$ and σ_U, the equivalency of the time and probabilistic averaging as well as a Gaussian distribution of U are assumed (Guza and Thornton, 1980; Kobayashi *et al.*, 1998). Then the bottom shear stress is reduced to

$$\tau_b = \frac{1}{2}\rho f_b \sigma_U^2 G_2(U_*) \quad ; \quad U_* = \frac{\overline{U}}{\sigma_U}, \tag{4.8}$$

where

$$G_2(r) = (1 + r^2)\mathrm{erf}\left(\frac{r}{\sqrt{2}}\right) + \sqrt{\frac{2}{\pi}} r \exp\left(-\frac{r^2}{2}\right). \tag{4.9}$$

r is an arbitrary variable with $r = U_*$ from equation (4.8) and erf is the error function. The arbitrary variable, r, is retained in order to maintain the equation's validity under variable r values as are imposed in section 4.3.

The dissipation due to friction also includes the assumptions stated above and can be expressed as

$$D_f = \frac{1}{2}\rho f_b \sigma_U^3 G_3(U_*), \tag{4.10}$$

where

$$G_3(r) = (3r + r^3)\mathrm{erf}\left(\frac{r}{\sqrt{2}}\right) + \sqrt{\frac{2}{\pi}}(r^2 + 2)\exp\left(-\frac{r^2}{2}\right). \tag{4.11}$$

The functions, G_2 and G_3 for the range of $|r| < 1$ can be approximated as $G_2 \simeq 1.64r$ and $G_3 \simeq (1.6 + 2.6r^2)$.

The energy dissipation rate due to wave breaking, D_B, from equation (4.1) is estimated using the formulation by Battjes and Stive (1985).

$$D_B = \frac{\rho g \alpha Q H_B^2}{4T_p} \quad ; \quad \frac{Q-1}{lnQ} = \left(\frac{H_{rms}}{H_m}\right)^2 \quad ; \quad H_m = \frac{0.88}{k_p}\tanh\left(\frac{\gamma k_p \overline{h}}{0.88}\right) \tag{4.12}$$

where α is an empirical coefficient, suggested as $\alpha = 1$ (Battjes and Stive, 1985); Q is the fraction of breaking waves with $Q = 0$ for no wave breaking, and $Q = 1$ for all breaking waves; H_B is the wave height used to estimate D_B where $H_B = H_m$ in the model presented by Battjes and Stive (1985); H_m is the local depth limited wave height; and γ is the breaker ratio parameter with $H_m = \gamma\overline{h}$ in shallow water. k_p is the wave number given by $k_p = 2\pi/(C_p T_p)$. It is implied from the restrictions on Q that $H_{rms} \leq H_m$. This does not hold in very shallow water. In that case, $Q = 1$ and $H_B = H_{rms}$ rather than $H_B = H_m$.

The empirical parameter, $\alpha = 1$ was introduced by Kobayashi *et al.* (2005).

$$\alpha = \frac{1}{3} S_b T_p \sqrt{g\overline{h}} \geq 1, \tag{4.13}$$

such that $\alpha = 1$ in a region with a large depth and small bottom slope, S_b. The computed value of α increases from 1 to about 10 near the shoreline. Increasing the value of γ can also increase D_B due to its dependance on H_m in shallow water where γ increases with beach slope (Raubenheimer *et al.*, 1996). The slope effect was included in $\beta_r = (0.1 + S_b) \geq 0.1$, where β_r is the roller front slope in equation (4.3).

Equations (4.1) and (4.3) are solved using a finite difference method with a constant grid spacing, Δx, which is small relative to the offshore wave height (on the order of 1 cm for the small scale tests and 8 cm for the large scale tests). The measured bottom elevation, $z_b(x)$, is specified for $x \geq 0$. $x = 0$ is at the seaward boundary, outside of the surf zone. The measured values of T_p, $\overline{\eta}$, $H_{rms} = \sqrt{8}\sigma_\eta$ and $q_r = 0$ ($x = 0$), outside of the surf zone are specified as the seaward boundary conditions for the tests. This boundary was located at the position of wave gauge

1 for the small scale tests, and 20 m from the wave maker for the large scale tests. Landward marching computations are continued until the computed mean water depth, $\overline{h}$, is essentially zero. Computations were conducted with and without the roller, IROLL=1 and IROLL=0 respectively, for all eight tests and are discussed in Chapter 5. For IROLL=0, both the roller volume flux, $q_r = 0$, and equation (4.3) are not included.

4.2 Suspended sediment transport

The sediment transport model proposed here is very simple. Suspended sediment is assumed to be driven mostly by flow directed offshore, distributed over the water column, while bedload transport is assumed to be directed primarily in the onshore direction and remains close to the local bed. The conservation of suspended sediment volume is given by

$$\frac{\partial V_s}{\partial t} + \frac{\partial}{\partial x}(q_s) = \overline{S} - w_f \frac{V_s}{\overline{h}} \tag{4.14}$$

where t is the morphological time associated with the beach profile change, $\overline{S}$ is the time-averaged sediment suspension rate directed vertically upward from the bottom, w_f is the fall velocity, V_s is the time-averaged suspended sediment volume per unit horizontal area, and q_s is the suspended sediment transport rate. The conservation of bedload sediment volume is given by

$$(1 - n_p)\frac{\partial z_b}{\partial t} + \frac{\partial q_b}{\partial x} = w_f \frac{V_s}{\overline{h}} - \overline{S}, \tag{4.15}$$

where n_p is the porosity of sand, taken to be 0.4, z_b is the vertical elevation of the bed, and q_b is the bedload transport rate. Combining equations (4.15) and (4.14) gives the conservation of total sediment volume

$$(1 - n_p)\frac{\partial z_b}{\partial t} + \frac{\partial V_s}{\partial t} + \frac{\partial}{\partial x}(q_s) + \frac{\partial}{\partial x}(q_b) = 0, \tag{4.16}$$

where the temporal change of V_s is normally neglected in comparison to the bottom elevation change.

Kobayashi and Johnson (2005) developed a formulation for the volume of suspended sediment, V_s per unit area.

$$V_s = \frac{e_B D_B + e_f D_f}{\rho g (s-1) w_f} P_s, \tag{4.17}$$

where the values of e_B and e_f, empirical parameters associated with D_B and D_f, were calibrated to be 0.005 and 0.01 respectively. P_s is the probability of sediment suspension. When the roller effect is included, D_B in equation (4.17) is replaced by the roller dissipation rate, D_r from equation (4.3). The introduction of P_s is made to ensure that $V_s = 0$ if no sediment suspension occurs.

Sediment suspension in the surf zone is intermittent, and individual events are difficult to predict accurately (Kobayashi and Tega, 2002). P_s may be estimated using experimental results obtained by Kobayashi *et al.* (2005) where three equilibrium profiles were generated with sand that had a fall velocity, w_f of 2.0 cm/s, a specific gravity, s=2.6, and a d_{50} of 0.18 mm. These results showed that the turbulent velocities measured in the vicinity of the bottom were more related to the energy dissipation rate due to bottom friction than due to wave breaking. The magnitude of the turbulent velocity near the bottom can be represented by $(D\prime_f/\rho)^{1/3}$, where $D\prime_f$ is the time-varying energy dissipation rate due to bottom friction and is assumed to be given by equation (4.7) without the overbar. The probability of sediment suspension can be estimated as the probability that $(D\prime_f/\rho)^{1/3} > w_f$. The probability distribution of the horizontal velocity is assumed to be Gaussian.

Letting the probabilistic variable, $r = \frac{U-\overline{U}}{\sigma_U}$, then suspension occurs if

$$|r + u_*| > \left(\frac{2}{f_b}\right)^{1/3} \frac{w_f}{\sigma_U} = R_s \quad ; \quad U_* = \frac{\overline{U}}{\sigma_U} < 0. \tag{4.18}$$

Then the probability of suspension is

$$P_s = \frac{1}{2}\mathrm{erfc}\left(\frac{R_s + U_*}{\sqrt{2}}\right) + \frac{1}{2}\mathrm{erfc}\left(\frac{R_s - U_*}{\sqrt{2}}\right), \tag{4.19}$$

where erfc is the complementary error function.

Kobayashi *et al.* (2005) experimentally examined the onshore suspended sediment rate, q_{on}, due to the correlation between the horizontal velocity and suspended sediment concentration as well as the offshore suspended sediment transport rate, q_{off} due to the undertow current. The volumetric transport rates per unit width were approximately expressed as $q_{on} = 0.8\sigma_*\sigma_U V_s$ and $q_{off} = 0.9(-\overline{U})V_s$, where the return current $\overline{U}$ was negative and V_s was estimated using equation (4.17) with P_s taken to be 1. The net suspended transport rate, q_s, is then given by $q_s = (q_{on} - q_{off})$. Using equations (4.4) and (4.6) with q_r taken to be zero for simplicity, q_s is then

$$q_s = a\overline{U}\ V_s. \tag{4.20}$$

a is an empirical parameter equalling 0.1 for P_s=1. For the three small scale tests conducted by Kobayashi *et al.* (2005), the calculated values of P_s using equation (4.19) are on the order of 0.7. Since a may have an uncertainty of factor 2, a=0.1 and 0.2 have been tried. Computed results in Chapter 5 are based on $a = 0.2$ which gives better overall agreement. Equation (4.20) implies that the sediment volume per unit bottom area is transported by the depth-averaged current, $\overline{U}$, with the empirical reduction factor, a.

4.3 Bedload transport rate

Sediment motion very near to the bed is normally related to the bottom shear stress, $\tau\prime_b$ in steady unidirectional flow. The instantaneous bed shear stress is normalized as the Shields parameter, Ψ, expressing the entraining force divided by the submerged grain weight, defined as

$$\Psi = \frac{\tau\prime_b}{\rho g(s-1)d_{50}} = \frac{f_b|U|U}{2g(s-1)d_{50}}, \tag{4.21}$$

where d_{50} is the median diameter of the sand and $\tau\prime_b$ is the instantaneous bottom shear stress given by equation (4.7) without the overbar. This assumption was verified experimentally by Cox *et al.* (1996).

To initiate sediment movement, $|\Psi| > \Psi_c$, where Ψ_c is the critical Shields parameter taken as 0.05 (Madsen and Grant, 1976). The probability of sediment movement can then be defined as

$$|r + U_*| > \sqrt{\frac{2}{f_b}} \frac{\sqrt{g(s-1)d_{50}}}{\sigma_U} \sqrt{\Psi_c} = R_b,$$

which yields

$$P_b = \frac{1}{2}\text{erfc}(\frac{R_b + U_*}{\sqrt{2}}) + \frac{1}{2}\text{erfc}\frac{(R_b - U_*)}{\sqrt{2}}, \tag{4.22}$$

where the probabilistic variable, r, is defined as in equation (4.18). Sediment particles need to be entrained before they are suspended, therefore, P_s must be constrained to be always less than or equal to P_b.

A widely used bedload formula was developed by Meyer-Peter and Mueller (e.g. Ribberink, 1998), which was originally developed for coarse sediments. The instantaneous bedload transport rate, $q\prime_b(t)$ under the assumption of quasi-steady response is

$$\frac{q\prime_b(t)}{\sqrt{g(s-1)d_{50}}d_{50}} = \alpha(|\Psi| - \Psi_c)^{1.5}\frac{\Psi}{|\Psi|} \quad ; \quad \frac{\Psi}{|\Psi|} = \frac{U}{|U|}, \tag{4.23}$$

where α is an empirical parameter different from the one defined in equation (4.13) ≈ 10. In order to obtain a simple analytical expression for the bedload transport rate, the bedload transport rate is time averaged and simplified as

$$\frac{q_b}{\sqrt{g(s-1)d_{50}}d_{50}} = \alpha P_b \overline{|\Psi|^{0.5}\Psi}, \tag{4.24}$$

where the probability, P_b, accounts for the initiation of sediment motion. The time-averaged bedload transport rate is derived from the quasi-steady application of equation (4.24) along with equation (4.21),

$$q_b = \alpha \left(\frac{f_b}{2}\right)^{1.5} \frac{P_b \overline{U^3}}{g(s-1)}. \tag{4.25}$$

Under the assumption that time-averaging is approximately the same as probabilistic averaging, $\overline{U^3} = \sigma_U^3 \overline{(r + U_*)^3}$, and

$$\overline{(r + U_*)^3} = b_* = S_U + 3U_* + U_*^3$$

because

$$\overline{r} = 0, \overline{r^2} = 1, \text{ and } \overline{r^3} = S_U, \tag{4.26}$$

where S_U is the skewness of the velocity, U and is equal to 0 for a Gaussian distribution. An expression for q_b is obtained as

$$q_b = \frac{bP_b\sigma_U^3}{g(s-1)} \quad ; \quad b = \alpha\left(\frac{f_b}{2}\right)^{1.5} b_*. \tag{4.27}$$

For S_U=0 and $U_* = \overline{U}/\sigma_U < 0$ for $\overline{U} < 0$, $b_* < 0$ and $q_b < 0$, or that bedload is always offshore due to a negative mean velocity, which is contrary to reality that q_b is onshore in most situations. Researchers have tried to predict the skewness, which is generally positive due to wave non-linearity, however it is hard to predict, and even with a positive S_U, profile changes consistently. In this study the bedload parameter, b is assumed to be constant.

4.3.1 Comparison of bedload formulation with data

The bedload formulation was calibrated with data sets from four tests under monochromatic non-breaking waves in a wave flume with bedforms present (Dohmen-Janssen and Hanes, 2002). The sediment used in the experiment had a median diameter, $d_{50} = 0.24$ mm, a specific gravity, $s = 2.65$, and a sediment density, $\rho_s = 2650$ kg/m^3. The fall velocity is estimated as $w_f = 3.2$ cm/s. The offshore water depth in the wave flume was 3.5 m, with wave heights of 1.2 to 1.6 m. The period of the waves was 6.5 s or 9.1 s. In addition, 20 tests in a water tunnel (Ribberink and Al-Salem, 1994) were also used to calibrate b. Irregular second-order Stokes waves, based on a JONSWAP spectrum were used to generate oscillatory flows over both a rippled and a plane bed. Regular second-order Stokes waves were used only over a plane bed. The sediment used had a median diameter, $d_{50} = 0.21$ mm, with a fall velocity, $w_f = 2.6$ cm/s, and a specific gravity taken as $s = 2.65$. Equations (4.20) and (4.27) were used to estimate q_s and q_b for each test. D_B= 0 for nonbreaking waves and D_f is given by equation (4.10). For the 20 water tunnel

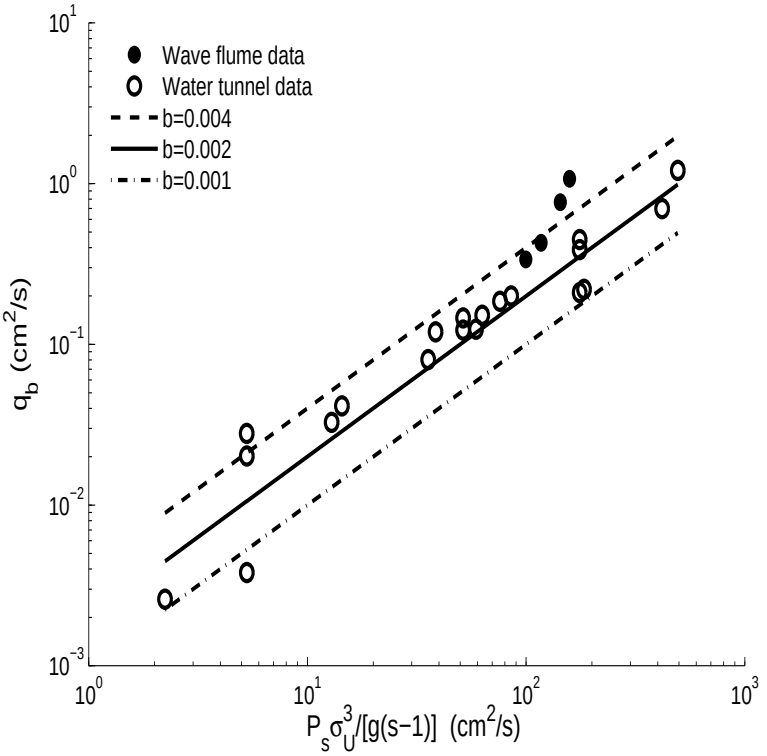

Figure 4.1: Bedload vs. $P_b\sigma_U^3/(g(s-1))$ giving a slope related to the bedload parameter b. The open circles indicate water tunnel data. (Ribberink and Al-Salem, 1994), while the closed circles indicate wave flume data. (Dohmen-Janssen and Hanes, 2002). The solid line indicates, $b = 0.002$, while the dotted lines show a factor of two difference.

tests, -0.1 $< U_* <$ 0.1 and $G_3 = 1.6$ for irregular waves with weak currents. For regular waves, use is made of $G_3 = \overline{|U|^3} = 1.2$ based on sinusoidal waves. The wave flume data (Dohmen-Janssen and Hanes, 2002) was based on regular non-breaking waves where $U_* = \overline{U}/\sigma_U$ was in the range of -0.076 to -0.056. For all sets of data (Dohmen-Janssen and Hanes, 2002; Ribberink and Al-Salem, 1994), the bedload is shown in Table 4.1 to be the dominant mode of sediment transport. Figure 4.1 shows the data for 24 tests with lines indicating the range of b values.

Using this data, it can be seen that b can be calibrated to the value of 0.002

reasonably within a factor of two. In addition, for the fixed values of the empirical parameter defined in equation (4.23), $\alpha = 10$ and the bottom friction, $f_b = 0.015$, $b = 0.0065\ b_*$ from equation (4.27). This then gives b_*=0.3 for $b = 0.002$. Since typically the skewness, S_U is on the order of 0.6 and $U_* \simeq -0.1$, $b_* \approx 0.3$ which is the correct order of magnitude. Using b=0.002 for the bedload parameter with equation (4.27) and equation (4.20) for q_s, we can calculate the total sediment transport, $q_s + q_b$, and compare this with the measured transport, q_m for each test. The results are shown in Tables 4.1 and 4.2. It can be seen that $q_b > 0$ and q_s/q_b =-0.022 to 0.017, predicting onshore transport for non-breaking nonlinear waves. The increase of b for the wave flume data may be partly attributed to the onshore streaming in the wave flume (Dohmen-Janssen and Hanes, 2002), however the choice of $b = 0.002$ was more consistent with other formulas as is explained further.

Although equation (4.27) does predict bedload transport in the direction of the nonlinear wave propagation, it does not predict that $q_b = 0$ for sinusoidal waves. For sinusoidal waves with a current, equation (4.27) may be applicable if the direction of q_b is assumed to be in the same direction as the current.

In order to test this assumption, comparison is made of experiments conducted in a water tunnel consisting of 24 sheet flow tests(Dohmen-Janssen *et al.*, 2002). The horizontal velocity, U was varied with time, t, in the form of $U = [\overline{U} + \sqrt{2}\sigma_U \cos(\omega t)]$ where ω is the angular frequency. The values of $\overline{U}$ and σ_U were tabulated. For the 24 tests, $U_* = 0.2$ to 1.2, indicating strong currents. Fine ($d_{50} = 0.13$ mm), medium ($d_{50} = 0.21$ mm), and coarse ($d_{50} = 0.32$ mm) grained sands were used to investigate transport rates. The fall velocities were $w_f = 1.14$, 2.60, and 4.29 cm/s respectively. The specific gravity for these sands is taken to be s=2.65. The values of q_s and q_b are calculated. The calculated probabilities and transport rates are tabulated in Tables 4.3 and 4.4.

Figure 4.2 shows the comparison of the measured transport values, q_m and

Table 4.1: Calculated probabilities of sediment movement and suspension for tests conducted in a wave flume (Dohmen-Janssen and Hanes, 2002) and in a water tunnel (Ribberink and Al-Salem, 1994)

	σ_u (cm/s)	$\overline{u}$ (cm/s)	q_m (cm^2/s)	d_{50} (cm)	w_f (cm/s)	R_b	R_s	P_b	P_s
mi	59	-4.50	0.3380	0.024	3.2	0.273	0.277	0.786	0.782
mh	62	-3.70	0.4290	0.024	3.2	0.260	0.264	0.796	0.792
mf	66	-3.70	0.7670	0.024	3.2	0.244	0.248	0.808	0.805
me	68	-5.20	1.0730	0.024	3.2	0.237	0.240	0.813	0.811
1	48	0.80	0.1226	0.021	2.6	0.314	0.277	0.754	0.754
2	32	-0.30	0.0327	0.021	2.6	0.470	0.415	0.638	0.638
3	43	-1.60	0.0804	0.021	2.6	0.350	0.309	0.726	0.726
4	48	0.10	0.1461	0.021	2.6	0.314	0.277	0.754	0.754
5	33	0.05	0.0414	0.021	2.6	0.456	0.403	0.648	0.648
6	44	-2.40	0.1196	0.021	2.6	0.342	0.302	0.733	0.733
7	50	4.80	0.1242	0.021	2.6	0.301	0.266	0.764	0.764
8	70	3.80	0.3885	0.021	2.6	0.215	0.190	0.830	0.830
9	92	3.00	0.6983	0.021	2.6	0.164	0.144	0.870	0.870
10	54	2.00	0.1856	0.021	2.6	0.279	0.246	0.781	0.781
11	70	2.20	0.4483	0.021	2.6	0.215	0.190	0.830	0.830
12	97	2.90	1.2088	0.021	2.6	0.155	0.137	0.877	0.877
13	70	1.00	0.2100	0.021	2.6	0.215	0.190	0.830	0.830
14	71	-6.40	0.2200	0.021	2.6	0.212	0.187	0.833	0.833
15	51	3.00	0.1520	0.021	2.6	0.295	0.260	0.768	0.768
16	56	0.50	0.2000	0.021	2.6	0.269	0.237	0.788	0.788
17	20	0.62	0.0026	0.021	2.6	0.753	0.664	0.452	0.452
18	25	0.51	0.0202	0.021	2.6	0.602	0.531	0.547	0.547
19	25	0.51	0.0038	0.021	2.6	0.602	0.531	0.547	0.547
20	25	-0.11	0.0279	0.021	2.6	0.602	0.531	0.547	0.547

Table 4.2: Calculated parameter values from water tunnel and wave flume tests. Tests designated with m indicate wave flume tests (Dohmen-Janssen and Hanes, 2002), while test 1 through 20 are the tests conducted in the water tunnel. (Ribberink and Al-Salem, 1994)

	σ_u (cm/s)	$\overline{u}$ (cm/s)	$G3$	V_s (cm)	q_m (cm^2/s)	q_b (cm^2/s)	q_s (cm^2/s)	q_s/q_b (%)
mi	59	-4.50	1.2	0.0028	0.3380	0.1994	-0.0025	-1.26
mh	62	-3.70	1.2	0.0033	0.4290	0.2343	-0.0024	-1.04
mf	66	-3.70	1.2	0.0040	0.7670	0.2869	-0.0030	-1.04
me	68	-5.20	1.2	0.0044	1.0730	0.3160	-0.0046	-1.46
1	48	0.80	1.6	0.0024	0.1226	0.1030	0.0004	0.37
2	32	-0.30	1.6	0.0006	0.0327	0.0258	-0.0000	-0.14
3	43	-1.60	1.6	0.0016	0.0804	0.0714	-0.0005	-0.74
4	48	0.10	1.6	0.0024	0.1461	0.1030	0.0000	0.05
5	33	0.05	1.6	0.0007	0.0414	0.0288	0.0000	0.02
6	44	-2.40	1.6	0.0018	0.1196	0.0771	-0.0009	-1.11
7	50	4.80	1.2	0.0020	0.1242	0.1181	0.0020	1.66
8	70	3.80	1.2	0.0061	0.3885	0.3518	0.0046	1.32
9	92	3.00	1.2	0.0145	0.6983	0.8372	0.0087	1.04
10	54	2.00	1.2	0.0026	0.1856	0.1519	0.0011	0.69
11	70	2.20	1.2	0.0061	0.4483	0.3517	0.0027	0.76
12	97	2.90	1.2	0.0171	1.2088	0.9887	0.0099	1.00
13	70	1.00	1.2	0.0061	0.2100	0.3517	0.0012	0.35
14	71	-6.40	1.2	0.0064	0.2200	0.3683	-0.0082	-2.22
15	51	3.00	1.2	0.0022	0.1520	0.1259	0.0013	1.04
16	56	0.50	1.2	0.0030	0.2000	0.1710	0.0003	0.17
17	20	0.62	1.6	0.0001	0.0026	0.0045	0.0000	0.29
18	25	0.51	1.6	0.0002	0.0202	0.0106	0.0000	0.24
19	25	0.51	1.6	0.0002	0.0038	0.0106	0.0000	0.24
20	25	-0.11	1.6	0.0002	0.0279	0.0106	-0.0000	-0.05

Table 4.3: Calculated probabilities of sediment motion and suspension for sand of varying diameter (Dohmen-Janssen *et al.*, 2002)

	σ_u (cm/s)	$\overline{u}$ (cm/s)	q_m (cm^2/s)	d_{50} (cm)	w_f (cm/s)	R_b	R_s	P_b	P_s
$H2$	48	23.00	0.1880	0.013	1.14	0.247	0.121	0.826	0.826
$H3$	66	24.00	0.3490	0.013	1.14	0.179	0.088	0.867	0.867
$H4$	77	25.00	0.4000	0.013	1.14	0.154	0.076	0.884	0.884
$H5$	92	24.00	0.5170	0.013	1.14	0.129	0.063	0.901	0.901
$H6$	104	24.00	0.6550	0.013	1.14	0.114	0.056	0.912	0.912
$H7$	35	42.00	0.1560	0.013	1.14	0.338	0.166	0.868	0.868
$H8$	47	43.00	0.4740	0.013	1.14	0.252	0.124	0.868	0.868
$H9$	66	43.00	0.8570	0.013	1.14	0.179	0.088	0.885	0.885
$H24$	48	24.00	0.1280	0.013	1.14	0.247	0.121	0.828	0.828
$H44$	75	25.00	0.0900	0.013	1.14	0.158	0.078	0.881	0.881
$H212$	48	23.00	0.1990	0.013	1.14	0.247	0.121	0.826	0.826
$J1$	75	24.00	0.4630	0.021	2.60	0.201	0.177	0.849	0.849
$J2$	91	25.00	0.7440	0.021	2.60	0.165	0.146	0.873	0.873
$E2$	104	23.00	1.1180	0.021	2.60	0.145	0.128	0.888	0.888
$J3$	33	41.00	0.0900	0.021	2.60	0.456	0.403	0.829	0.829
$J4$	46	41.00	0.2530	0.021	2.60	0.327	0.289	0.825	0.825
$E4$	67	44.00	0.8440	0.021	2.60	0.225	0.198	0.856	0.856
$J5$	74	24.00	0.2920	0.021	2.60	0.203	0.179	0.847	0.847
$J6$	77	23.00	0.4920	0.021	2.60	0.196	0.173	0.852	0.852
$I1$	104	26.00	0.9400	0.032	4.29	0.179	0.211	0.863	0.838
$I2$	120	25.00	1.5230	0.032	4.29	0.155	0.183	0.880	0.858
$I3$	46	42.00	0.2360	0.032	4.29	0.404	0.476	0.789	0.751
$I4$	65	42.00	0.5330	0.032	4.29	0.286	0.337	0.816	0.784
$I5$	106	45.00	1.9370	0.032	4.29	0.175	0.207	0.873	0.850

Table 4.4: Calculated suspended and bedload transport rates for sediment of varying grain size (Dohmen-Janssen *et al.*, 2002)

	σ_u (cm/s)	$\overline{u}$ (cm/s)	$G3$	V_s (cm)	q_m (cm^2/s)	q_b (cm^2/s)	q_s (cm^2/s)	q_s/q_b (%)
$H2$	48	23.00	1.8	0.0068	0.1880	0.1128	0.0312	27.64
$H3$	66	24.00	1.6	0.0158	0.3490	0.3078	0.0758	24.62
$H4$	77	25.00	1.5	0.0244	0.4000	0.4986	0.1219	24.45
$H5$	92	24.00	1.4	0.0395	0.5170	0.8669	0.1895	21.86
$H6$	104	24.00	1.3	0.0560	0.6550	1.2672	0.2690	21.23
$H7$	35	42.00	5.3	0.0081	0.1560	0.0460	0.0677	147.26
$H8$	47	43.00	3.5	0.0130	0.4740	0.1113	0.1115	100.18
$H9$	66	43.00	2.4	0.0245	0.8570	0.3142	0.2104	66.97
$H24$	48	24.00	1.9	0.0070	0.1280	0.1131	0.0336	29.73
$H44$	75	25.00	1.5	0.0227	0.0900	0.4594	0.1135	24.70
$H212$	48	23.00	1.8	0.0068	0.1990	0.1128	0.0312	27.64
$J1$	75	24.00	1.5	0.0094	0.4630	0.4424	0.0453	10.23
$J2$	91	25.00	1.4	0.0165	0.7440	0.8133	0.0824	10.13
$E2$	104	23.00	1.3	0.0237	1.1180	1.2338	0.1091	8.84
$J3$	33	41.00	5.6	0.0030	0.0900	0.0368	0.0246	66.77
$J4$	46	41.00	3.4	0.0049	0.2530	0.0992	0.0401	40.43
$E4$	67	44.00	2.4	0.0110	0.8440	0.3182	0.0964	30.29
$J5$	74	24.00	1.5	0.0091	0.2920	0.4241	0.0436	10.29
$J6$	77	23.00	1.4	0.0100	0.4920	0.4804	0.0460	9.57
$I1$	104	26.00	1.4	0.0139	0.9400	1.1988	0.0725	6.05
$I2$	120	25.00	1.3	0.0211	1.5230	1.8780	0.1055	5.62
$I3$	46	42.00	3.5	0.0028	0.2360	0.0948	0.0234	24.70
$I4$	65	42.00	2.3	0.0055	0.5330	0.2770	0.0459	16.56
$I5$	106	45.00	1.7	0.0185	1.9370	1.2843	0.1664	12.96

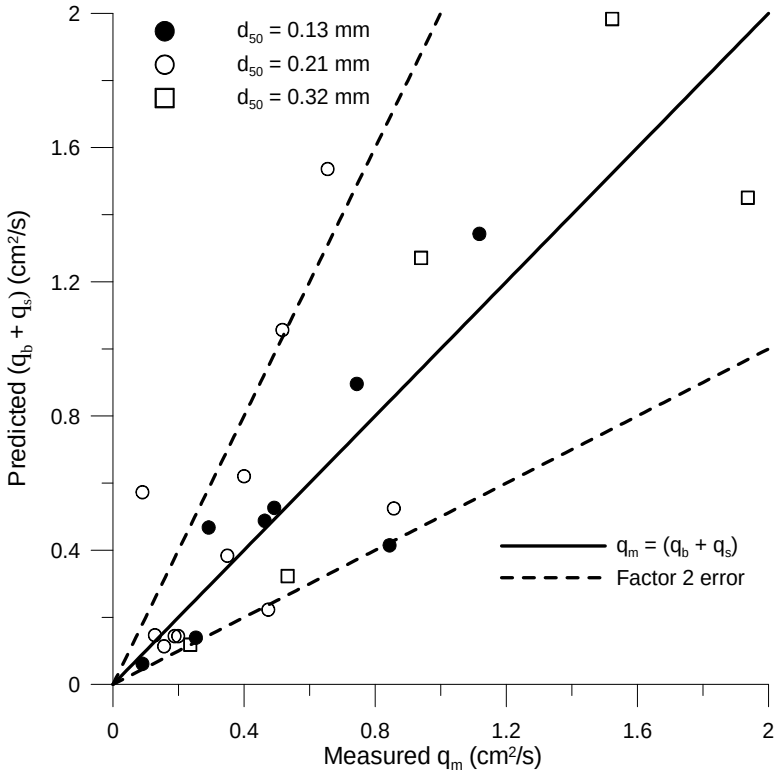

Figure 4.2: Predicted transport, $q_s + q_b$ vs. measured transport, q_m. Solid dots indicate a $d_{50} = 0.13$ mm, open circles indicate a $d_{50} = 0.21$ mm, and open squares indicate a $d_{50} = 0.32$ mm. The solid line signifies $q_m = q_s + q_b$, while the dotted lines indicate $q_m = 0.5(q_s + q_b)$ and $q_m = 2(q_s + q_b)$.

the calculated values, $q = (q_s + q_b)$ for the 24 tests. The coefficients for suspended load, a, and bedload, b, are 0.2 and 0.002 respectively. $a = 0.2$ in equation (4.20) accounts for the onshore suspended sediment transport rate due to the correlation between the horizontal velocity and concentration. This is acceptable in these tests perhaps due to time lags between the fluid velocity and concentration (Dohmen-Janssen *et al.*, 2002). The agreement is within a factor of about 2 for the three sands.

4.3.2 Bedload parameter

The choice of the bedload parameter, b, is partially justified by the data presented above, however, the limited conditions of the above data require additional justification for this choice.

The transport formula developed by Trowbridge and Young (1989) was used to predict onshore bar migration at Duck, N.C. during low wave energy conditions between February and August, 1982. The formula for q_b is

$$q_b = w_f K \frac{\tau_b}{\rho g(s-1)} \quad ; \quad \tau_b = \frac{D_f}{\sqrt{g\overline{h}}} > 0. \tag{4.28}$$

K is a fitted empirical parameter, and the time-averaged bed shear stress is small and directed onshore for random waves. If equation (4.10) is used to describe D_f then equation (4.28) becomes

$$q_b = \frac{K f_b}{2g(s-1)} \frac{w_f}{\sqrt{g\overline{h}}} \sigma_U^3 G_3(U_*). \tag{4.29}$$

This equation is similar to equation (4.27). If equation (4.29) is expressed in the form of equation (4.27), then

$$bP_b = (Kf_b/2) G_3 w_f / \sqrt{g\overline{h}} \tag{4.30}$$

G_3 is then taken to be 1.6 for $U_* \simeq 0$, where no current was accounted for in the formulation. The fall velocity for the conditions was 1.8 cm/s for sand with s=2.65 and $d_{50} = 0.16$ mm on the bar crest at Duck, NC. The calibrated Kf_b value was approximately 0.5. The bar crest was located in the water depth $\overline{h} \simeq 3.5$ m. Using these values, the value for q_b becomes

$$q_b = 0.0012 \frac{\sigma_U^3}{g(s-1)} = bP_b \frac{\sigma_U^3}{g(s-1)}. \tag{4.31}$$

If P_b is assumed to be on the order of 0.5 outside the surf zone, as is presented later, then equation (4.28) is consistent with equation (4.27) with b on the order of 0.002.

The present bedload formula is also consistent with the energetics-based bedload formula by Bagnold (1966) for steady flow if the latter formula is applied in the following time-averaged manner instead of the time-varying application made by Bailard and Inman (1981). The time-averaged immersed weight bedload transport rate, $\rho g(s-1)q_b$ is assumed to be proportional to the time-averaged energy dissipation rate, D_f, due to bottom friction where the energy dissipation due to wave breaking, D_B is neglected for the bedload. Using this relation and equation (4.10) results in the following

$$q_b = bP_b \frac{\sigma_U^3}{g(s-1)} \quad ; \quad bP_b = \frac{e_b}{\tan\phi}\frac{f_b}{2}G_3 \tag{4.32}$$

where e_b is the bedload efficiency, and ϕ is the internal friction angle of the sediment. The bottom slope effect is neglected in this study which is limited to sands. The value of $(e_b/\tan\phi)$ was adopted as 0.18 by Bagnold (1966), 0.33 by Bailard and Inman (1981), 0.32 by Guza and Thornton (1985), and 0.21 by Thornton *et al.* (1996) and Gallagher *et al.* (1998). For $(e_b/\tan\phi) = 0.2$, $f_b = 0.015$, and $G_3 = 1.6$, the value of bP_b from equation (4.32) is 0.0024 which is twice as large as the value based on equation (4.28). For a P_b value of 0.7, the bedload parameter $b \simeq 0.0034$ which is similar to the results found for the large-scale wave flume data. Therefore, the value of the bedload parameter, chosen to be, $b = 0.002$, is substantiated within a factor of two, that is, within the range, $b = 0.001 - 0.004$.

An equilibrium profile is derived from equation (4.20) and equation (4.27) where $(q_b + q_s) = 0$ for an equilibrium beach profile. Equation (4.20) is simplified by introducing e_c, the combined suspension efficiency such that $(e_b D_B + e_f D_f) = e_c(D_B + D_f)$. The suspended sediment volume is then proportional to the cross-shore gradient of the wave energy flux, F, using equation (4.1). Approximations of $C_g = \sqrt{g\overline{h}}$ and constant $\sigma_* = \sigma_\eta/\overline{h}$ are made for F given by equation (4.2). The probabilities, P_s and P_b are assumed to be constant or the same. Using equations

(4.4) and (4.6) with $q_r = 0$, the condition of $(q_b + q_s) = 0$ yields

$$\overline{h} = A(x_s - x)^{2/3} \quad ; \quad A = (\frac{3bP_b}{5aP_s e_c \sigma_*})^{2/3} (\frac{w_f^2}{g})^{1/3} \tag{4.33}$$

where x_s is the cross-shore location of $\overline{h}$=0 and $(x_s - x)$ is the offshore distance from the shoreline. The parameter A is the typical coefficient for equilibrium beach profiles developed by Dean (1991). Equation (4.33) describes the equilibrium profile used by (Dean, 1991) who presented the empirical relationship between A and w_f This relation was approximated by Kriebel *et al.* (1991) to be $a = 2.3\beta$ for sands where $\beta = (w_f^2/g)^{1/3}$. Bowen (1980) used a simple model to derive $A = 3.8\beta$ analytically. Then for $b/a = 0.01$, e_c =0.008, and $\sigma_* = 0.2$, equation (4.33) yields $A = 2.4\beta$, which may be regarded as typical inside the surf zone on sand beaches. However, it is recognized that the approximation of σ_* given in equation (4.4) is not accurate for barred beaches or near the shoreline. Thus, the expression for bedload transport given in equation (4.27) is reasonable even inside the surf zone. However, the bedload parameter, b, will vary in the cross-shore within a factor of about 2.

Equation (4.16) for sediment continuity is simplified by neglecting the $\partial V_s/\partial t$ term. This gives the continuity equation

$$(1 - n_p)\frac{\partial z_b}{\partial t} + \frac{\partial q}{\partial x} = 0 \quad ; \quad q = q_s + q_b. \tag{4.34}$$

This can be solved using a finite difference method with a constant Δx but a variable Δt. The value Δt is based on the numerical stability criterion of the Lax-Wendroff method used to compute z_b at the next time level (e.g. Nairn and Southgate, 1993; Tega and Kobayashi, 1999), where H_{rms}, $\overline{\eta}$, $\overline{U}$, and σ_U are computed at each time level as explained at the end of section 4.1. This computation is repeated starting from the initial bottom profile until the end of each profile evolution test. The computation time is on the order of 10^{-3} of the test duration.

Using the numerical model outlined in this chapter, eight tests (3 equilibrium, 2 small scale profile change, and 3 large scale tests) are simulated with and without

the roller effect in order to examine the accuracy of the model predictions. The results of these comparisons with experimental data are discussed in Chapter 5.

Chapter 5

MODEL COMPARISONS

The new model was tested using eight experimental data sets to check the validity of the new bedload formula described in Chapter 4 as well as the ability of the model to accurately predict profile change. Three equilibrium profiles were tested at peak periods of 1.6, 2.6, and 4.8 s (Kobayashi *et al.*, 2005). Data was obtained for erosive (Test E) and accretive (Test A) events as described in Chapter 2 and analyzed as in Chapter 3. Tabulated data used in model comparisons can be found in Appendices A and B. Three large scale tests, Test 1a, Test 1b, and Test 1c were also used to test the model (Roelvink and Reniers, 1995). A brief introduction to this data and the analysis used is found in Chapter 3. Tabulated data for these tests is found in Appendices C through E. Using this data, comparisons are made with the wave setup, $\overline{\eta}$ and standard deviation, σ_η, the mean horizontal velocity, $\overline{U}$ and standard deviation, σ_U, the turbulent velocities in the form of the turbulent kinetic energy, k, suspended sediment volume, V_s, the suspended sediment transport rate, q_s, as well as the final profile change. Comparisons for the three equilibrium cases are examined at length in Kobayashi *et al.* (2005) and are not displayed within the body of this text with the exception of final profile change results.

Comparisons for each test are displayed including the roller effect and not including this effect. Kobayashi *et al.* (2005) showed that the roller effect did not improve the agreement for the three equilibrium cases, however they did not compute the profile evolution.

5.1 Small scale tests

The breaker ratio parameter, γ, was calibrated using values of 0.6, 0.7, and 0.8. The cross shore variation of σ_η is related to the wave energy equation (4.1). γ was calibrated for the small scale tests using the three equilibrium profiles. It was found to be 0.8 for T_p=2.6 s and 0.6 for T_p=1.6 s and 4.8 s (Kobayashi *et al.*, 2005). The value of $f_b = 0.015$ was calibrated and used in the time-dependent computations for wave runup (Raubenheimer *et al.*, 2001) and sand suspension (Kobayashi and Johnson, 2001; Kobayashi and Tega, 2002). For each test, the model was run in increments of wave bursts. The three equilibrium cases were computed using three time steps: 0, 10 bursts, and 20 bursts, where the burst duration, t_b for each equilibrium case was 300 s, 400 s, and 900 s for tests with a T_p of 1.6, 2.6 and 4.8 s respectively. The erosive (Test E) and accretive (Test A) small scale tests also used a burst duration of 400 s, however the computations were done at each burst of 400 s rather than every 10 bursts and 20 bursts, and were computed to 23 bursts for Test E, and 20 bursts for Test A. The breaker ratio, γ was taken to be 0.8, the value for equilibrium profile of the same peak period. Inputs to the model included the initial beach profile, the H_{rms} wave height, T_p, and $\overline{\eta}$ at the position of wave gauge 1, $x = 0$. The averaged offshore wave conditions for the five small scale tests are displayed in Table 5.1.

Table 5.1: Offshore wave conditions for five small-scale tests.

Test	t_b **(s)**	**d (cm)**	$\overline{\eta}$ **(cm)**	T_p **(s)**	H_{rms} **(cm)**
4.8	900	80.6	-0.10	4.8	11.5
1.6	300	57.0	-0.13	1.6	11.7
2.6	400	71.4	-0.15	2.6	13.0
E	400	76.0	-0.16	2.6	12.8
A	400	77.2	-0.07	2.7	8.1

5.1.1 Free surface

The computed cross-shore variation of $\overline{\eta}$ and σ_η are shown in Figures 5.1 and 5.2 for Test E and Test A respectively. For the purposes of display, all computational variations for each test were averaged so as to only display one line for the wave set up and σ_η. This is consistent throughout the chapter. Individual data comparisons for each burst are displayed in Appendices A and B for Test E and Test A respectively. These individual comparisons were sufficiently similar to justify averaging over the entire test duration since the deviation between individually predicted values is smaller than the disagreement between the measured and predicted values. The measured wave signals at eight cross-shore locations for each burst are displayed on the averaged model result. Two results are shown. The inclusion of the roller effect is indicated by IROLL=1, while no inclusion of the roller effect is indicated by IROLL=0. For these and all subsequent figures, squares indicate measured values, the solid line indicates IROLL=0, and the dashed line indicates IROLL=1. For Test E, Figure 5.1 shows the location of the bar crest and the terrace edge of the beach profile as two kinks in $\overline{\eta}$ and σ_η (see Figure A.12). The kink indicating the bar crest is less pronounced in Figure 5.2 due to the bar's migration onshore in Test A (see Figure B.10). The effect of the roller was minimal in affecting $\overline{\eta}$ and σ_η however, of the two tests, the roller affected Test E more, especially in the bar region with an onshore shift of the wave setup. The agreement is acceptable for IROLL=0 and IROLL=1.

5.1.2 Reflection coefficient

Reflection coefficients were calculated from the measured data as described in section 2.1.10. These measured values were compared to the computed reflection coefficients for IROLL=1 and IROLL=0 using the simple method proposed by Kobayashi *et al.* (2005). Figure 5.3 shows the results for the two small scale tests. Incident and reflected wave data for Test E and Test A can be found in Appendices

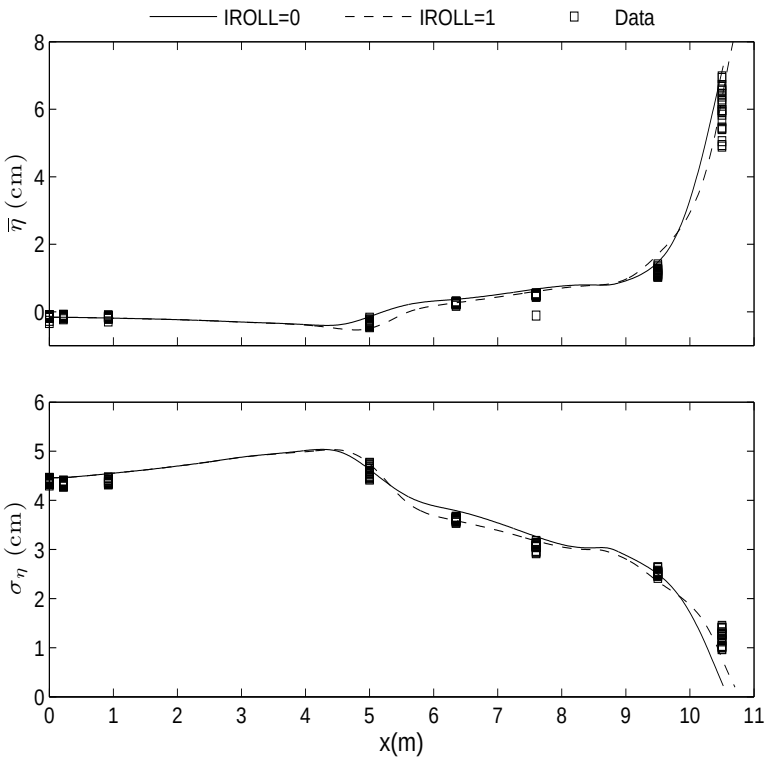

Figure 5.1: Test E: Measured and predicted (top) mean and (bottom) standard deviation of free surface elevation, η.

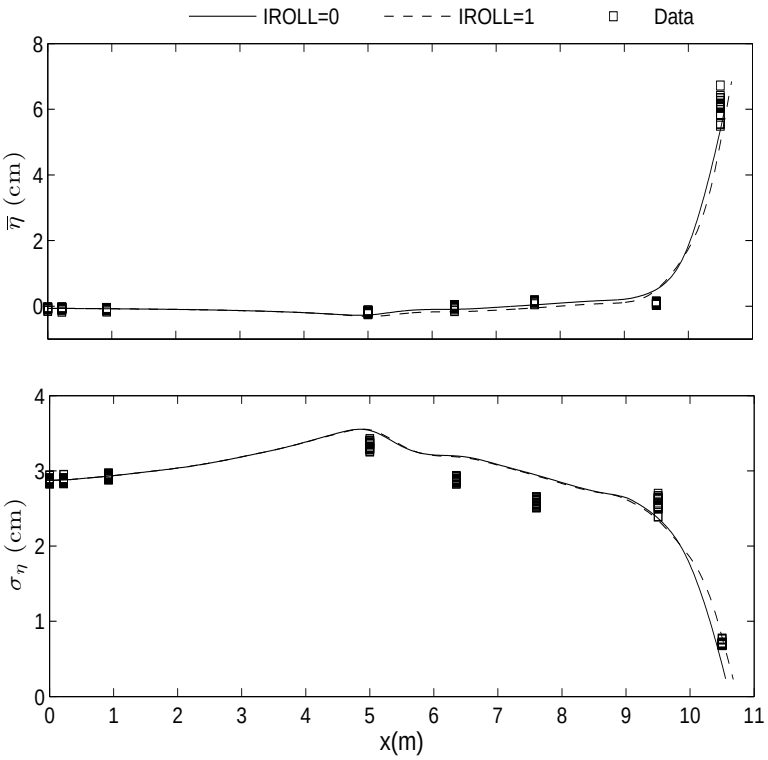

Figure 5.2: Test A: Measured and predicted (top) mean and (bottom) standard deviation of free surface elevation, η.

A and B respectively. They show that the model is overpredicting the reflection

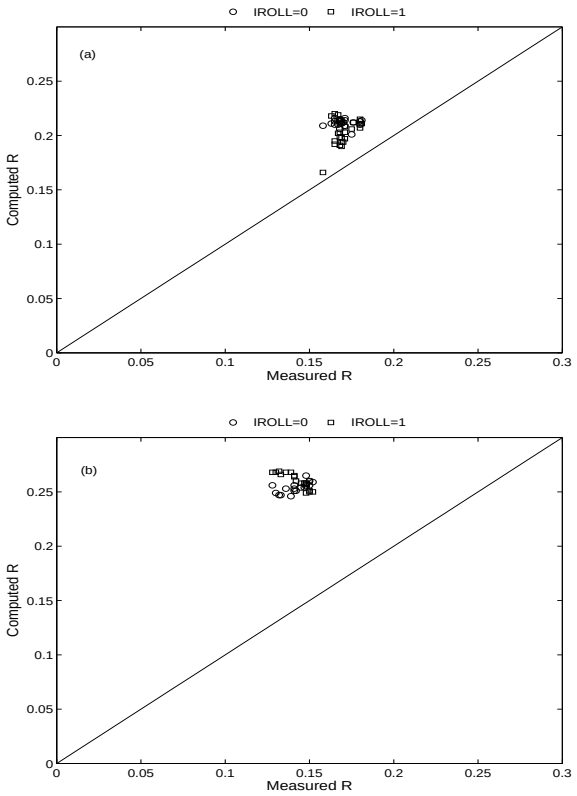

Figure 5.3: Measured and predicted reflection coefficients for (top) Test E and (bottom) Test A. The solid line would indicate predicted values = measured values. Circles indicate IROLL=0, while squares indicate IROLL=1.

coefficient for both the erosion and accretion tests.

5.1.3 Horizontal velocity

The inclusion of the roller is directly important to velocity comparisons, as the effect of the roller is to increase the magnitude of offshore velocity, thus increasing suspended load. From the analysis performed in Chapter 3, the value plotted for the erosion and accretion tests was taken to be the measured value for each burst

due to its lack of any coherent depth trend. The cross-shore variation in $\overline{U}$ and σ_U for Tests E and A are shown in Figures 5.4 and 5.5 respectively. For Test E,

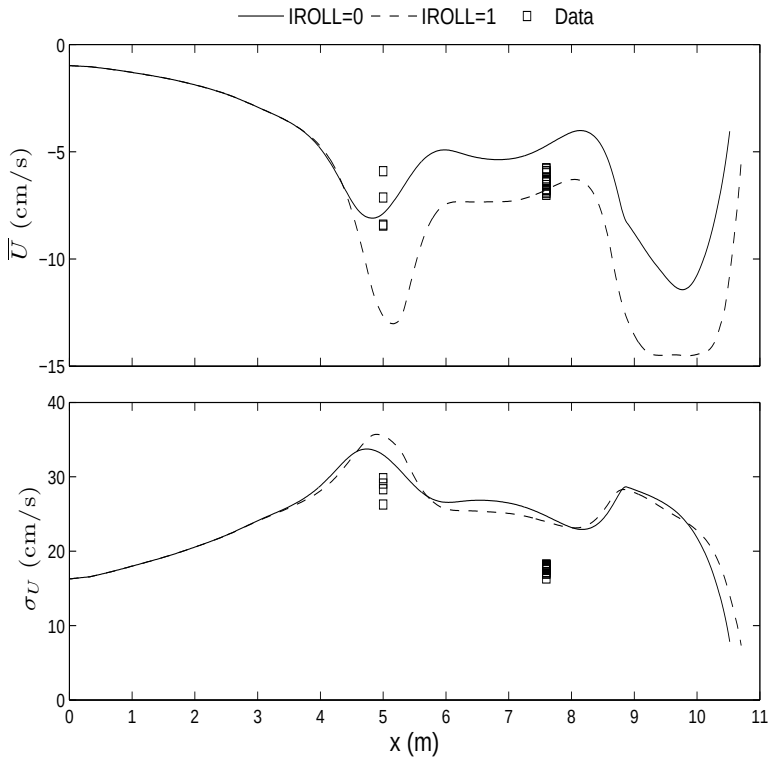

Figure 5.4: Test E: Measured and predicted (top) mean and (bottom) standard deviation of horizontal fluid velocity, U.

IROLL=1 increases the magnitude of the undertow current throughout the surf zone with peaks in the breaker region near the bar and in the transition region between the surf and swash zones. Outside of the surf zone, the roller has no effect. For Test A, the wave height was reduced and the bar moved onshore, so the breaker region near the bar was not as intense as in Test E. The undertow currents were are much less in this region than they were in Test E. The roller effect has less of an impact on the magnitude in this region, but still has a significant effect in the transition region. The roller still has no effect outside of the surf zone, and its effect

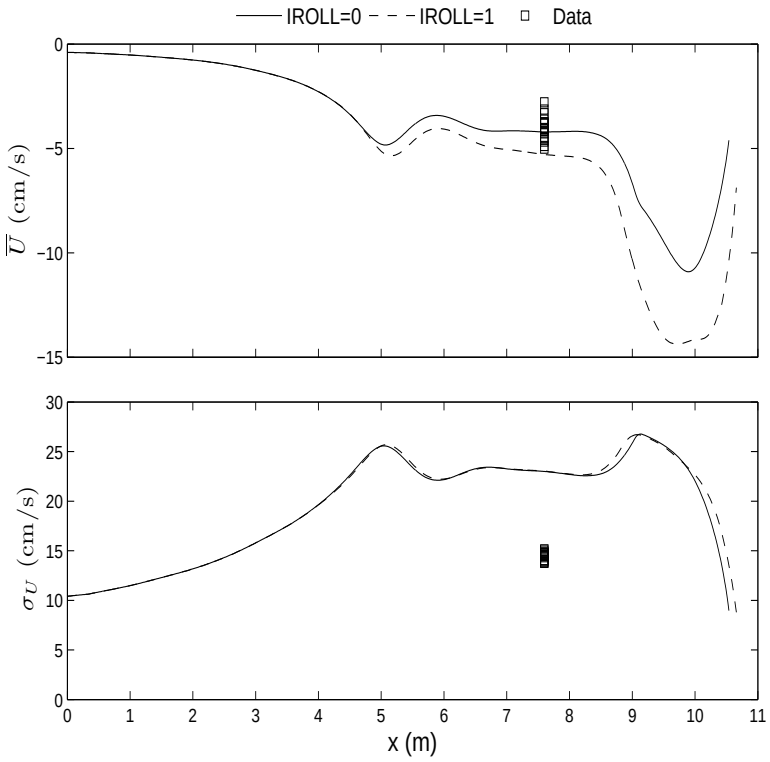

Figure 5.5: Test A: Measured and predicted (top) mean and (bottom) standard deviation of horizontal fluid velocity, U.

increases shoreward until the large peak in the transition region. On the other hand the model overpredicts the standard deviation, σ_η, somewhat.

While the computed results show significant differences in depth averaged velocities for IROLL=1 and IROLL=0, the measured velocity data seems to fit better without the roller effect included. This is consistent with the equilibrium profiles that were tested under similar experimental conditions (Kobayashi *et al.*, 2005) where it was found that the roller increased the magnitude of the velocity too much. The model cannot predict the mean velocity, $\overline{U}$, accurately, as was also the case with the previous comparisons by Kobayashi *et al.* (2005).

In section 3.1.2, the measured turbulent velocity, $\sqrt{k}$, is obtained, which is assumed to correspond to $(D_f/\rho)^{(1/3)}$, where (D_f) is the computed energy dissipation rate due to bottom friction. Figures 5.6 and 5.7 show the computed cross-shore variation of the turbulent velocities for Test E and Test A respectively. From Figure 5.6, it is seen that the roller somewhat increases the computed energy dissipation rate due to bottom friction at the bar crest for Test E, while in Figure 5.7, it can be seen that the computed dissipation rate remains about the same at the bar crest. In both tests, the turbulent velocities due to bottom friction increase onshore until the peak at the bar area. For Test E, they decrease until another peak in the transition region between the surf zone and the swash zone. This peak is due to the corresponding peak of the standard deviation, σ_η, shown in Figures 5.1 and 5.2. This peak is of similar magnitude in both tests, while the peak at the bar area is larger in Test E due to the larger value of σ_η over the bar. From the data shown, IROLL=0 provides better agreement with the measured data.

5.1.4 Sediment transport

Figures 5.8 and 5.9 show the predicted cross-shore variations of the probabilities, P_b and P_s, and the sediment transport rates, q_s, q_b, and $q = (q_b + q_s)$ for Tests E and A respectively. For all five small scale tests, $P_s = P_b$, and suspension occurs

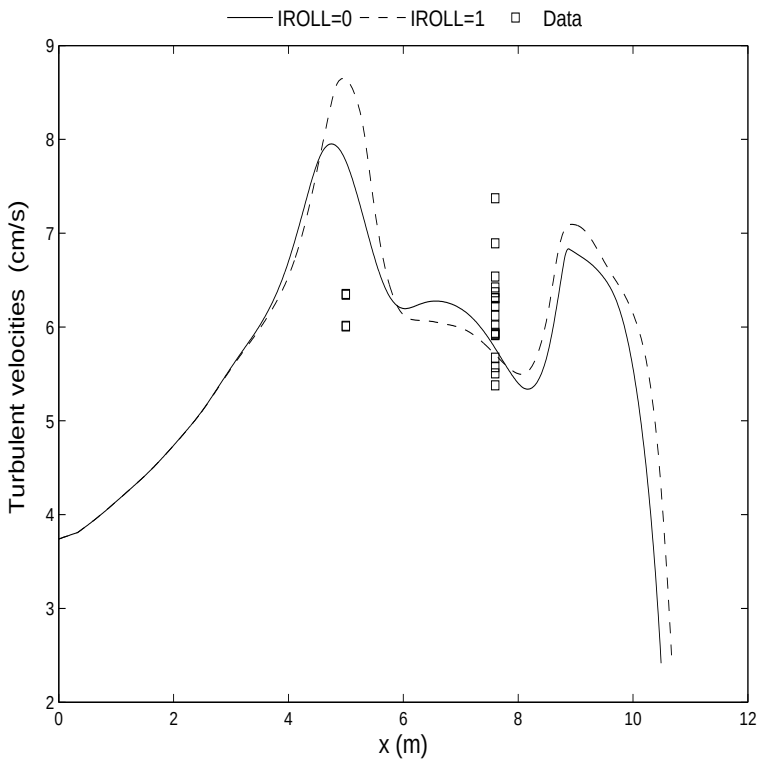

Figure 5.6: Test E: Comparison between the estimated turbulent velocity, derived from measured data, and the computed turbulent velocity, $(D_f/\rho)^{(1/3)}$.

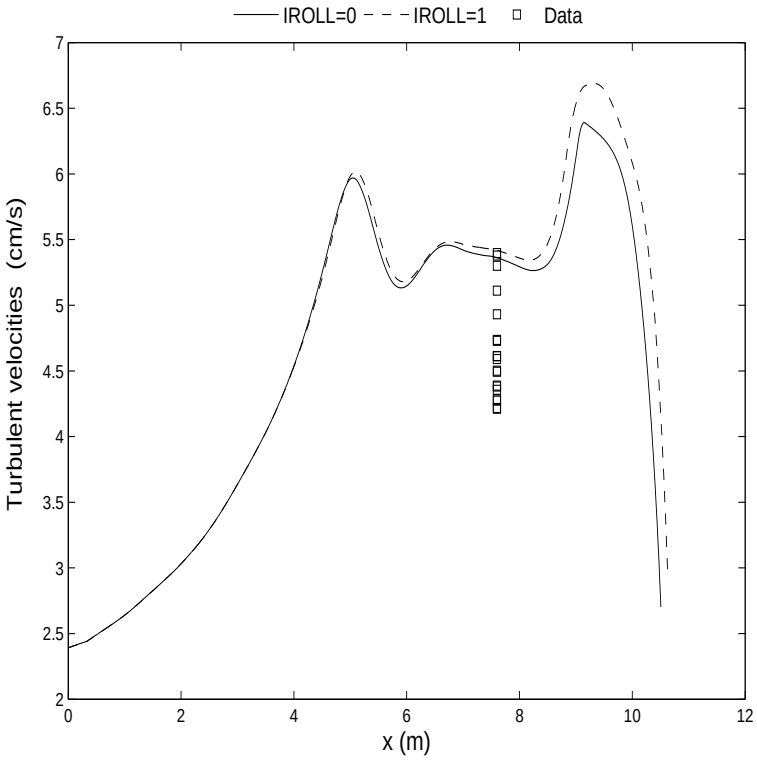

Figure 5.7: Test A: Comparison between the estimated turbulent velocity, derived from measured data, and the computed turbulent velocity, $(D_f/\rho)^{(1/3)}$.

when the sediment movement is initiated in these tests. The probabilities increase onshore and reach approximately 0.7 in the surf zone, and then decrease rapidly in the swash zone. Outside of the surf zone, the suspended sediment transport rate, q_s, is very small. It becomes large in the breaker zone, and decreases onshore except for the peak in between the surf and swash zone for Test E. Test A had much less intense wave breaking over the bar area, and subsequently, the suspended sediment transport rate in this area is much smaller than that of Test E. Both tests had comparable suspension in the transition region. The cross-shore variation of the bedload transport rate, q_b is similar to $(-q_s)$ except that the decrease offshore is more gradual. The net transport rate, q is on the order of 0.01 cm^2/s or 1 m^2/yr which is small compared to the measured values obtained in the water tunnel and wave flume tests discussed in Chapter 4.

Calculation of the suspended sediment transport rate from the measured values of U and C, $\overline{q_s}$, is explained in section 3.1.3. These measured values were compared with computed results with and without the roller effect. The comparisons are shown in Figures 5.8(b) and 5.9(b).

For the small scale tests, the model computations underpredict the suspended sediment transport rate. The measured magnitude is much larger than the computed value. Since the calculated value from measurements was based on vertically-averaged quantities, where the measured C had an uncertainty of 20%, its accuracy of the small net transport may be only within an order of magnitude. The measured $\overline{q_s}$ was negative (offshore) as assumed in the formula for q_s.

The cross-shore variation of the volume of suspended sediment per unit bottom area, V_s is shown for Test E and Test A in Figures 5.10 and 5.11. The measured volume of suspended sediment, V_s was calculated using equation (3.12) for $\overline{V_a}$. Measured values for Test E and Test A are also displayed in Figures 5.10 and 5.11.

For IROLL=1, the volume of suspended sediment is less at the bar crest

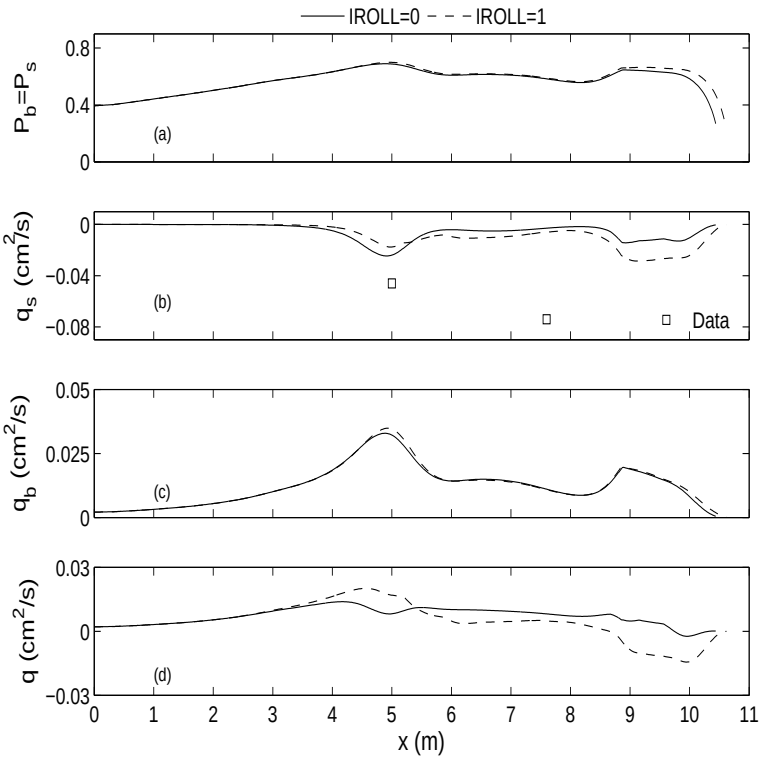

Figure 5.8: Test E: Predicted cross-shore variations of (a) P_b, where $P_s = P_b$ for this test, (b) q_s and measured data, (c) q_b, and (d) $q = (q_s + q_b)$.

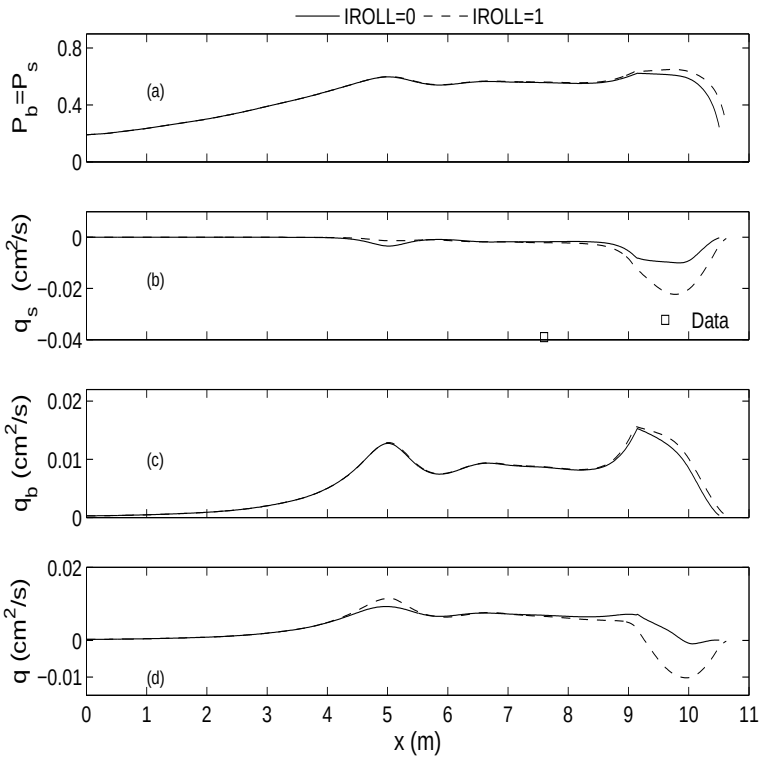

Figure 5.9: Test A: Predicted cross-shore variations of (a) P_b, where $P_s = P_b$ for this test, (b) q_s and measured data, (c) q_b, and (d) $q = (q_s + q_b)$.

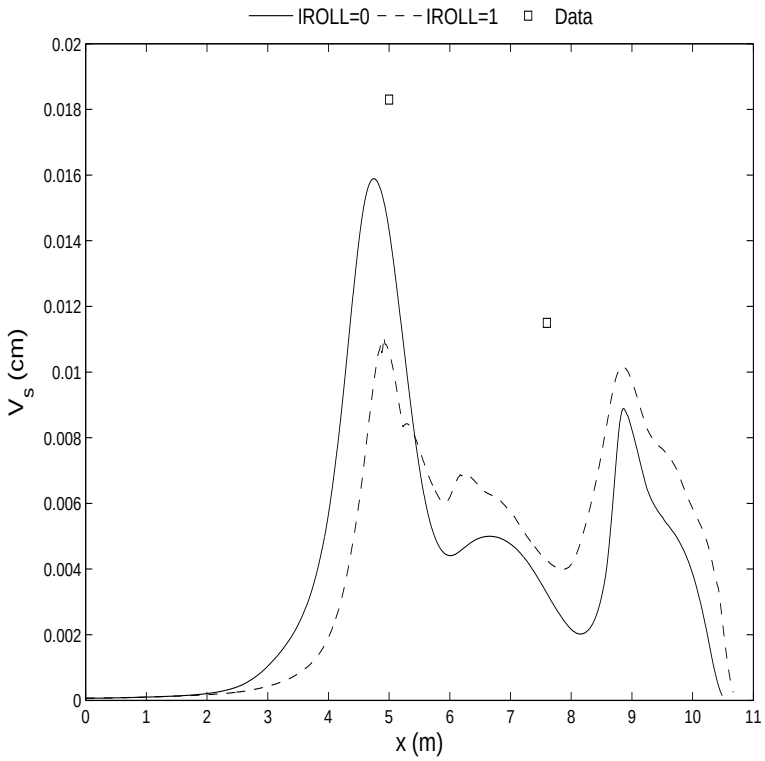

Figure 5.10: Test E: Comparison of total suspended sediment volume per unit area, V_s.

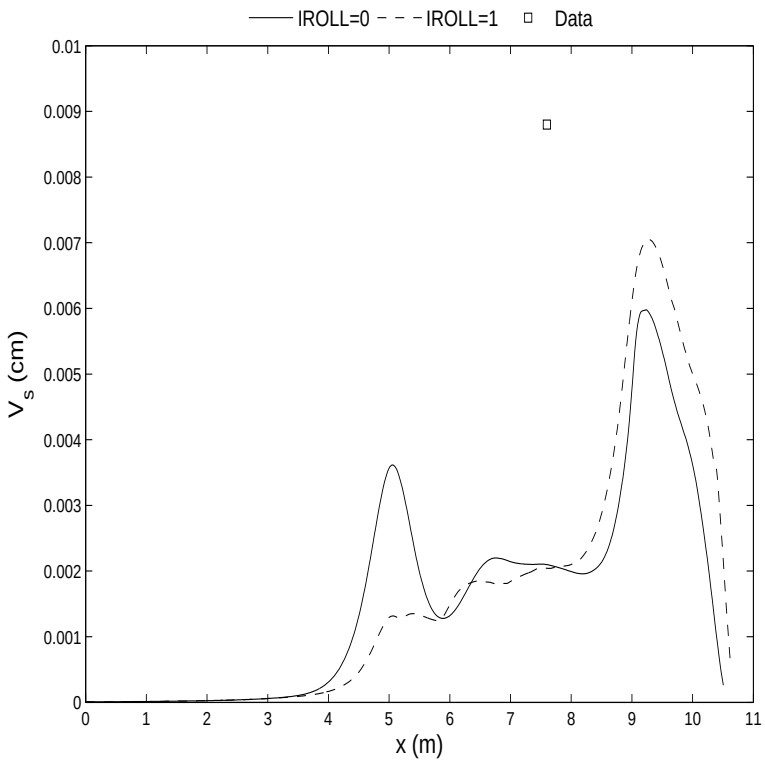

Figure 5.11: Test A: Comparison of total suspended sediment volume per unit area, V_s.

than for IROLL=0 because the roller effect shifts the breaker energy dissipation shoreward. The peaks of suspension at the transition area near the swash zone are of greater magnitude with the roller. At the bar crest, the peak for Test E is reduced significantly by including the roller, and for Test A, there is almost no peak at all. The volume of suspended sediment increases at its seaward peak near the swash zone. In both tests, there is virtually no suspended sediment volume in the offshore area, The suspended sediment volume was underpredicted in the surf zone by the model for the small scale tests. The measured V_s is not very accurate since the concentration was not measured simultaneously over the depth. Computed results and measured results are on the same order of magnitude. The computed results for IROLL=0 or IROLL=1 are similar in light of the accuracy of the measured data.

5.1.5 Profile change

The equilibrium profile tests was presented in Kobayashi *et al.* (2005). Figure 5.12 shows the final computed profile evolution results after 20 bursts for the equilibrium profiles. The computation duration was chosed since the measured bottom change was less than 1 cm after 20 bursts. For all profile evolution results, the solid line indicates IROLL=0, the dashed line indicates IROLL=1, the dot-dash line represents the measured profile (if applicable), and the dotted line represents the initial profile. Figure 5.12 shows that for IROLL=1, the difference between the equilibrium profiles and the predicted profiles is larger than the difference computed with IROLL=0. The burst duration for each test is 900 ,300, and 400 s for Test 4.8, 1.6 and 2.6 respectively. The equilibrium profile for Test 1.6 was predicted satisfactorily for both IROLL=0 and IROLL=1. For Test 2.6, IROLL=0 predicts the equilibrium profile, but IROLL=1 predicts vertical accretion of about 3 cm on the bar crest and slightly below the still water level. It also predicts vertical erosion of about 2 cm above the still water level. For Test 4.8, the predicted profile deviates from the equilibrium profile by up to 4 cm for IROLL=0 and 6 cm for IROLL=1.

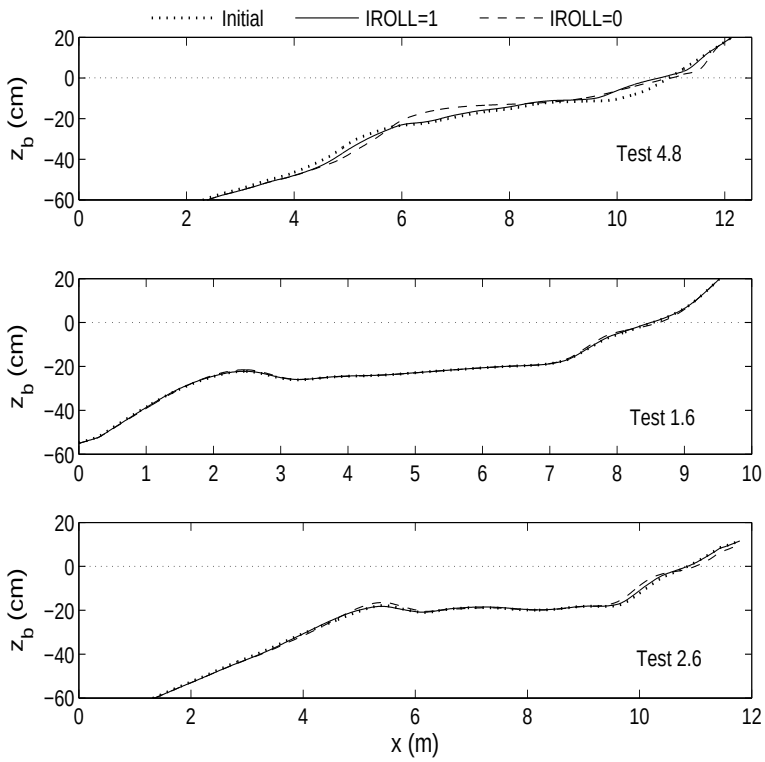

Figure 5.12: Equilibrium test (top) 4.8, (middle) 1.6, and (bottom) 2.6: Final profile comparisons after 20 bursts.

The difficulty in predicting the three equilbrium profiles using the formulas given by equations (4.20) and (4.27) arises partially from the choice of the fixed parameters, a=0.2 and b=0.002. In reality, these parameters could vary in the cross-shore by a factor of about 2.

For the remaining two small scale tests, computed profiles for IROLL=0 and IROLL=1 were compared to measured profiles at each time level of noticeable profile changes. These comparisons can be found in Appendices A and B for Test E and Test A respectively. The final comparison after the conclusion of each test, are shown in Figures 5.13 through 5.15. Each of these figures displays the computed profiles for IROLL=0 and IROLL=1 with the final measured profile (top), with the initial profile (middle), and the change in elevation from the initial profile for IROLL=0, IROLL=1, and measured (bottom). This display format is followed for all final profile comparisons with the exception of the equilibrium profiles that were already discussed. Measured profiles were collected after 1, 2, 3, 6, 10, 14, 19, 23, and 43 bursts for Test E. Measured profiles collected after 2, 4, 7, 11, 15, and 20 bursts for Test A. For Test E, profiles are displayed after 23 bursts in Figre 5.13 (final profile after the end of the erosion test) and after 43 bursts in Figure 5.14 (final profile after the end of the image test, described in Chapter 2). For Test A, profiles are displayed after 20 bursts in Figure 5.15.

In Figure 5.13, for test E, the lower swash zone and the bar trough were eroded, whereas the upper swash zone and the transition zone between the surf and swash zone were accreted. The vertical elevation change was less than 3 cm. The numerical model with IROLL=1 predicts the profile change near the shoreline fairly well but overpredicts the bar growth which is predicted by IROLL=0 better. Figure 5.14 shows that the disagreement persists after an additional 20 bursts. In Figure 5.15, for Test A, the bar moved onshore and the zone below the still water level was eroded. The vertical elevation change was less than 5 cm. The numerical

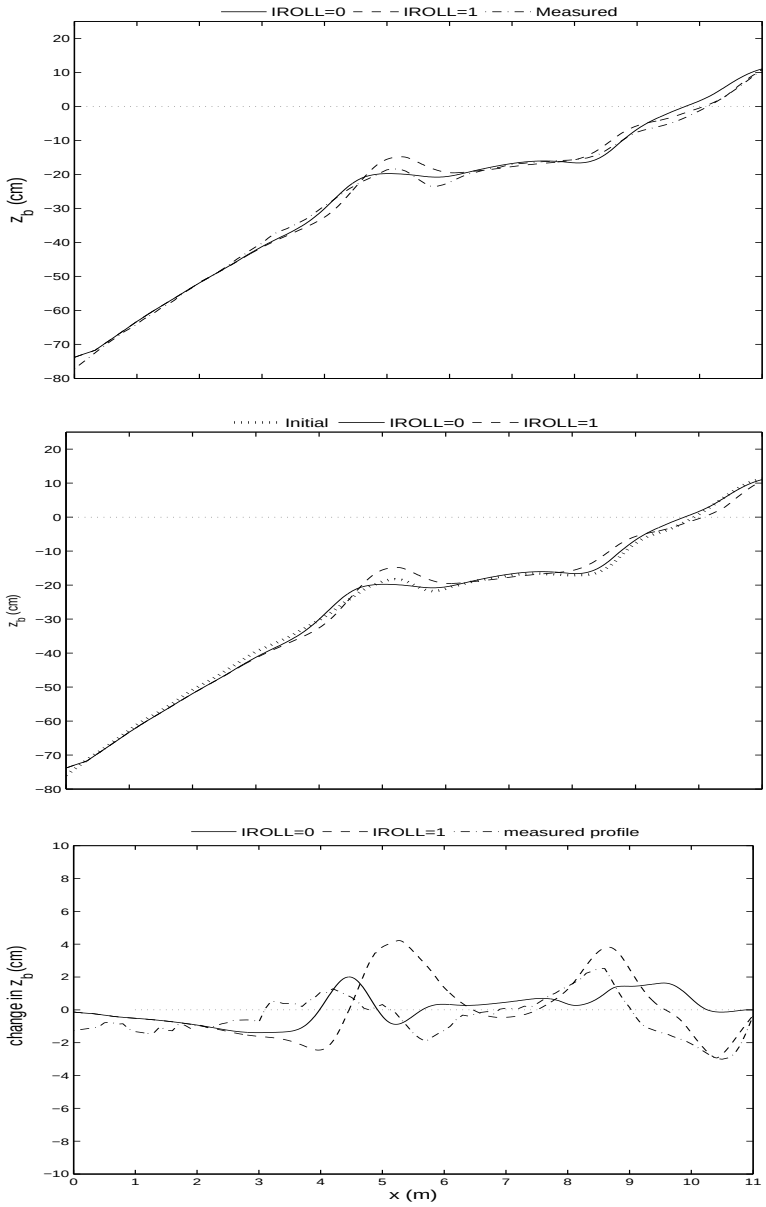

Figure 5.13: Test E: (top) Computed and measured profiles for $t = 9200s$, (middle) Computed and initial profile for $t = 9200s$, (bottom) Computed change from the initial profile for $t = 9200s$.

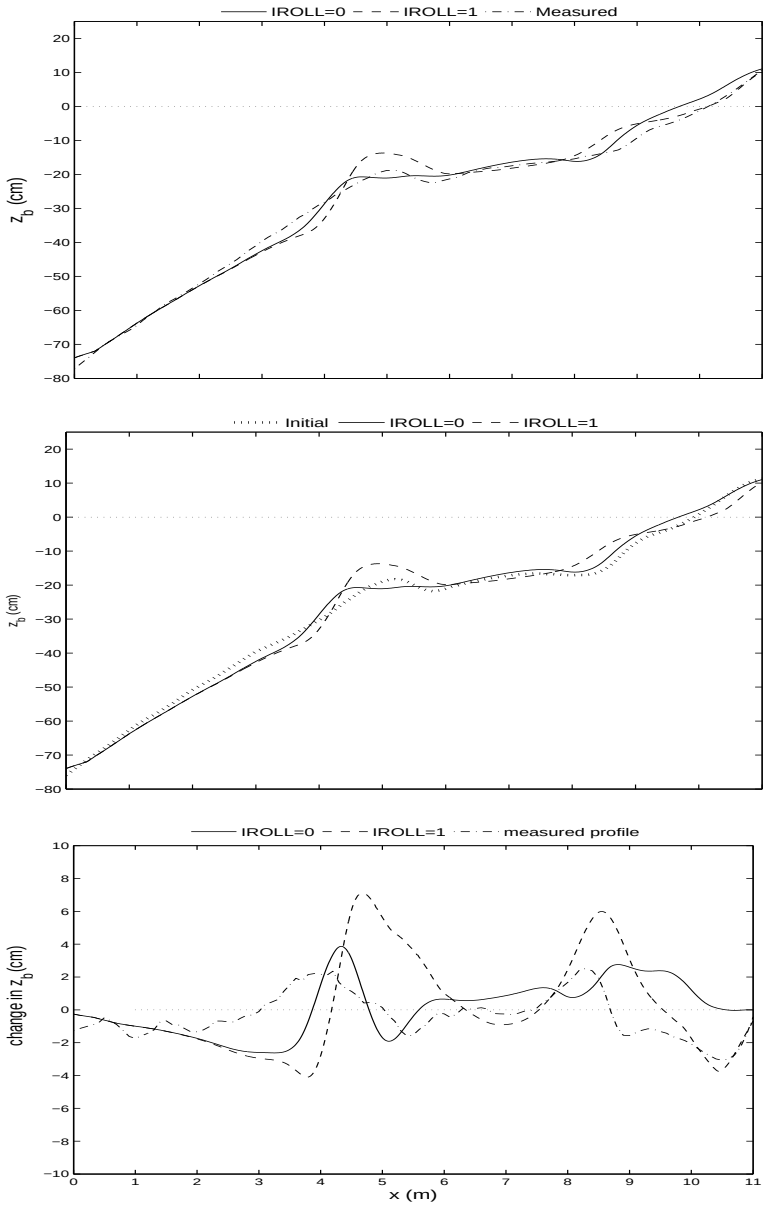

Figure 5.14: Test E: (top) Computed and measured profiles for $t = 17200s$, (middle) Computed and initial profile for $t = 17200s$, (bottom) Computed change from the initial profile for $t = 17200s$.

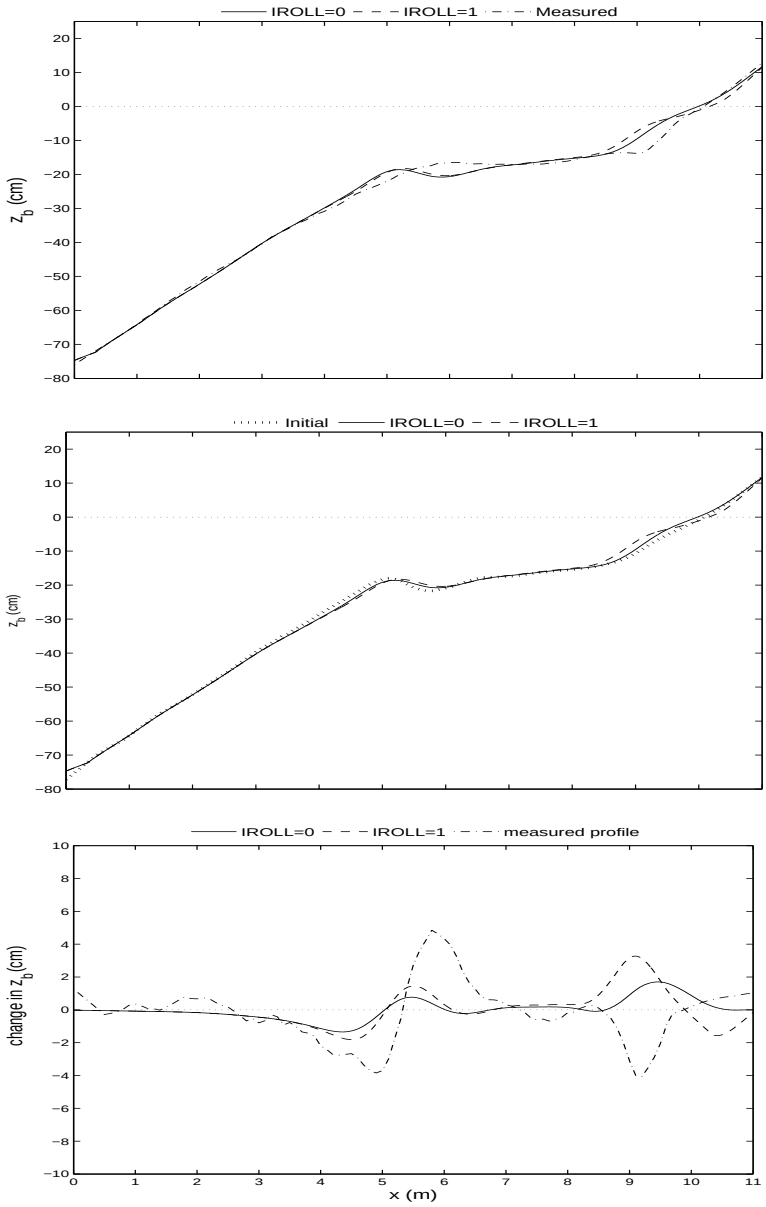

Figure 5.15: Test A: (top) Computed and measured profiles for $t = 8000s$, (middle) Computed and initial profile for $t = 8000s$, (bottom) Computed change from the initial profile for $t = 8000s$.

model with IROLL=0 and 1 underpredicts the onshore bar migration considerably and predicts slight accretion in the erosion zone below the still water level.

5.2 Large scale tests

The data obtained for the large scale test is reviewed and tabulated in Roelvink and Reniers (1995). For each of these tests, 1a, 1b, and 1c, the calibrated value of the breaker ratio, γ, was 0.7. Model computations were performed at each wave burst interval, similarly to Test E and Test A. Burst duration for the large scale tests was 1 hour. Averaged offshore wave conditions for the three large scale tests were obtained from Roelvink and Reniers (1995) and are shown in Table 5.2. t_t is defined as the total time of the test.

Table 5.2: Offshore wave conditions for three large-scale tests.

Test	t_t **(hr)**	**d (cm)**	$\overline{\eta}$ **(cm)**	T_p **(s)**	H_{rms} **(cm)**
1a	12	409	-1.1	4.8	64
1b	18	406	-3.3	5.0	93
1c	13	407	-0.8	8.0	39

5.2.1 Free surface

For each of the large scale tests, wave gauges were placed to measure the free surface at three different locations for each wave hour. The placement scheme is outline in Chapter 3. Here, Test 1b data is not displayed, as wave gauges were only located at 20 m from the wave-maker, taken to be $x = 0$, and these values were used as input parameters for the computation, so serve no purpose in comparison. For both the Test 1a and Test1c, the cross-shore variations of $\overline{\eta}$ and σ_η are compared with measured values in Figures 5.16 and 5.17. Measured data is tabulated and presented for the large scale data in Appendices C through E.

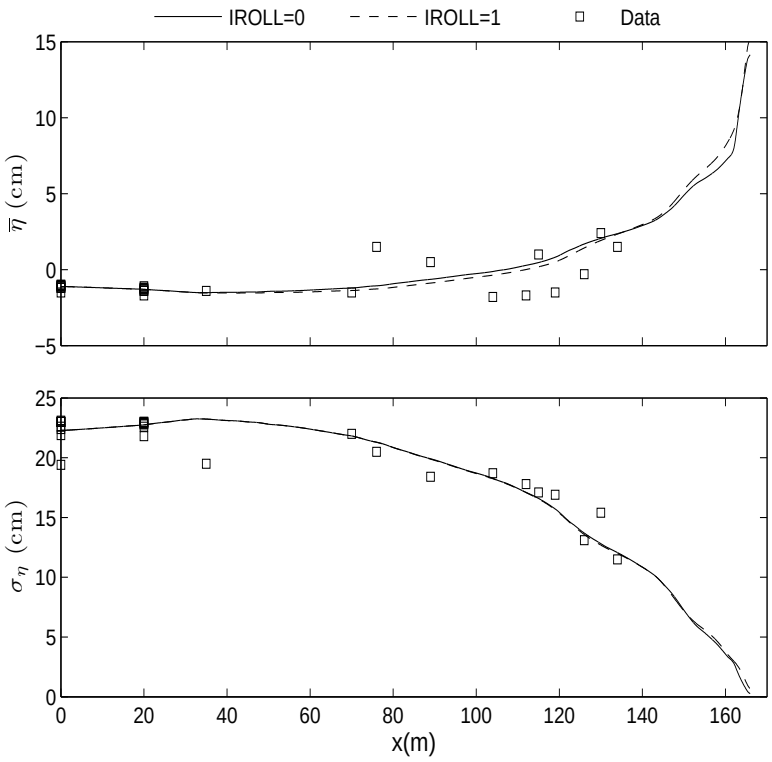

Figure 5.16: Test 1a: Measured and predicted (top) mean and (bottom) standard deviation of free surface elevation, $\overline{\eta}$.

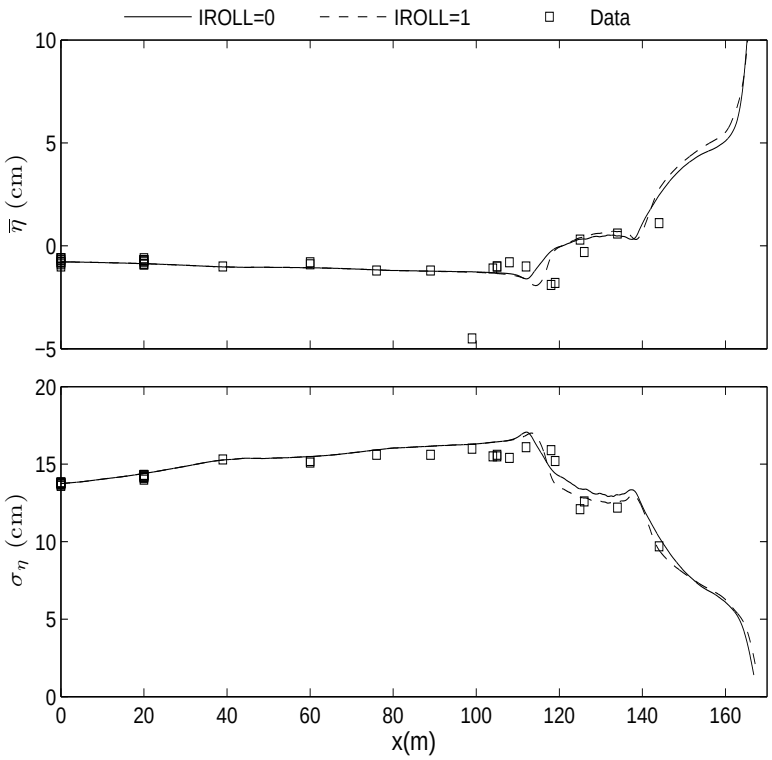

Figure 5.17: Test 1c: Measured and predicted (top) mean and (bottom) standard deviation of free surface elevation, $\overline{\eta}$.

The free surface elevation, η is dependent on the shape of the underlying profile (see Figures 5.27 through 5.29 for the measured bottom profiles) as can be seen from the differences between Test 1a and Test 1c. It is also dependent on wave conditions shown in Table 5.2. In Figure 5.17, there are two kinks in the cross-shore variation that indicate the locations of the bar crest and the terrace edge (see Figure 5.29). In Figure 5.16, the cross-shore variation is smooth, with no noticeable kinks. This is due to the smooth equilibrium profile. The bar and terrace have yet to form so the profile continues to look almost like an idealized equilibrium profile (see Figure 5.27). The agreement with measured data is similar, as IROLL=1 does not change the computed $\overline{\eta}$ and σ_η significantly.

5.2.2 Horizontal velocity

The cross-shore variation of the mean and standard deviation of the horizontal velocity, U, for Tests 1a, 1b, and 1c are shown in Figure 5.18 through 5.20. Measured velocities were collected at the cross-shore locations displayed in Table 3.6. The measured values of $\overline{U}$ were fitted by a parabolic undertow model and averaged as described in section 3.2.2. This averaged velocity was plotted as the measured data point of $\overline{U}$. The standard deviation, was vertically averaged as the vertical variations were small. This averaged value was plotted as the data point for σ_U. Tabulated values for each test can be found in Appendices C through E.

For both Test 1a and 1b, the velocity profiles look similar, with Test 1b being of slightly higher magnitude due to the larger offshore wave height shown in Table 5.2. But in each case, the roller increases the magnitude of the undertow current, and this effect grows continuously moving onshore with peaks in the bar area and over the terrace. However for Test 1c, there is virtually no difference in IROLL=1 and IROLL=0 except in the breaker regions at the bar crest, terrace and near the shoreline. There is no continuous roller effect on the velocity outside the surf zone, since the wave height is reduced and the period increased. The numerical

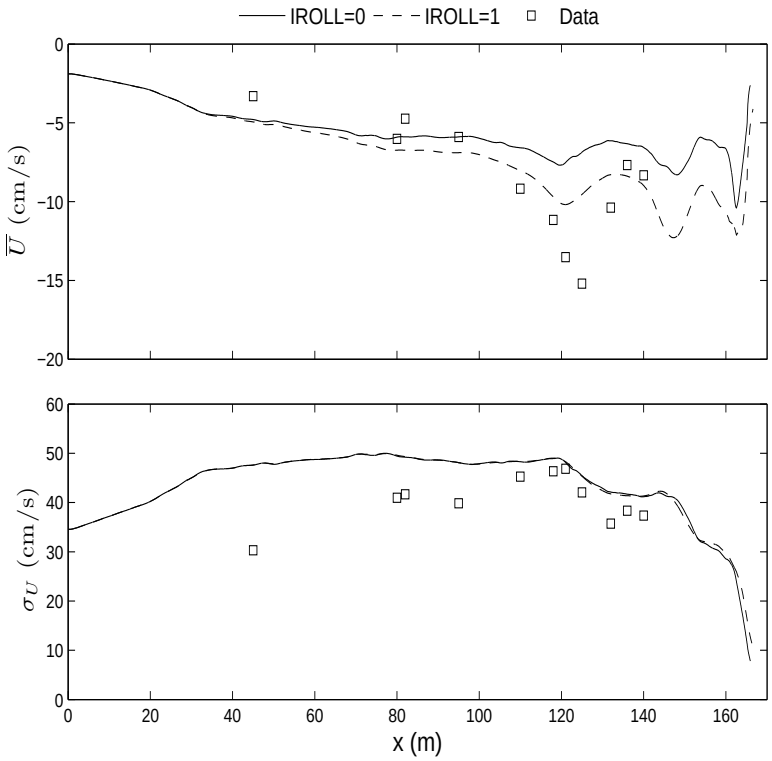

Figure 5.18: Test 1a: Measured and predicted (top) mean and (bottom) standard deviation of horizontal fluid velocity, U.

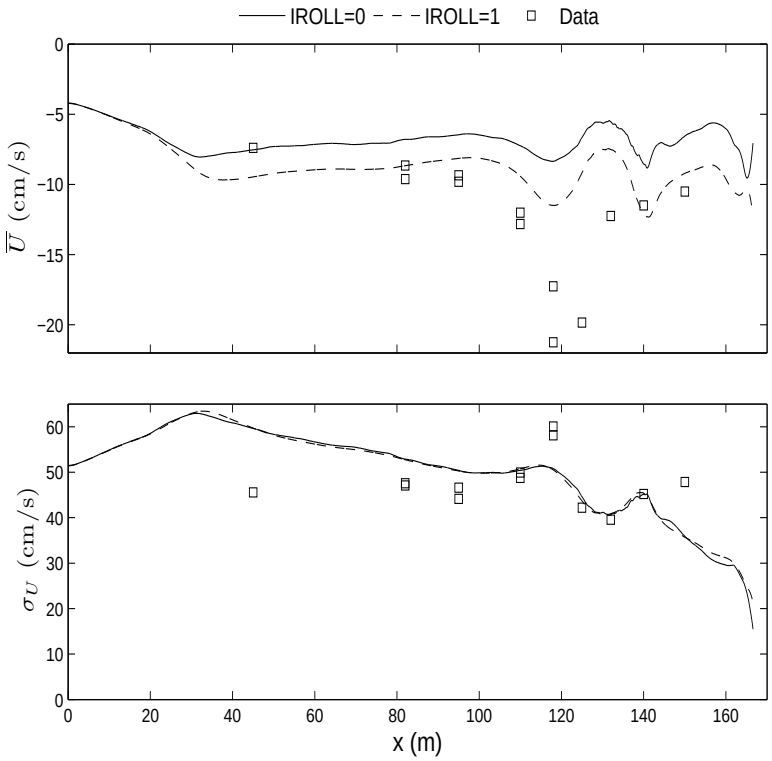

Figure 5.19: Test 1b: Measured and predicted (top) mean and (bottom) standard deviation of horizontal fluid velocity, U.

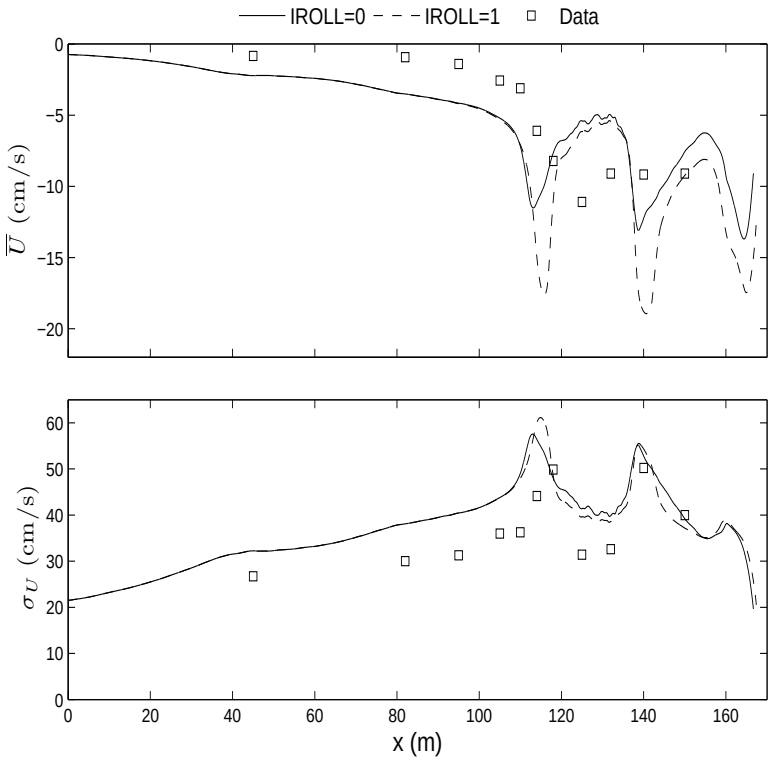

Figure 5.20: Test 1c: Measured and predicted (top) mean and (bottom) standard deviation of horizontal fluid velocity, U.

model is found to not predict $\overline{U}$ well, as was the case in Kobayashi *et al.* (2005). Underprediction of $\overline{U}$ is most noted in the bar region for Tests 1a and 1b where the accuracy of the measured $\overline{U}$ was not discussed by Roelvink and Reniers (1995). The agreement with σ_U is better than that of $\overline{U}$, however the model tends to overpredict σ_U somewhat.

5.2.3 Suspended sediment

The computed cross-shore variation of the probabilities, P_b and P_s, as well as sediment transport rates, q_s, q_b, and $q = (q_s + q_b)$ are shown in Figures 5.21 through 5.23. In each case, the probability of suspension, P_s, is the same as the probability of sediment movement, P_b, in the three large scale tests.

In comparison to the small scale tests, the probability of movement was increased to about 0.8 in the surf zone before the rapid decrease in the swash zone for the large scale tests, where the bottom slope was gentler and the offshore wave height was larger relative to the offshore depth in Tests 1a and 1b (Tables 5.1 and 5.2). Test 1c, with the smaller value of H_{rms}, does increase in the offshore region outside the surf zone. For all three tests, the net transport remains directed onshore for the entire cross-shore distance, where in the small scale tests there was a negative peak at the terrace edge. The magnitudes of q_b and q_s are much larger than those computed for the small scale tests. For all three tests, q_b and q_s appear to be the mirror images of each other, with bedload transport dominating in these tests.

The cross-shore variation of the suspended sediment volume per unit area, V_s, is compared with measured values calculated using equation (3.12). The numerical model cannot predict V_s accurately, which was also the case in the small scale tests, although then V_s was underpredicted, whereas in the large scale tests, the model tends to overpredict V_s.

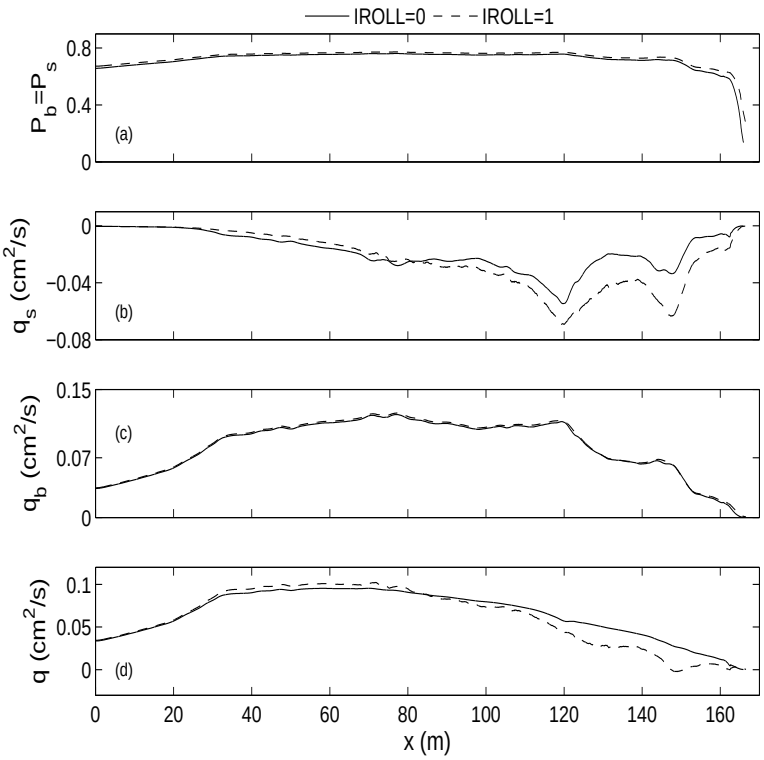

Figure 5.21: Test 1a: Predicted cross-shore variations of (a) P_b, where $P_s = P_b$ for this test, (b) q_s, (c) q_b, and (d) $q = (q_s + q_b)$.

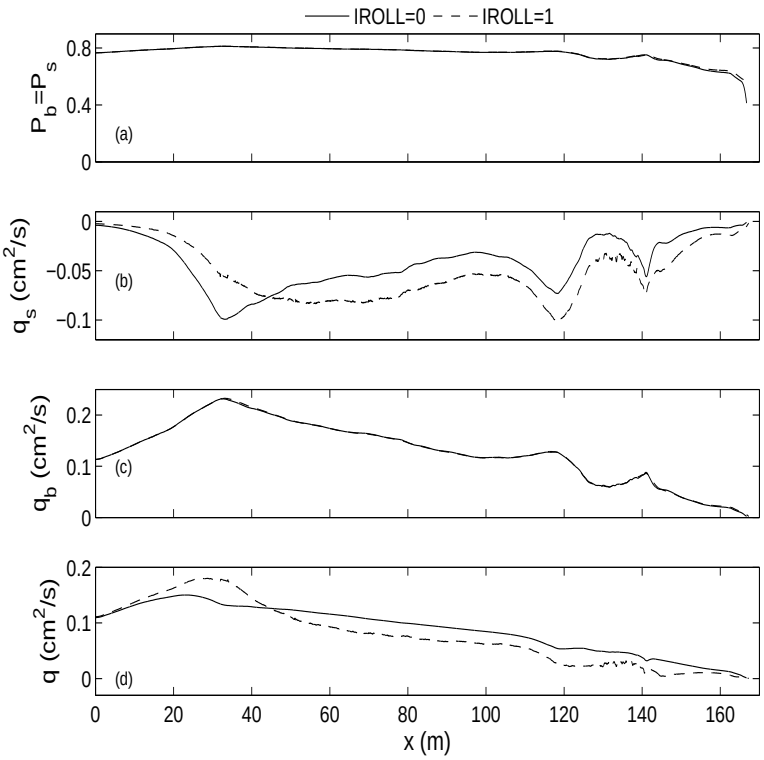

Figure 5.22: Test 1b: Predicted cross-shore variations of (a) P_b, where $P_s = P_b$ for this test, (b) q_s, (c) q_b, and (d) $q = (q_s + q_b)$.

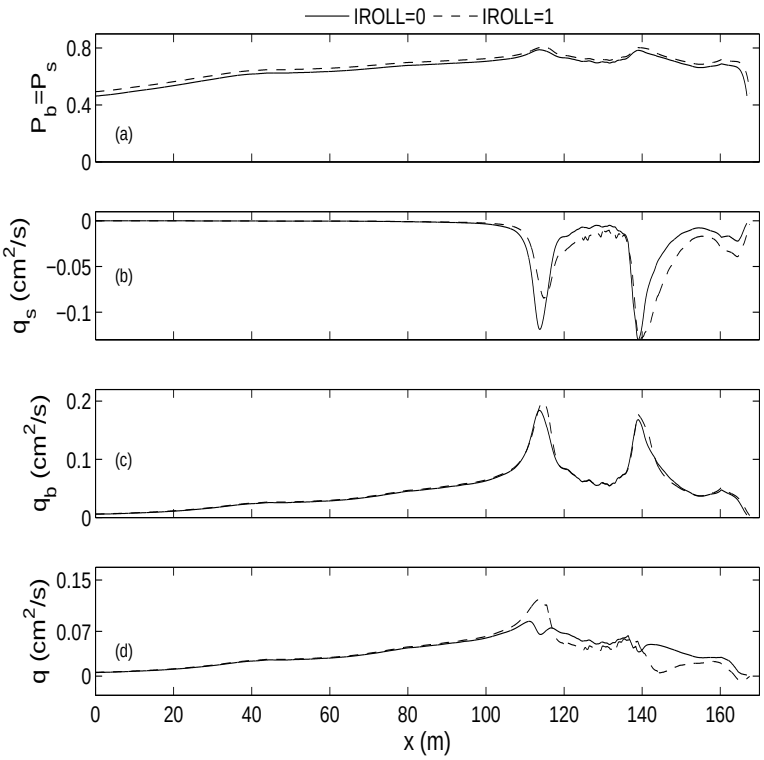

Figure 5.23: Test 1c: Predicted cross-shore variations of (a) P_b, where $P_s = P_b$ for this test, (b) q_s, (c) q_b, and (d) $q = (q_s + q_b)$.

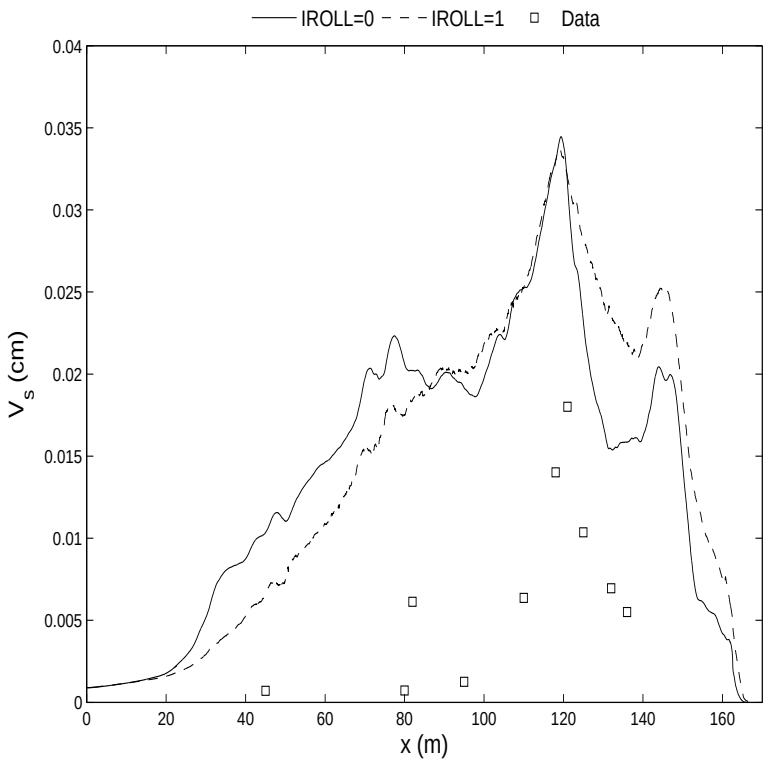

Figure 5.24: Test 1a: Comparison of total suspended sediment volume per unit area, V_s.

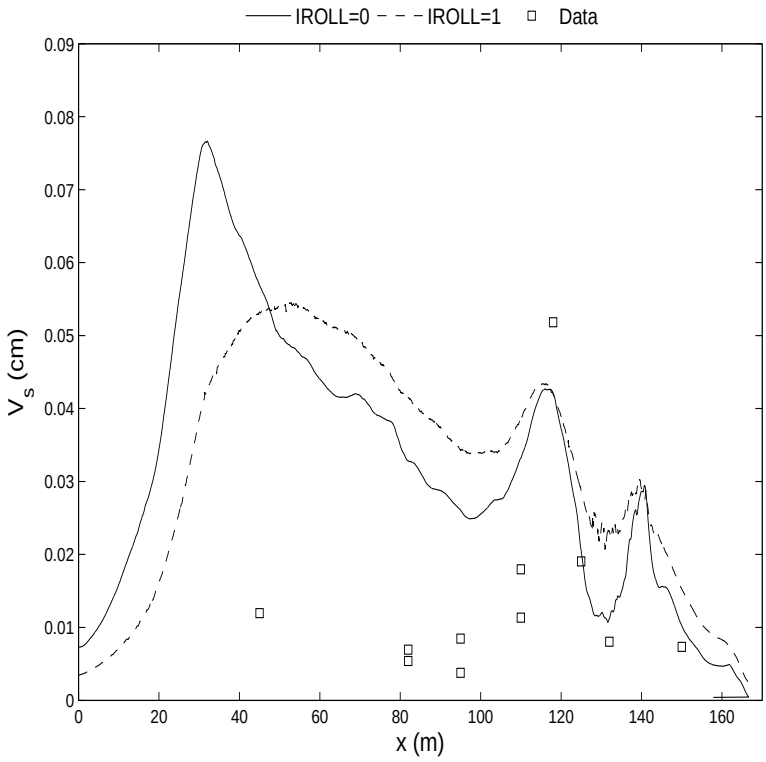

Figure 5.25: Test 1b: Comparison of total suspended sediment volume per unit area, V_s.

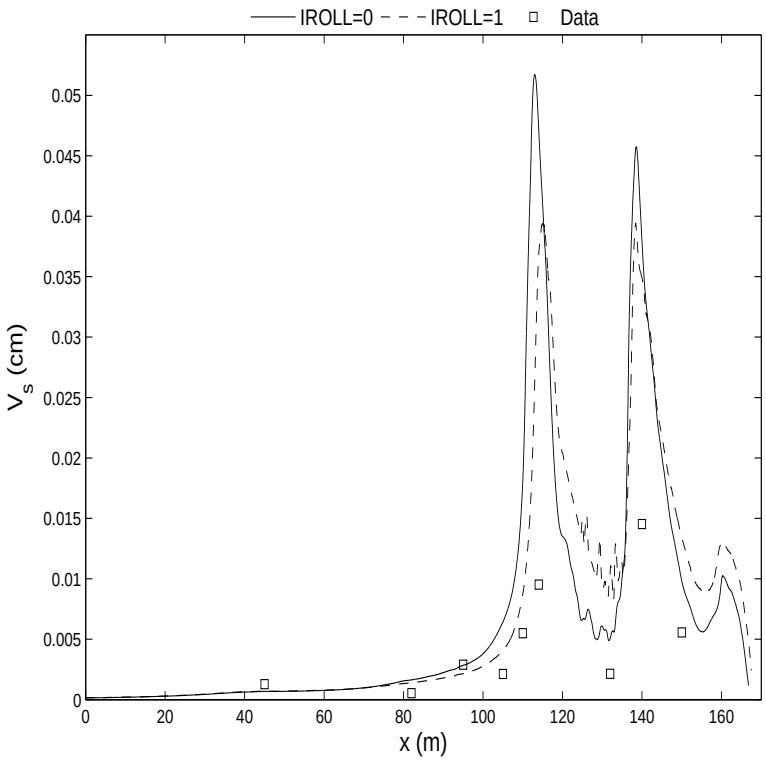

Figure 5.26: Test 1c: Comparison of total suspended sediment volume per unit area, V_s.

5.2.4 Profile change

Figures 5.27 through 5.29 show the final model computations for profile change in the large scale tests. Each figure shows the comparisons with the final measured values (top), the model computations with respect to the initial profile (middle), and the net change from the initial profile (bottom). Comparisons with the model were made at the time level that each measured profile was taken. These can be viewed in Appendices C through E for the large scale data.

For the first large scale test, Test 1a, the conditions were slightly erosive. Measured profiles were taken at 0, 2, 3, 4, 5, 6, 7 and 12 hours. The test was a total of 12 hours long. Final computations are displayed in Figure 5.27.

Test 1a showed very little measured profile change, less than 0.1 m, and the computations support this claim with change of less than 0.5 m. This indicates that the constructed equilibrium profile based on equation (4.33) with A=0.1 $m^{(1/3)}$ connected to a uniform slope near the shoreline was indeed at quasi-equilibrium. It is seen, especially from the change from initial that including the roller in the large scale tests improves agreement slightly. The model predicts erosive and accretive conditions at the same cross-shore locations in which they occurred experimentally with the exception that the numerical model does not predict erosion in the swash zone.

The total test time for Test 1b was 18 hours. Profiles were measured at 0, 1, 2, 3, 4, 5, 6, 7, 8, 9, 12, and 18 hours. The final computations are compared in Figure 5.28.

The measured profile change was less than 0.3 m over the 18 hour wave action, whereas the computed profile changes were less than 0.1 m. The model does not predict the growth and offshore migration of the bar crest and the erosion in the bar trough sufficiently. van Rijn *et al.* (2003) found it necessary to introduce the increased roughness due to ripples in the bar trough in order to reproduce the

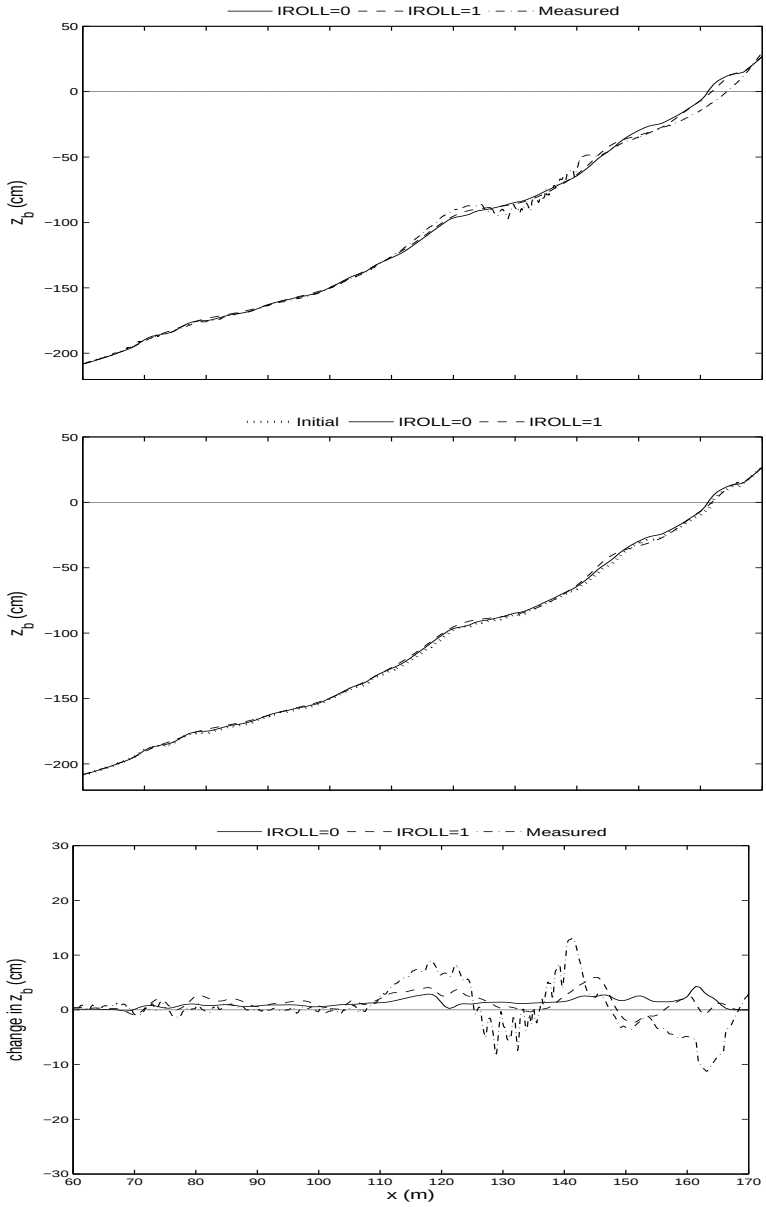

Figure 5.27: Test 1a: (top) Computed and measured profiles for $t = 12$ hr, (middle) Computed and initial profile for $t = 12$hr, (bottom) Computed change from the initial profile for $t = 12$ hr.

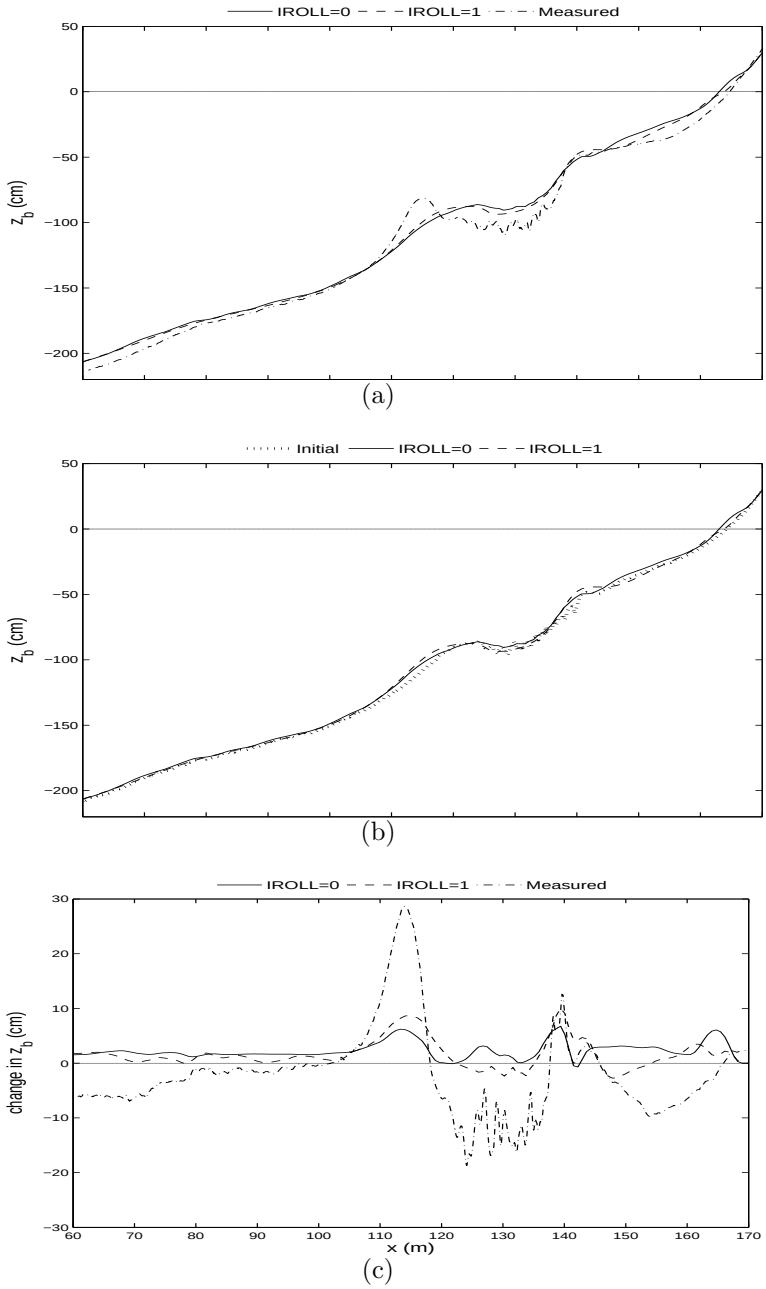

Figure 5.28: Test 1b: (top) Computed and measured profiles for $t = 18$ hr, (middle) Computed and initial profile for $t = 18$ hr, (bottom) Computed change from the initial profile for $t = 18$ hr.

bar growth. Throughout the cross-shore region, the model predicts the location of erosive or accretive areas qualitatively, however underestimates their magnitude. When the roller is included, the magnitude of the profile change increases, however does not accurately reproduce the experimental magnitude.

The test duration for Test 1c was 13 hours, and profiles were measured at 1, 2, 3, 4, 7, 10, and 13 hours. Figure 5.29 shows the computed and experimental change.

The measured profile change was less than 0.3 m, whereas the numerical model with IROLL=0 predicts change less than 0.1 m, and with IROLL=1 predicts change less than 0.3 m. The magnitude of IROLL=1 has much better agreement than IROLL=0, however the predicted onshore migration is not sufficient. Detailed profile changes are found to be difficult to predict accurately using simple equations such as equations (4.20) and (4.27).

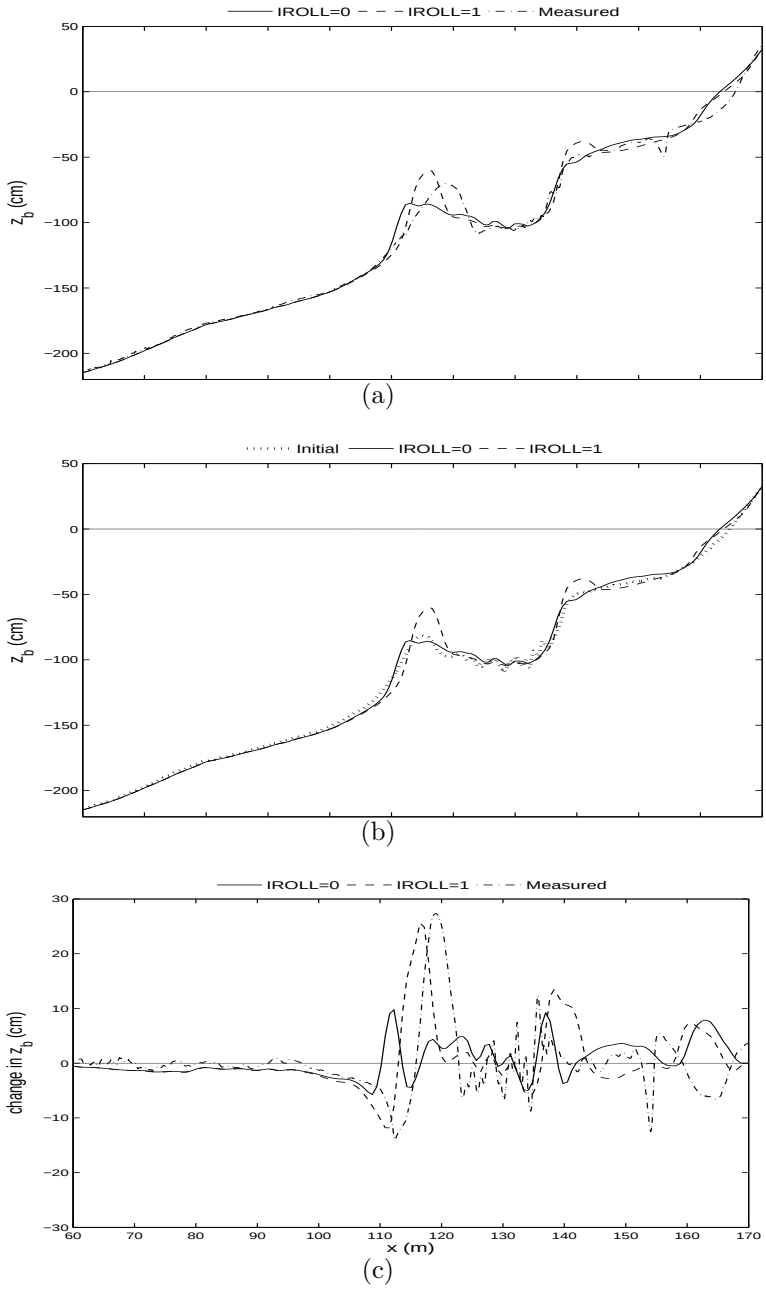

Figure 5.29: Test 1c: (top) Computed and measured profiles for $t = 13$ hr, (middle) Computed and initial profile for $t = 13$ hr, (bottom) Computed change from the initial profile for $t = 13$ hr.

Chapter 6

VISUALIZATION OF SUSPENSION EVENTS UNDER SPILLING AND PLUNGING BREAKING WAVES

The trend of sediment suspension events under waves has been studied extensively. Outside of the surf zone, sediment transport is attributed to bed load motion due to the nonlinearity of the waves and acceleration skewness (Hoefel and Elgar, 2003). However, at the break point and into the surf zone, intense and temporally short suspension events have been observed (e.g. Brenninkmeyer, 1976; Hay and Bowen, 1994; Jaffe and Sallenger, 1992; Cox and Kobayashi, 2000). There are many theories as to the cause of these suspension events. The turbulence generated by waves breaking in shallow water is suspected to be directly responsible for sediment suspension and transport. Cox and Kobayashi (2000) found that intense turbulent events generated by wave breaking were an order of magnitude greater than the turbulence generated at the boundary and extended into the bottom boundary layer.

An overview of breaking waves in the surf zone and the transformation of waves is found in Battjes (1988) and Peregrine (1983). Breaking occurs when the water particle velocities exceed the wave celerity, which occurs before the wave face becomes vertical, accelerations on the front face of the wave exceed gravity, and an extensive region has low accelerations on and below the backface of the wave (Peregrine, 1983). Plunging breakers are identified by the curl over of the wave with its eventual plunge into the water column in front of the wave face and subsequent

splashes. The circulation around the enclosed air interface as the jet plunges into the water column forms a vortex, in addition to the rotation caused by the actual jet impingement on the water column (Pedersen *et al.*, 1995). Spilling breakers are marked by an air-water interface starting on the tip of the front side of the wave, and progressing down the front face of the wave, until the entire front face of the wave is fully turbulent. At this point, the turbulent velocities can be greater than the mean flow, and the turbulent effects become important (Peregrine, 1983).

The importance of wave breaking to sediment suspension is recognized, but the exact mechanisms for large suspension events are not understood. Iverson (1952) observed that maximum horizontal and vertical velocities occurred ahead of the wave front near the plunge point of a plunging wave. The descent and rise of the air-water interface after the plunging and splashing of a plunging breaker is thought to cause vertical eddies. These eddies, combined with the suction generated by the ascent of air pushed into the water column was observed to suspend clouds of sediments several meters wide in the field (Brenninkmeyer, 1976). Nadaoka *et al.* (1989) have shown the production of stationary three-dimensional vertical eddies that remain after a spilling wave passes, called "obliquely descending eddies" (ODE) that may be responsible for sand suspension in the surf zone. These events are believed to be the result of large velocities occurring at the plunge-point of waves.

Many mechanisms for large, temporally short suspension events have been introduced, but a lack of measurements has made it difficult to substantiate any one theory. This study attempts to combine both temporal and spatial analysis to examine intense suspension events under violent breaking waves over an nearshore sand bar.

6.1 Classification of events

The wave train that is analyzed here is composed of irregular waves with a peak period, T_p of 2.6 s. These conditions cause each individual wave to be

different from the previous or next wave. Therefore, a classification scheme must be developed in order to compare suspension events. It is reasonable to assume that sediment suspension events under plunging and spilling breaking waves will have different temporal or spatial structures due to the different mechanisms for generating turbulence which were described earlier. Wave events of each type were visually isolated from the time series of images, with plunging breakers identified by the curl over of the wave with its eventual plunge into the water column in front of the wave face and subsequent splashes. Spilling breakers are marked by an air-water interface starting on the tip of the front side of the wave, and progressing down the front face of the wave. Each extracted set of images contained about 20 frames starting from the trough before the crest of the wave enters the field of view, to the trough following the crest's motion through the field of view.

Other characteristics need to be taken into account when dealing with an irregular wave train. The waves selected for the analysis were chosen so that each selection acted primarily as one wave, without another wave coming directly after it. However, this is idealized, as interactions between waves are always a factor. There is a significant amount of sediment that remains suspended between wave events. The fall velocity, w_f, of the sediment was tested experimentally as described in Chapter 2 and was found to be 2.0 cm/s. With a peak period of 2.6 s, the sediment would theoretically fall 5.2 cm within the period of one idealized wave. Since the depth of the water column in the area analyzed ranges from 20 cm to 40 cm, and sediment was suspended up to and above the still water level, it is obvious that the sediment will not entirely fall out in between suspension events. This becomes more obvious when the center of mass and length scales of suspension events are discussed in subsequent sections.

A total of 48 spilling events and 48 plunging events were separated and analyzed. The events were rectified in the coordinate system outlined in Chapter 2,

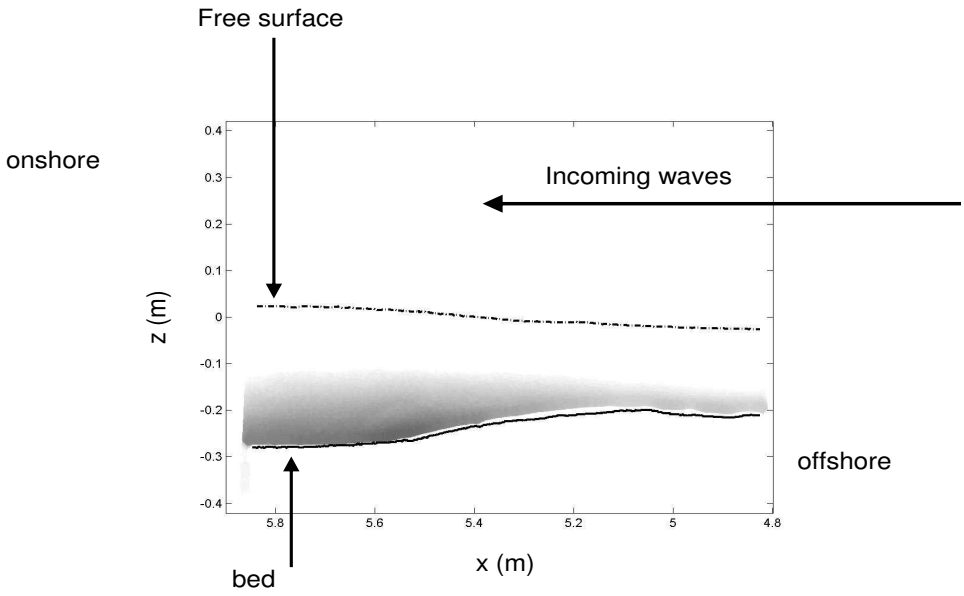

Figure 6.1: Description of the coordinate system used to analyze images.

with x=0 at the position of wave gauge 1. Figure 6.1 shows an example of an analyzed image with the spatial coordinate system used. The waves enter the field of view from offshore (right) and exit shoreward (left). The free surface is displayed with a dashed line, and the bed is shown as a solid line.

6.2 Visual observations

One example of a visualized plunging event is shown in Figure 6.2 with a plunge point that occurs in the middle of the frame (frame 2). The three frames immediately after the plunge hits the water column, is the time of large suspension. At the point where the plunger hits the water column, the suspension increased in intensity significantly, and the height and width of the plume increased. This was observed in almost all plunging cases. While the entire event could not be observed with the instrumentation used, it may be possible in future studies to use multiple cameras to view the entire surf zone. It has been observed in other studies, that in large breaking suspension events, some of the sediment continues to be carried

under the bore shoreward, while much of it settles out as the wave passes. Some of this settling can be seen in the rest of the event snapshots. The plume widens and settles, however the settling time is much larger than the large suspension time. Brenninkmeyer (1976) also observed this with point measurements in the field.

It can be seen from this example, that suspension under the breaking events does not settle to the bed by the end of the event. Therefore, in most of the events that were analyzed under these conditions, there is suspension present at the start of an event. Due to the choice of events, the suspension is mainly located in the same region, just onshore of the bar. It can be seen from the above plunging event, that the suspension cloud has a spatial peak under the front face of the wave, which is consistent with previous observations. (Brenninkmeyer, 1976).

An example of a spilling breaking event can be seen in Figure 6.3. In this case, the wave begins to spill as it enters the field of view, and is almost fully formed as it leaves the frame of view. Figure 6.3 shows that the suspension under spilling breaking waves appears different than that of plunging breaking waves. The majority of suspension occurs at the plunge point in the plunging breakers due to the disruption of the flow field after the impinging jet, and the vortex that is formed as the jet traps air between it and the front face of the wave. In spilling breaking waves, it has been postulated that three dimensional vortices on the backface of the spilling breaker extend all the way to the bed, and can cause significant suspension (Nadaoka *et al.*, 1989). Figure 6.3 shows much more suspension on the back face of the wave than on the front could be in support of this theory. It could also be partly due to ripples in the bar trough.

Direct quantification of sediment concentration from the collected images was not possible due to a lack of in situ data, however if the pixel values of the image matrix are taken to be indicators of suspension, it is possible to quantify characteristics of the suspension event such as the center of mass, spatial, and temporal

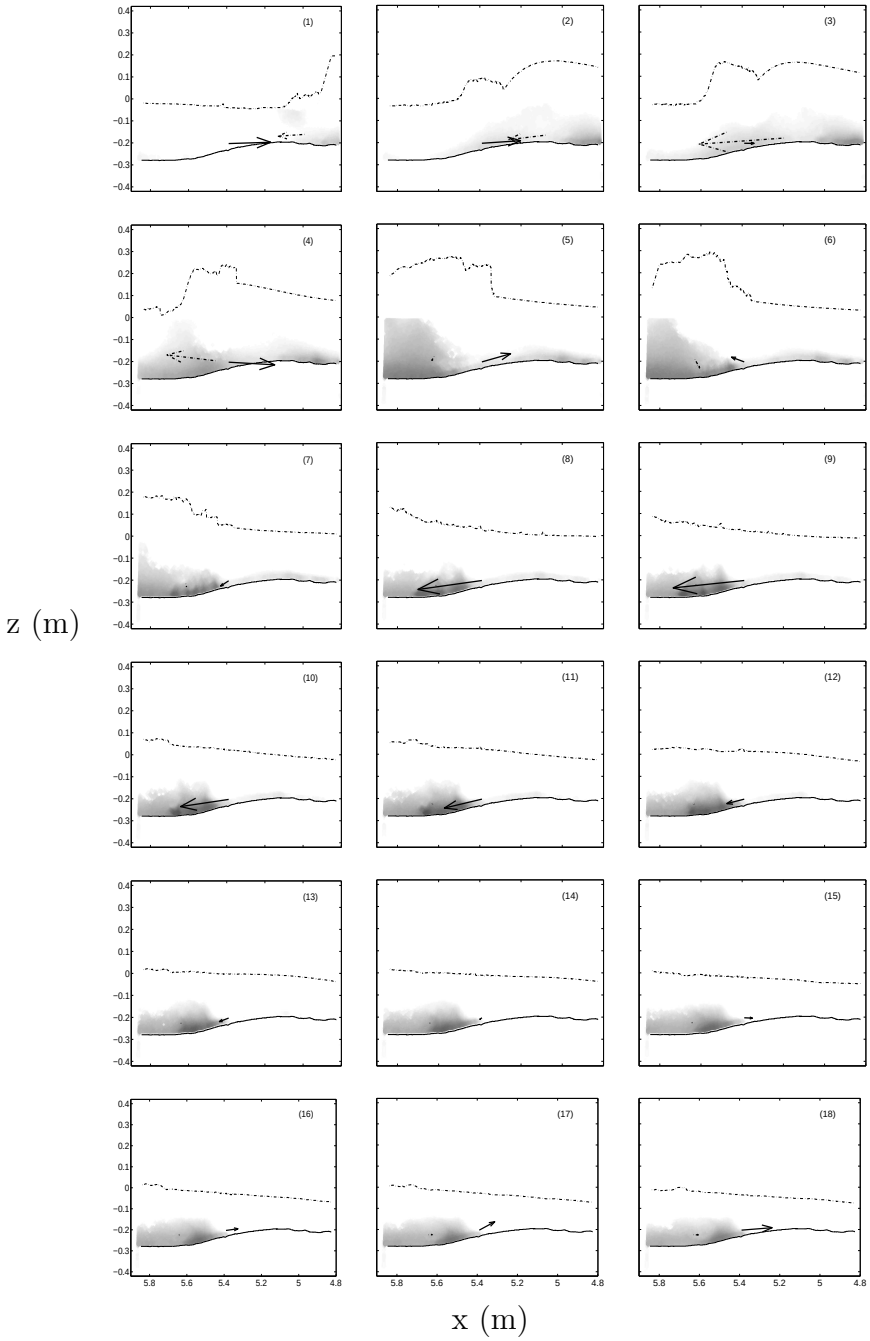

Figure 6.2: Sequence of images displaying one plunging breaking event. The free surface is designated by the dashed line. The bed is designated by the solid line. Two arrows display the measured velocity (m/s) from the ADV's (solid arrow), and the velocity (0.2m/s)of the center of mass of the suspension cloud (dotted line). The sediment suspension is indicated by darker areas. The suspension colour range is fixed for all images.

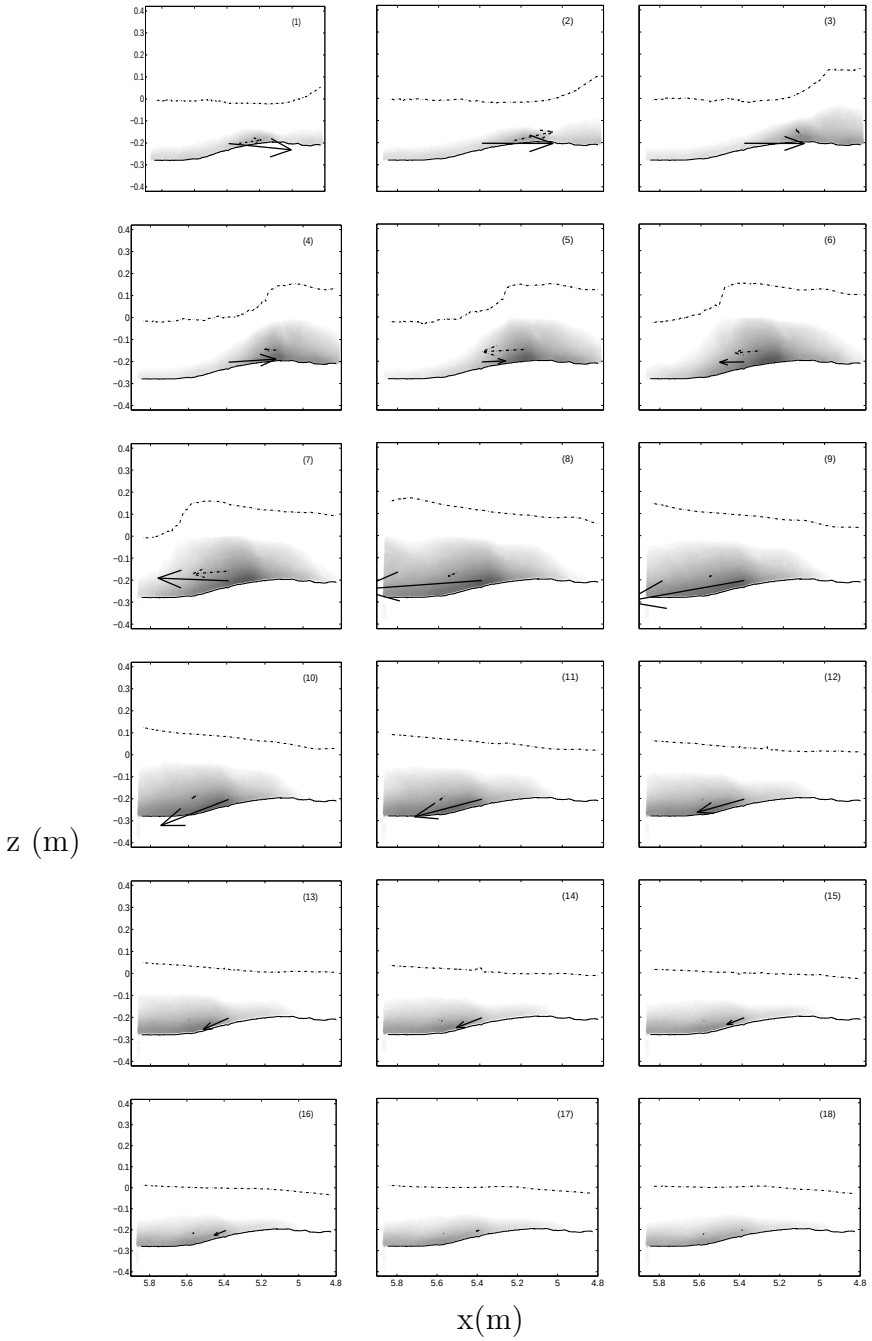

Figure 6.3: Sequence of images displaying one spilling breaking event. The free surface is designated by the dashed line. The bed is designated by the solid line. Two arrows display the measured velocity (m/s) from the ADV's (solid arrow), and the velocity (0.2 m/s) of the center of mass of the suspension cloud (dotted line). The sediment suspension is indicated by darker areas. The suspension colour range is fixed for all images.

scales.

6.3 Center of mass calculations

The center of mass was calculated from the image using moments of the pixel values,

$$x = \frac{\sum_1^i \sum_1^j p_{ij} x_j}{\sum p_{ij}} \quad ; \quad z = \frac{\sum_1^j \sum_1^i p_{ij} z_i}{\sum p_{ij}} \tag{6.1}$$

where i and j represent the resolution of the image or the pixel coordinate locations, and p_{ij} is the brightness value of the pixel at location (x_i, z_j) (0 indicates no suspension). From Figures 6.2 and 6.3, it can be seen that the center of mass moves with the wave as it breaks and travels through. The exact structure of this motion was examined for both types of waves. One description of this motion is shown in Figure 6.4, displaying the direction of motion of the trajectory of the center of mass, which was similar for all cases. Each x mark in the trajectory indicates a time increment of 110 milliseconds. It is seen that the suspension of the plume of sediment or the motion upwards in z is much shorter than the time that it takes to settle. Five examples of plunging and spilling events are shown in Figures 6.5 and 6.6 respectively. The structure for each event is similar, moving clockwise with the majority of the upwards vertical motion occurring within about 0.4 s. The trajectory of the center of mass is virtually closed in almost every event, both plunging and spilling. Since the beach is in quasi-equilibrium, the closed form of the trajectory could indicate no net sediment transport.

The trajectory for each event is tilted at an angle that is similar for all those events in its category (plunging or spilling). This indicates that as sediment is suspended up into the water column, it is also being pulled offshore. It then gets pushed onshore as it settles out of the water column. The temporal variation of these events are discussed in section 6.4. As discussed before, the suspension never entirely falls out in between waves, as the period of the waves is not long enough.

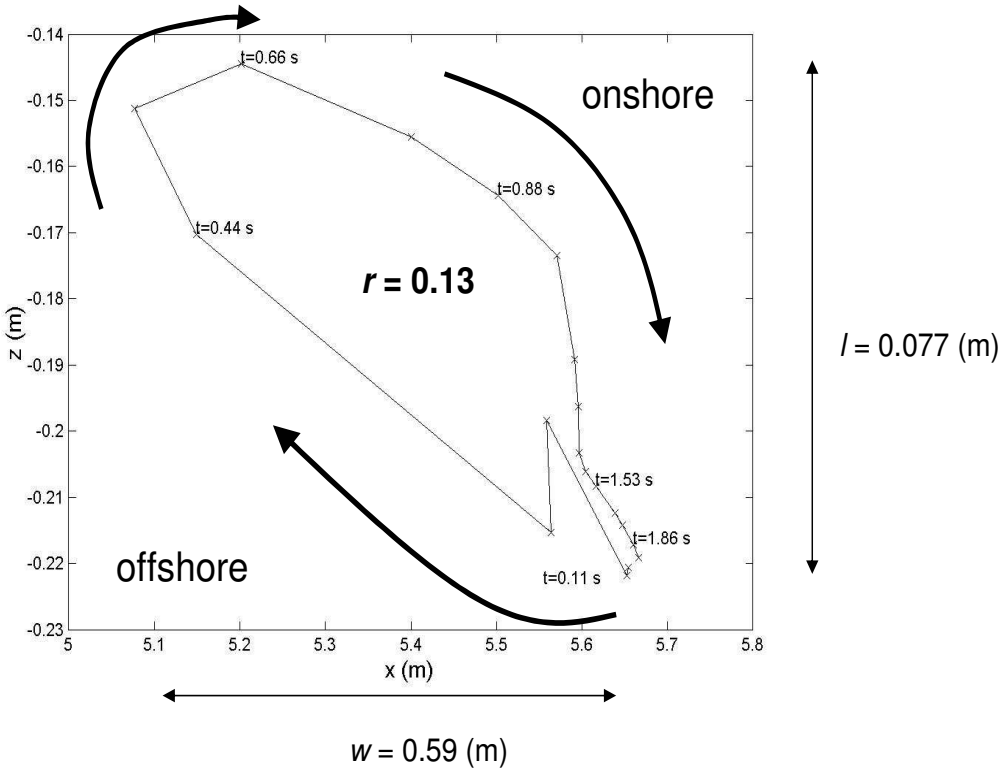

Figure 6.4: Example of a center of mass trajectory and the calculation of its shape parameter, r

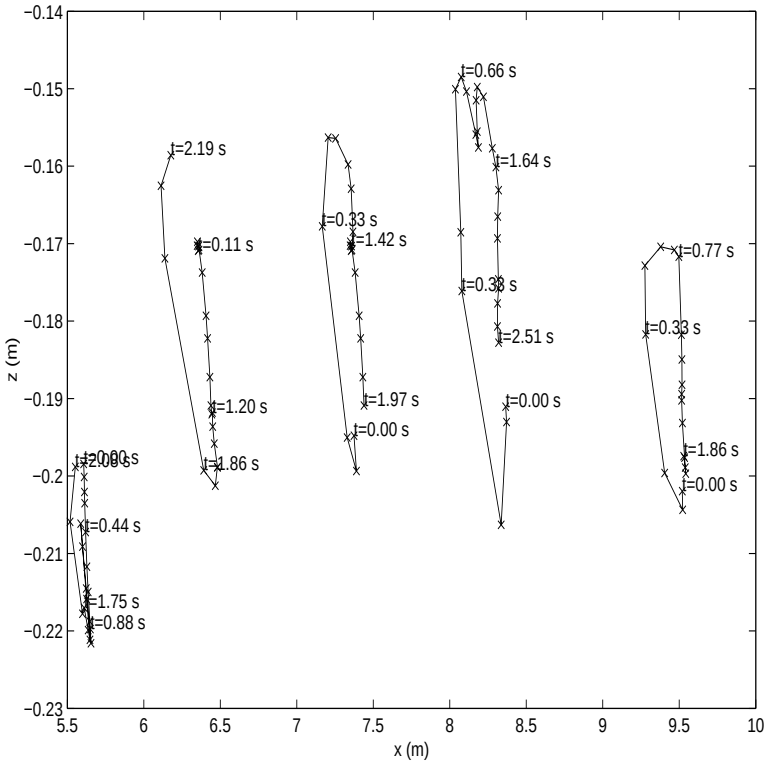

Figure 6.5: Five trajectories of the centre of mass through plunging wave events. Each trajectory is offset by 1 m in the x direction.

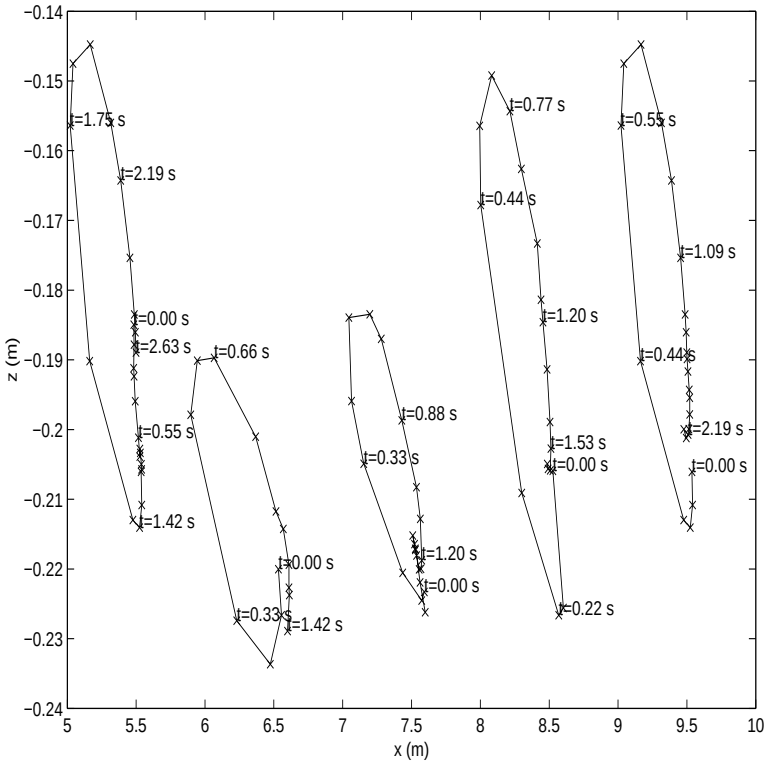

Figure 6.6: Five trajectories of the center of mass through spilling wave events. Each is offset by 1 m in the x direction.

Assuming that the trajectory is symmetric about a line set at angle θ from vertical, θ can be estimated from a linear fit of the data. The mean and standard deviation of θ for the plunging and spilling cases are shown in Table 6.1.Each event was then

Table 6.1: Spatial statistics for the center of mass trajectories under plunging and spilling breaking waves.

	Plunging		**Spilling**	
	mean	standard deviation	mean	standard deviation
θ (degrees)	-2.8	0.92	-3.3	1.2
r	0.15	0.034	0.14	0.042

normalized by its length and width, l and w, where l is a measure of the vertical distance traveled, and w is a measure of the horizontal distance traveled. l and w are labeled in Figure 6.4. The quantity, $r = l/w$ is used as a shape parameter to compare events for each classification. Larger values of r indicate that the center of mass moved higher in the water column, while staying in roughly the same horizontal position. Smaller values of r indicate that the center of mass stayed roughly in the same vertical location and traveled a large horizontal distance. Values for the mean and standard deviation of r are shown in Table 6.1. While both events do have a minor deviation from the vertical, their shape is almost elliptical and symmetric around the angled axis. The shape parameter differences are negligible indicating that the shape of the center of mass trajectory, ie the vertical motion over the horizontal motion is the same. Neither spilling nor plunging suspension clouds have a tendency to rise further up in the water column with respect to its horizontal spreading. The difference in θ between plunging and spilling waves is significant at 0.5 degrees. Under no waves, the trajectory of a suspended particle would have a nearly infinite r value and θ would be zero. If the suspension cloud is treated as a particle at the point of the center of mass, then plunging breaking waves have less affect on the natural tendencies of suspension than do spilling waves.

6.4 Time-dependent length scales

Figures 6.2 and 6.3 show significant differences in suspension patterns between spilling and plunging breaking waves, which is contrary to what was described by the center of mass motion, where the shape parameters were found to be almost identical. This indicates the limitation of the center of mass to describe the suspension event. Alternatively, the temporal variability of the events is examined, as the mean motion is not significantly different. The spatial standard deviation of sediment suspension, or the square root of the second moments can give an expression for suspended sediment cloud size. The time variance of this quantity can lead to better understanding of suspension events. The use of the instantaneous wave height, defined as the elevation above the free surface at the wave crest, was chosen as a comparison value for the length scales.

If squared length scales in x and z of the suspended sediment cloud are given by

$$\sigma_x^2 = \frac{\sum_1^i \sum_1^j p_{ij} x_j^2}{\sum p_{ij}} - x^2 \quad ; \quad \sigma_z^2 = \frac{\sum_1^j \sum_1^i p_{ij} z_i^2}{\sum p_{ij}} - z^2 \tag{6.2}$$

where x and z are given by equation 6.1. The horizontal and vertical spread of the cloud are then σ_x and σ_z. These can then be compared to wave quantities over the time period of the wave event. First examining the horizontal length scales of the plunging event, Figure 6.7 shows that the horizontal length scale reaches it maximum simultaneously with the maximum wave height. In each of these subsequent figures, the wave height is indicated by a solid line, the length scales are indicated by a dashed line, and the peak of the wave height is designated by a dotted vertical line. Defining a wave height peak for the instantaneous plunging breaker height was somewhat arbitrary as the wave forms are jagged due to the splashing of the plunging breaker. However, the peaks chosen for this analysis were defined as the first spike in values as shown in Figure 6.7. To ensure that this was not an abberation, the plunging events were analyzed to determine if the peaks of the horizontal length

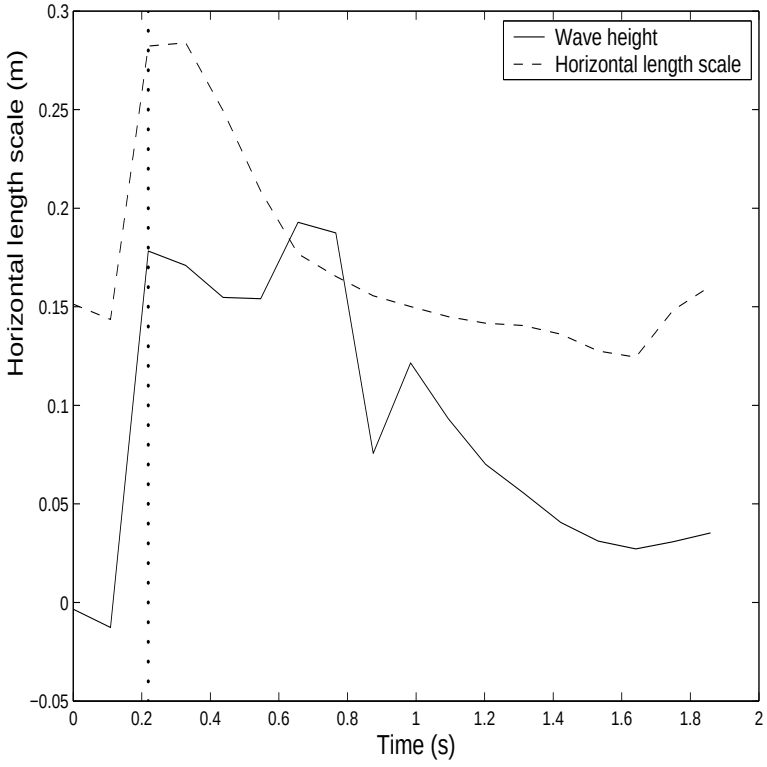

Figure 6.7: Plunging: Comparison of horizontal length scales of the suspension cloud and wave height.

scales were in fact in phase with the wave height maxima. The mean time offset between the peak of wave height and the horizontal length scale was 0.04 s and practically zero with a standard deviation of 0.12. The majority of the plunging cases had time offsets of exactly zero.

Vertical length scales are compared in Figure 6.8. The wave height was reduced by a factor of 10 for comparison purposes. The wave height peaks before

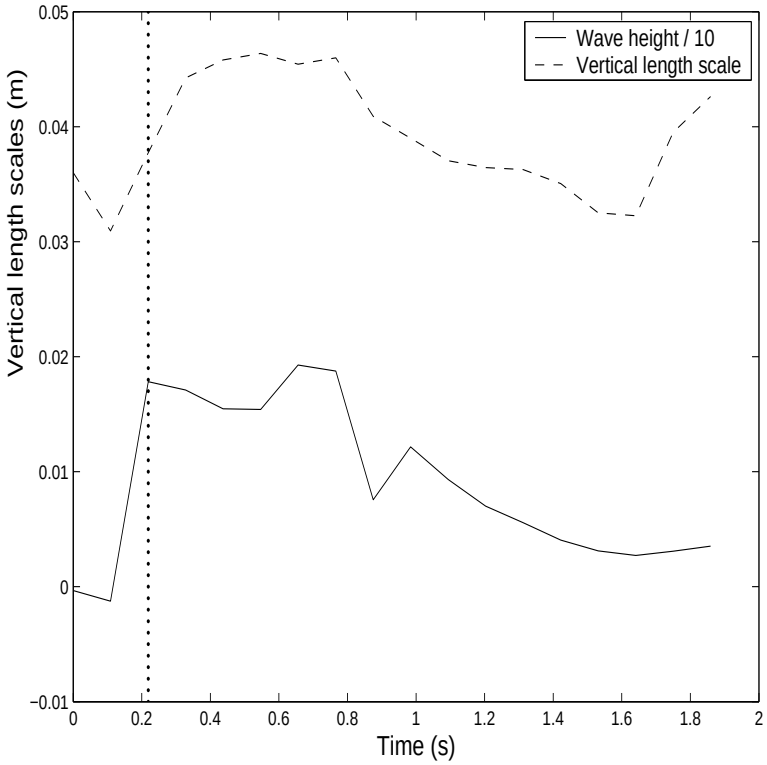

Figure 6.8: Plunging: Comparison of the vertical length scale of the suspension cloud to the wave height.

the peak of vertical suspension, at about the inflection point. However, the plunging case has a maximum vertical and horizontal spread at about the same time contrary to the spilling case which is shown in Figures 6.9 and 6.10. While the wave height and horizontal spread peaks slightly before the vertical in this case, overall there is

no clear phase lag. In addition, the peaks are prolonged. Plunging waves essentially cause the largest suspension in both directions simultaneously. It is concluded that plunging breaking waves directly impact sediment suspension underneath them with the suspension event following the wave event in both the x and z directions.

Figure 6.9 shows the comparison of the horizontal length scale to wave height

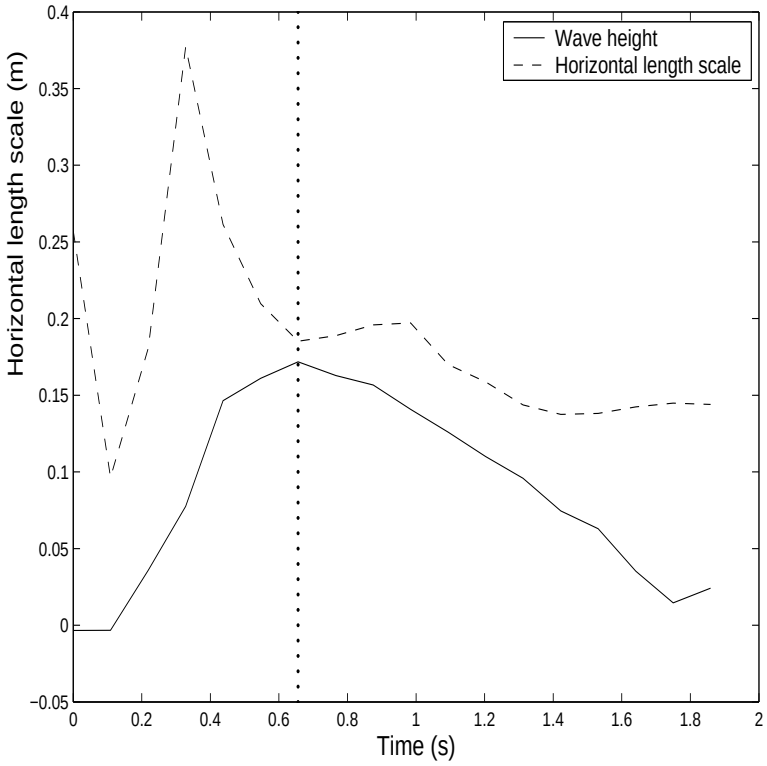

Figure 6.9: Spilling: Comparison of the horizontal length scale of the suspension cloud to the wave height.

for one spilling event. The peak of the x length scale occurs right before the peak of the wave, such that the cloud is at its widest right before the wave height reaches its maximum. The time difference between the peaks was calculated to be 0.43 s with a standard deviation of 0.20 s. The above example had a difference of 0.32 s between peaks. The variability is likely due to the irregular nature of the waves

that were propagated. Each wave was different, although the phase shift in peaks was visible in the great majority of cases.

Figure 6.10 shows the comparison of the vertical length scale to the wave height. The wave height was again reduced by a factor of 10 for visual comparison. The maximum of the vertical length scale and the wave height occur simultaneously.

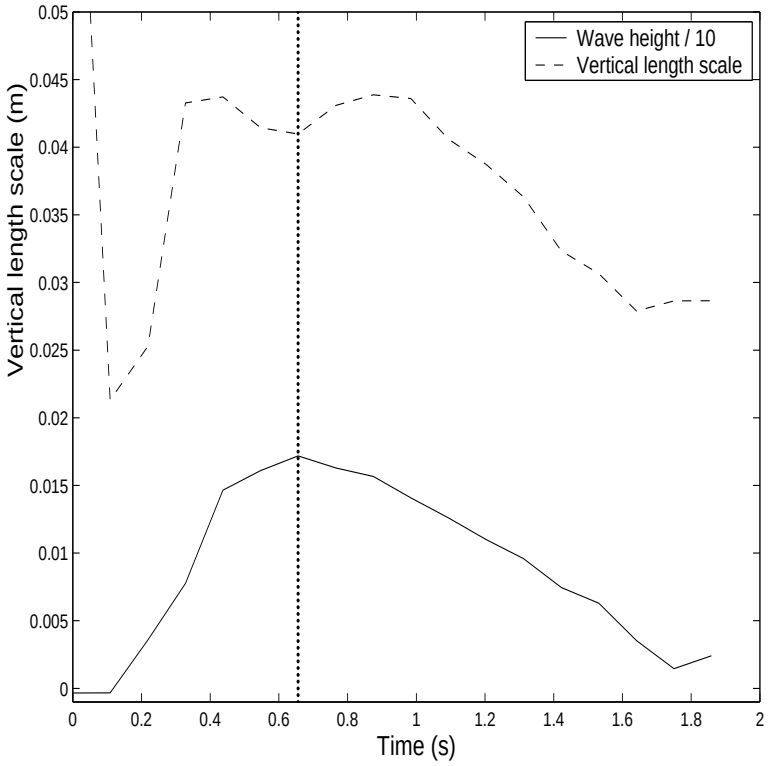

Figure 6.10: Spilling: Comparison of vertical length scale of suspension event to wave height.

Note that the large value of vertical spreading at $t = 0$ is related to pre-suspended sediment in the water column. This observation combined with the observations on the horizontal length scales indicate that the suspension cloud is at its highest point in the water column when it is most horizontally condensed.

Figures 6.2 and 6.3 show these differences between spilling and plunging events. In the spilling case, the sediment cloud is more horizontally spread, whereas the plunging event causes a more horizontally condensed sediment cloud. However, the major difference between the two is that the time scale of the peak of vertical spread is almost double the time for spilling breakers than for plunging breakers. This may indicate the findings of Nadaoka *et al.* (1989) of ODE's on the back face of the spilling breaker, however could also be due to the effect of ripples on the trough side of the bar.

The analysis of suspension events showed that spilling and plunging breaking waves have similar spatial structure, however, there are significant temporal differences. Both spilling and plunging breakers have center of mass trajectories that are offset from a vertical ellipse by a small angle, however remained symmetric about the angled axis. Plunging breakers are more aligned to vertical than spilling breakers. The trajectories were almost all virtually closed indicating that the center of mass did not undergo a net onshore or offshore motion. There was a temporal phase shift in the peak of the horizontal length scale in comparison to the instantaneous wave height for spilling events. The vertical length scale in spilling events retained its peak for about twice as long as plunging events, which may indicate the presence of "obliquely descending eddies" on the back face of the wave, or could be due to ripple effects on the trough side of the bar. Overall, the use of imaging techniques on suspension events under breaking waves has the potential to yield much knowledge about these events since it encompasses both time and space.

Chapter 7

CONCLUSIONS

Simple formulas are developed to predict the time-averaged rates of cross-shore suspended sediment and bedload transport. The offshore suspended sediment transport rate q_s is expressed as $q_s = a\bar{U}V_s$ where $\bar{U}$ is the depth-averaged return current and V_s is the time-averaged suspended sediment volume per unit bottom area. The suspended load parameter a of the order of 0.2 accounts for the reduction due to the onshore suspended sediment transport caused by the correlation of the time-varying horizontal velocity and suspended sediment concentration. The formula for V_s is modified to include the probability of sediment suspension. The onshore bedload transport rate q_b is expressed as $q_b = bP_b\sigma_U^3/[g(s-1)]$ where P_b is the probability of sediment movement, σ_U is the standard deviation of the horizontal velocity, g is the gravitational acceleration, and s is the sediment specific gravity. The bedload parameter b of the order of 0.002 includes the detailed sediment dynamics neglected in this simple formula.

The proposed formulas are compared with 24 tests in which net sand transport rates were measured under nonbreaking, nonlinear waves with weak currents. For these tests, q_s is shown to be small relative to q_b and b is in the range of 0.001 to 0.004. The formulas are also compared with 24 sheet flow tests in which net sand transport rates were measured under sinusoidal waves with strong currents. For these sinusoidal wave tests, q_b is assumed to be in the direction of the current and the parameter a for q_s is assumed to account for the time lag of the suspended sediment. Under these assumptions, the agreement is within a factor of about 2. The

proposed bedload formula is also shown to be consistent with the sheet flow model for onshore bar migration by Trowbridge and Young (1989) and the energetics-based bedload formula for steady flow by Bagnolds (1966) if the steady flow formula is applied in a time-averaged manner. Moreover, the condition of $(q_b + q_s) = 0$ for an equilibrium profile along with additional assumptions is shown to yield the equilibrium profile popularized by Dean (1991). The calibrated formulas for q_s and q_b are incorporated into the time-averaged wave model by Kobayashi *et al.* (2005). The continuity equation of bottom sediment is solved numerically to predict the beach profile evolution. The numerical model is compared with the three equilibrium profile tests by Kobayashi *et al.* (2005) and the erosion and accretion tests conducted in this study. The numerical model cannot explain all the three equilibrium profiles produced under three different spectral periods. The fairly subtle changes of the beach profile are difficult to predict accurately.

The numerical model is also compared with three large-scale tests. The numerical model predicts the cross-shore variations of $\bar{\eta}$, σ_η and σ_U satisfactorily where $\bar{\eta}$ and σ_η are the mean and standard deviation of the free surface elevation η. The cross-shore variations of $\bar{U}$ and V_s are difficult to predict accurately as was the case with the previous comparison with small-scale tests. The profile change predicted by the numerical model is in agreement for the first test whose initial profile was based on the equilibrium profile by Dean [1991]. The numerical model cannot predict the growth and migration of the bar in the second and third tests sufficiently.

The comparisons made in this study are limited to the median sand diameter d_{50} in the range of 0.13 to 0.32 mm. The proposed formulas for q_s and q_b will need to be compared with coarser sediment data. These formulas will also need to be extended to obliquely incident waves with longshore currents in order to allow the comparison of the formulas with field data. The numerical model will be extended

to predict dune erosion and overwash during a storm. The simplicity of the formulas and numerical model may facilitate various future extensions.

Appendix A

TEST E

A.1 Free surface

Table A.1: Test E: Free surface measurements consisting of 23 bursts of E1 to E23.

test	x (m)	d (cm)	$\overline{\eta}$ (cm)	σ_η (cm)
	0	75.96	-0.14	4.50
	0.22	72.94	-0.12	4.45
	0.92	63.76	-0.15	4.48
	5.00	18.96	-0.35	4.83
E1	6.35	19.32	NR	NR
	7.60	16.76	0.54	3.22
	9.50	3.80	1.24	2.55
	10.5	-7.09	7.09	1.00
	0	75.95	-0.15	4.40
	0.22	72.93	-0.16	4.40
	0.92	63.76	-0.16	4.42
	5.00	19.01	-0.41	4.84
E2	6.35	19.56	0.31	3.62
	7.60	16.86	0.54	3.09
	9.50	4.39	1.40	2.46
	10.5	-5.48	6.31	1.04
	0	75.95	-0.15	4.53
	0.22	72.93	-0.16	4.47
	0.92	63.76	-0.17	4.52
	5.00	17.97	-0.47	4.79
E3	6.35	18.96	0.23	3.63
	7.60	16.42	0.52	3.16
	9.50	4.26	1.45	2.51
	10.5	-5.40	6.75	1.02

test	x (m)	d (cm)	$\overline{\eta}$ (cm)	σ_η (cm)
	0	75.96	-0.29	4.50
	0.22	72.93	-0.19	4.44
	0.92	63.76	-0.22	4.52
	5.00	17.65	-0.35	4.71
E4	6.35	18.27	0.27	3.64
	7.60	15.75	0.56	3.11
	9.50	5.13	1.35	2.51
	10.5	-4.62	5.68	0.98
	0	75.96	-0.34	4.52
	0.22	72.93	-0.23	4.47
	0.92	63.76	-0.29	4.53
	5.00	17.65	-0.41	4.67
E5	6.35	18.27	0.20	3.68
	7.60	15.75	-0.09	3.14
	9.50	5.13	1.29	2.54
	10.5	-4.62	5.43	1.03
	0	75.96	-0.15	4.52
	0.22	72.93	-0.15	4.46
	0.92	63.76	-0.20	4.54
	5.00	17.65	-0.42	4.62
E6	6.35	18.27	0.27	3.67
	7.60	15.75	0.54	3.17
	9.50	5.13	1.31	2.55
	10.5	-4.62	5.48	1.05

test	x (m)	d (cm)	$\overline{\eta}$ (cm)	σ_η (cm)
E7	0	76.18	-0.12	4.44
	0.22	73.16	-0.16	4.39
	0.92	63.98	-0.19	4.44
	5.00	16.02	-0.38	4.52
	6.35	18.02	0.29	3.64
	7.60	14.93	0.56	3.12
	9.50	3.84	1.28	2.51
	10.5	-5.68	7.02	1.13
E8	0	76.18	-0.15	4.47
	0.22	73.16	-0.14	4.42
	0.92	63.98	-0.18	4.48
	5.00	16.02	-0.34	4.51
	6.35	18.02	0.28	3.59
	7.60	14.93	0.55	3.13
	9.50	3.84	1.28	2.54
	10.5	-5.68	6.57	1.17
E9	0	76.18	-0.12	4.47
	0.22	73.16	-0.12	4.43
	0.92	63.98	-0.17	4.48
	5.00	16.02	-0.32	4.54
	6.35	18.02	0.29	3.63
	7.60	14.93	0.55	3.10
	9.50	3.84	1.29	2.54
	10.5	-5.68	6.61	1.18

test	x (m)	d (cm)	$\overline{\eta}$ (cm)	σ_η (cm)
E10	0	76.18	-0.12	4.48
	0.22	73.16	-0.12	4.44
	0.92	63.98	-0.19	4.49
	5.00	16.02	-0.31	4.49
	6.35	18.02	0.31	3.60
	7.60	14.93	0.55	3.10
	9.50	3.84	1.30	2.57
	10.5	-5.68	6.71	1.19
E11	0	76.18	-0.14	4.40
	0.22	73.16	-0.12	4.35
	0.92	63.98	-0.13	4.40
	5.00	16.64	NR	NR
	6.35	18.24	0.30	3.67
	7.60	15.71	0.47	2.97
	9.50	4.39	1.08	2.53
	10.5	-5.17	6.40	1.27
E12	0	76.18	-0.14	4.44
	0.22	73.16	-0.13	4.40
	0.92	63.98	-0.14	4.44
	5.00	16.64	-0.44	4.56
	6.35	18.24	0.30	3.67
	7.60	15.71	0.50	3.01
	9.50	4.39	1.15	2.56
	10.5	-5.17	6.17	1.27

test	x (m)	d (cm)	$\overline{\eta}$ (cm)	σ_η (cm)
	0	76.18	-0.12	4.46
	0.22	73.16	-0.10	4.41
	0.92	63.98	-0.13	4.45
	5.00	16.64	-0.41	4.57
E13	6.35	18.24	0.32	3.70
	7.60	15.71	0.46	2.99
	9.50	4.39	1.22	2.57
	10.5	-5.17	6.13	1.30
	0	76.18	-0.16	4.44
	0.22	73.16	-0.14	4.39
	0.92	63.98	-0.16	4.42
	5.00	16.64	-0.43	4.67
E14	6.35	18.24	0.32	3.72
	7.60	15.71	0.51	3.00
	9.50	4.39	1.15	2.58
	10.5	-5.17	6.31	1.32
	0	75.04	-0.18	4.46
	0.22	72.56	-0.18	4.40
	0.92	65.79	-0.16	4.43
	5.00	18.51	-0.18	4.67
E15	6.35	19.69	0.30	3.70
	7.60	16.20	0.55	3.11
	9.50	4.67	1.18	2.57
	10.5	-4.67	6.02	1.40

test	x (m)	d (cm)	$\overline{\eta}$ (cm)	σ_η (cm)
	0	75.04	-0.18	4.49
	0.22	72.56	-0.16	4.44
	0.92	65.79	-0.16	4.48
	5.00	18.51	-0.23	4.66
E16	6.35	19.69	0.26	3.71
	7.60	16.20	0.53	3.14
	9.50	4.67	1.17	2.59
	10.5	-4.67	6.00	1.42
	0	75.04	-0.18	4.41
	0.22	72.56	-0.18	4.35
	0.92	65.79	-0.17	4.40
	5.00	18.51	-0.30	4.64
E17	6.35	19.69	0.26	3.67
	7.60	16.20	0.53	3.09
	9.50	4.67	1.14	2.56
	10.5	-4.67	5.96	1.42
	0	75.04	-0.18	4.44
	0.22	72.56	-0.20	4.37
	0.92	65.79	-0.15	4.42
	5.00	18.51	-0.27	4.61
E18	6.35	19.69	0.25	3.65
	7.60	16.20	0.51	3.10
	9.50	4.67	1.16	2.58
	10.5	-4.67	5.87	1.41

test	x (m)	d (cm)	$\overline{\eta}$ (cm)	σ_η (cm)
E19	0	75.04	-0.16	4.46
	0.22	72.56	-0.13	4.40
	0.92	65.79	-0.17	4.44
	5.00	18.51	-0.29	4.64
	6.35	19.69	0.26	3.67
	7.60	16.20	0.53	3.11
	9.50	4.67	1.13	2.58
	10.5	-4.67	6.01	1.46
E20	0	75.04	-0.14	4.37
	0.22	72.56	-0.16	4.35
	0.92	65.79	-0.17	4.41
	5.00	18.37	-0.24	4.74
	6.35	20.18	0.27	3.67
	7.60	16.43	0.55	3.11
	9.50	5.29	1.19	2.61
	10.5	-3.77	5.51	1.22
E21	0	75.04	-0.18	4.41
	0.22	72.56	-0.15	4.38
	0.92	65.79	-0.21	4.43
	5.00	18.37	-0.33	4.78
	6.35	20.18	0.27	3.69
	7.60	16.43	0.52	3.10
	9.50	5.29	1.09	2.67
	10.5	-3.77	4.97	1.28

test	x (m)	d (cm)	$\overline{\eta}$ (cm)	σ_η (cm)
E22	0	75.04	-0.10	4.42
	0.22	72.56	-0.09	4.40
	0.92	65.79	-0.11	4.45
	5.00	18.37	-0.30	4.80
	6.35	20.18	0.26	3.68
	7.60	16.43	0.53	3.17
	9.50	5.29	1.08	2.67
	10.5	-3.77	5.09	1.29
E23	0	75.04	-0.12	4.43
	0.22	72.56	-0.13	4.39
	0.92	65.79	-0.15	4.45
	5.00	18.37	-0.37	4.75
	6.35	20.18	0.28	3.69
	7.60	16.43	0.54	3.16
	9.50	5.29	1.10	2.66
	10.5	-3.77	4.93	1.29

Table A.2: Test E: Incident and reflected wave characteristics for 43 bursts.

test	$\bar{\eta}$(cm)	$\sigma_\eta(cm)$	Incident spectral		Reflection	Incident Time Series	
			H_{mo} (cm)	T_p (s)	coefficient	H_s (cm)	T_s (s)
E1	-0.14	4.50	17.6	2.57	0.165	17.5	2.23
E2	-0.15	4.40	17.4	2.57	0.167	17.5	2.32
E3	-0.15	4.53	17.8	2.57	0.163	17.4	2.24
E4	-0.29	4.50	17.7	2.57	0.168	17.5	2.23
E5	-0.34	4.52	17.8	2.57	0.175	17.5	2.24
E6	-0.15	4.52	17.8	2.57	0.176	17.4	2.23
E7	-0.12	4.44	17.4	2.57	0.180	17.2	2.24
E8	-0.15	4.47	17.6	2.57	0.180	17.4	2.24
E9	-0.12	4.47	17.6	2.57	0.181	17.2	2.22
E10	-0.12	4.48	17.6	2.57	0.180	17.2	2.22
E11	-0.14	4.40	17.3	2.57	0.171	17.0	2.23
E12	-0.14	4.44	17.4	2.57	0.171	17.0	2.24
E13	-0.12	4.46	17.5	2.57	0.168	17.1	2.23
E14	-0.16	4.43	17.4	2.57	0.167	17.1	2.24
E15	-0.18	4.46	17.4	2.57	0.169	17.1	2.24
E16	-0.18	4.49	17.6	2.57	0.171	17.3	2.24
E17	-0.18	4.41	17.3	2.57	0.168	17.0	2.24
E18	-0.18	4.44	17.4	2.57	0.170	17.2	2.25
E19	-0.16	4.46	17.5	2.57	0.169	17.4	2.24
E20	-0.14	4.37	17.3	2.57	0.165	16.9	2.29
E21	-0.18	4.41	17.4	2.57	0.169	17.0	2.23
E22	-0.10	4.42	17.4	2.57	0.165	17.1	2.25
E23	-0.12	4.43	17.4	2.57	0.168	17.1	2.26

test	$\bar{\eta}$(cm)	$\sigma_\eta(cm)$	Incident spectral		Reflection	Incident Time Series	
			H_{mo} (cm)	T_p (s)	coefficient	H_s (cm)	T_s (s)
E24	-0.18	4.53	17.8	2.57	0.160	17.5	2.24
E25	-0.26	4.63	18.2	2.57	0.162	17.9	2.25
E26	-0.28	4.63	18.2	2.57	0.162	17.9	2.25
E27	-0.12	4.62	18.1	2.57	0.160	17.9	2.24
E28	-0.13	4.61	18.1	2.57	0.159	17.9	2.26
E29	-0.14	4.60	18.1	2.57	0.161	17.9	2.25
E30	-0.15	4.60	18.1	2.57	0.160	17.8	2.25
E31	-0.12	4.60	18.0	2.57	0.161	17.9	2.24
E32	-0.13	4.59	18.0	2.57	0.156	17.7	2.23
E33	-0.16	4.55	17.8	2.57	0.156	17.6	2.25
E34	-0.15	4.61	18.1	2.57	0.155	17.8	2.25
E35	-0.16	4.65	18.2	2.57	0.155	18.0	2.25
E36	-0.16	4.65	18.2	2.57	0.155	17.8	2.24
E37	-0.17	4.65	18.2	2.57	0.156	17.9	2.25
E38	-0.14	4.62	18.2	2.57	0.153	18.0	2.23
E39	-0.14	4.62	18.2	2.57	0.156	17.8	2.25
E40	-0.14	4.63	18.2	2.57	0.156	17.9	2.26
E41	-0.17	4.63	18.2	2.57	0.157	18.1	2.23
E42	-0.19	4.62	18.2	2.57	0.158	17.9	2.25
E43	-0.18	4.62	18.2	2.57	0.157	18.0	2.24

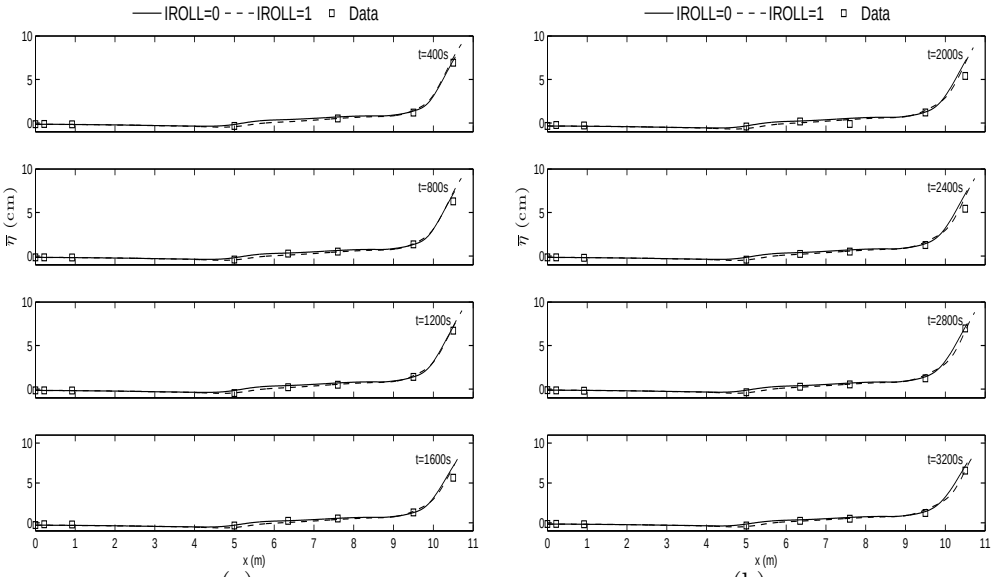
IROLL=0 - - - IROLL=1 Data
t=400s
t=800s
t=1200s
t=1600s
t=2000s
t=2400s
t=2800s
t=3200s
η (cm)
x (m)

(a) (b)

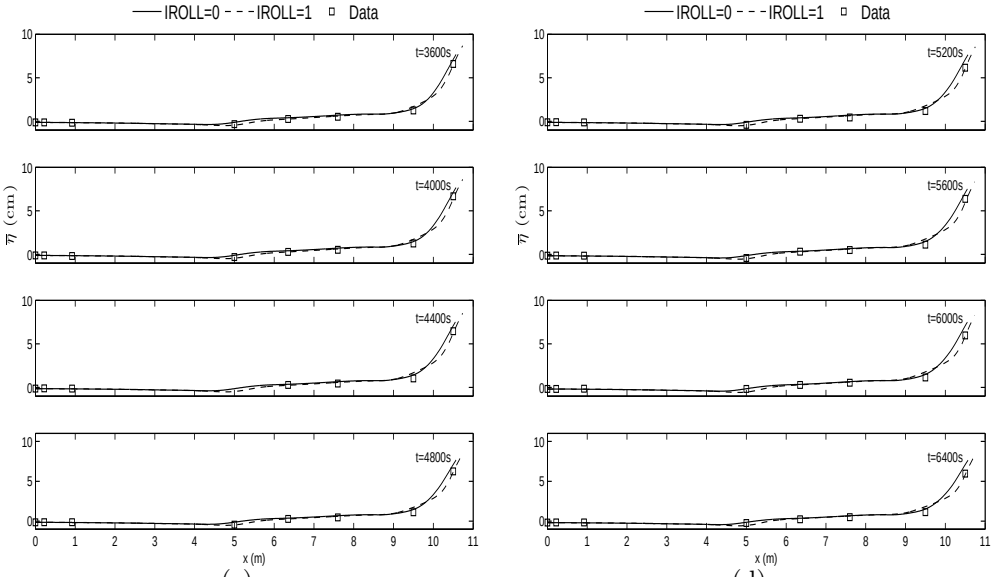
IROLL=0 - - - IROLL=1 Data
t=3600s
t=4000s
t=4400s
t=4800s
t=5200s
t=5600s
t=6000s
t=6400s
η (cm)
x (m)

(c) (d)

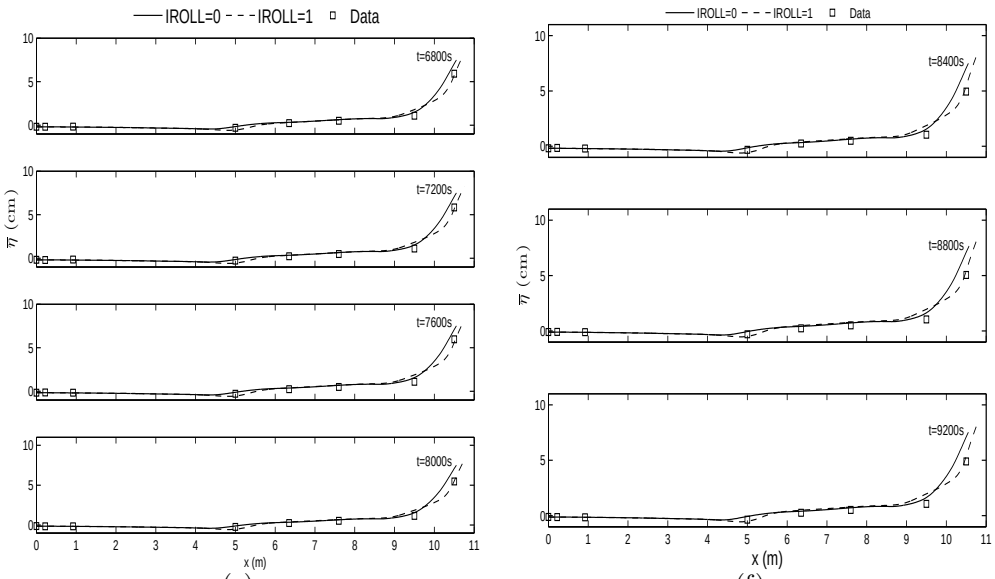

Figure A.1: Test E: Individual measured and predicted mean of the free surface elevation, η, for (a) t=400 to 1600 s, (b) 2000 to 3200 s, (c) 3600 to 4800 s, (d) 5200 to 6400 s, (e) 6800 s to 8000 s, and (f) 8400 s to 9200 s

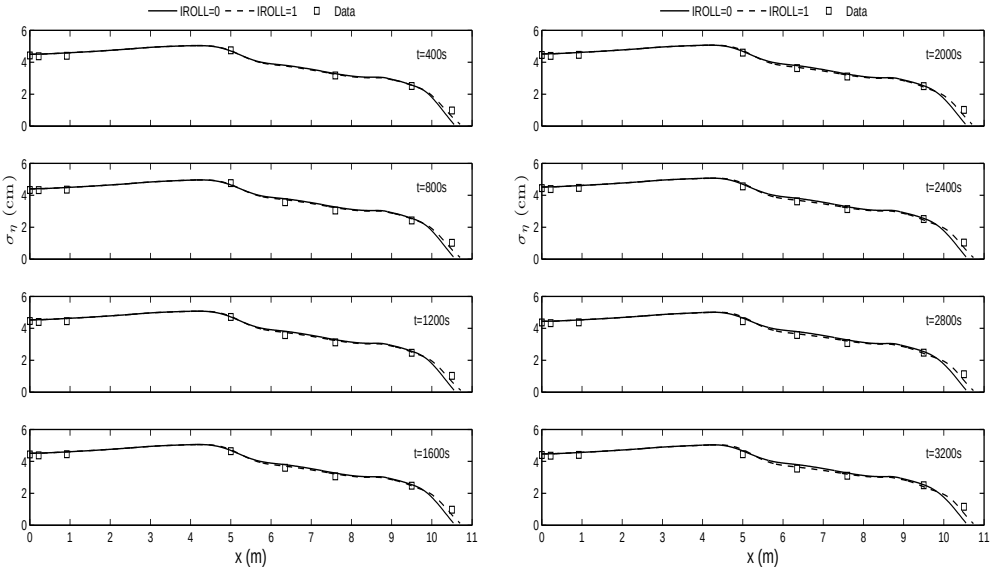
IROLL=0
IROLL=1
Data
t=400s
t=800s
t=1200s
t=1600s
t=2000s
t=2400s
t=2800s
t=3200s
σ_η (cm)
x (m)

(a) (b)

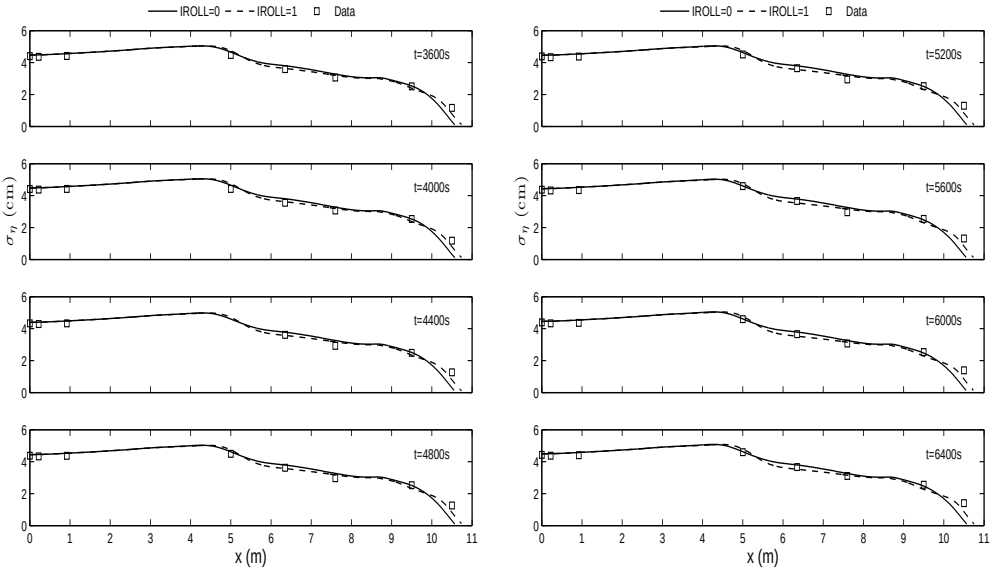
IROLL=0
IROLL=1
Data
t=3600s
t=4000s
t=4400s
t=4800s
t=5200s
t=5600s
t=6000s
t=6400s
σ_η (cm)
x (m)

(c) (d)

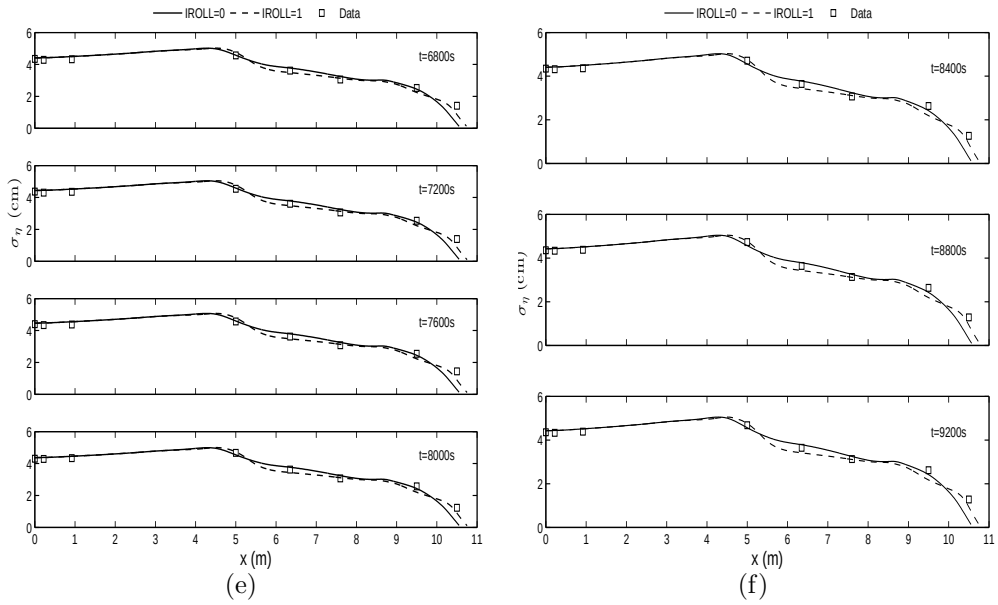

Figure A.2: Test E: Individual measured and predicted standard deviation of the free surface elevation, η, for (a) t=400 to 1600 s, (b) 2000 to 3200 s, (c) 3600 to 4800 s, (d) 5200 to 6400 s, (e) 6800 s to 8000 s, and (f) 8400 s to 9200 s

A.2 Velocity

Table A.3: Test E: Horizontal velocity measurements for 23 bursts where the profile was measured after 1, 2, 3, 6, 10 , 14, 18, and 23 bursts.

profile	test	x(m)	z_m(cm)	$\bar{U}$ (cm/s)	σ_U (cm/s)
P1	E1		8	-6.64	18.37
P2	E2		8	-6.17	18.48
P3	E3		6	-6.48	18.39
	E4		6	-7.20	18.32
	E5	7.6	6	-7.08	18.08
P6	E6		6	-6.80	18.04
	E7		6	-6.40	17.90
	E8		6	-6.09	18.22
	E9		6	-6.12	18.17
P10	E10		6	-6.57	17.82
	E11		4	-8.74	30.33
	E12		4	-8.72	29.56
	E13	5	2	-7.42	28.81
P14	E14		2	-6.04	26.72
	E15		4	-6.93	17.47
	E16		4	-7.06	17.71
	E17		4	-6.56	17.76
	E18		4	-6.97	18.01
P19	E19		2	-7.11	18.47
	E20	7.6	2	-5.91	16.58
	E21		2	-6.50	17.38
	E22		2	NR	NR
P23	E23		2	-5.95	17.21

Table A.4: Test E: Turbulent velocity measurements for 23 bursts.

test	x	z_m	$\overline{u'^2}$	$\overline{v'^2}$	$\overline{w'^2}$	$\sqrt{k}$
	(m)	(com)	(cm^2/s^2)	(cm^2/s^2)	(cm^2/s^2)	(cm/s)
E1		8	39.28	30.04	13.53	6.44
E2		8	53.20	27.46	17.43	7.00
E3		6	48.20	27.54	13.18	6.67
E4		6	42.59	23.51	8.88	6.12
E5	7.6	6	41.36	23.04	8.23	6.03
E6		6	43.90	23.59	12.78	6.33
E7		6	47.89	24.82	9.57	6.41
E8		6	46.67	25.90	12.00	6.50
E9		6	49.40	23.78	12.73	6.55
E10		6	42.70	23.06	11.80	6.23
E11		4	39.72	18.78	25.21	6.47
E12		4	40.70	19.99	14.67	6.14
E13	5	2	42.80	16.76	15.81	6.13
E14		2	64.00	11.26	9.00	6.49
E15		4	37.63	20.74	8.31	5.77
E16		4	42.62	20.16	10.15	6.04
E17		4	30.13	22.04	7.82	5.48
E18		4	34.98	20.37	9.11	5.68
E19	7.6	2	35.95	20.72	6.20	5.61
E20		2	87.86	21.27	4.56	7.54
E21		2	47.38	19.32	6.15	6.04
E22		2	NR	12.53	3.27	NR
E23		2	50.32	16.29	5.83	6.02

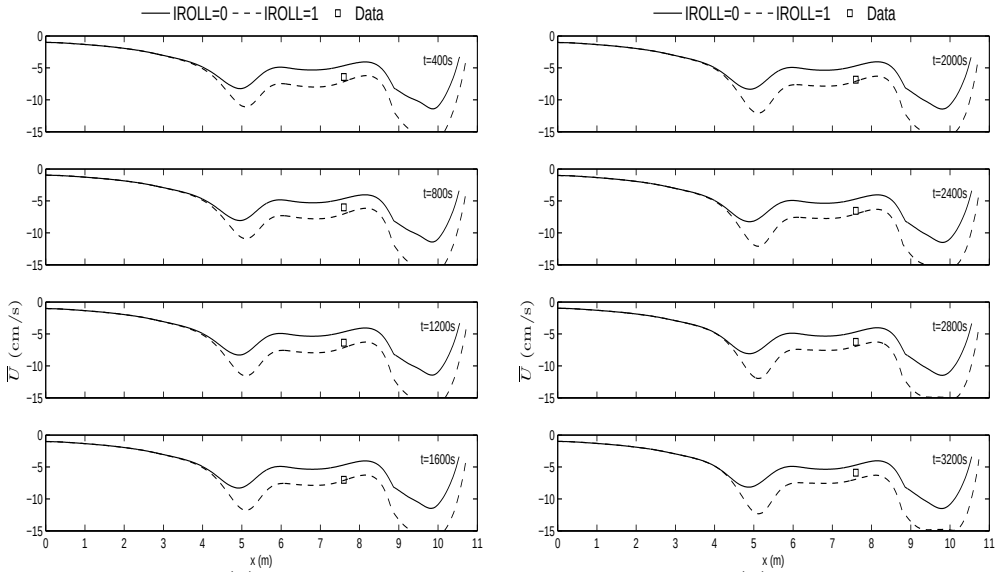
IROLL=0
IROLL=1
Data
t=400s
t=800s
t=1200s
t=1600s
t=2000s
t=2400s
t=2800s
t=3200s
$\overline{U}$ (cm/s)
x (m)

(a) (b)

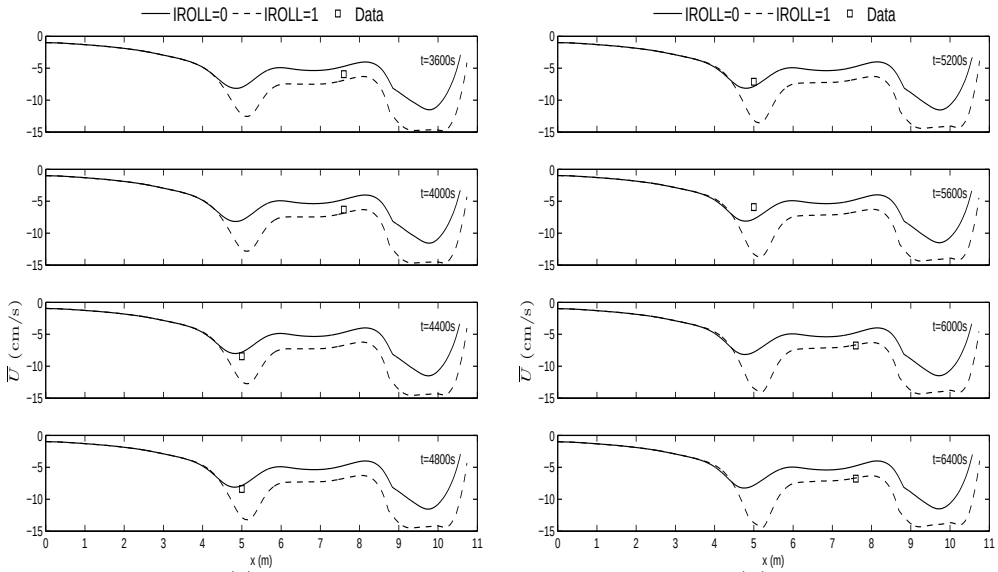
IROLL=0
IROLL=1
Data
t=3600s
t=4000s
t=4400s
t=4800s
t=5200s
t=5600s
t=6000s
t=6400s
$\overline{U}$ (cm/s)
x (m)

(c) (d)

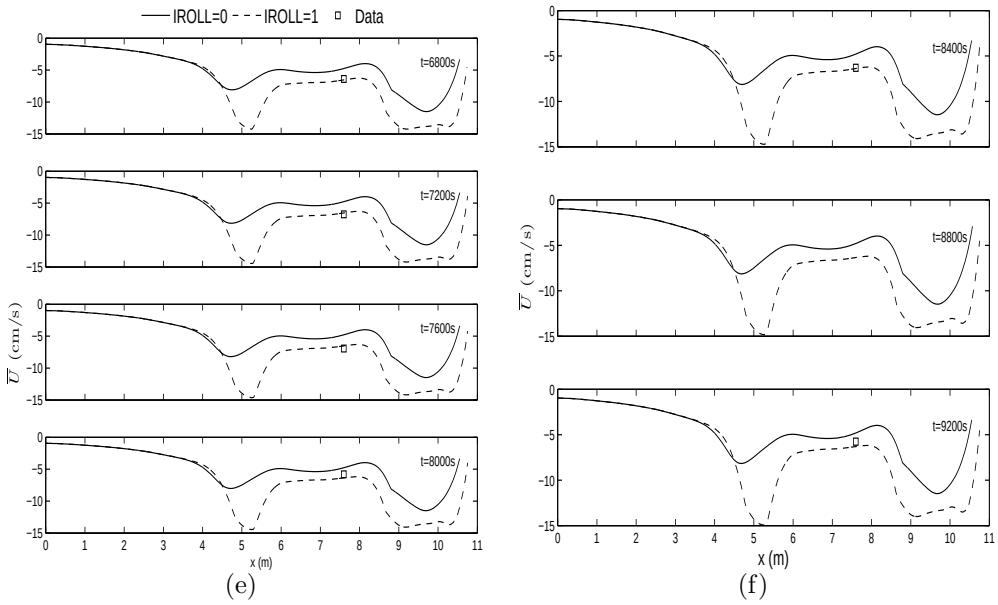

Figure A.3: Test E: Individual measured and predicted mean of the horizontal fluid velocity, U, for (a) t=400 to 1600 s, (b) 2000 to 3200 s, (c) 3600 to 4800 s, (d) 5200 to 6400 s, (e) 6800 s to 8000 s, and (f) 8400 s to 9200 s

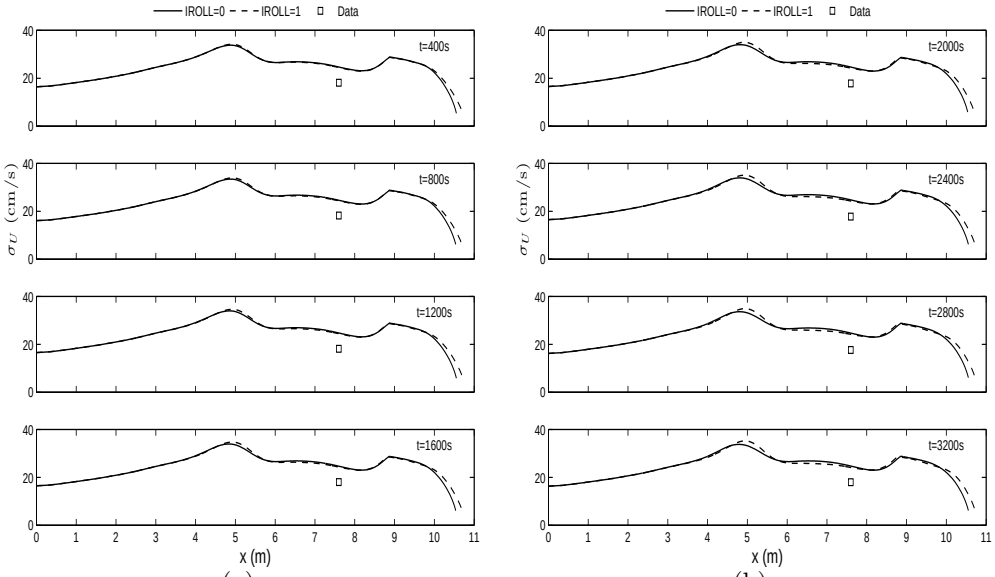
IROLL=0
IROLL=1
Data
t=400s
t=800s
t=1200s
t=1600s
σ_U (cm/s)
x (m)

(a)

IROLL=0
IROLL=1
Data
t=2000s
t=2400s
t=2800s
t=3200s
σ_U (cm/s)
x (m)

(b)

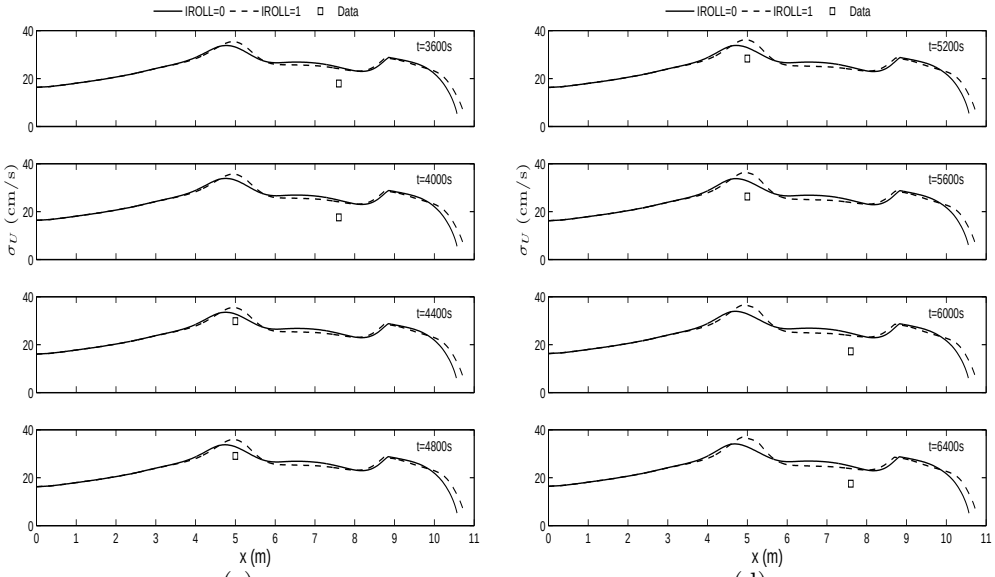
IROLL=0
IROLL=1
Data
t=3600s
t=4000s
t=4400s
t=4800s
σ_U (cm/s)
x (m)

(c)

IROLL=0
IROLL=1
Data
t=5200s
t=5600s
t=6000s
t=6400s
σ_U (cm/s)
x (m)

(d)

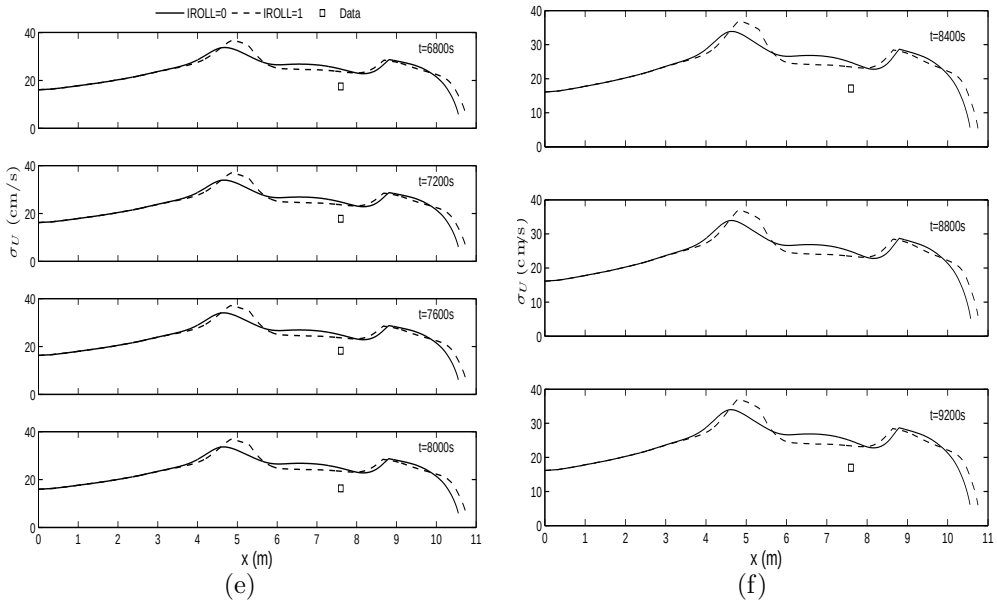

Figure A.4: Test E: Individual measured and predicted standard deviation of the horizontal fluid velocity, U, for (a) t=400 to 1600 s, (b) 2000 to 3200 s, (c) 3600 to 4800 s, (d) 5200 to 6400 s, (e) 6800 s to 8000 s, and (f) 8400 s to 9200 s

A.3 Concentration

Table A.5: Test E: Concentration measurements for 23 bursts.

profile	test	x(m)	z_m(cm)	$\bar{C}$	σ_C	γ_{UC}
P1	E1		8	0.0017	0.00061	0.10
P2	E2		8	0.0010	0.00042	0.06
P3	E3		8	NR	NR	NR
	E4		6	0.00068	0.00028	0.17
	E5	7.6	6	0.00085	0.00030	0.14
P6	E6		6	0.00085	0.00024	0.19
	E7		6	0.00084	0.00029	0.17
	E8		6	0.00088	0.00026	0.13
	E9		6	0.00084	0.00027	0.14
P10	E10		6	0.00086	0.00026	0.18
	E11		4	0.00132	0.00158	0.15
	E12		4	0.00147	0.00153	0.17
	E13	5	2	0.00196	0.00189	0.21
P14	E14		2	0.00179	0.00178	0.24
	E15		4	0.00048	0.00027	0.19
	E16		4	0.00056	0.00026	0.21
	E17		4	0.00070	0.00032	0.18
	E18		4	0.00071	0.00031	0.23
P19	E19		2	0.00103	0.00056	0.24
	E20	7.6	2	0.00098	0.00067	0.23
	E21		2	0.00117	0.00081	0.23
	E22		2	0.00127	0.00096	NR
P23	E23		2	0.00138	0.00093	0.23

A.4 Profile change

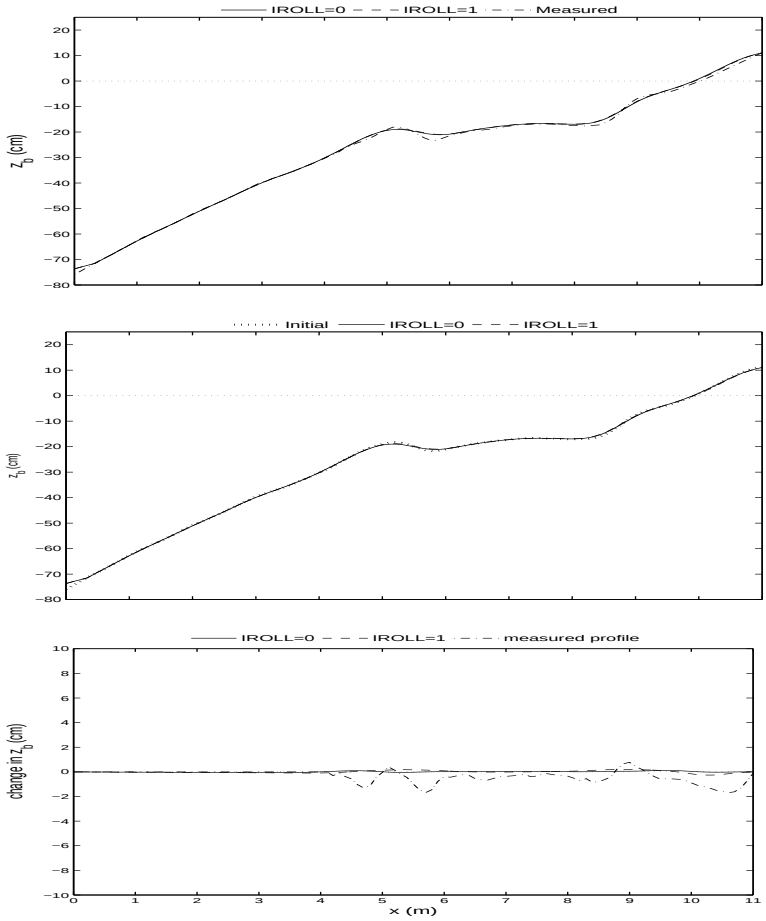

Figure A.5: Erosion test: (top) Computed and measured profiles for $t = 400$ s, (middle) Computed and initial profile for $t = 400$ s, (bottom) Computed change from the initial profile for $t = 400$ s.

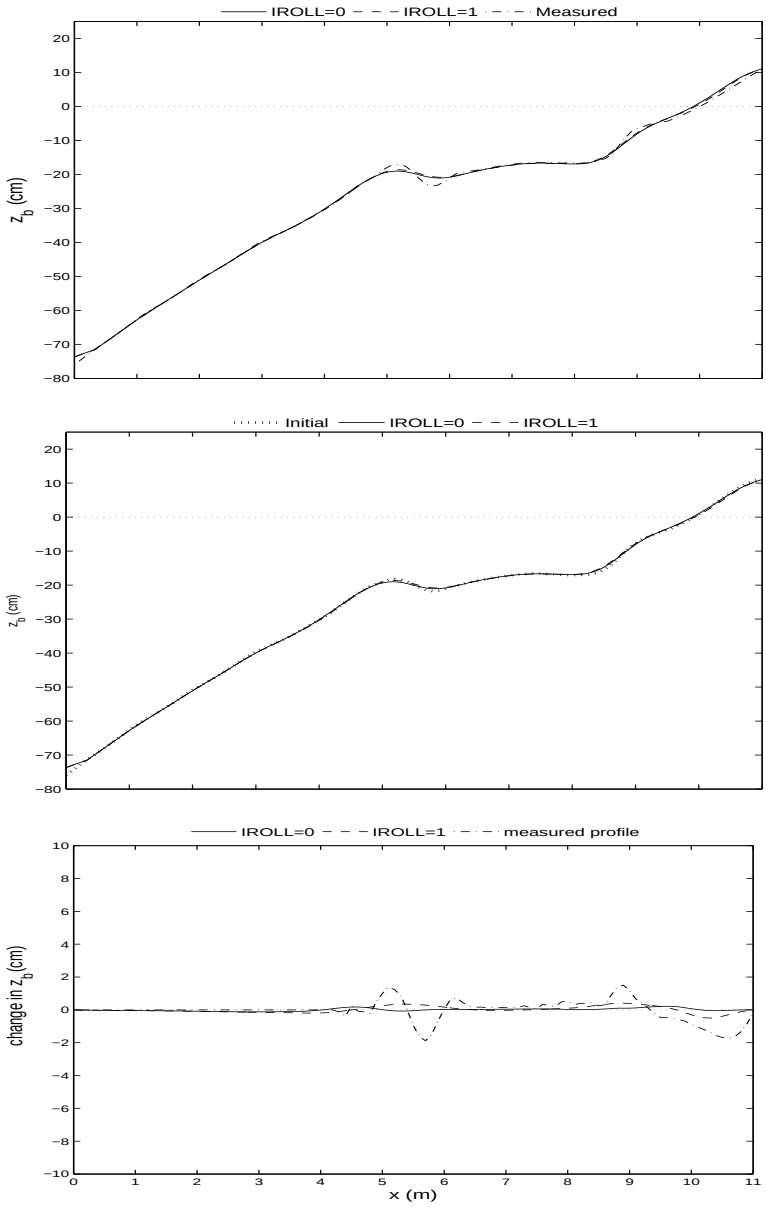

Figure A.6: Erosion test: (top) Computed and measured profiles for $t = 800$ s, (middle) Computed and initial profile for $t = 800$ s, (bottom) Computed change from the initial profile for $t = 800$ s.

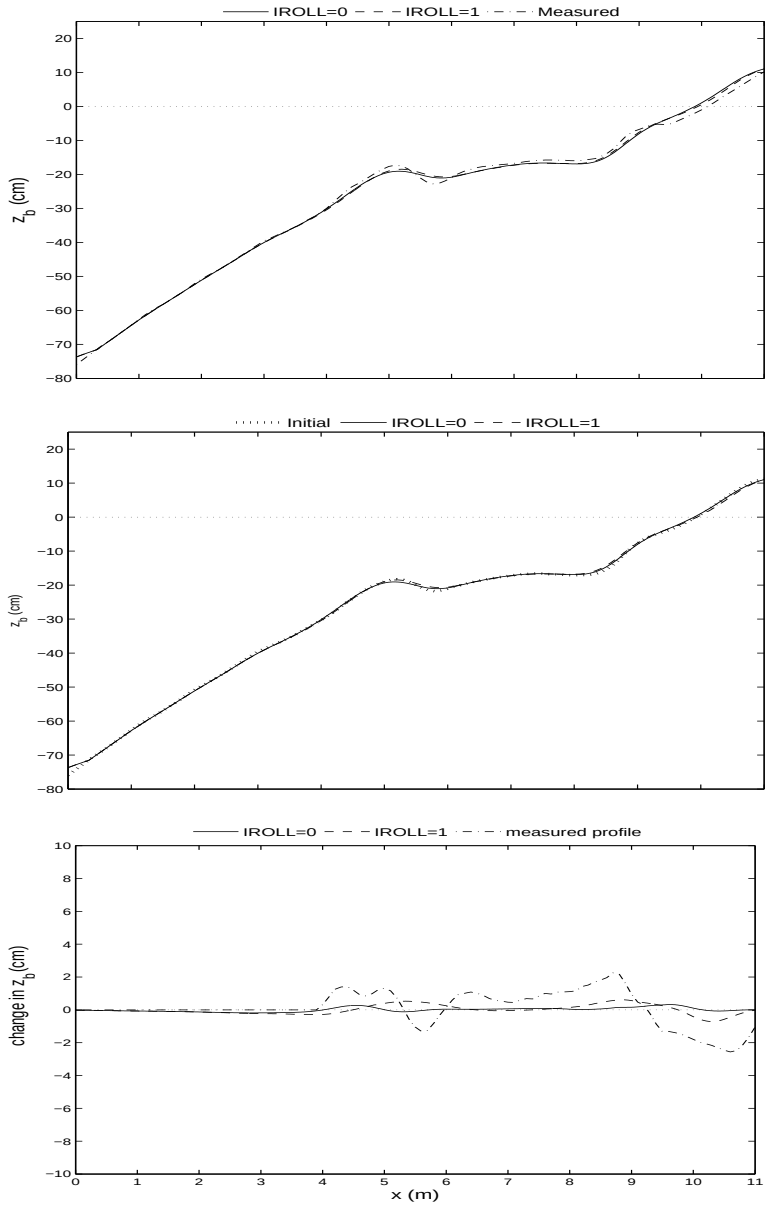

Figure A.7: Erosion test: (top) Computed and measured profiles for $t = 1200$ s, (middle) Computed and initial profile for $t = 1200$ s, (bottom) Computed change from the initial profile for $t = 1200$ s.

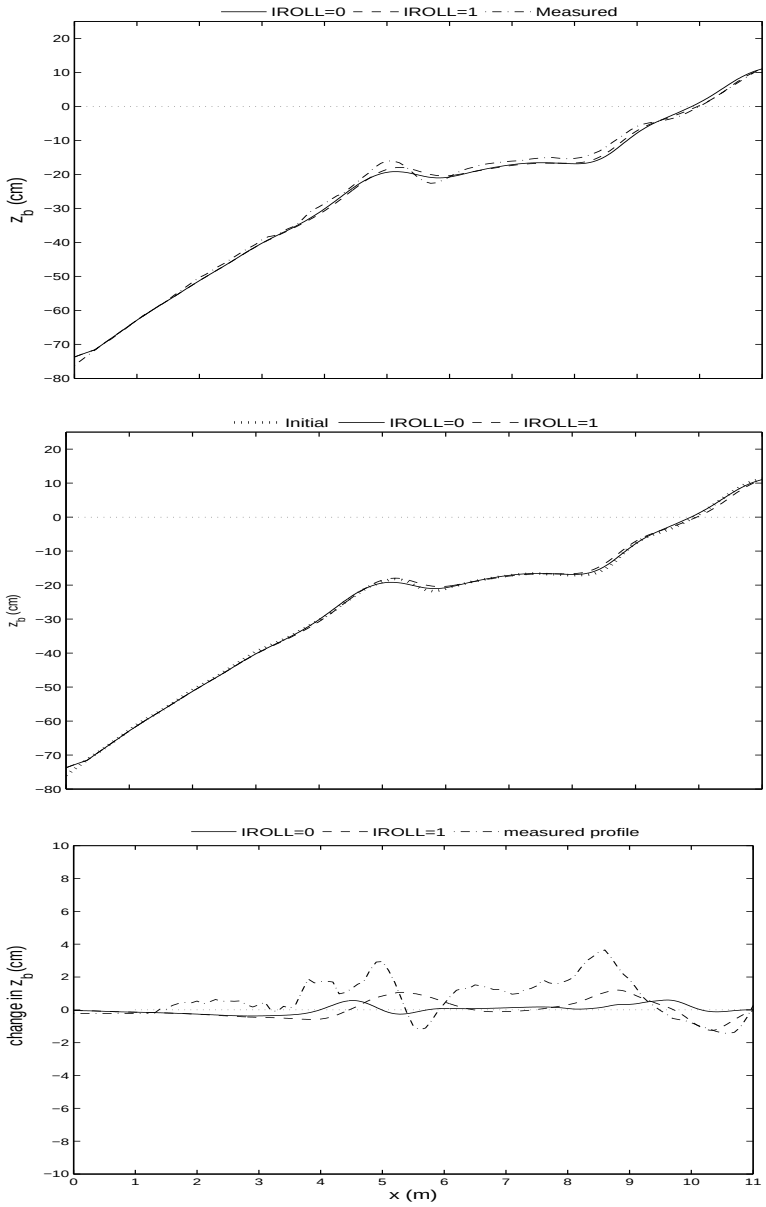

Figure A.8: Erosion test: (top) Computed and measured profiles for $t = 2400$ s, (middle) Computed and initial profile for $t = 2400$ s, (bottom) Computed change from the initial profile for $t = 2400$ s.

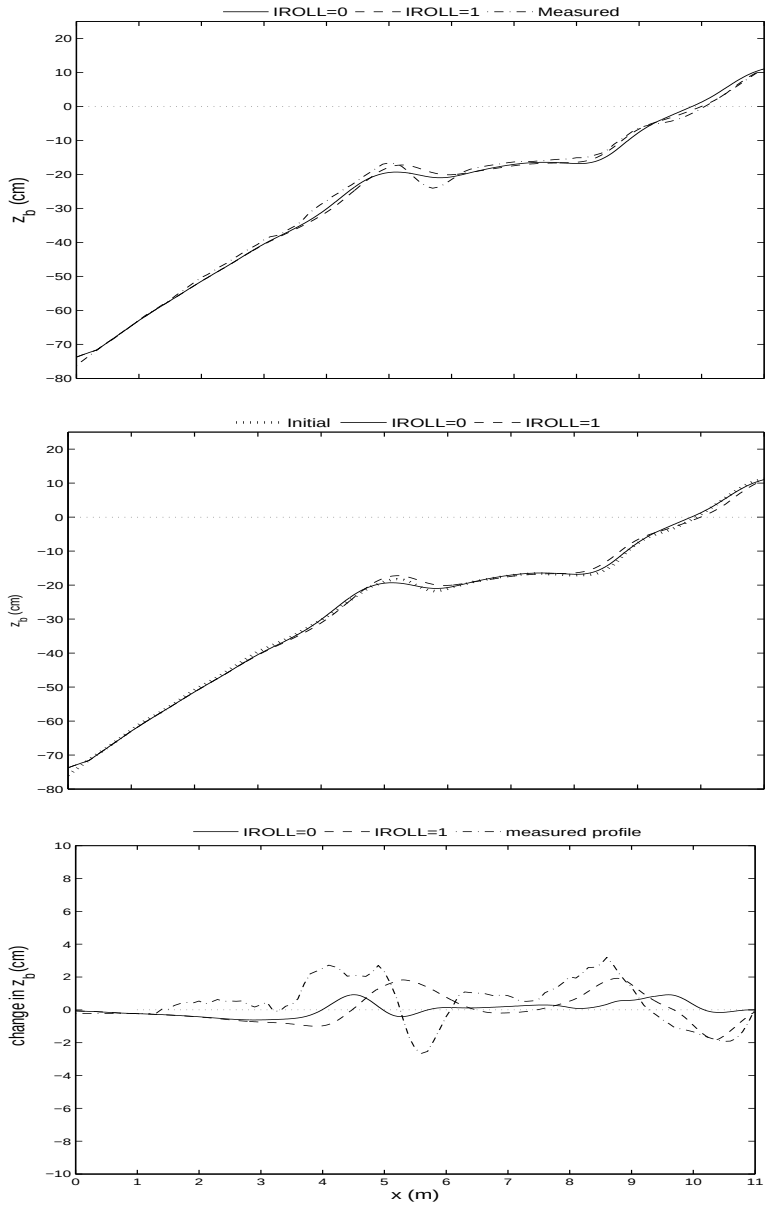

Figure A.9: Erosion test: (top) Computed and measured profiles for $t = 4000$ s, (middle) Computed and initial profile for $t = 4000$ s, (bottom) Computed change from the initial profile for $t = 4000$ s.

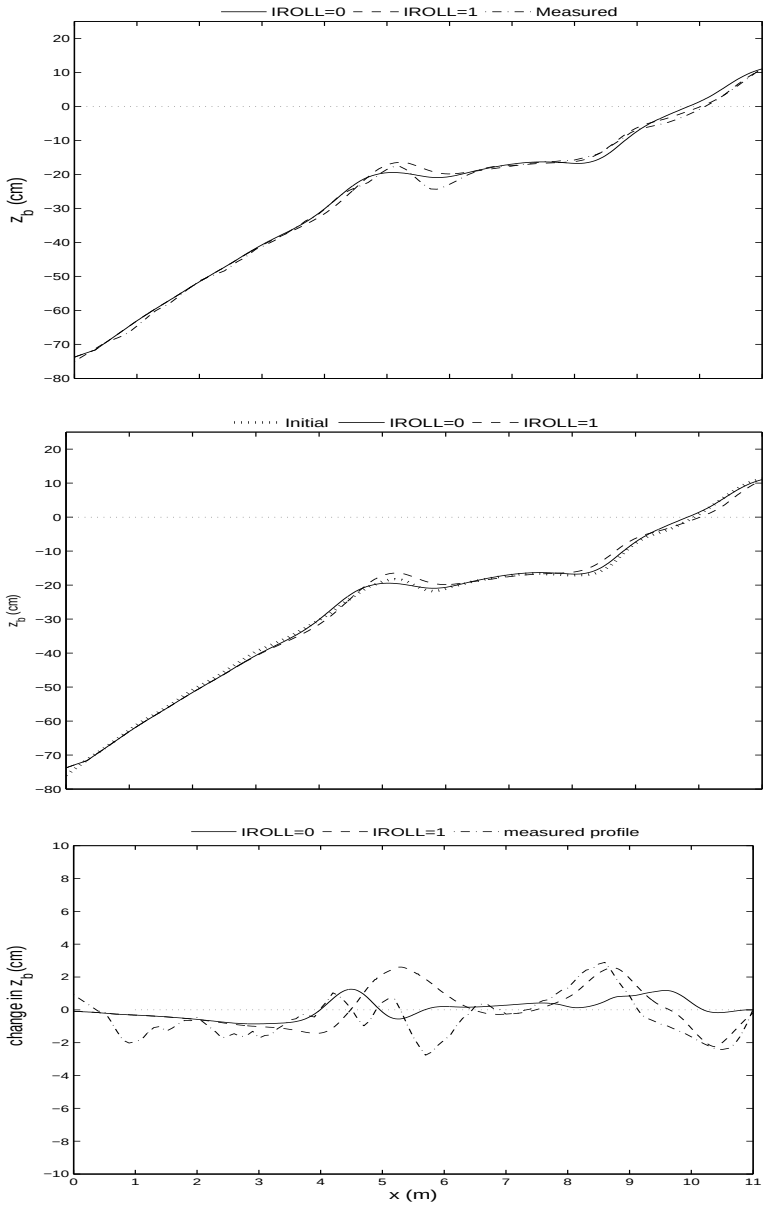

Figure A.10: Erosion test: (top) Computed and measured profiles for $t = 5600$ s, (middle) Computed and initial profile for $t = 5600$ s, (bottom) Computed change from the initial profile for $t = 5600$ s.

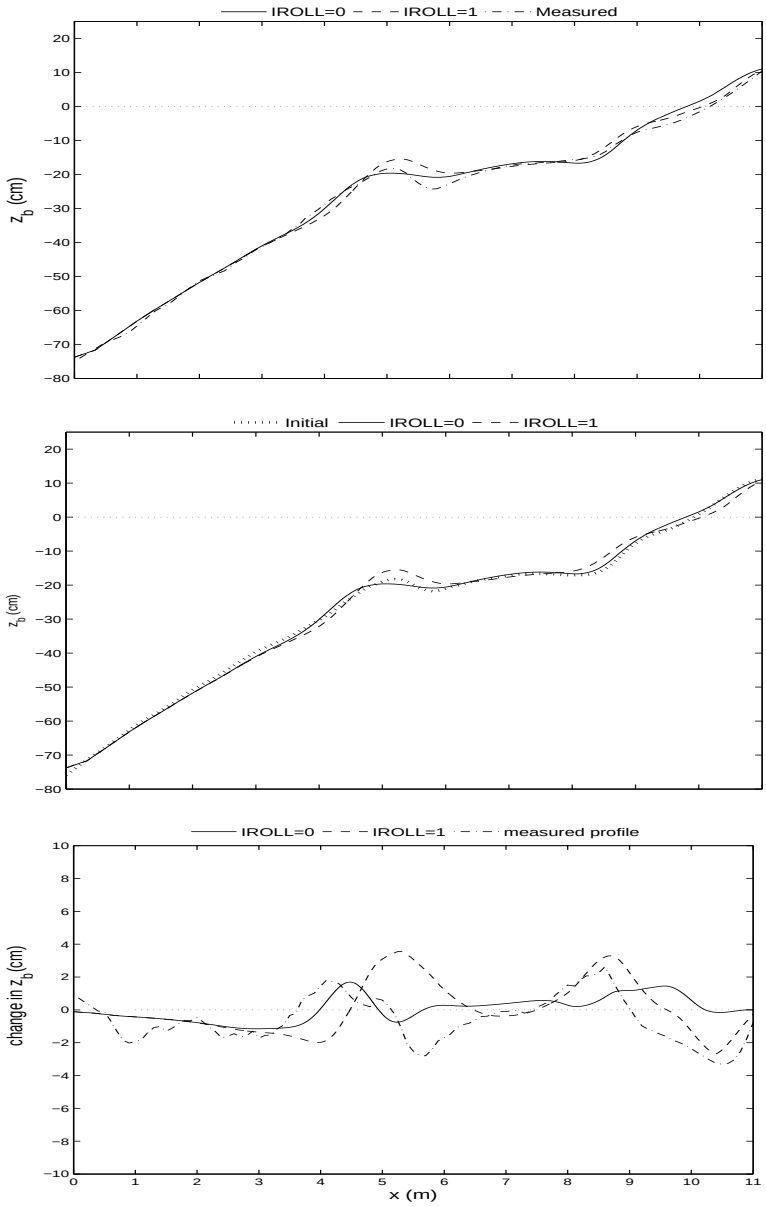

Figure A.11: Erosion test: (top) Computed and measured profiles for $t = 7600$ s, (middle) Computed and initial profile for $t = 7600$ s, (bottom) Computed change from the initial profile for $t = 7600$ s.

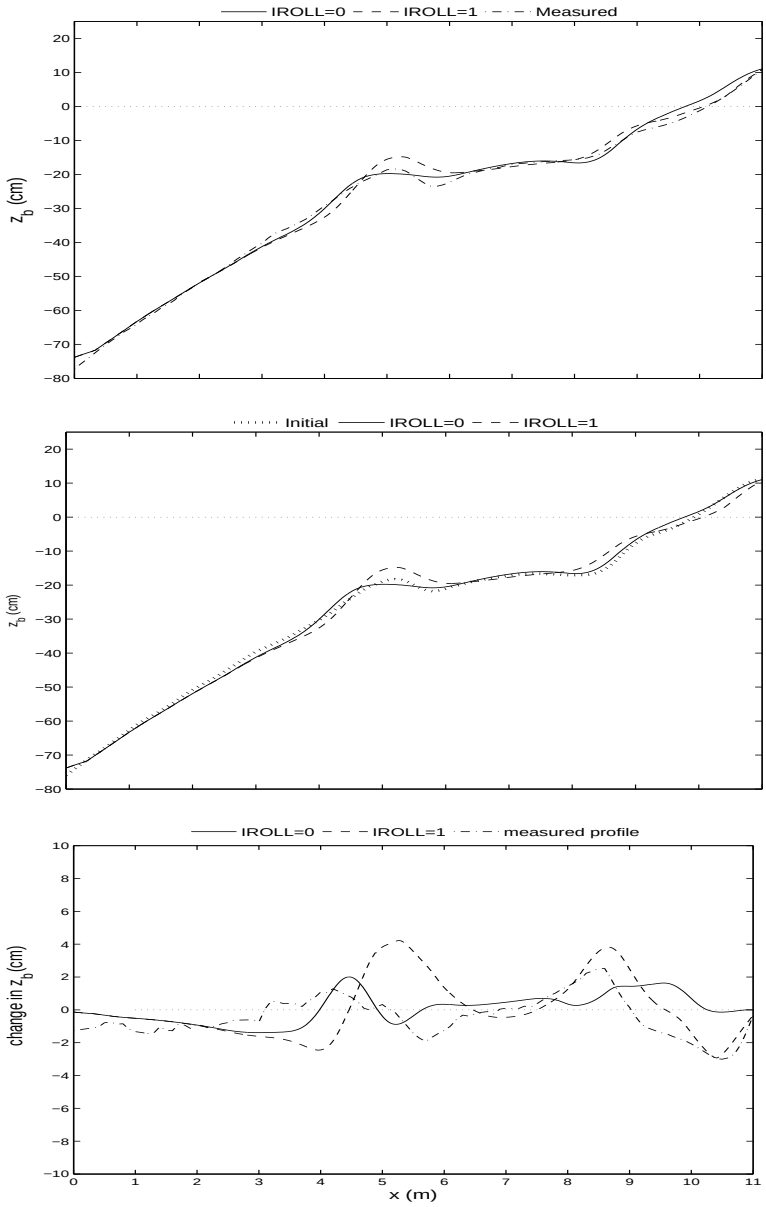

Figure A.12: Erosion test: (top) Computed and measured profiles for $t = 9200$ s, (middle) Computed and initial profile for $t = 9200$ s, (bottom) Computed change from the initial profile for $t = 9200$ s.

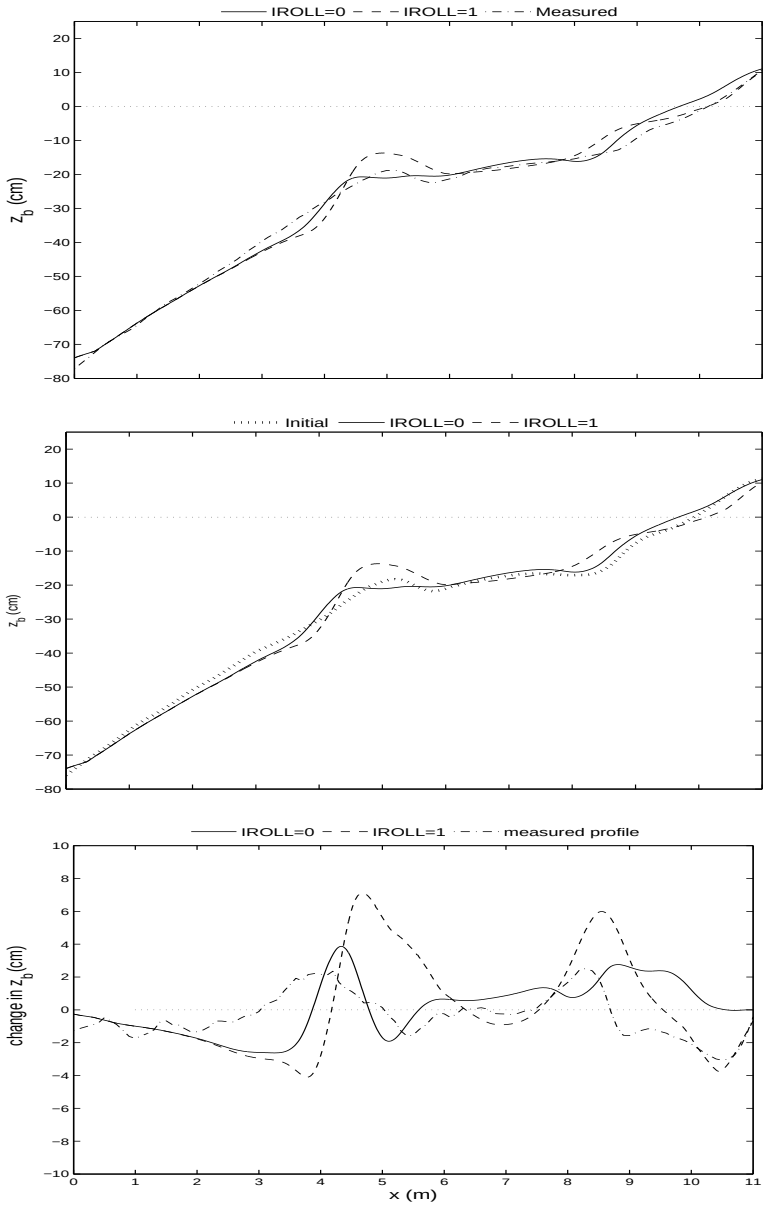

Figure A.13: Erosion test: (top) Computed and measured profiles for $t = 17200$ s, (middle) Computed and initial profile for $t = 17200$ s, (bottom) Computed change from the initial profile for $t = 17200$ s.

Appendix B

TEST A

B.1 Free surface

Table B.1: Test A: Free surface measurements consisting of 20 bursts of A1 to A20.

test	x (m)	d (cm)	$\overline{\eta}$ (cm)	σ_η (cm)
A1	0.00	77.21	-0.055	2.85
	0.22	73.94	-0.088	2.85
	0.92	65.43	-0.065	2.88
	5.00	18.32	-0.22	3.36
	6.35	18.85	-0.15	2.87
	7.60	16.12	0.088	2.61
	9.50	5.23	0.040	2.39
	10.5	-4.78	5.50	0.70
A2	0.00	77.21	-0.047	2.89
	0.22	73.94	-0.087	2.88
	0.92	65.43	-0.091	2.91
	5.00	18.32	-0.24	3.39
	6.35	18.85	-0.039	2.89
	7.60	16.12	0.13	2.62
	9.50	5.23	0.14	2.40
	10.5	-4.78	6.57	0.69
A3	0	76.25	-0.14	2.88
	0.22	73.50	-0.12	2.87
	0.92	65.39	-0.12	2.91
	5.00	18.43	-0.20	3.38
	6.35	17.69	-0.046	2.89
	7.60	15.08	0.062	2.62
	9.50	5.79	0.12	2.51
	10.5	-5.37	6.40	0.71

test	x (m)	d (cm)	$\overline{\eta}$ (cm)	σ_η (cm)
A4	0	76.25	-0.044	2.90
	0.22	73.50	-0.049	2.89
	0.92	65.39	-0.073	2.94
	5.00	18.43	-0.19	3.40
	6.35	17.69	0.002	2.88
	7.60	15.08	0.15	2.61
	9.50	5.79	0.11	2.53
	10.5	-5.37	5.63	0.70
A5	0	77.37	-0.096	2.89
	0.22	74.01	-0.10	2.89
	0.92	64.65	-0.09	2.90
	5.00	19.49	-0.24	3.36
	6.35	18.19	-0.058	2.92
	7.60	15.36	0.15	2.64
	9.50	6.21	0.048	2.50
	10.5	-5.04	5.55	0.76
A6	0	77.37	-0.071	2.94
	0.22	74.01	-0.063	2.95
	0.92	64.65	-0.080	2.96
	5.00	19.49	-0.17	3.42
	6.35	18.19	-0.031	2.93
	7.60	15.36	0.13	2.65
	9.50	6.21	0.11	2.58
	10.5	-5.04	5.85	0.77

test	x (m)	d (cm)	$\overline{\eta}$ (cm)	σ_η (cm)
A7	0	77.37	-0.049	2.93
	0.22	74.01	-0.054	2.94
	0.92	64.65	-0.071	2.97
	5.00	19.49	-0.19	3.40
	6.35	18.19	0.014	2.92
	7.60	15.36	0.12	2.64
	9.50	6.21	0.083	2.56
	10.5	-5.04	5.64	0.77
A8	0	77.37	-0.13	2.84
	0.22	74.01	-0.17	2.85
	0.92	64.65	-0.16	2.89
	5.00	20.36	-0.20	3.34
	6.35	18.17	-0.10	2.87
	7.60	15.94	0.14	2.55
	9.50	6.37	0.094	2.50
	10.5	-5.59	6.72	0.70
A9	0	77.37	-0.063	2.87
	0.22	74.01	-0.048	2.88
	0.92	64.65	-0.053	2.93
	5.00	20.36	-0.19	3.37
	6.35	18.17	0.035	2.90
	7.60	15.94	0.14	2.58
	9.50	6.37	0.12	2.53
	10.5	-5.59	6.32	0.71
A10	0	77.37	-0.051	2.89
	0.22	74.01	-0.079	2.90
	0.92	64.65	-0.11	2.94
	5.00	20.36	-0.18	3.37
	6.35	18.17	0.002	2.92
	7.60	15.94	0.14	2.57
	9.50	6.37	0.14	2.53
	10.5	-5.59	6.33	0.71

test	x (m)	d (cm)	$\overline{\eta}$ (cm)	σ_η (cm)
A11	0	77.37	-0.067	2.89
	0.22	74.01	-0.060	2.90
	0.92	64.65	-0.087	2.95
	5.00	20.36	-0.15	3.37
	6.35	18.17	0.010	2.89
	7.60	15.94	0.14	2.56
	9.50	6.37	0.11	2.53
	10.5	-5.59	6.24	0.72
A12	0	76.32	-0.083	2.84
	0.22	73.52	-0.090	2.85
	0.92	64.69	-0.11	2.90
	5.00	21.82	-0.19	3.30
	6.35	18.44	-0.028	2.84
	7.60	16.81	0.16	2.56
	9.50	6.88	0.047	2.63
	10.5	-5.42	6.24	0.69
A13	0	76.32	-0.070	2.86
	0.22	73.52	-0.052	2.87
	0.92	64.69	-0.071	2.92
	5.00	21.82	-0.16	3.30
	6.35	18.44	-0.036	2.87
	7.60	16.81	0.15	2.57
	9.50	6.88	0.044	2.66
	10.5	-5.42	6.04	0.68
A14	0	76.32	-0.063	2.88
	0.22	73.52	-0.039	2.89
	0.92	64.69	-0.079	2.94
	5.00	21.82	-0.15	3.32
	6.35	18.44	-0.049	2.89
	7.60	16.81	0.17	2.61
	9.50	6.88	0.065	2.69
	10.5	-5.42	6.05	0.70

test	x (m)	d (cm)	$\overline{\eta}$ (cm)	σ_η (cm)
A15	0	76.32	-0.047	2.86
	0.22	73.52	-0.053	2.87
	0.92	64.69	-0.098	2.91
	5.00	21.82	-0.16	3.30
	6.35	18.44	-0.018	2.85
	7.60	16.81	0.15	2.60
	9.50	6.88	0.086	2.66
	10.5	-5.42	6.11	0.69
A16	0	76.32	-0.074	2.85
	0.22	73.52	-0.068	2.86
	0.92	64.69	-0.13	2.91
	5.00	21.48	-0.15	3.29
	6.35	17.23	0.025	2.88
	7.60	16.51	0.16	2.56
	9.50	7.20	0.048	2.61
	10.5	-5.45	6.17	0.69
A17	0	76.32	-0.061	2.87
	0.22	73.52	-0.060	2.87
	0.92	64.68	-0.093	2.93
	5.00	21.48	-0.16	3.30
	6.35	17.23	0.028	2.87
	7.60	16.51	0.16	2.53
	9.50	7.20	0.061	2.63
	10.5	-5.45	6.16	0.70
A18	0	76.32	-0.047	2.85
	0.22	73.52	-0.043	2.86
	0.92	64.68	-0.070	2.91
	5.00	21.48	-0.14	3.29
	6.35	17.23	0.023	2.87
	7.60	16.51	0.18	2.54
	9.50	7.20	0.063	2.63
	10.5	-5.45	6.15	0.70

test	x (m)	d (cm)	$\overline{\eta}$ (cm)	σ_η (cm)
A19	0	76.32	-0.042	2.84
	0.22	73.52	-0.046	2.84
	0.92	64.68	-0.071	2.90
	5.00	21.48	-0.14	3.27
	6.35	17.23	-0.065	2.83
	7.60	16.51	0.14	2.51
	9.50	7.20	0.081	2.63
	10.5	-5.45	6.06	0.70
A20	0	76.32	-0.046	2.83
	0.22	73.52	-0.049	2.83
	0.92	64.68	-0.074	2.89
	5.00	21.48	-0.13	3.26
	6.35	17.23	-0.051	2.84
	7.60	16.51	0.14	2.52
	9.50	7.20	0.060	2.64
	10.5	-5.45	6.09	0.70

Table B.2: Test A: Incident and reflected wave characteristics for 20 bursts

test	$\bar{\eta}$(cm)	$\sigma_\eta(cm)$	Incident spectral		Reflection	Incident Time Series	
			H_{mo} (cm)	T_p (s)	coefficient	H_s (cm)	T_s (s)
A1	-0.055	2.85	11.2	2.68	0.128	10.9	2.46
A2	-0.047	2.89	11.3	2.68	0.130	11.0	2.48
A3	-0.14	2.88	11.2	2.68	0.133	11.0	2.48
A4	-0.044	2.90	11.3	2.68	0.132	11.1	2.48
A5	-0.096	2.89	11.2	2.68	0.136	10.9	2.46
A6	-0.071	2.94	11.4	2.68	0.139	11.2	2.47
A7	-0.049	2.93	11.3	2.68	0.141	11.1	2.47
A8	-0.13	2.84	11.0	2.68	0.141	10.9	2.46
A9	-0.063	2.87	11.1	2.68	0.141	11.0	2.48
A10	-0.051	2.89	11.2	2.68	0.142	11.1	2.47
A11	-0.067	2.89	11.2	2.68	0.145	11.1	2.48
A12	-0.08	2.85	11.0	2.68	0.150	10.9	2.46
A13	-0.069	2.86	11.1	2.68	0.148	11.0	2.47
A14	-0.063	2.88	11.2	2.68	0.147	11.0	2.49
A15	-0.046	2.86	11.1	2.68	0.148	11.0	2.48
A16	-0.074	2.85	11.1	2.68	0.148	11.0	2.47
A17	-0.061	2.87	11.1	2.68	0.148	11.0	2.48
A18	-0.047	2.85	11.1	2.68	0.150	11.0	2.48
A19	-0.041	2.84	11.0	2.68	0.150	10.8	2.48
A20	-0.046	2.83	11.0	2.68	0.152	10.8	2.49

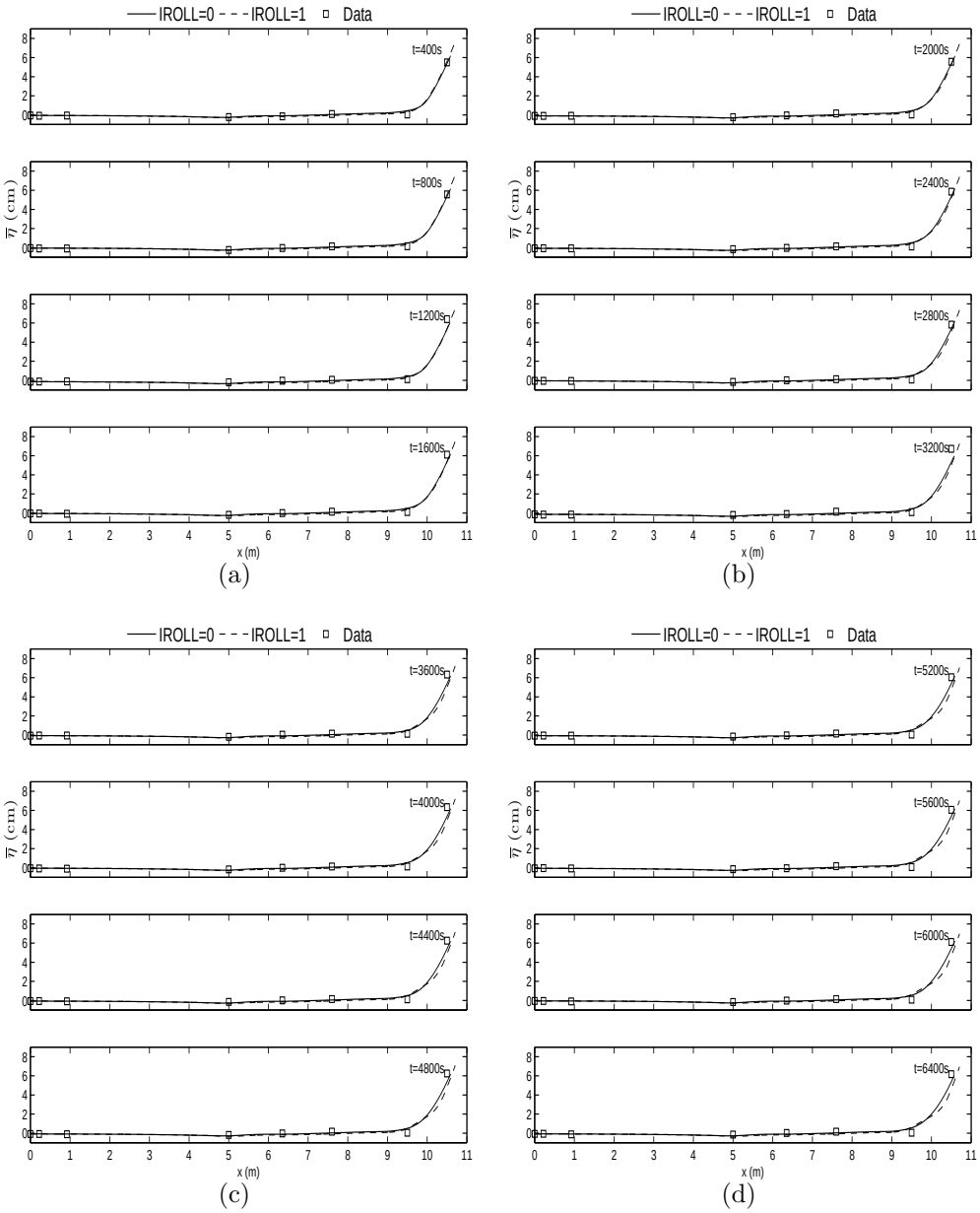
IROLL=0
IROLL=1
Data
t=400s
t=800s
t=1200s
t=1600s
t=2000s
t=2400s
t=2800s
t=3200s
t=3600s
t=4000s
t=4400s
t=4800s
t=5200s
t=5600s
t=6000s
t=6400s
$\overline{\eta}$ (cm)
x (m)
(a)
(b)
(c)
(d)

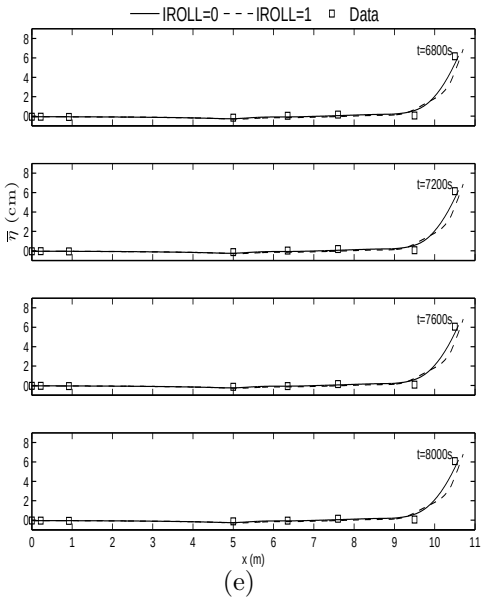

(e)

Figure B.1: Test A: Individual measured and predicted mean of the free surface elevation, η, for (a) t=400 to 1600 s, (b) 2000 to 3200 s, (c) 3600 to 4800 s, (d) 5200 to 6400 s, and (e) 6800 s to 8000 s.

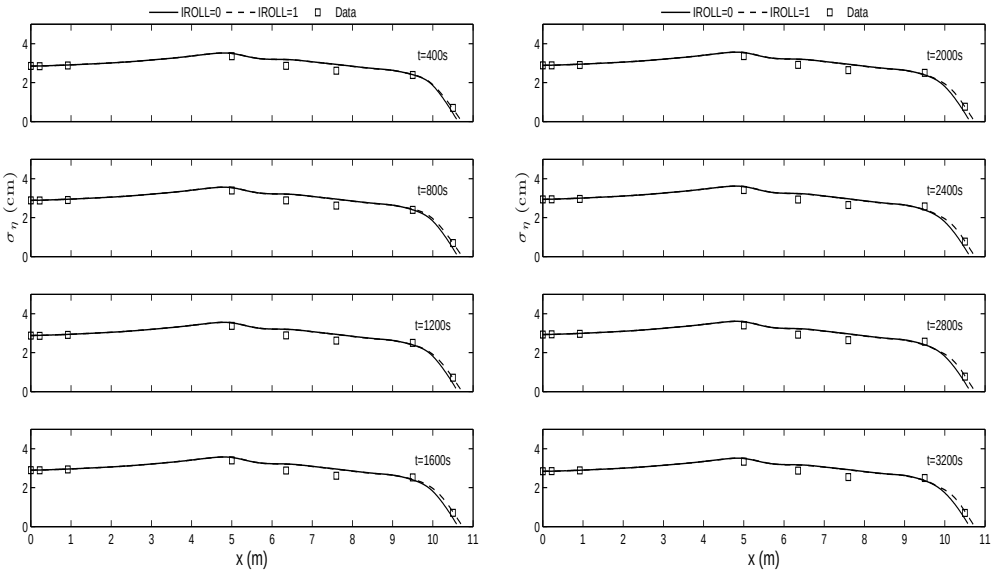
IROLL=0
IROLL=1
Data
t=400s
t=800s
t=1200s
t=1600s
σ_η (cm)
x (m)

(a)

IROLL=0
IROLL=1
Data
t=2000s
t=2400s
t=2800s
t=3200s
σ_η (cm)
x (m)

(b)

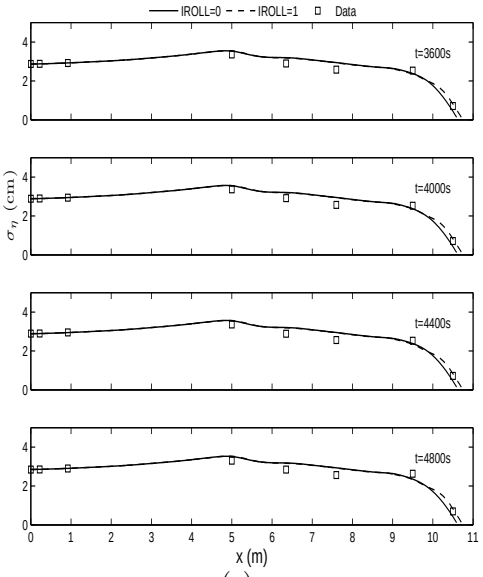
IROLL=0
IROLL=1
Data
t=3600s
t=4000s
t=4400s
t=4800s
σ_η (cm)
x (m)

(c)

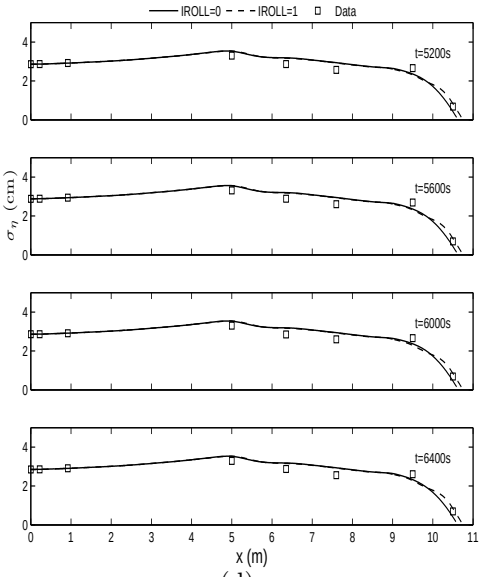
IROLL=0
IROLL=1
Data
t=5200s
t=5600s
t=6000s
t=6400s
σ_η (cm)
x (m)

(d)

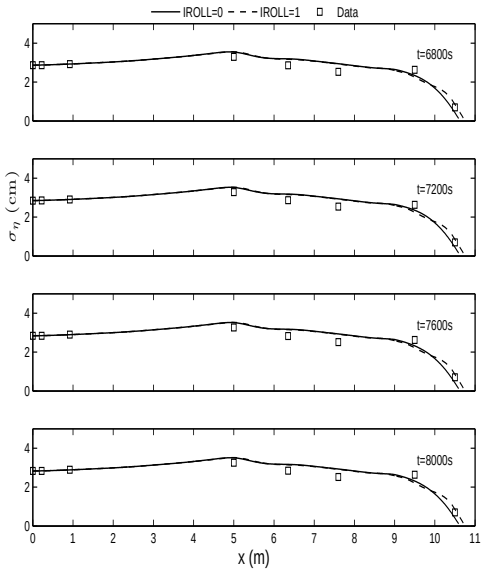

(e)

Figure B.2: Test A: Individual measured and predicted standard deviation of the free surface elevation, η, for (a) t=400 to 1600 s, (b) 2000 to 3200 s, (c) 3600 to 4800 s, (d) 5200 to 6400 s, and (e) 6800 s to 8000 s.

B.2 Velocity

Table B.3: Test A: Horizontal velocity measurements for 20 bursts where the profile was measured after 2, 4, 7, 11, 15 and 20 bursts.

profile	test	x(m)	z_m(cm)	$\bar{U}$ (cm/s)	σ_U (cm/s)
	A1		4	-4.07	15.14
P2	A2		4	-4.89	15.01
	A3		4	-4.15	14.82
P4	A4		4	-4.67	14.74
	A5		6	-3.76	14.60
	A6		6	-3.81	14.83
P7	A7		6	-4.15	14.75
	A8		8	-2.79	14.47
	A9		8	-3.76	14.51
	A10	7.6	8	-3.14	14.62
P11	A11		8	-3.31	14.58
	A12		2	NR	NR
	A13		2	-5.01	14.55
	A14		2	-4.50	14.51
P15	A15		2	-4.28	14.35
	A16		4	-4.58	14.04
	A17		4	-4.02	13.84
	A18		6	-3.62	14.07
	A19		6	-3.81	13.94
P20	A20		6	-4.07	13.77

Table B.4: Test A: Turbulent velocity measurements for 20 bursts.

test	x (m)	z_m (com)	$\overline{u'^2}$ (cm^2/s^2)	$\overline{v'^2}$ (cm^2/s^2)	$\overline{w'^2}$ (cm^2/s^2)	$\sqrt{k}$ (cm/s)
A1	7.6	4	20.12	11.09	6.74	4.36
A2	7.6	4	18.07	11.32	7.28	4.28
A3	7.6	4	17.63	12.16	6.73	4.27
A4	7.6	4	20.49	10.27	4.72	4.21
A5	7.6	6	25.36	12.75	4.03	4.59
A6	7.6	6	24.30	13.94	6.62	4.74
A7	7.6	6	25.58	11.36	5.63	4.61
A8	7.6	8	33.04	16.15	8.65	5.38
A9	7.6	8	26.06	15.99	6.58	4.93
A10	7.6	8	31.35	15.96	8.88	5.30
A11	7.6	8	32.22	17.38	8.66	5.40
A12	7.6	2	NR	NR	NR	NR
A13	7.6	2	18.33	10.89	6.35	4.22
A14	7.6	2	23.56	11.29	5.54	4.49
A15	7.6	2	21.31	11.65	5.42	4.38
A16	7.6	4	21.68	11.28	5.55	4.39
A17	7.6	4	22.29	12.86	7.38	4.61
A18	7.6	6	28.75	14.32	9.17	5.11
A19	7.6	6	23.91	14.17	6.65	4.73
A20	7.6	6	22.37	12.29	5.87	4.50

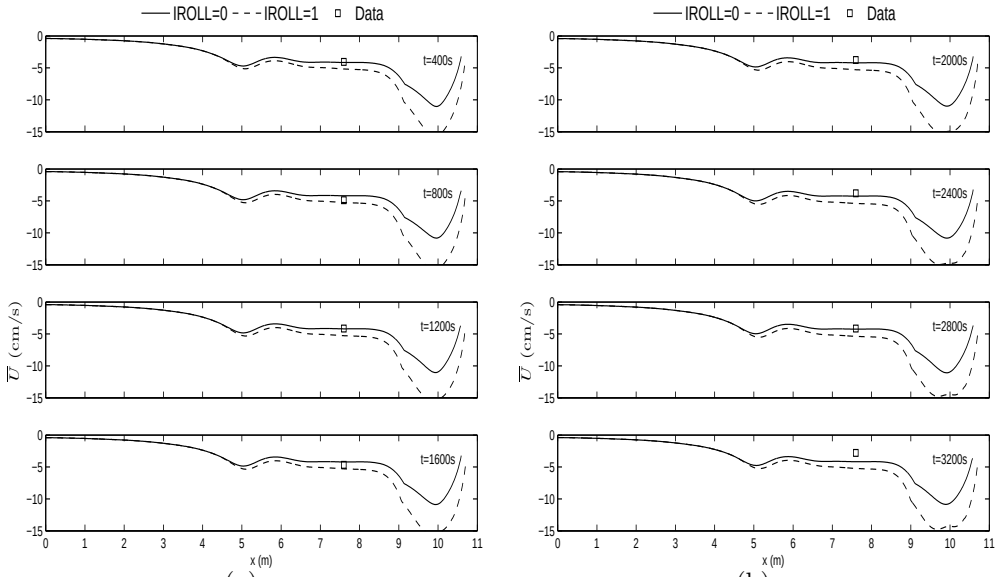
IROLL=0 - - - IROLL=1 Data
t=400s
t=800s
t=1200s
t=1600s
t=2000s
t=2400s
t=2800s
t=3200s
$\overline{U}$ (cm/s)
x (m)

(a) (b)

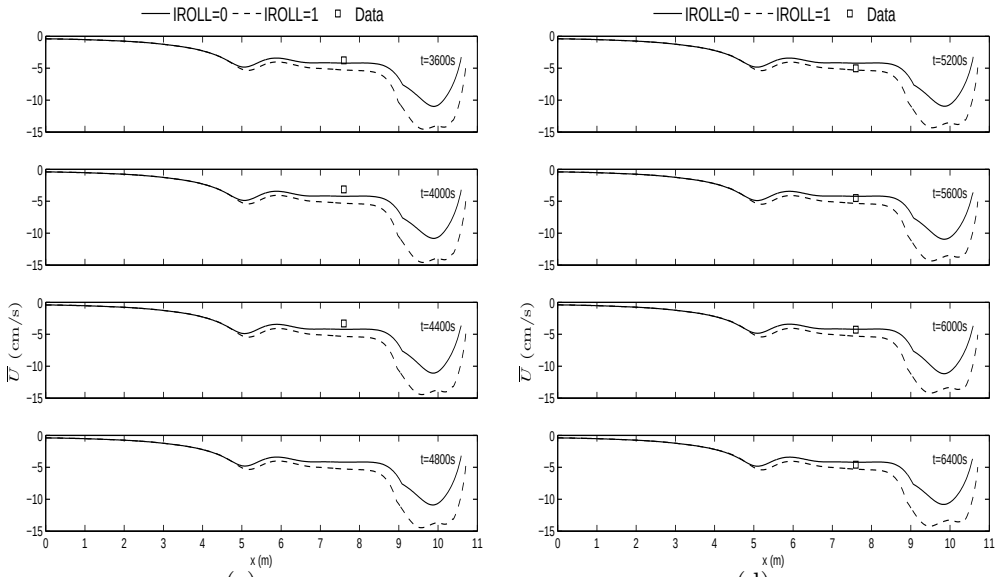
IROLL=0 - - - IROLL=1 Data
t=3600s
t=4000s
t=4400s
t=4800s
t=5200s
t=5600s
t=6000s
t=6400s
$\overline{U}$ (cm/s)
x (m)

(c) (d)

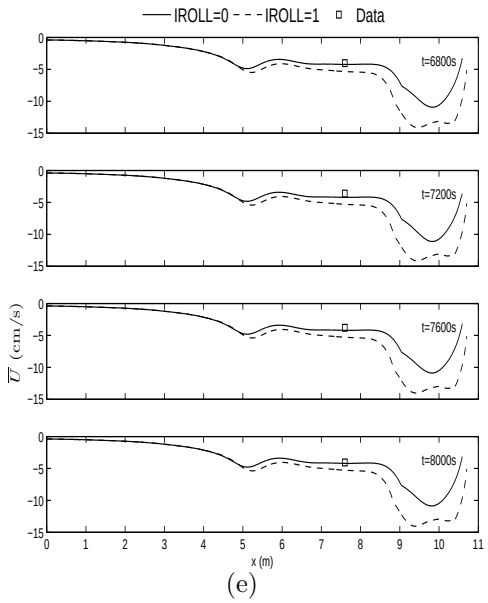

(e)

Figure B.3: Test A: Individual measured and predicted mean of the horizontal fluid velocity, U, for (a) t=400 to 1600 s, (b) 2000 to 3200 s, (c) 3600 to 4800 s, (d) 5200 to 6400 s, and (e) 6800 s to 8000 s.

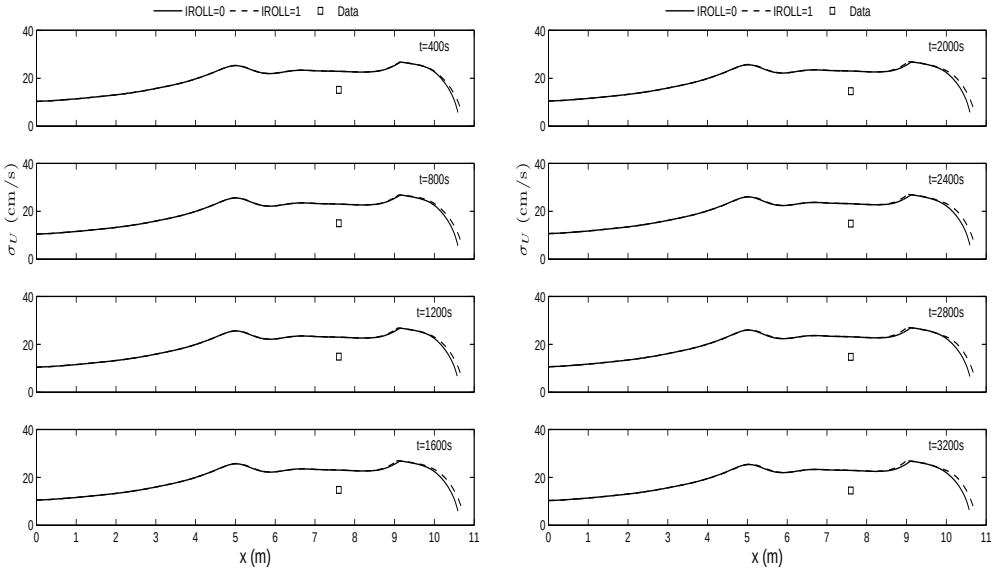
IROLL=0
IROLL=1
Data
t=400s
t=800s
t=1200s
t=1600s
σ_U (cm/s)
x (m)

(a)

IROLL=0
IROLL=1
Data
t=2000s
t=2400s
t=2800s
t=3200s
σ_U (cm/s)
x (m)

(b)

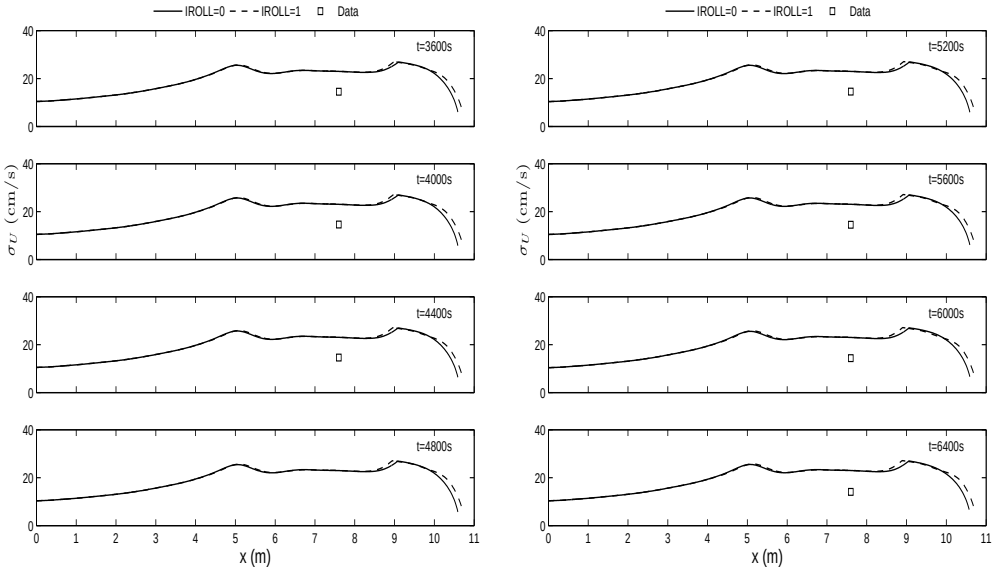
IROLL=0
IROLL=1
Data
t=3600s
t=4000s
t=4400s
t=4800s
σ_U (cm/s)
x (m)

(c)

IROLL=0
IROLL=1
Data
t=5200s
t=5600s
t=6000s
t=6400s
σ_U (cm/s)
x (m)

(d)

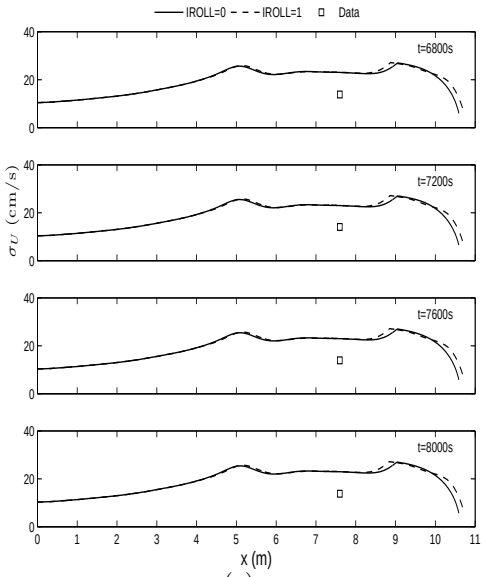

(e)

Figure B.4: Test A: Individual measured and predicted standard deviation of the horizontal fluid velocity, U, for (a) t=400 to 1600 s, (b) 2000 to 3200 s, (c) 3600 to 4800 s, (d) 5200 to 6400 s, and (e) 6800 s to 8000 s.

B.3 Concentration

Table B.5: Test A: Measured concentration values for 20 bursts.

profile	test	x(m)	z_m(cm)	$\bar{C}$	σ_C	γ_{UC}
	A1		4	0.00093	0.00028	0.20
P2	A2		4	0.00094	0.00026	0.18
	A3		4	0.00068	0.00028	0.18
P4	A4		4	0.00084	0.00028	0.20
	A5		6	0.00055	0.00020	0.19
	A6		6	0.00055	0.00016	0.21
P7	A7		6	0.00057	0.00013	0.30
	A8		8	0.00047	0.00017	0.18
	A9		8	0.00058	0.00017	0.15
	A10	7.6	8	0.00064	0.00015	0.17
P11	A11		8	0.00069	0.00017	0.15
	A12		2	0.0011	0.00063	0.11
	A13		2	0.0016	0.00094	0.15
	A14		2	0.0013	0.00074	0.13
P15	A15		2	0.0013	0.00070	0.11
	A16		4	0.00049	0.00021	0.22
	A17		4	0.00048	0.00020	0.18
	A18		6	0.00044	0.00016	0.12
	A19		6	0.00056	0.00017	0.22
P20	A20		6	0.00061	0.00016	0.18

B.4 Profile change

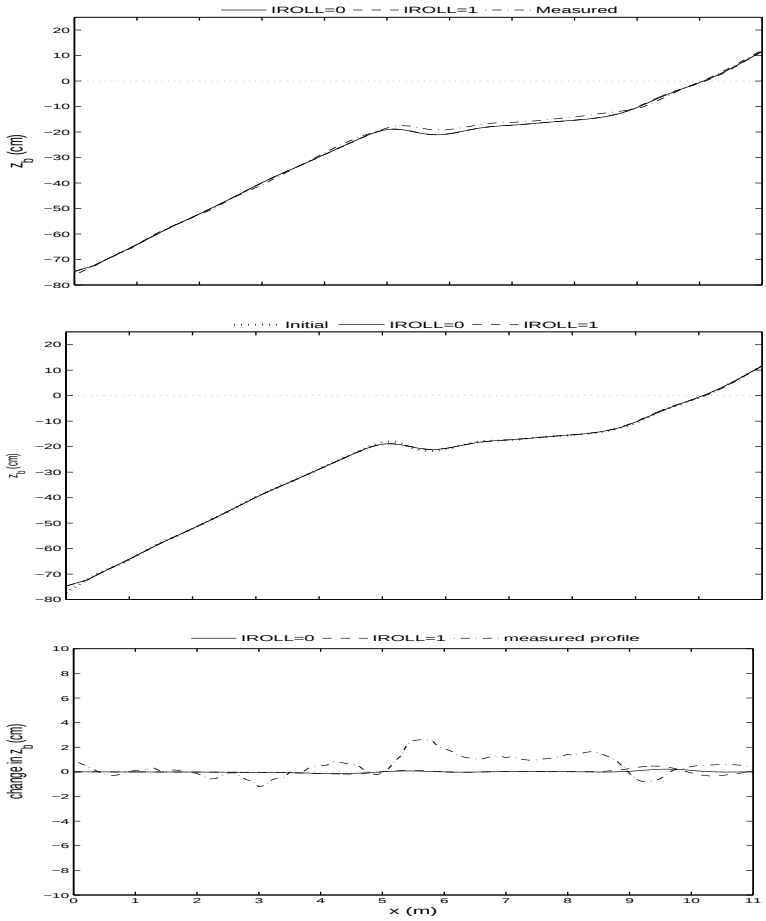

Figure B.5: Accretion Test: (top) Computed and measured profiles for $t = 800$ s, (middle) Computed and initial profile for $t = 800$ s, (bottom) Computed change from the initial profile for $t = 800$ s.

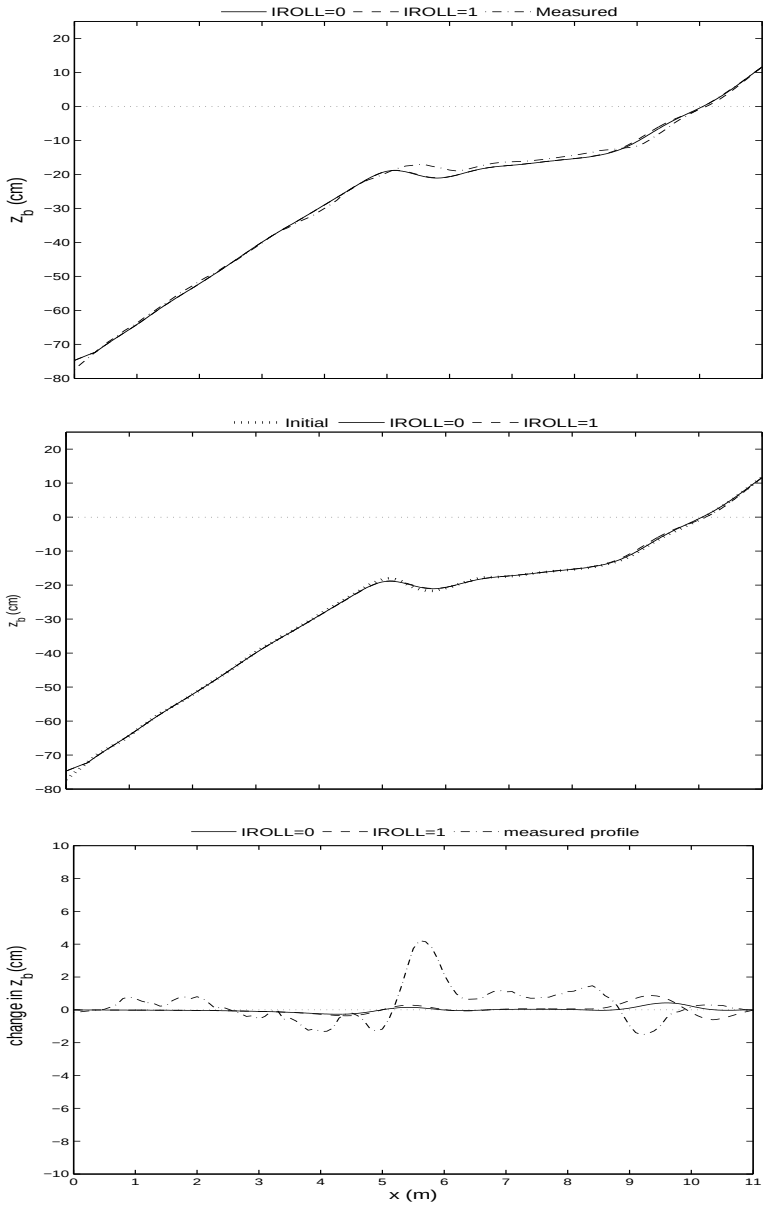

Figure B.6: Accretion Test: (top) Computed and measured profiles for $t = 1600$ s, (middle) Computed and initial profile for $t = 1600$ s, (bottom) Computed change from the initial profile for $t = 1600$ s.

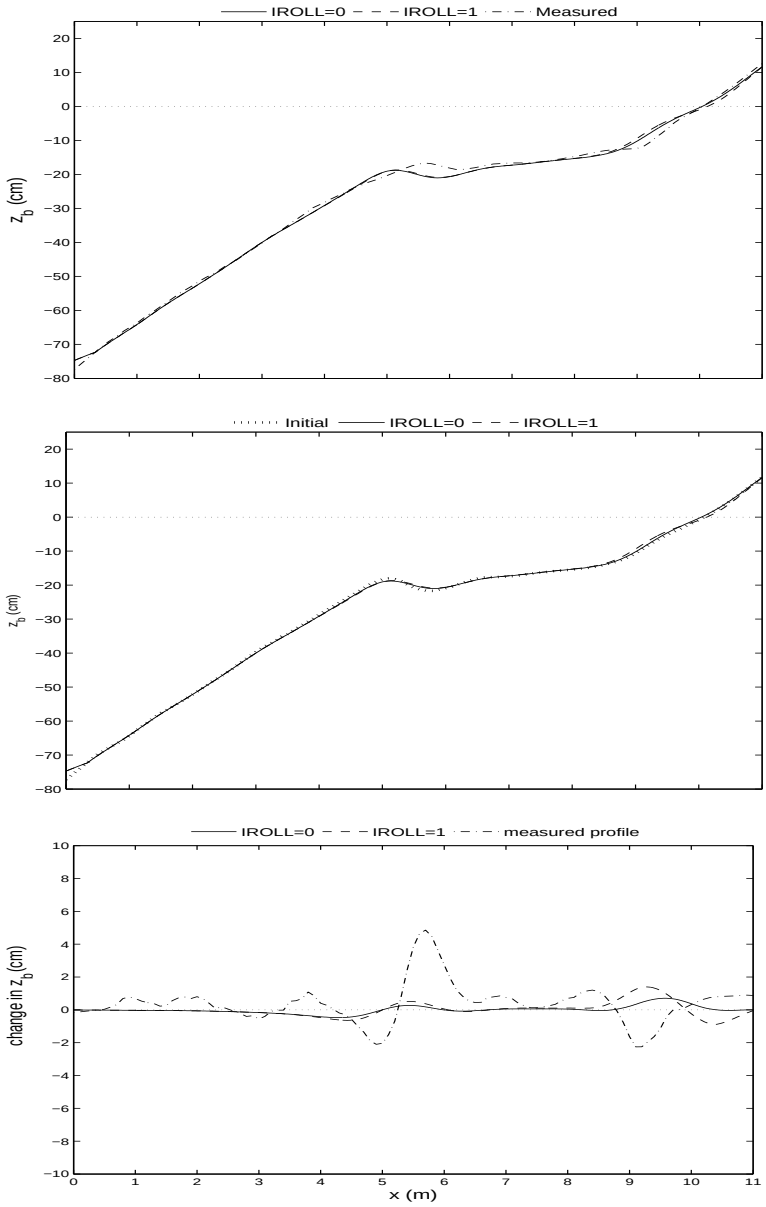

Figure B.7: Accretion test: (top) Computed and measured profiles for $t = 2800$ s, (middle) Computed and initial profile for $t = 2800$ s, (bottom) Computed change from the initial profile for $t = 2800$ s.

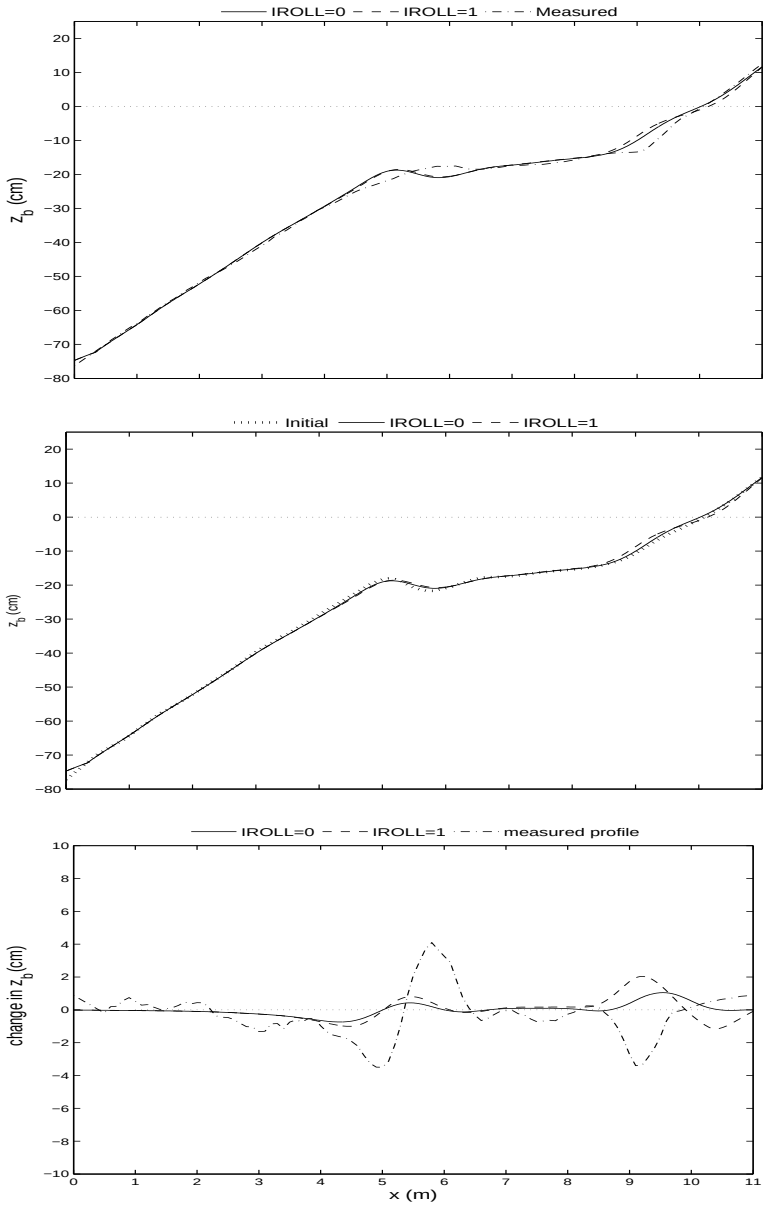

Figure B.8: Accretion test: (top) Computed and measured profiles for $t = 4400$ s, (middle) Computed and initial profile for $t = 4400$ s, (bottom) Computed change from the initial profile for $t = 4400$ s.

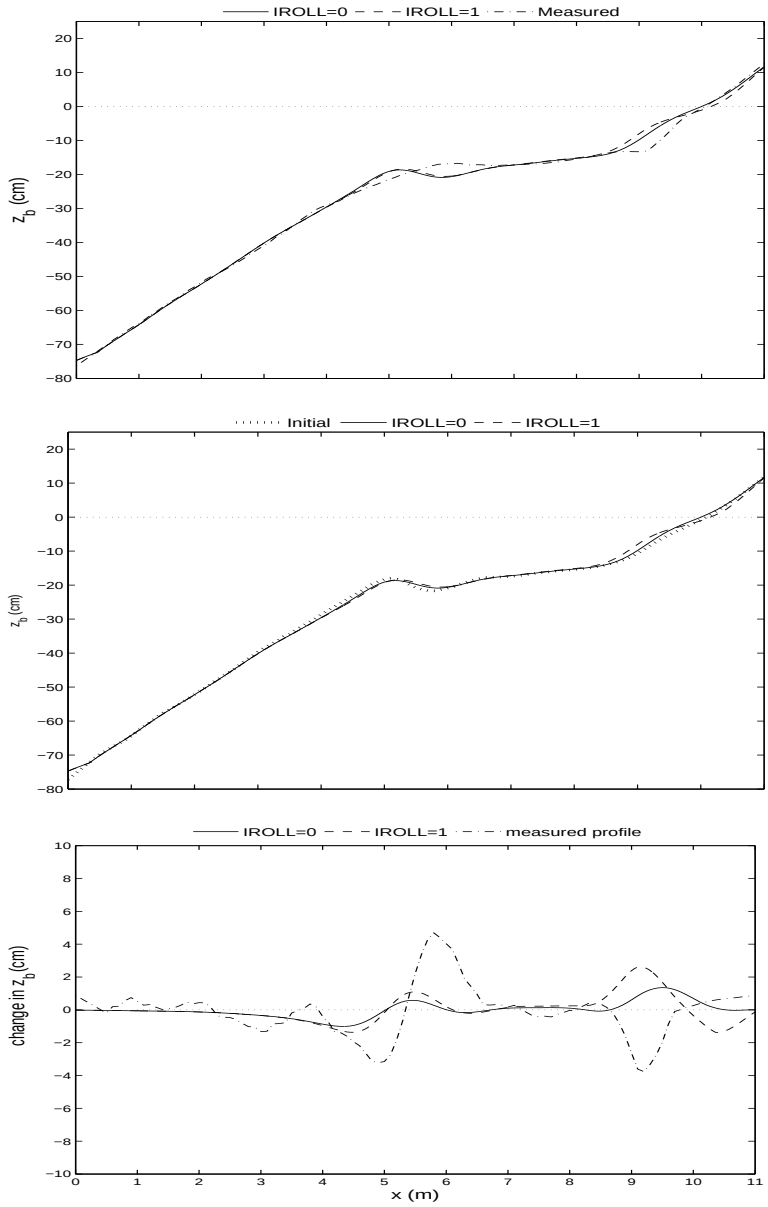

Figure B.9: Accretion Test: (top) Computed and measured profiles for $t = 6000$ s, (middle) Computed and initial profile for $t = 6000$ s, (bottom) Computed change from the initial profile for $t = 6000$ s.

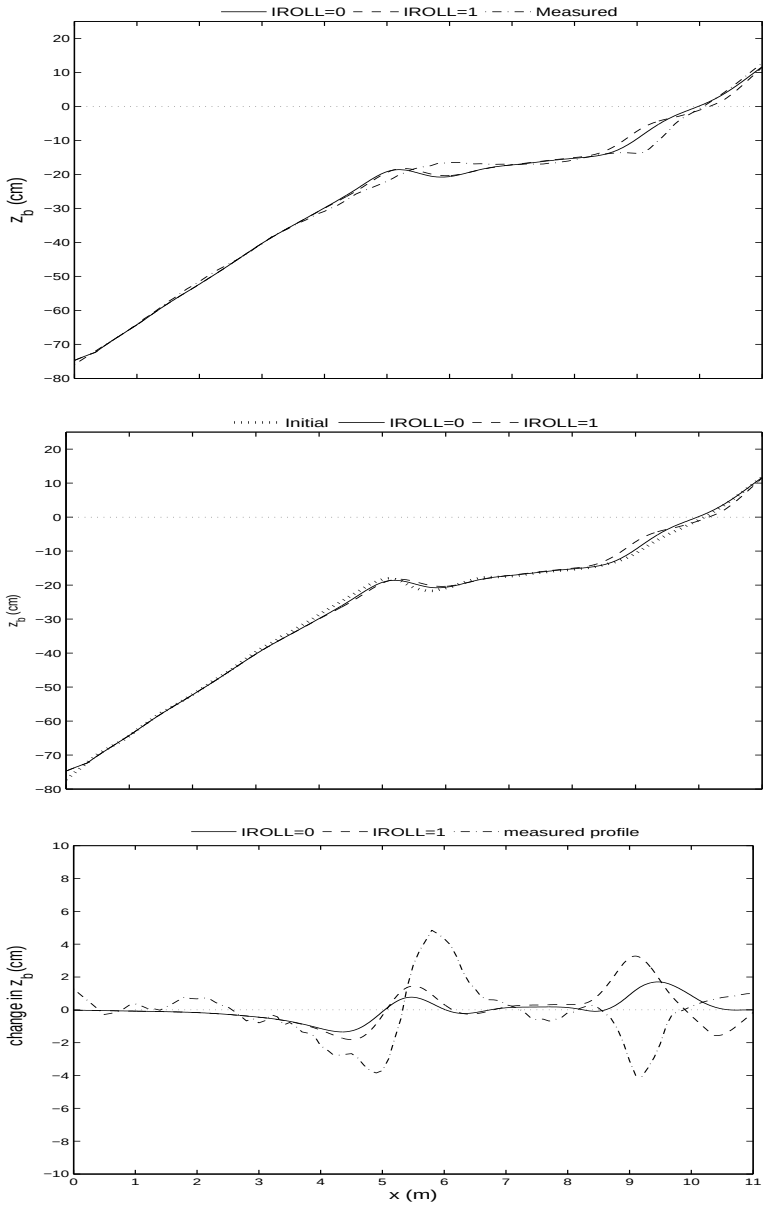

Figure B.10: Accretion test: (top) Computed and measured profiles for $t = 8000$ s, (middle) Computed and initial profile for $t = 8000$ s, (bottom) Computed change from the initial profile for $t = 8000$ s.

Appendix C

TEST 1A

C.1 Free surface

Table C.1: Test 1a: Hourly free surface measurements during 12 hours.

test	**x(m)**	**d (cm)**	$\overline{\eta}$ **(m)**	σ_η **(m)**
1a.1	0	412	-0.010	0.194
	35	244	-0.014	0.195
	NaN	NaN	NaN	NaN
1a.2	0	412	-0.011	0.224
	70	190	-0.015	0.220
	NaN	NaN	NaN	NaN
1a.3	0	412	-0.012	0.219
	20	312	-0.012	0.218
	89	165	0.005	0.184
1a.4	0	411	-0.012	0.231
	20	314	-0.014	0.229
	104	142	-0.018	0.187
1a.5	0	410	-0.011	0.230
	20	313	-0.013	0.229
	112	123	-0.017	0.178
1a.6	0	409	-0.011	0.230
	20	313	-0.013	0.228
	119	98	-0.015	0.169

test	**x(m)**	**d (cm)**	$\overline{\eta}$ **(m)**	σ_η **(m)**
1a.7	0	406	-0.015	0.230
	20	313	-0.017	0.228
	126	89	-0.003	0.131
1a.8	0	406	-0.012	0.230
	20	312	-0.014	0.230
	134	78	0.015	0.115
1a.9	0	406	-0.011	0.230
	20	312	-0.013	0.230
	130	87	0.024	0.154
1a.10	0	406	-0.010	0.226
	20	312	-0.011	0.226
	115	111	0.010	0.171
1a.11	0	406	-0.010	0.230
	20	312	-0.012	0.230
	76	180	0.015	0.205
1a.12	NaN	NaN	NaN	NaN
	NaN	NaN	NaN	NaN
	NaN	NaN	NaN	NaN

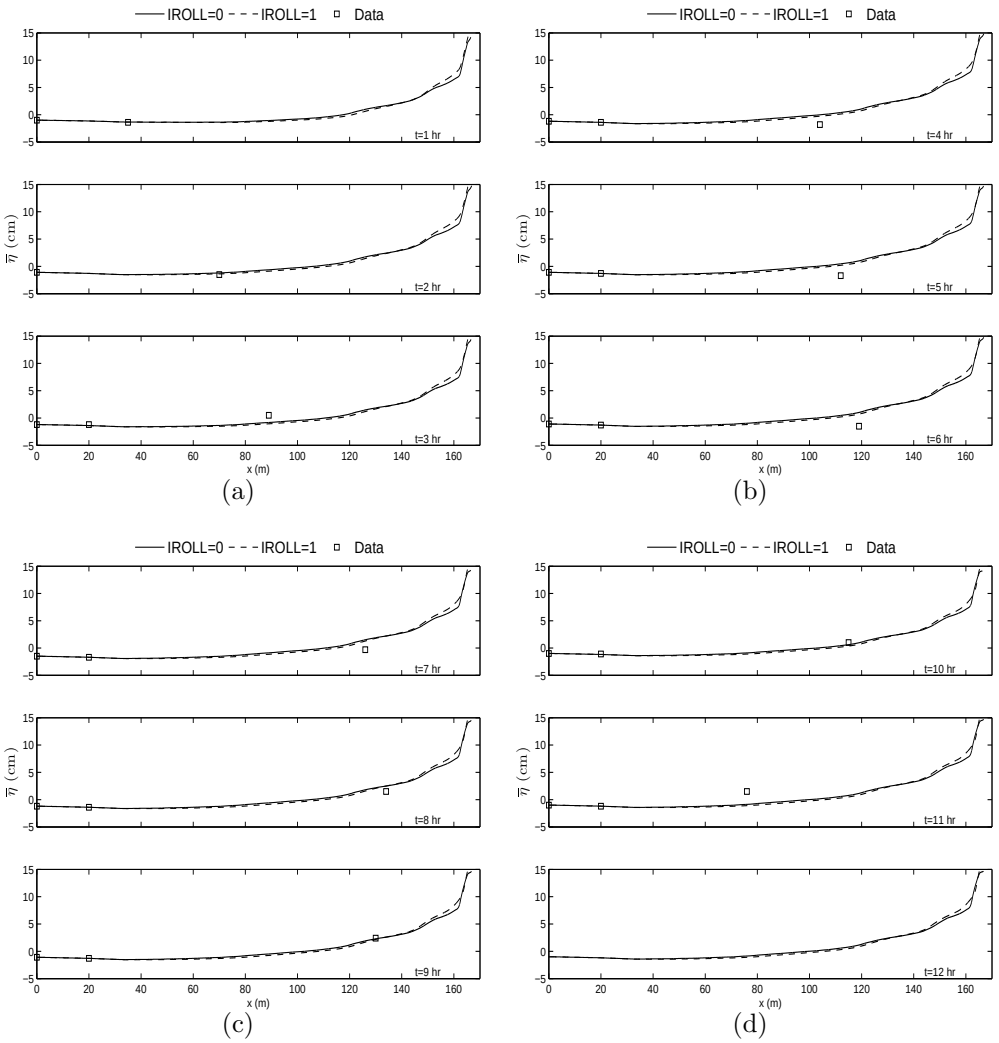

Figure C.1: Test 1a: Individual measured and predicted mean of free surface elevation, η, for (a) t=1 to 3 hr, (b) t=4 to 6 hr, (c) t=7 to 9 hr, and (d) t=10 to 12 hr.

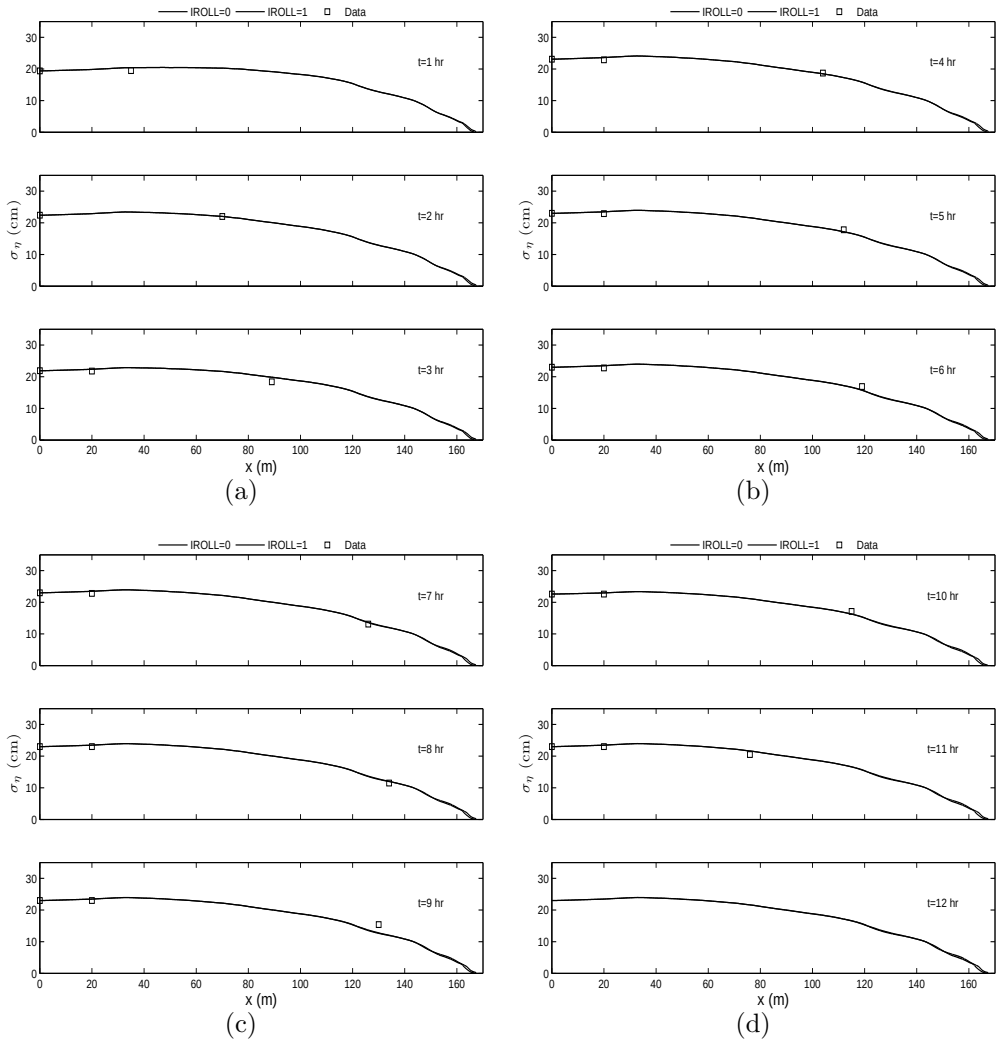

Figure C.2: Test 1a: Individual measured and predicted standard deviation of free surface elevation, η, for (a) t=1 to 3 hr, (b) t=4 to 6 hr, (c) t=7 to 9 hr, and (d) t=10 to 12 hr.

C.2 Velocity

Table C.2: Test1a: Hourly horizontal velocity measurements during 12 hours.

test	**x** (m)	**z** (cm)	$\overline{U}$ (cm/s)	σ_U (cm/s)	$\overline{U_0}$ (cm/s)	**average** σ_U (cm/s)
1a.1	45	10	-3.6	29.7	-3.31	30.3
		20	-4.5	29.9		
		40	-4.2	30.4		
		70	-4.0	31.2		
		110	NaN	NaN		
1a.2	80	10	-5.4	39.0	-6.02	40.96
		20	-7.0	39.6		
		40	-6.4	40.1		
		70	-5.2	41.3		
		110	-6.1	44.8		
1a.3	95	10	-6.5	37.8	-5.90	39.86
		20	-8.1	38.2		
		40	-7.4	39.2		
		70	-6.7	40.3		
		110	-5.7	43.8		
1a.4	110	10	-10.7	42.3	-9.18	45.26
		20	-11.5	42.9		
		40	-11.4	43.7		
		70	-10.6	45.4		
		110	0.0	52.0		

test	**x** (m)	**z** (cm)	$\overline{U}$ (cm/s)	σ_U (cm/s)	$\overline{U_0}$ (cm/s)	**average** σ_U (cm/s)
1a.5	118	10	-15.7	45.1	-11.16	46.35
		20	-16.1	45.6		
		40	-14.0	46.1		
		70	-9.0	48.6		
		110	NaN	NaN		
1a.6	125	10	-21.8	40.5	-15.21	42.05
		20	-21.1	40.8		
		40	-16.7	41.1		
		70	-3.4	45.8		
		110	NaN	NaN		
1a.7	132	10	-14.7	31.0	-10.38	35.73
		20	-14.0	32.2		
		40	-9.1	34.5		
		70	5.3	45.2		
		110	NaN	NaN		
1a.8	140	10	-11.3	35.7	-8.33	37.33
		20	-11.0	37.1		
		40	-6.8	39.2		
		70	NaN	NaN		
		110	NaN	NaN		
1a.9	136	10	-10.5	32.8	-7.68	38.35
		20	-9.9	34.3		
		40	-6.0	36.3		
		70	9.3	50.0		
		110	NaN	NaN		

test	**x** (m)	**z** (cm)	$\overline{U}$ (cm/s)	σ_U (cm/s)	$\overline{U_0}$ (cm/s)	**average** σ_U (cm/s)
1a.10	121	10	-19.3	44.4	-13.52	46.85
		20	-18.8	44.8		
		40	-14.2	45.7		
		770	-1.2	52.5		
		110	NaN	NaN		
1a.11	82	10	-4.8	40.0	-4.73	41.68
		20	-6.4	40.4		
		40	-6.5	40.8		
		70	-5.6	42.0		
		110	-5.3	45.2		
1a.12	NaN	10	NaN	NaN	NaN	NaN
		20	NaN	NaN		
		40	NaN	NaN		
		70	NaN	NaN		
		110	NaN	NaN		

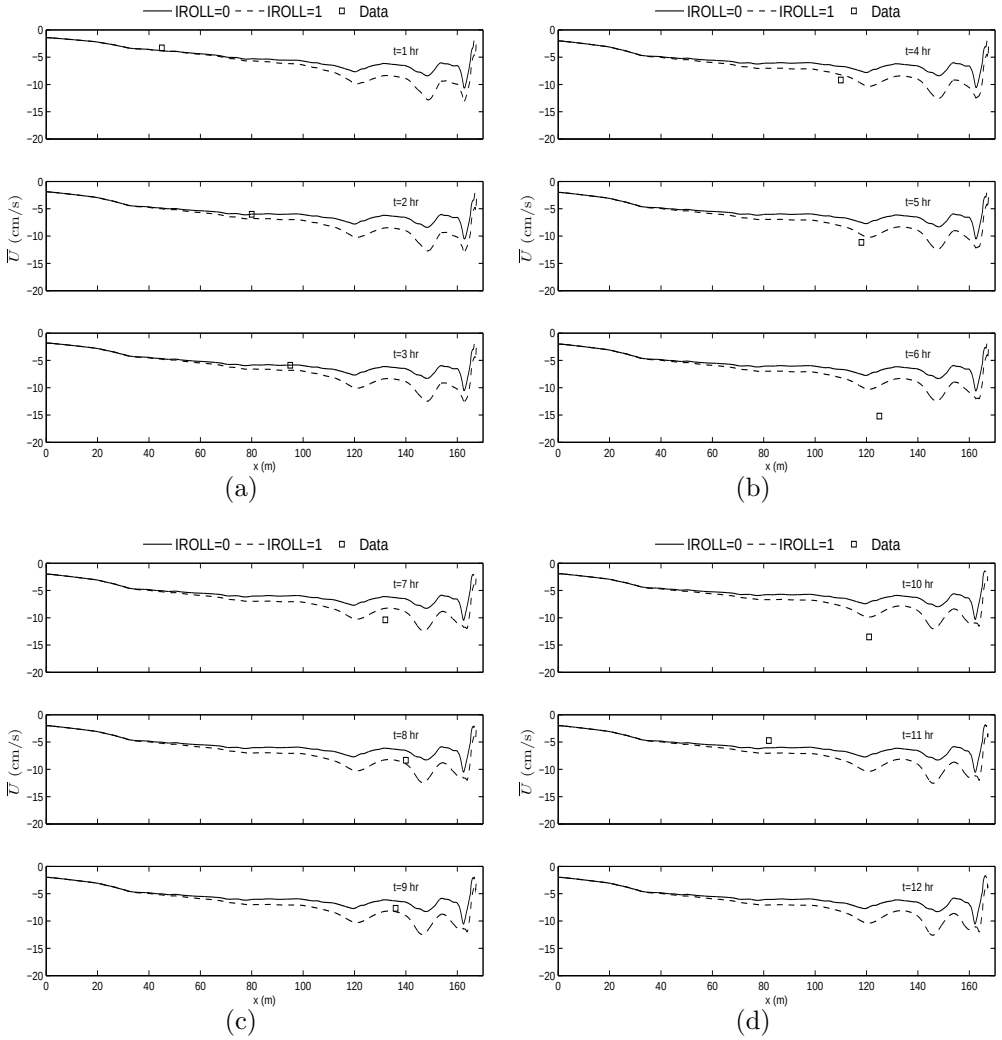

Figure C.3: Test 1a: Individual measured and predicted mean of the horizontal fluid velocity, U, for (a) t=1 to 3 hr, (b) t=4 to 6 hr, (c) t=7 to 9 hr, and (d) 10 to 12 hr.

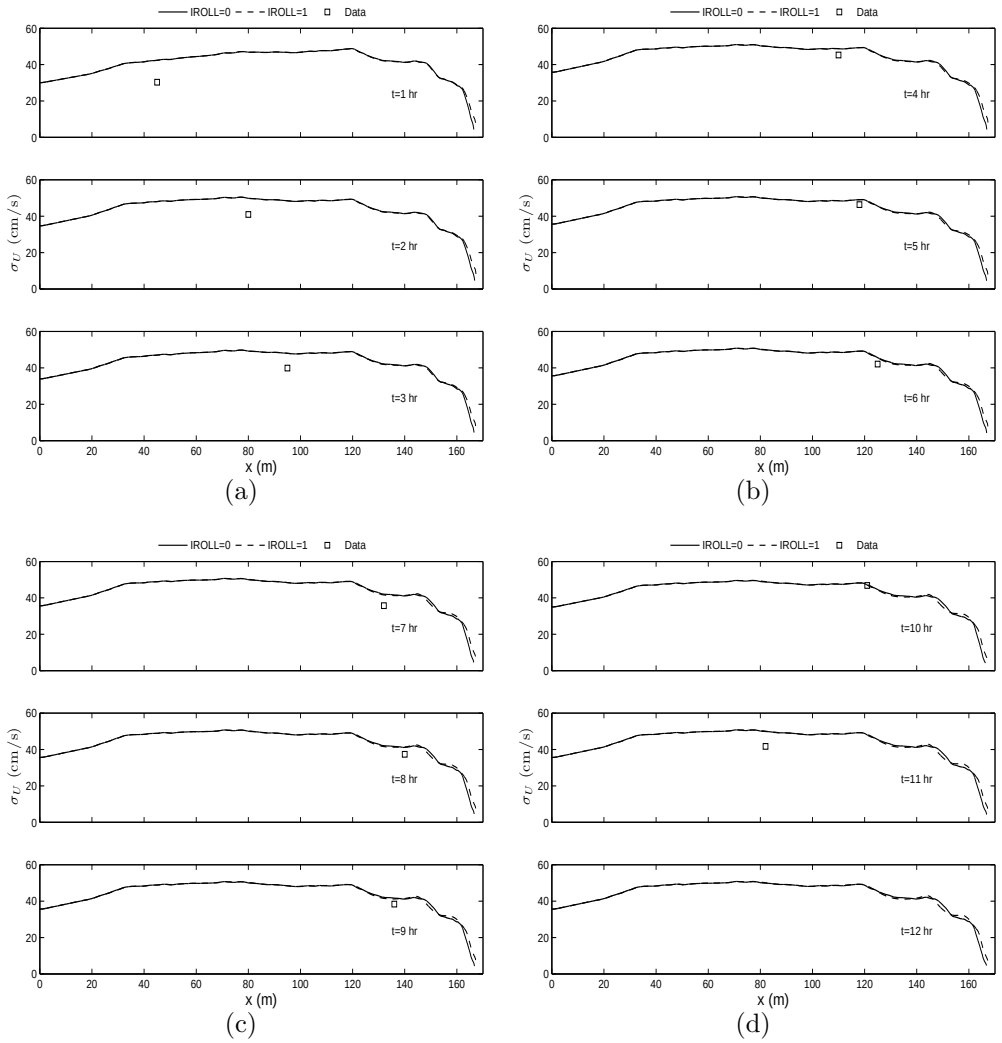

Figure C.4: Test 1a: Individual measured and predicted standard deviation of horizontal fluid velocity, U, for (a) t=1 to 3 hr, (b) t=4 to 6 hr, (c) t=7 to 9 hr, and (d) 10 to 12 hr.

C.3 Concentration

Table C.3: Test 1a: Hourly concentration measurements during 12 hours

test	**x(m)**	**z (cm)**	$\overline{C}$
1a.1	45	5.0	0.0000336
		7.5	0.0000215
		10.0	0.0000083
		13.0	0.0000075
		18.0	0.0000125
		25.5	0.0000049
		40.0	0.0000019
		65.0	NaN
		105.0	NaN
		155.0	NaN
1a.2	80	5.0	0.0000215
		7.5	0.0000223
		10.0	0.0000121
		13.0	0.0000117
		18.0	0.0000098
		25.5	0.0000060
		40.0	0.0000034
		65.0	0.0000015
		105.0	NaN
		155.0	NaN
1a.3	95	5.0	0.0000638
		7.5	0.0000362
		10.0	0.0000200
		13.0	0.0000162
		18.0	0.0000098
		25.5	0.0000102
		40.0	0.0000042
		65.0	0.0000019
		105.0	NaN
		155.0	NaN
1a.4	110	5.0	0.0001370
		7.5	0.0001030
		10.0	0.0000958
		13.0	0.0000966
		18.0	0.0000872
		25.5	0.0000785
		40.0	0.0000645
		65.0	0.0000370
		105.0	0.0000136
		155.0	NaN

test	x(m)	z (cm)	$\overline{C}$
1a.5	118	5.0	0.0002577
		7.5	0.0002751
		10.0	0.0002053
		13.0	0.0002321
		18.0	0.0001438
		25.5	0.0001328
		40.0	0.0001091
		65.0	0.0000913
		105.0	NaN
		155.0	NaN
1a.6	125	5.0	0.0002260
		7.5	0.0002060
		10.0	0.0001853
		13.0	0.0001547
		18.0	0.0001343
		25.5	0.0001075
		40.0	0.0001042
		65.0	0.0000751
		105.0	NaN
		155.0	NaN
1a.7	132	5.0	0.0002408
		7.5	0.0001713
		10.0	0.0001204
		13.0	0.0001181
		18.0	0.0001038
		25.5	0.0000891
		40.0	0.0000570
		65.0	0.0000404
		105.0	NaN
		155.0	NaN

test	x(m)	z (cm)	$\overline{C}$
1a.8	140	5.0	NaN
		7.5	NaN
		10.0	NaN
		13.0	NaN
		18.0	NaN
		25.5	NaN
		40.0	NaN
		65.0	NaN
		105.0	NaN
		155.0	NaN
1a.9	136	5.0	0.0001374
		7.5	0.0001094
		10.0	0.0000989
		13.0	0.0000992
		18.0	0.0000774
		25.5	0.0000706
		40.0	0.0000547
		65.0	0.0000370
		105.0	NaN
		155.0	NaN
1a.10	121	5.0	0.0004294
		7.5	0.0003781
		10.0	0.0002740
		13.0	0.0002706
		18.0	0.0002494
		25.5	0.0002004
		40.0	0.0001577
		65.0	0.0000966
		105.0	NaN
		155.0	NaN

test	**x(m)**	**z (cm)**	$\overline{C}$
1a.11	82	5.0	0.0003128
		7.5	0.0001717
		10.0	0.0001030
		13.0	0.0000823
		18.0	0.0000517
		25.5	0.0000351
		40.0	0.0000166
		65.0	0.0000106
		105.0	NaN
		155.0	NaN
1a.12	NaN	5.0	NaN
		7.5	NaN
		10.0	NaN
		13.0	NaN
		18.0	NaN
		25.5	NaN
		40.0	NaN
		65.0	NaN
		105.0	NaN
		155.0	NaN

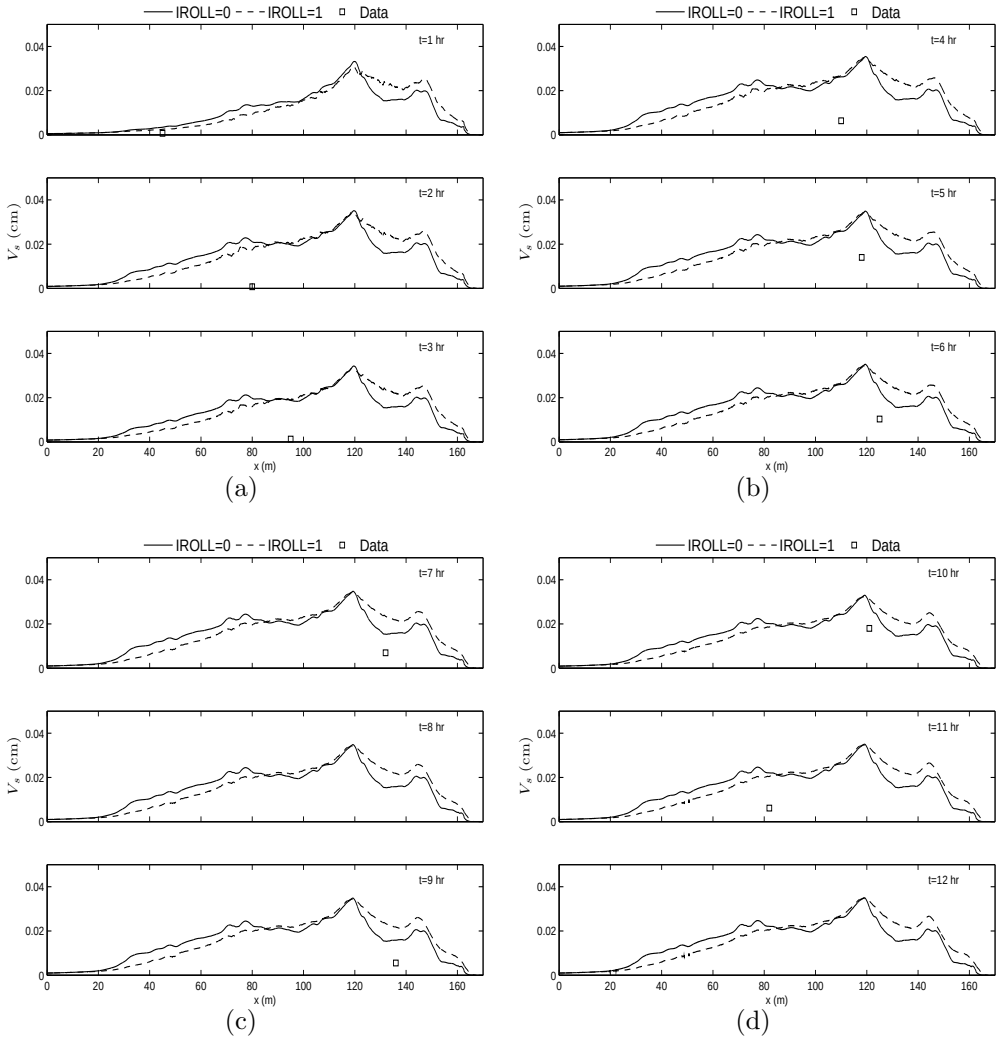

Figure C.5: Test 1a: Individual measured and predicted suspended sediment volume, V_s, per unit area for (a) t=1 to 3 hr, (b) t=4 to 6 hr, (c) t=7 to 9 hr, and (d) 10 to 12 hr.

C.4 Profile change

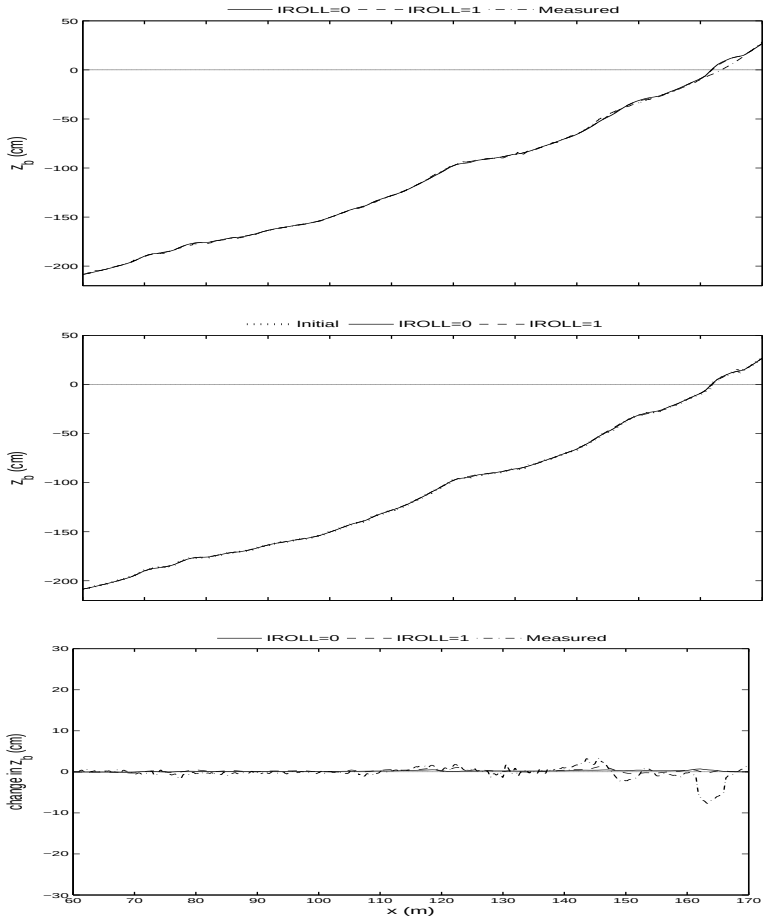

Figure C.6: Test 1a: (top) Computed and measured profiles for $t = 2$ hr, (middle) Computed and initial profile for $t = 2$ hr, (bottom) Computed change from the initial profile for $t = 2$ hr.

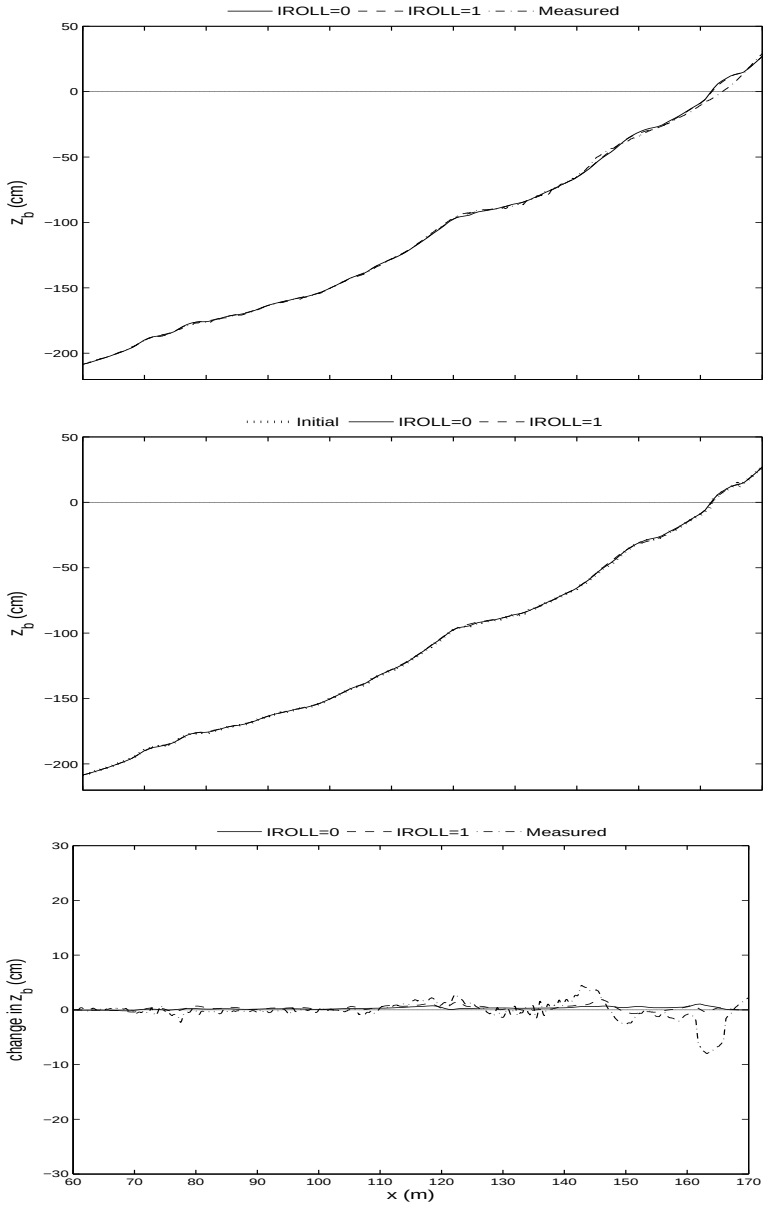

Figure C.7: Test 1a: (top) Computed and measured profiles for $t = 3$ hr, (middle) Computed and initial profile for $t = 3$ hr, (bottom) Computed change from the initial profile for $t = 3$ hr.

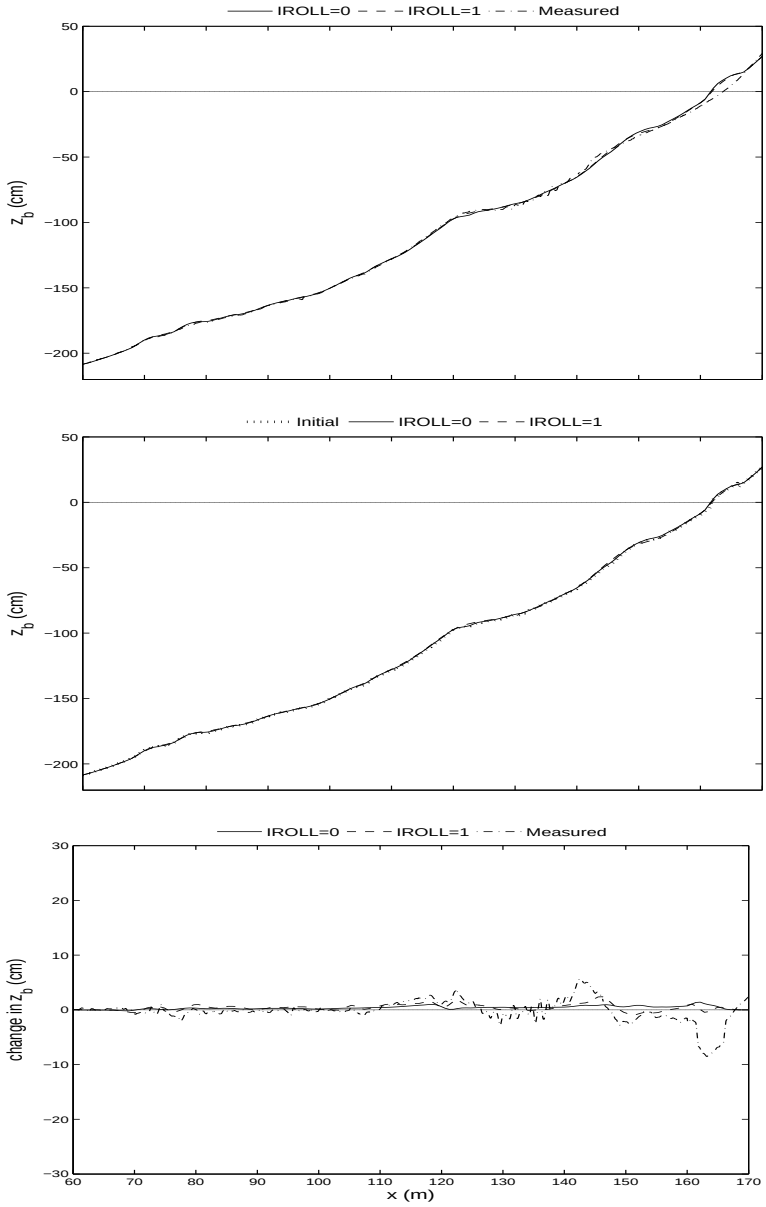

Figure C.8: Test 1a: (top) Computed and measured profiles for $t = 4$ hr, (middle) Computed and initial profile for $t = 4$ hr, (bottom) Computed change from the initial profile for $t = 4$ hr.

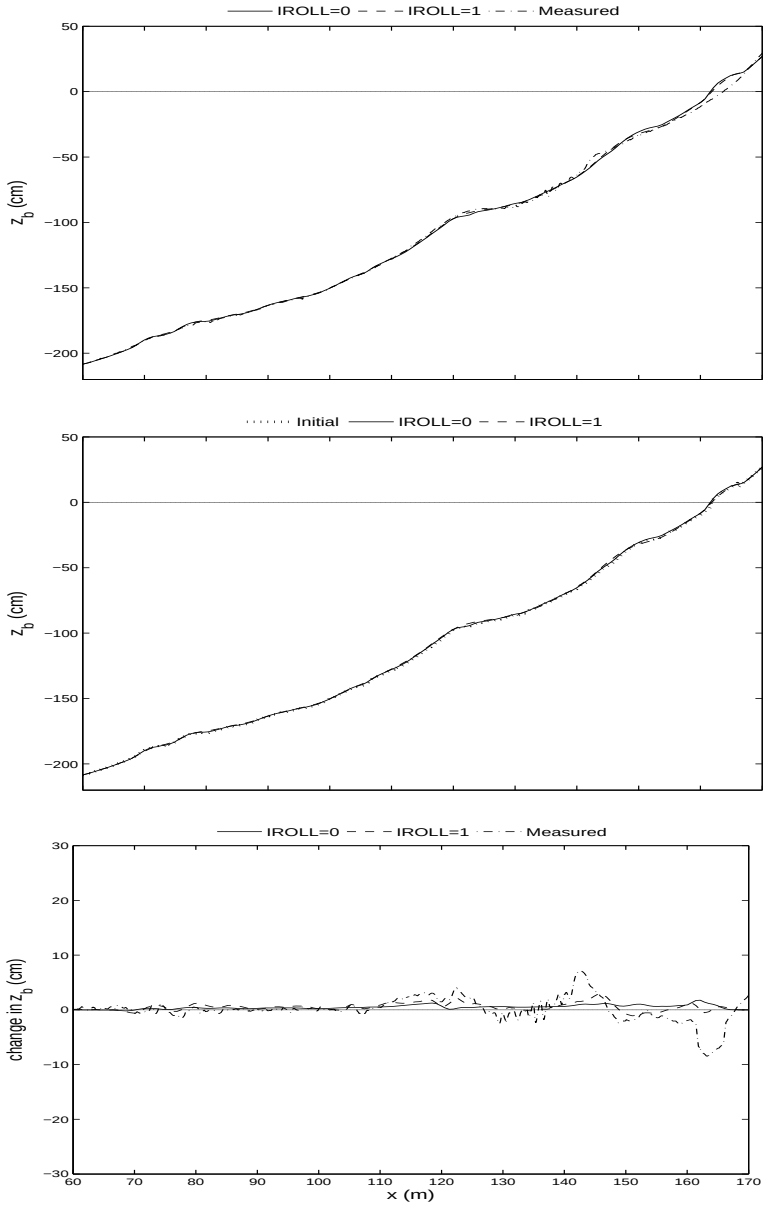

Figure C.9: Test 1a: (top) Computed and measured profiles for $t = 5$ hr, (middle) Computed and initial profile for $t = 5$ hr, (bottom) Computed change from the initial profile for $t = 5$ hr.

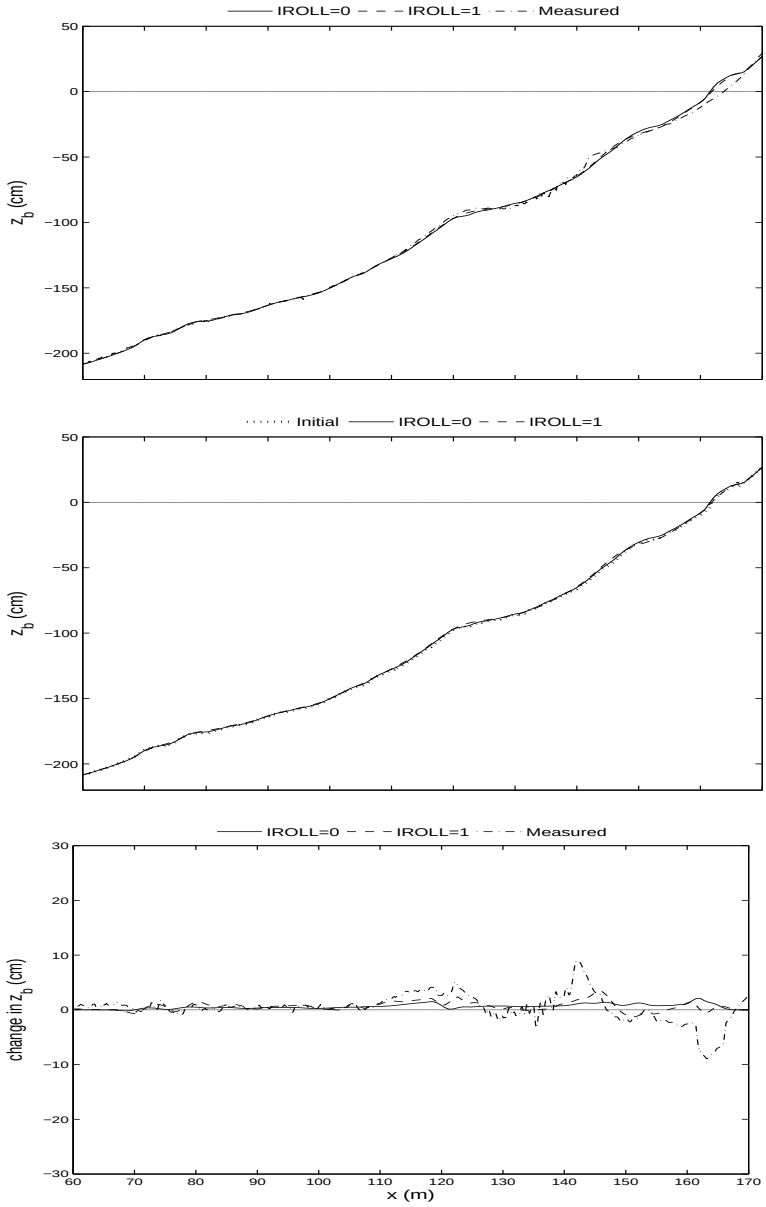

Figure C.10: Test 1a: (top) Computed and measured profiles for $t = 6$ hr, (middle) Computed and initial profile for $t = 6$ hr, (bottom) Computed change from the initial profile for $t = 6$ hr.

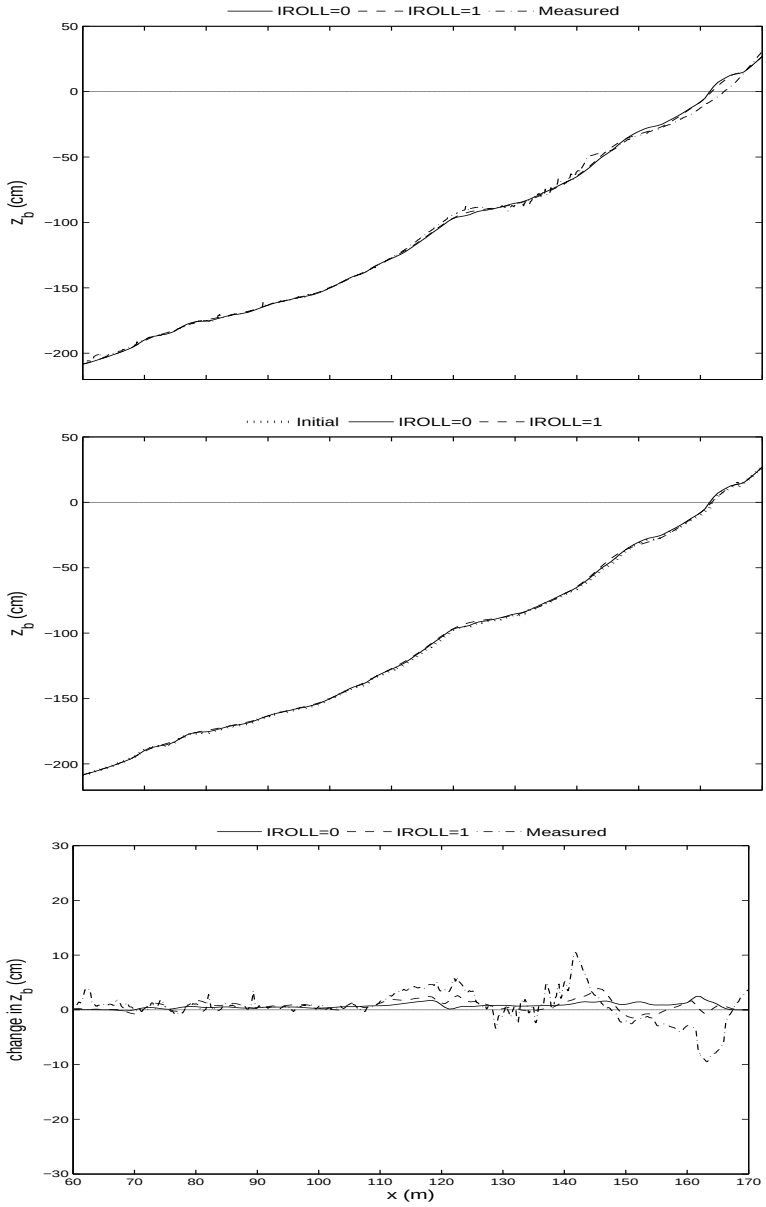

Figure C.11: Test 1a: (top) Computed and measured profiles for $t = 7$ hr, (middle) Computed and initial profile for $t = 7$ hr, (bottom) Computed change from the initial profile for $t = 7$ hr.

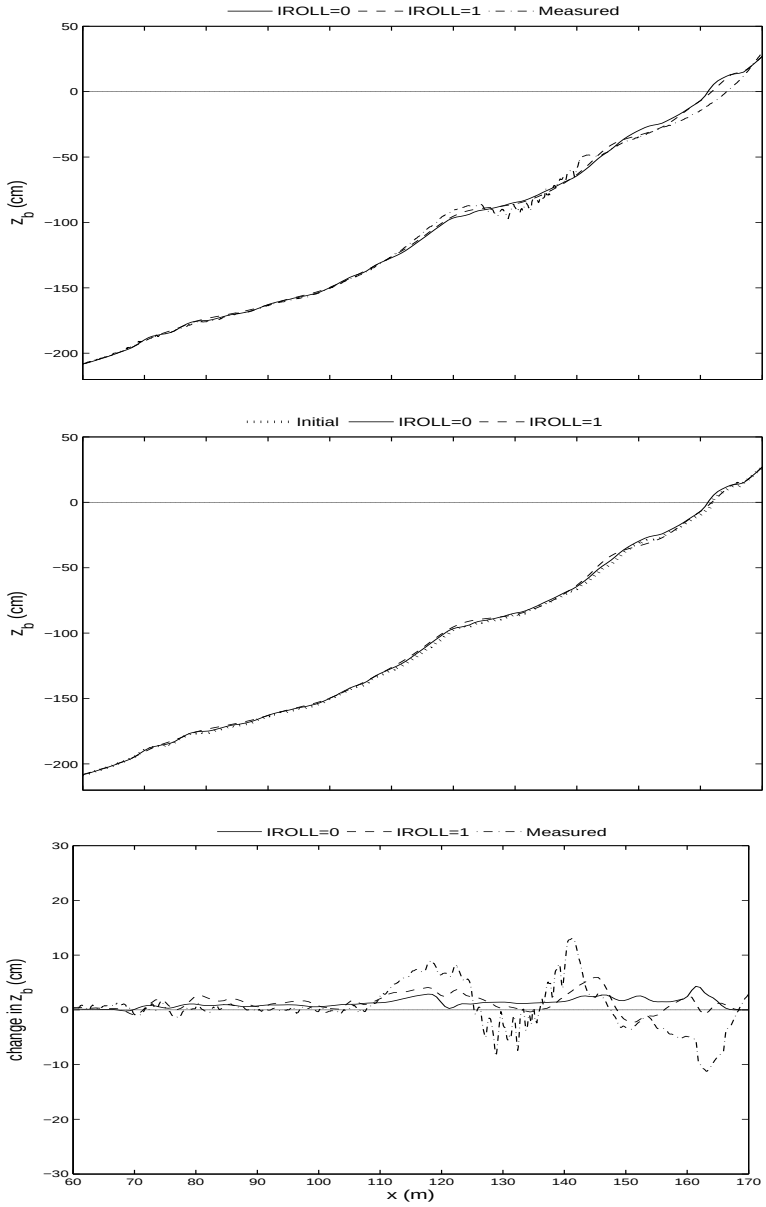

Figure C.12: Test 1a: (top) Computed and measured profiles for $t = 12$ hr, (middle) Computed and initial profile for $t = 12$ hr, (bottom) Computed change from the initial profile for $t = 12$ hr.

Appendix D

TEST 1B

D.1 Free Surface

Table D.1: Test 1b: Hourly free surface measurements during 18 hours.

test	**x (m)**	$\overline{\eta}$	σ_η
1b.1	NaN	NaN	NaN
1b.2	0.0	-0.031	0.316
1b.3	0.0	-0.023	0.316
1b.4	0.0	-0.023	0.329
1b.5	0.0	-0.027	0.328
1b.6	NaN	-0.055	0.300
1b.7	0.0	-0.056	0.336
1b.8	0.0	-0.032	0.337
1b.9	0.0	-0.036	0.337
1b.10	0.0	-0.031	0.337
1b.11	0.0	NaN	NaN
1b.12	0.0	-0.028	0.336
1b.13	0.0	-0.030	0.337
1b.14	0.0	-0.028	0.338
1b.15	0.0	-0.031	0.335
1b.16	0.0	-0.029	0.338
1b.17	0.0	-0.028	0.338
1b.18	NaN	NaN	NaN

D.2 Velocity

Table D.2: Test 1b: Hourly horizontal velocity measurements during 18 hours.

test	**x** (m)	**z** (cm)	$\overline{U}$ (cm/s)	σ_U (cm/s)	$\overline{U_0}$ (cm/s)	**average** σ_U (cm/s)
1b.1	45	10	-8.4	45.1	-7.4	45.6
		20	-9.6	45.5		
		40	-9.8	45.7		
		70	-9.6	46.7		
		110	-8.7	44.8		
1b.2	82	10	-11.2	44.7	-8.7	47.1
		20	-12.3	45.4		
		40	-12.1	46.4		
		70	-10.5	48.1		
		110	-7.8	50.9		
1b.3	95	10	-12.2	44.3	-9.8	46.6
		20	-12.8	45.1		
		40	-13.0	45.9		
		70	-12.2	47.5		
		110	-8.6	50.2		
1b.4	110	10	-15.9	45.7	-12.0	48.7
		20	-16.3	46.2		
		40	-14.6	46.9		
		70	-10.9	48.9		
		110	5.3	56.0		

test	**x**	**z**	$\overline{U}$	σ_U	$\overline{U_0}$	**average** σ_U
	(m)	(cm)	(cm/s)	(cm/s)	(cm/s)	(cm/s)
1b.5	118	10	-23.2	51.2	-17.3	54.4
		20	-22.7	51.7		
		40	-19.2	52.7		
		70	0.4	61.9		
		110	NaN	NaN		
1b.6	NaN	10	NaN	NaN	NaN	NaN
		20	NaN	NaN		
		40	NaN	NaN		
		70	NaN	NaN		
		110	NaN	NaN		
1b.7	125	10	-30.4	40.9	-19.8	42.2
		20	-28.2	40.9		
		40	-20.0	41.2		
		70	-2.5	45.8		
		110	NaN	NaN		
1b.8	132	10	-17.4	30.5	-12.25	32.9
		20	-17.2	31.7		
		40	-14.4	33.4		
		70	-5.9	36.1		
		110	NaN	NaN		
1b.9	140	10	-15.2	51.0	-11.5	52.5
		20	-14.7	51.2		
		40	-4.5	55.3		
		70	NaN	NaN		
		110	NaN	NaN		
1b.10	150	10	-13.6	43.2	-10.5	47.8
		20	-11.0	44.6		
		40	2.8	55.7		
		70	NaN	NaN		
		110	NaN	NaN		

test	**x** (m)	**z** (cm)	$\overline{U}$ (cm/s)	σ_U (cm/s)	$\overline{U_0}$ (cm/s)	**average** σ_U (cm/s)
1b.11	45	10	NaN	NaN	NaN	NaN
		20	NaN	NaN		
		40	NaN	NaN		
		70	NaN	NaN		
		110	NaN	NaN		
1b.12	82	10	-13.0	45.4	-9.6	47.6
		20	-13.8	46.2		
		40	-13.2	47.1		
		70	-11.7	48.3		
		110	-7.8	50.9		
1b.13	NaN	10	NaN	NaN	NaN	NaN
		20	NaN	NaN		
		40	NaN	NaN		
		70	NaN	NaN		
		110	NaN	NaN		
1b.14	NaN	10	NaN	NaN	NaN	NaN
		20	NaN	NaN		
		40	NaN	NaN		
		70	NaN	NaN		
		110	NaN	NaN		
1b.15	95	10	-12.9	44.2	-9.3	44.1
		20	-13.8	45.2		
		40	-13.6	46.1		
		70	-8.7	34.6		
		110	-7.7	50.6		
1b.16	110	10	-17.2	48.3	-12.8	49.9
		20	-17.5	49.4		
		40	-16.8	50.6		
		70	-9.7	39.5		
		110	6.4	61.8		

test	**x** (m)	**z** (cm)	$\overline{U}$ (cm/s)	σ_U (cm/s)	$\overline{U_0}$ (cm/s)	**average** σ_U (cm/s)
1b.17	118	10	-30.3	49.2	-21.2	48.0
		20	-29.9	48.9		
		40	-22.8	49.3		
		70	-4.0	44.5		
		110	NaN	NaN		
1b.18	NaN	10	NaN	NaN	NaN	NaN
		20	NaN	NaN		
		40	NaN	NaN		
		70	NaN	NaN		
		110	NaN	NaN		

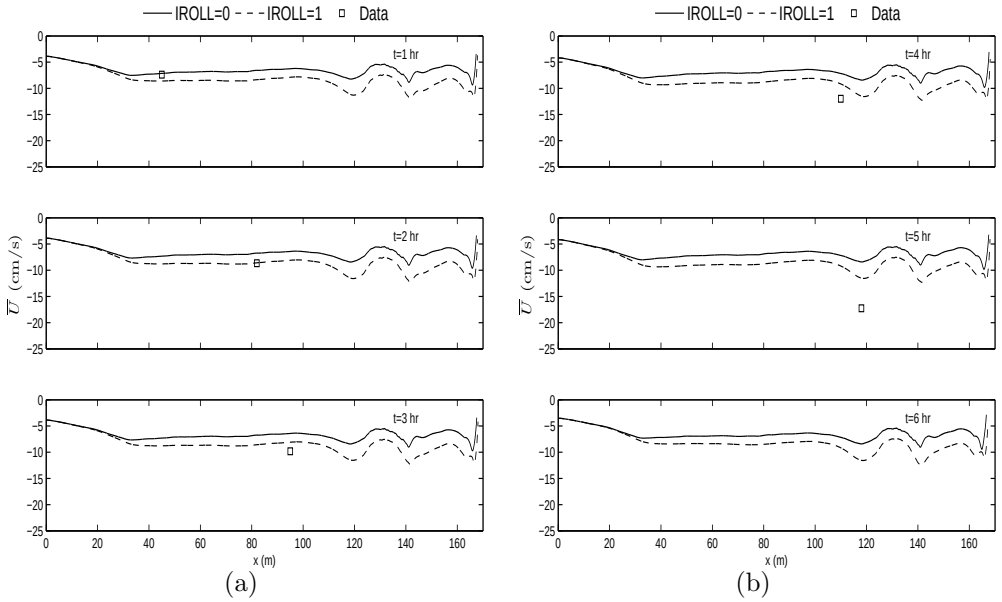
IROLL=0 - - - IROLL=1 Data
t=1 hr
t=2 hr
t=3 hr
t=4 hr
t=5 hr
t=6 hr
$\overline{U}$ (cm/s)
x (m)

(a) (b)

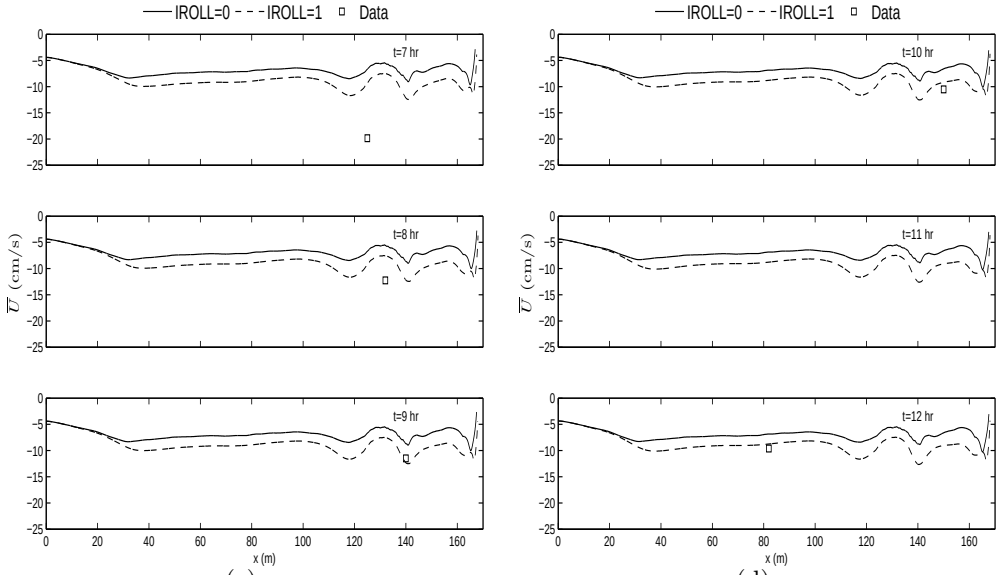
IROLL=0 - - - IROLL=1 Data
t=7 hr
t=8 hr
t=9 hr
t=10 hr
t=11 hr
t=12 hr
$\overline{U}$ (cm/s)
x (m)

(c) (d)

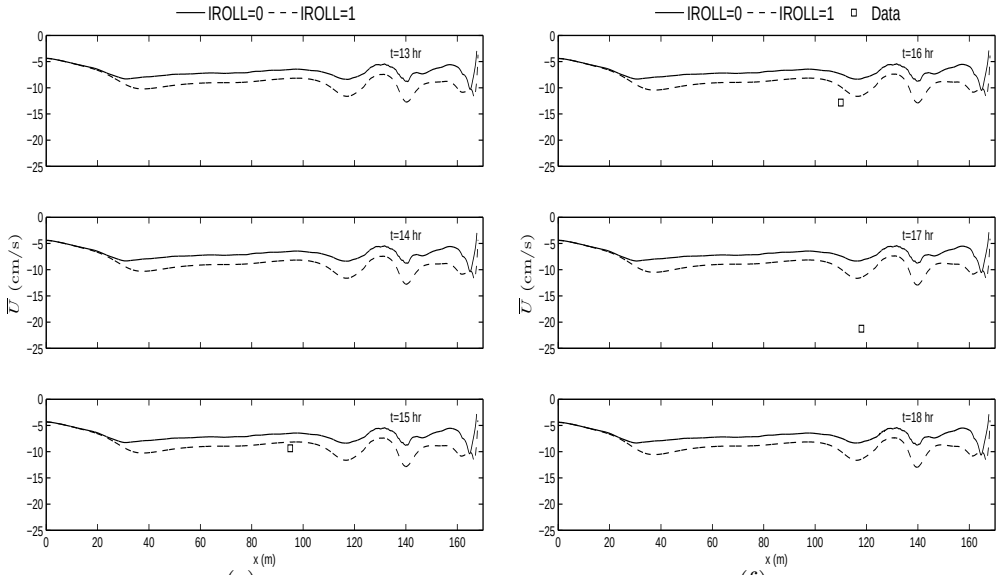

Figure D.1: Test 1b: Individual measured and predicted mean of the horizontal velocity, U, for (a) t=1 to 3 hr, (b) t=4 to 6 hr, (c) t=7 to 9 hr, (d) t=10 to 12 hr, (e) t=13 to 15 hr, and (f)16 to 18 hr.

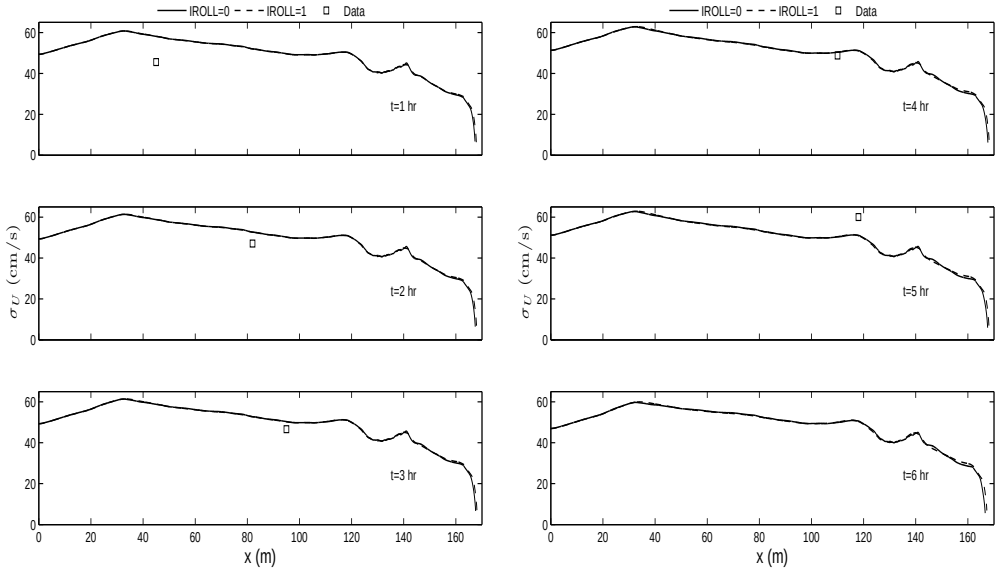
IROLL=0
IROLL=1
Data
t=1 hr
t=2 hr
t=3 hr
t=4 hr
t=5 hr
t=6 hr
σ_U (cm/s)
x (m)

(a) (b)

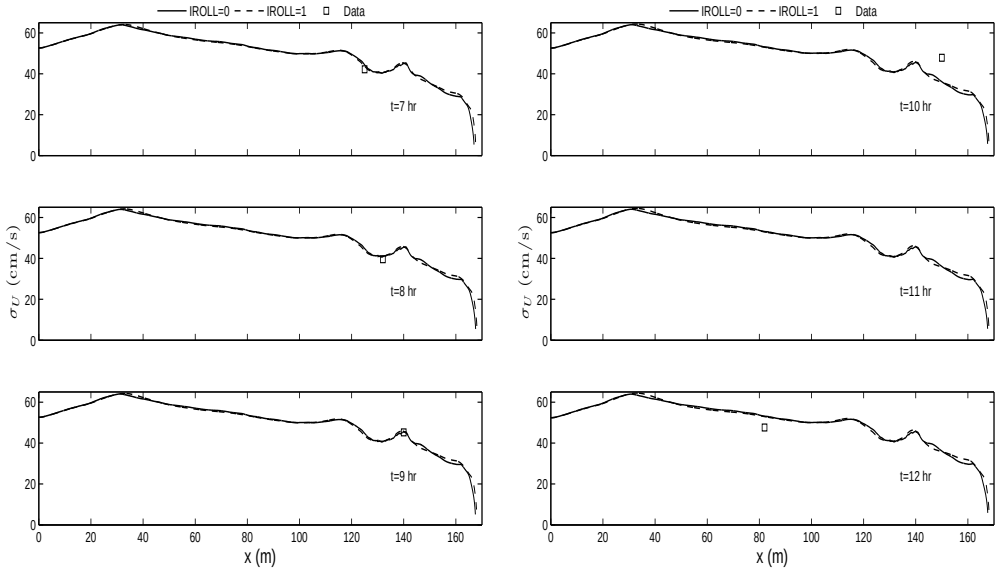
IROLL=0
IROLL=1
Data
t=7 hr
t=8 hr
t=9 hr
t=10 hr
t=11 hr
t=12 hr
σ_U (cm/s)
x (m)

(c) (d)

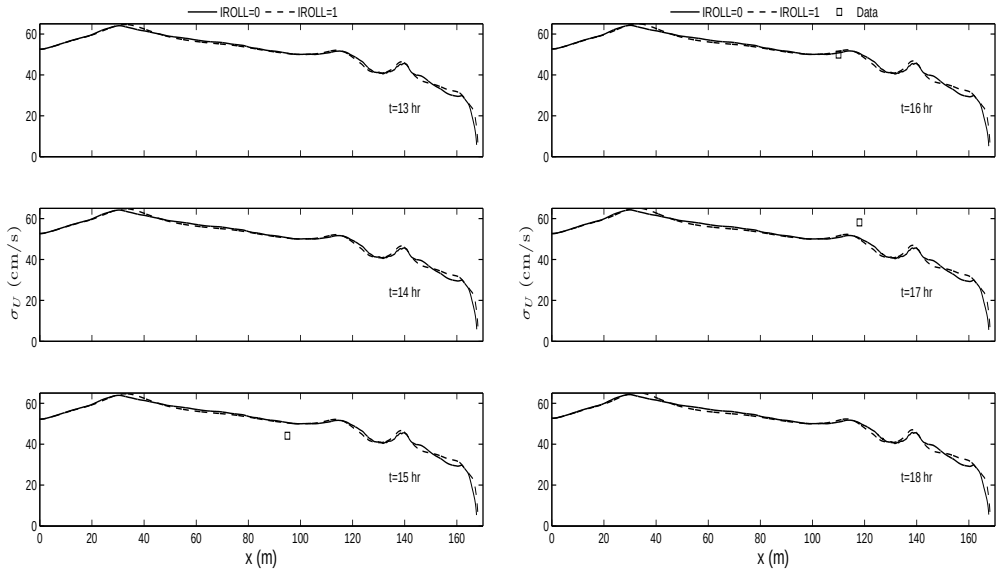

Figure D.2: Test 1b: Individual measured and predicted standard deviation of the horizontal velocity, U, for (a) t=1 to 3 hr, (b) t=4 to 6 hr, (c) t=7 to 9 hr,(d) 10 to 12 hr, (e) t=13 to 15 hr, and (f)16 to 18 hr.

D.3 Concentration

Table D.3: Test 1b: Hourly concentration measurements during 18 hours.

test	**x (m)**	**z (cm)**	$\overline{C}$
1b.1	45	5	0.000151
		8	0.000155
		10	0.000115
		13	0.000068
		18	0.000084
		26	0.000086
		40	0.000063
		65	0.000035
		105	0.000052
		155	0.000049
1b.2	82	5	0.000179
		8	0.000155
		10	0.000069
		13	0.000041
		18	0.000052
		26	0.000057
		40	0.000055
		65	0.000034
		105	0.000030
		155	0.000026
1b.3	95	5	0.000206
		8	0.000120
		10	0.000123
		13	0.000094
		18	0.000077
		26	0.000077
		40	0.000055
		65	0.000048
		105	0.000036
		155	NaN
1b.4	110	5	0.000206
		8	0.000172
		10	0.000137
		13	0.000137
		18	0.000122
		26	0.000116
		40	0.000101
		65	0.000082
		105	0.000055
		155	NaN

test	x (m)	z (cm)	$\overline{C}$
1b.5	118	5	NaN
		8	NaN
		10	NaN
		13	NaN
		18	NaN
		26	NaN
		40	NaN
		65	NaN
		105	NaN
		155	NaN
1b.6	NaN	5	NaN
		8	NaN
		10	NaN
		13	NaN
		18	NaN
		26	NaN
		40	NaN
		65	NaN
		105	NaN
		155	NaN
1b.7	125	5	0.000653
		8	0.000515
		10	0.000397
		13	0.000335
		18	0.000262
		26	0.000188
		40	0.000146
		65	0.000119
		105	NaN
		155	NaN

test	x (m)	z (cm)	$\overline{C}$
1b.8	132	5	0.000241
		8	0.000189
		10	0.000151
		13	0.000146
		18	0.000115
		26	0.000089
		40	0.000077
		65	0.000054
		105	NaN
		155	NaN
1b.9	140	5	NaN
		8	NaN
		10	NaN
		13	NaN
		18	NaN
		26	NaN
		40	NaN
		65	NaN
		105	NaN
		155	NaN
1b.10	150	5	0.000326
		8	0.000260
		10	0.000232
		13	0.000230
		18	0.000188
		26	0.000151
		40	0.000094
		65	NaN
		105	NaN
		155	NaN

test	**x (m)**	**z (cm)**	$\overline{C}$
1b.11	45	5	NaN
		8	NaN
		10	NaN
		13	NaN
		18	NaN
		26	NaN
		40	NaN
		65	NaN
		105	NaN
		155	NaN
1b.12	82	5	0.000086
		8	0.000069
		10	0.000048
		13	0.000060
		18	0.000054
		26	0.000048
		40	0.000027
		65	0.000027
		105	0.000028
		155	NaN
1b.13	NaN	5	NaN
		8	NaN
		10	NaN
		13	NaN
		18	NaN
		26	NaN
		40	NaN
		65	NaN
		105	NaN
		155	NaN

test	**x (m)**	**z (cm)**	$\overline{C}$
1b.14	NaN	5	NaN
		8	NaN
		10	NaN
		13	NaN
		18	NaN
		26	NaN
		40	NaN
		65	NaN
		105	NaN
		155	NaN
1b.15	95	5	0.000120
		8	0.000086
		10	0.000041
		13	0.000038
		18	0.000035
		26	0.000029
		40	0.000029
		65	0.000019
		105	0.000017
		155	NaN
1b.16	110	5	0.000292
		8	0.000292
		10	0.000226
		13	0.000206
		18	0.000214
		26	0.000208
		40	0.000173
		65	0.000120
		105	0.000077
		155	NaN

test	**x (m)**	**z (cm)**	$\overline{C}$
1b.17	118	5	0.001162
		8	0.001100
		10	0.000962
		13	0.000726
		18	0.000653
		26	0.000594
		40	0.000491
		65	0.000379
		105	NaN
		155	NaN
1b.18	NaN	5	NaN
		8	NaN
		10	NaN
		13	NaN
		18	NaN
		26	NaN
		40	NaN
		65	NaN
		105	NaN
		155	NaN

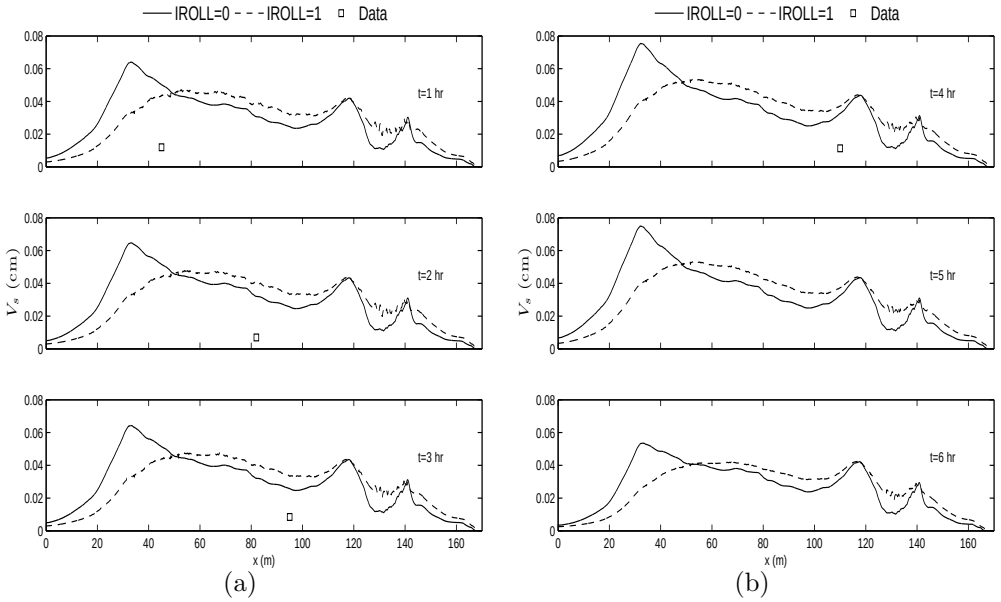
IROLL=0 - - - IROLL=1 Data
t=1 hr
t=2 hr
t=3 hr
t=4 hr
t=5 hr
t=6 hr
V_s (cm)
x (m)

(a) (b)

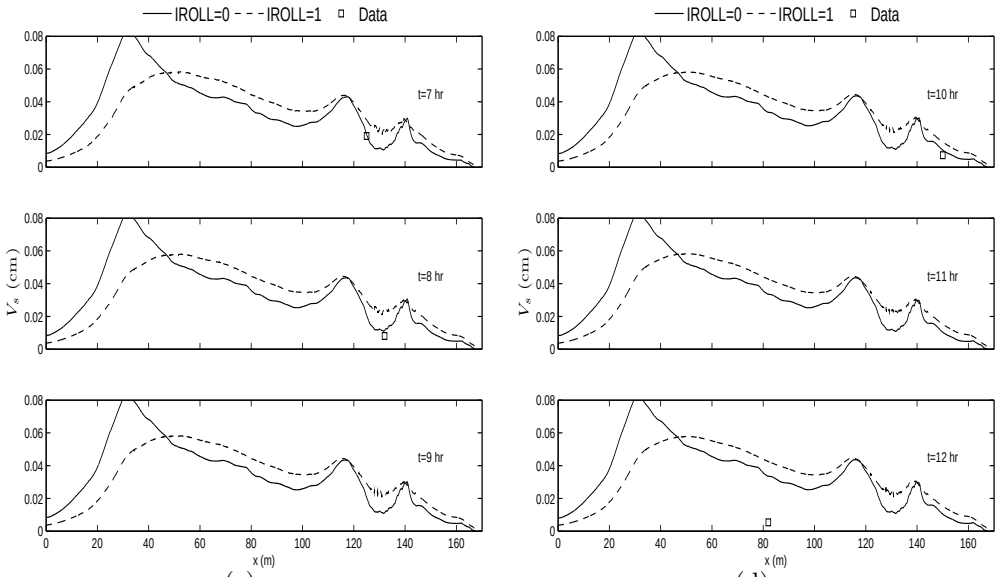
IROLL=0 - - - IROLL=1 Data
t=7 hr
t=8 hr
t=9 hr
t=10 hr
t=11 hr
t=12 hr
V_s (cm)
x (m)

(c) (d)

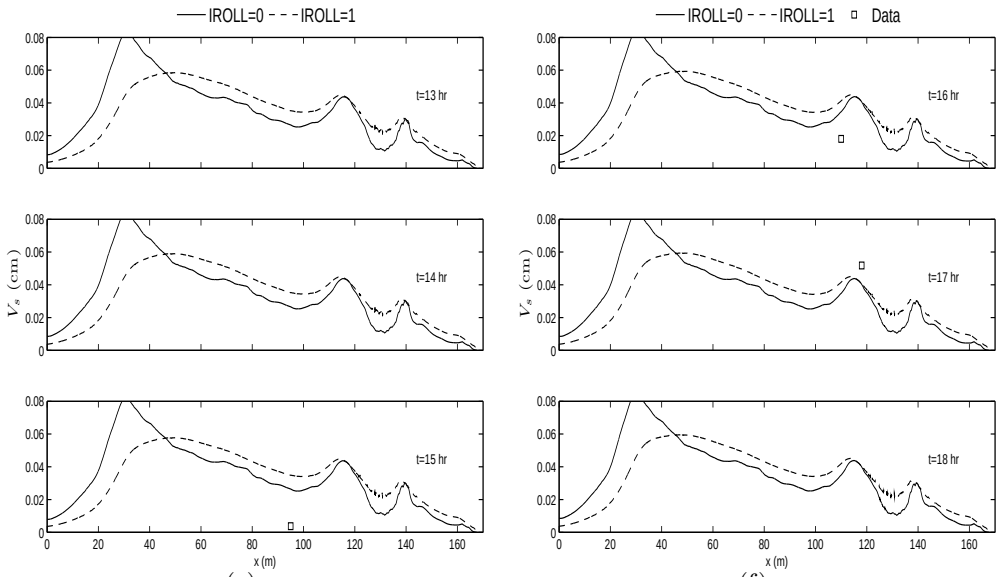

Figure D.3: Test 1b: Individual measured and predicted suspended sediment volume, V_s, per unit area for (a) t=1 to 3 hr, (b) t=4 to 6 hr, (c) t=7 to 9 hr, (d) t=10 to 12 hr, (e) t=13 to 15 hr, and (f)16 to 18 hr.

D.4 Profile change

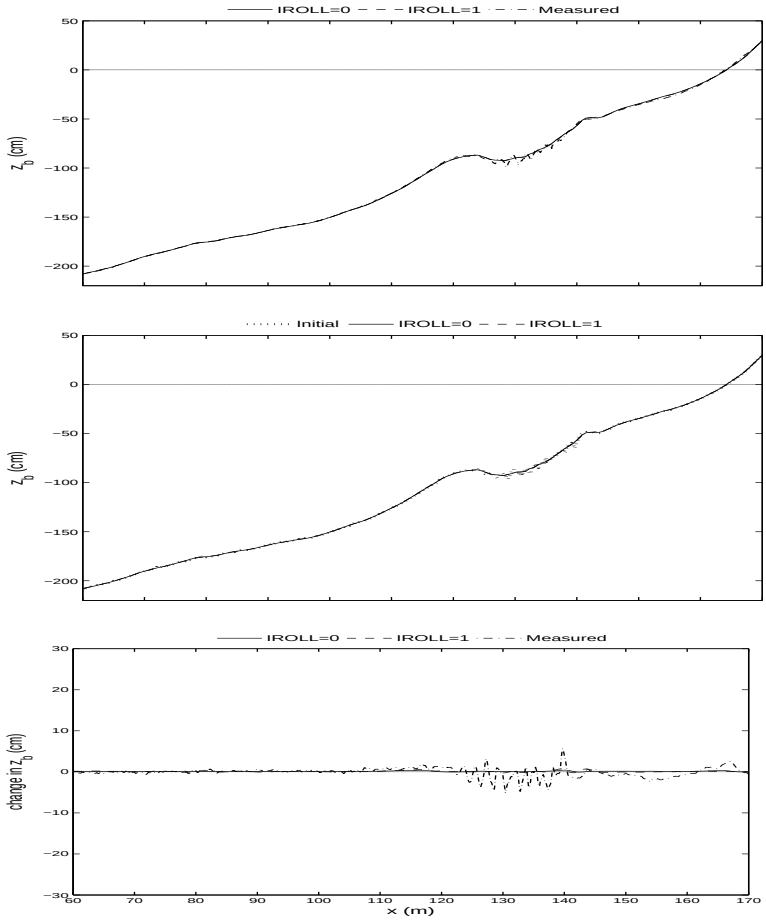

Figure D.4: LIP1b: (top) Computed and measured profiles for $t = 1$ hr, (middle) Computed and initial profile for $t = 1$ hr, (bottom) Computed change from the initial profile for $t = 1$ hr.

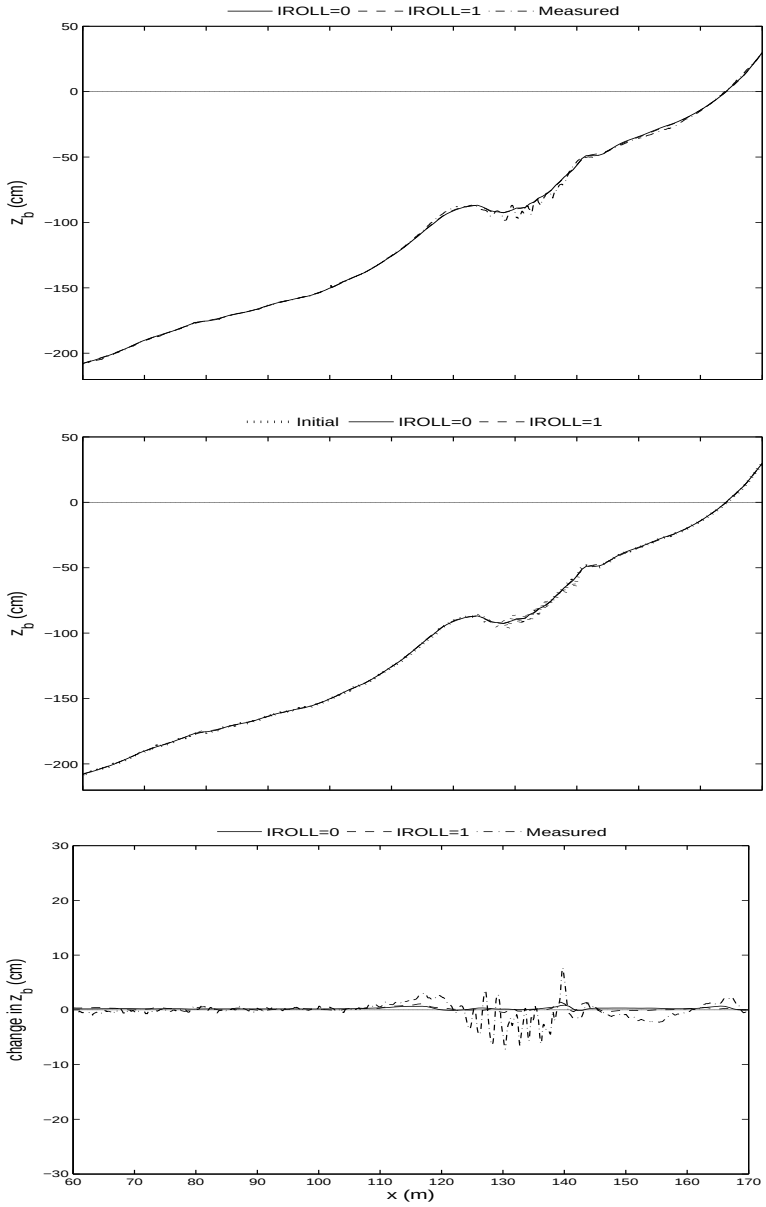

Figure D.5: LIP1b: (top) Computed and measured profiles for $t = 2$ hr, (middle) Computed and initial profile for $t = 2$ hr, (bottom) Computed change from the initial profile for $t = 2$ hr.

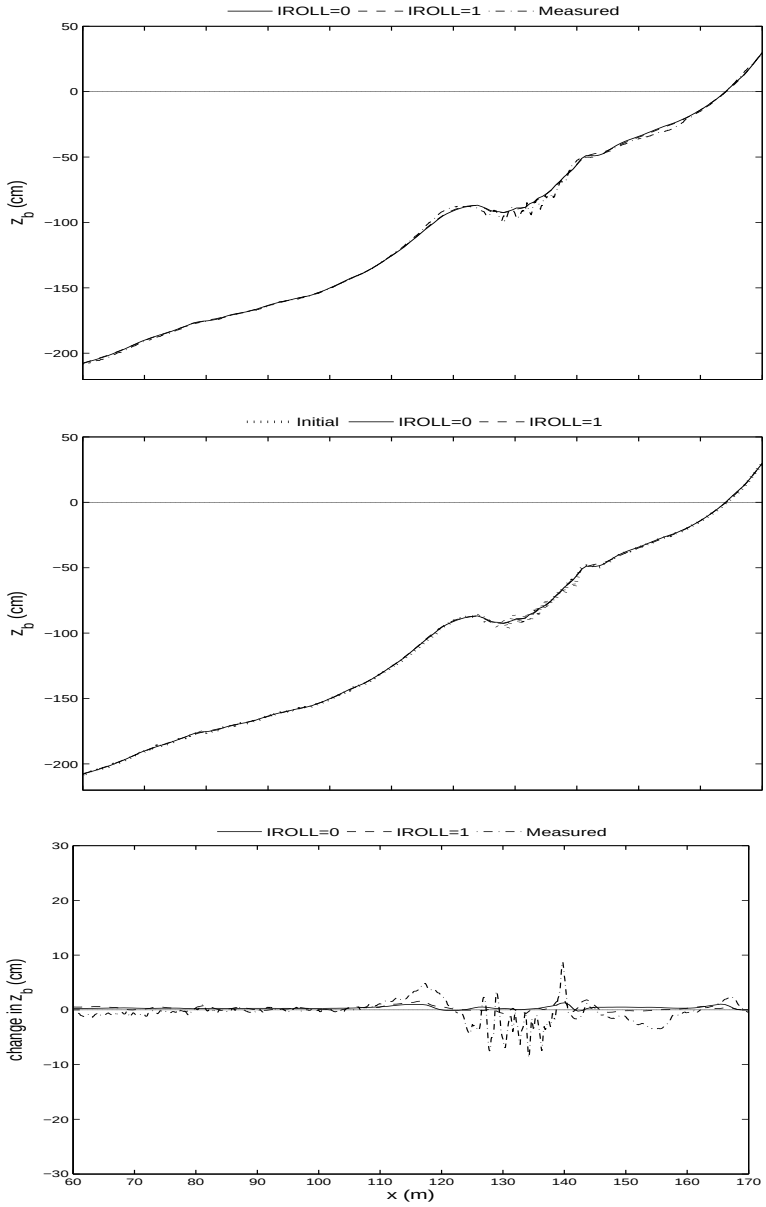

Figure D.6: LIP1b: (top) Computed and measured profiles for $t = 3$ hr, (middle) Computed and initial profile for $t = 3$ hr, (bottom) Computed change from the initial profile for $t = 3$ hr.

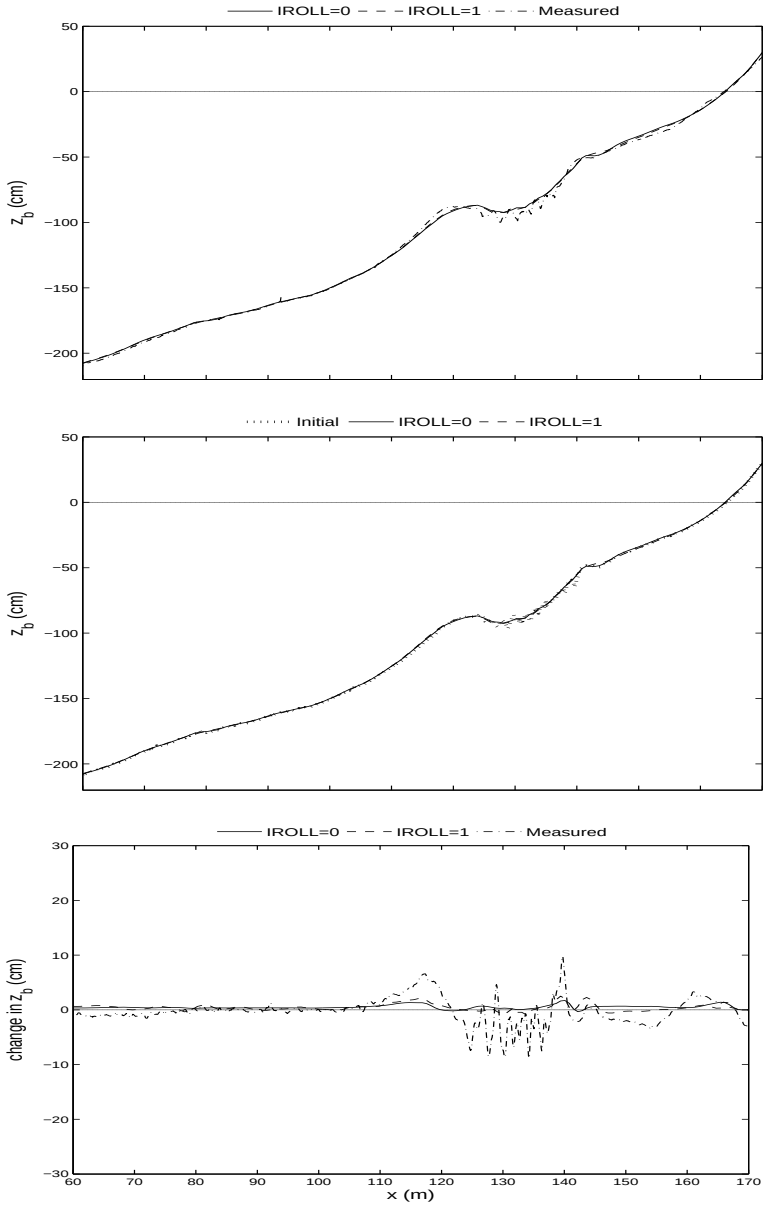

Figure D.7: LIP1b: (top) Computed and measured profiles for $t = 4$ hr, (middle) Computed and initial profile for $t = 4$ hr, (bottom) Computed change from the initial profile for $t = 4$ hr.

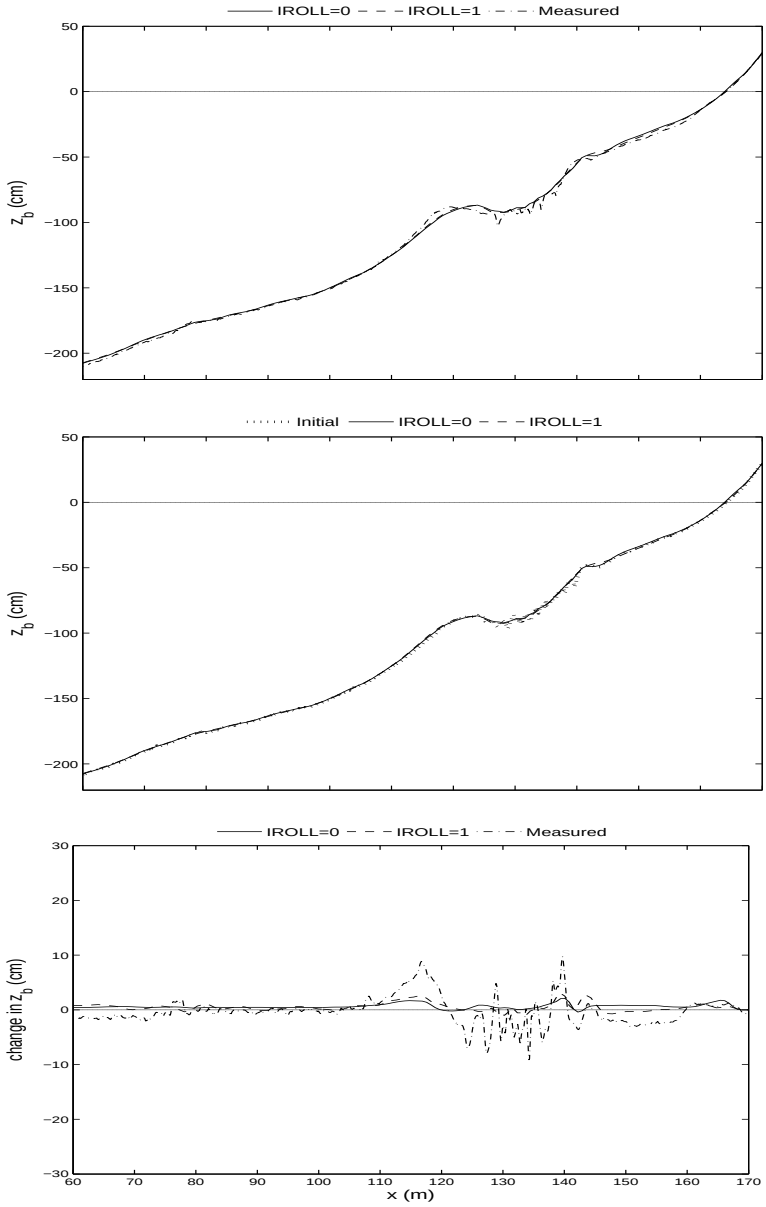

Figure D.8: LIP1b: (top) Computed and measured profiles for $t = 5$ hr, (middle) Computed and initial profile for $t = 5$ hr, (bottom) Computed change from the initial profile for $t = 5$ hr.

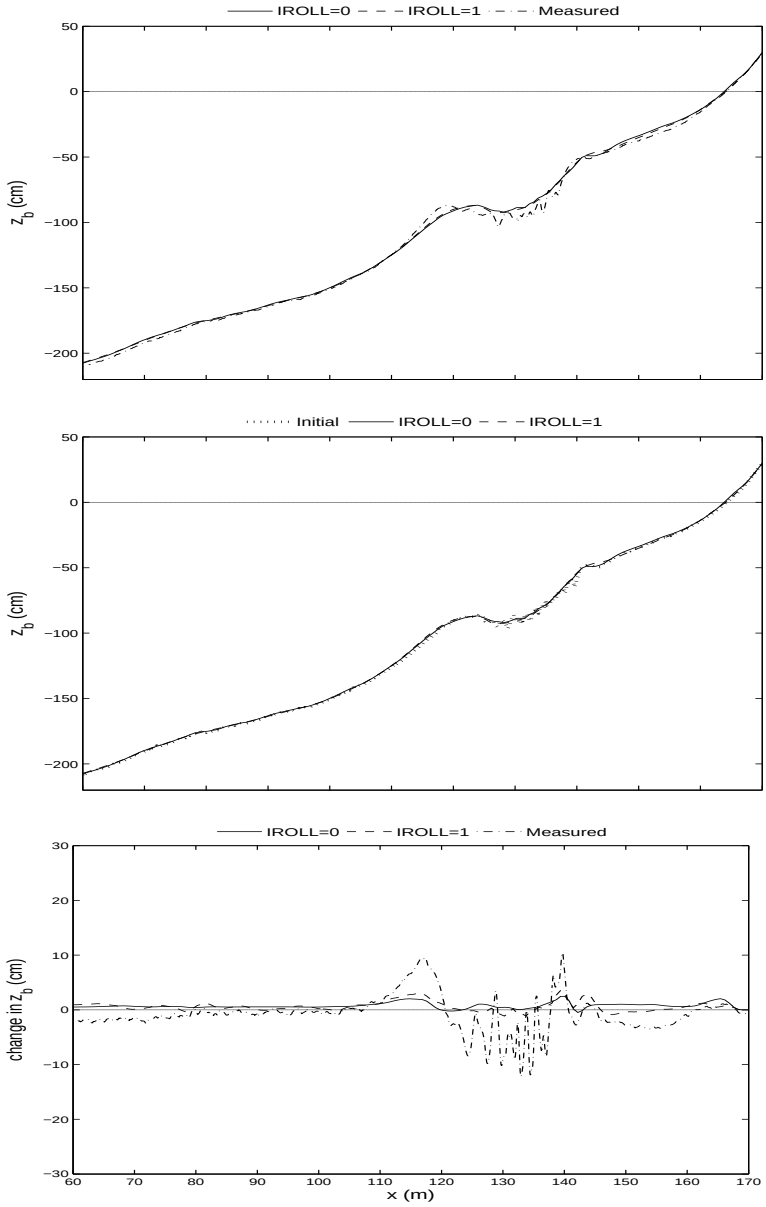

Figure D.9: LIP1b: (top) Computed and measured profiles for $t = 6$ hr, (top) Computed and initial profile for $t = 6$ hr, (top) Computed change from the initial profile for $t = 6$ hr.

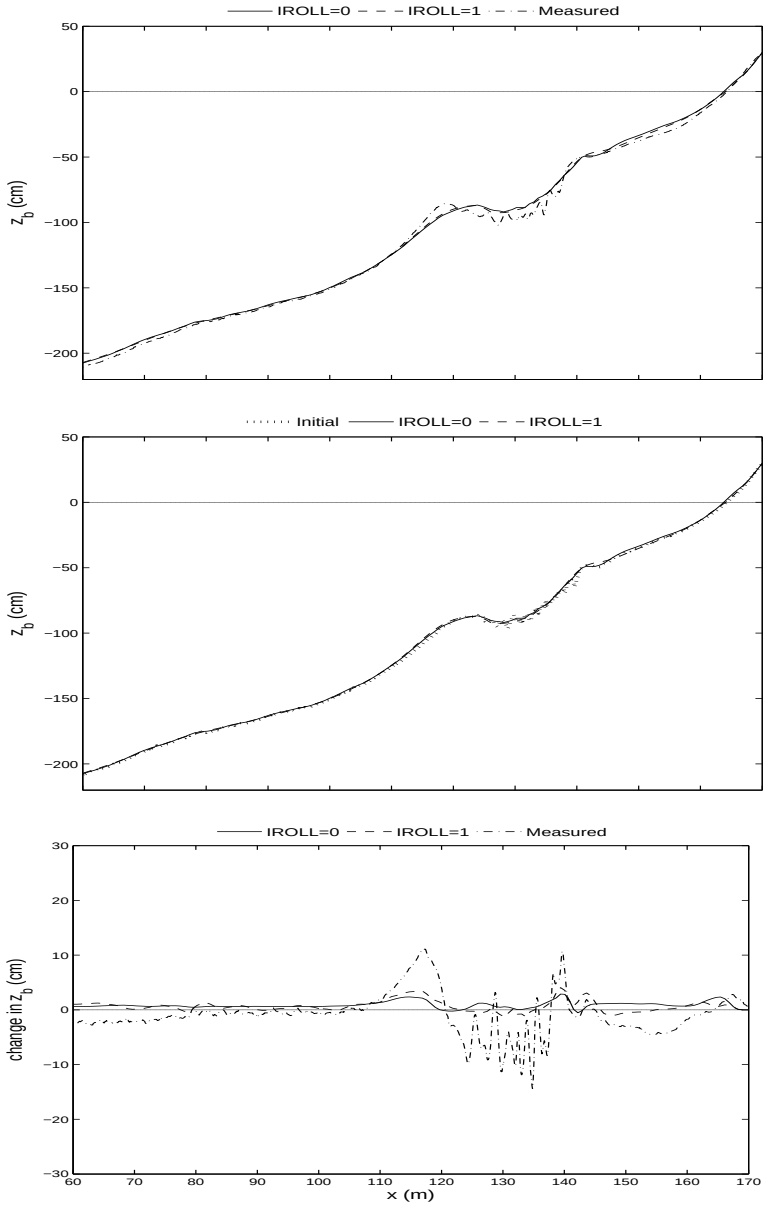

Figure D.10: LIP1b: (top) Computed and measured profiles for $t = 7$ hr, (middle) Computed and initial profile for $t = 7$ hr, (bottom) Computed change from the initial profile for $t = 7$ hr.

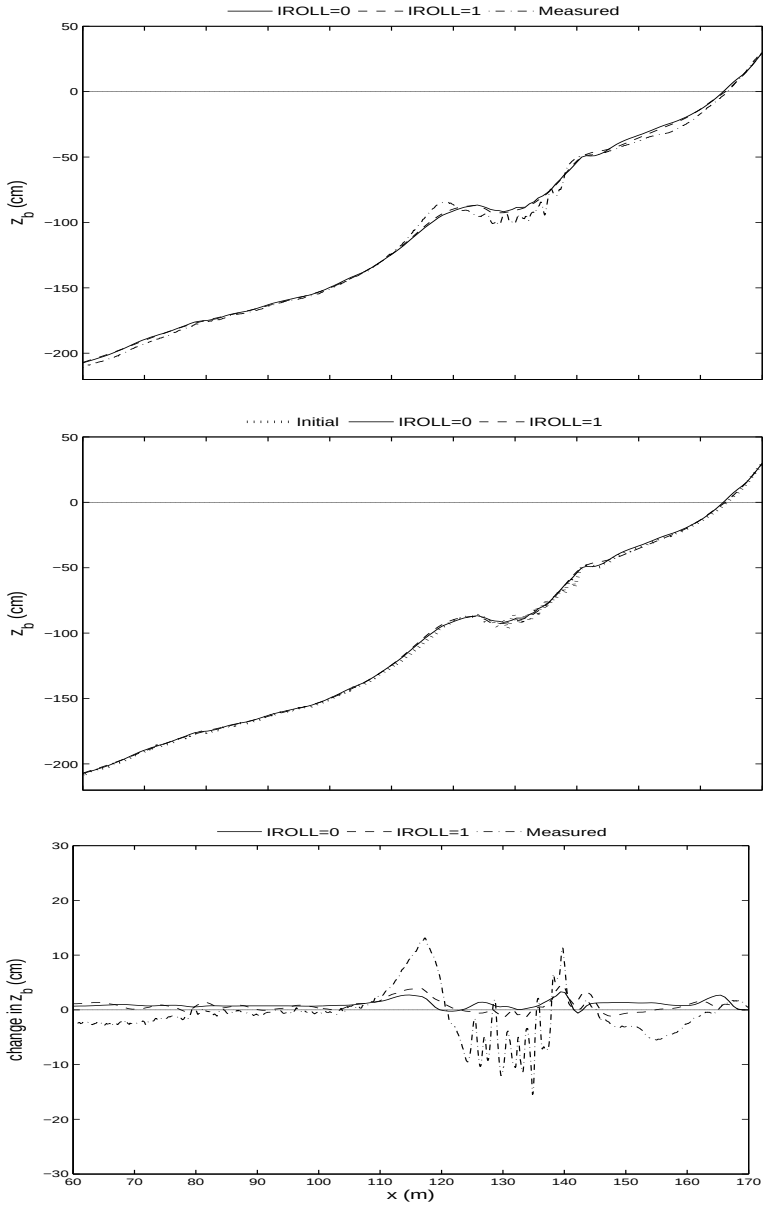

Figure D.11: LIP1b: (top) Computed and measured profiles for $t = 8$ hr, (middle) Computed and initial profile for $t = 8$ hr, (bottom) Computed change from the initial profile for $t = 8$ hr.

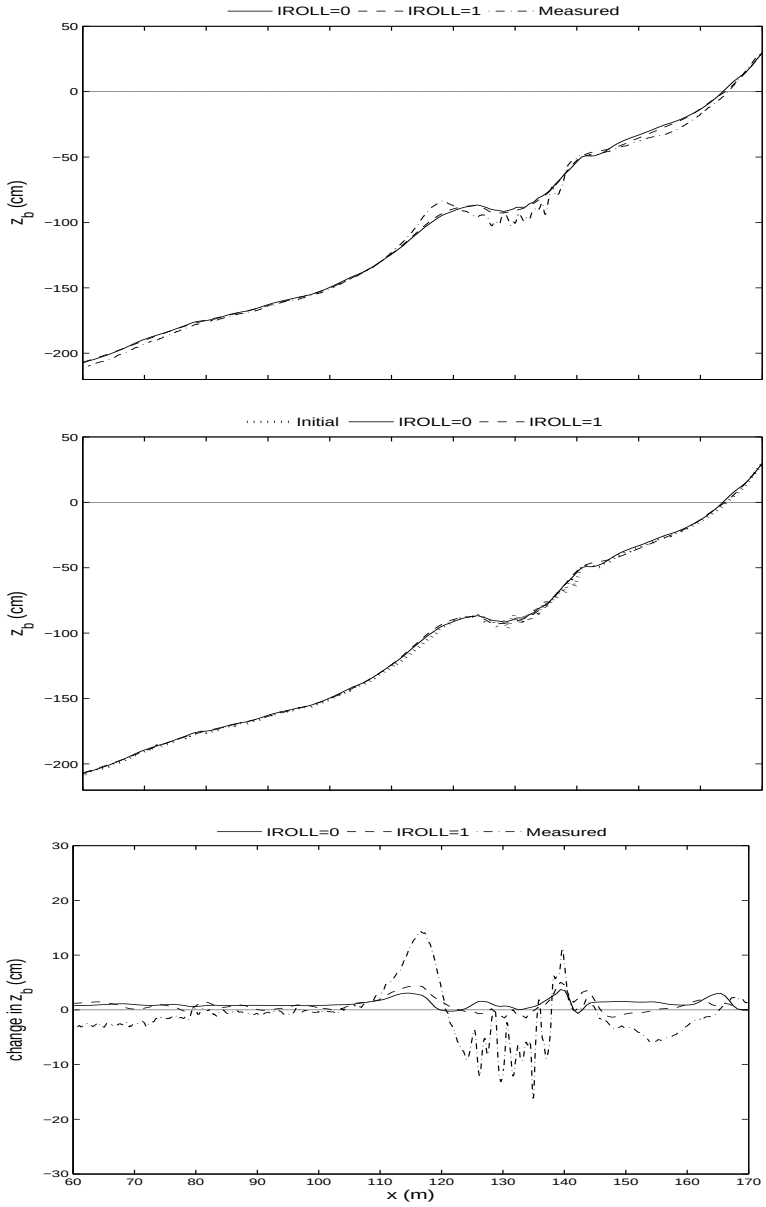

Figure D.12: LIP1b (top) Computed and measured profiles for $t = 9$ hr, (middle) Computed and initial profile for $t = 9$ hr, (bottom) Computed change from the initial profile for $t = 9$ hr.

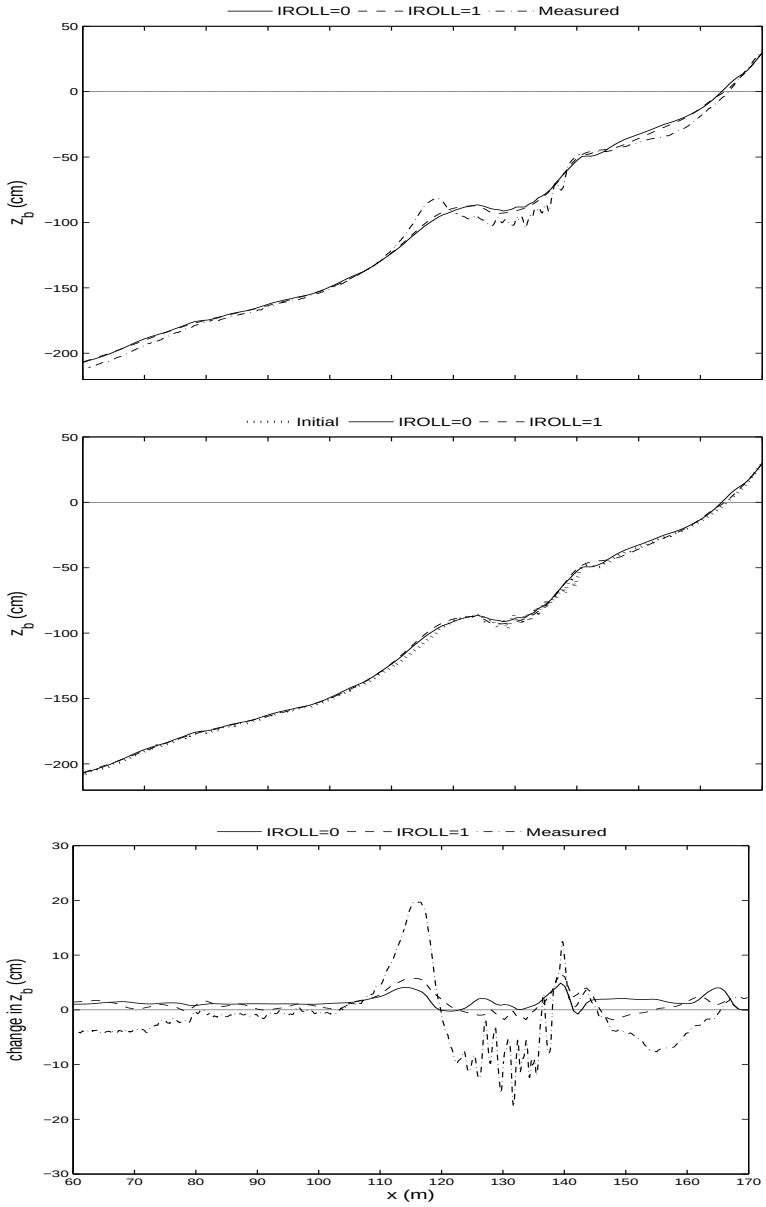

Figure D.13: LIP1b: (top) Computed and measured profiles for $t = 12$ hr, (middle) Computed and initial profile for $t = 12$ hr, (bottom) Computed change from the initial profile for $t = 12$ hr.

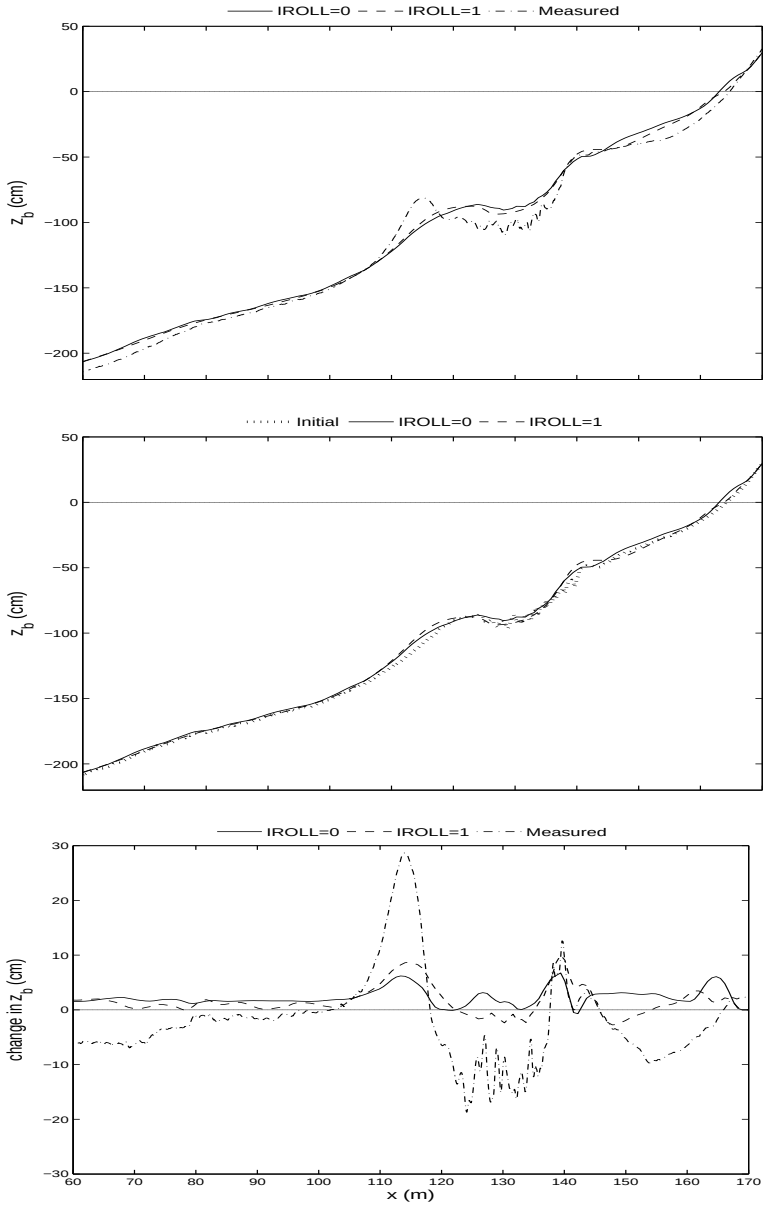

Figure D.14: LIP1b: (top) Computed and measured profiles for $t = 18$ hr, (middle) Computed and initial profile for $t = 18$ hr, (bottom) Computed change from the initial profile for $t = 18$ hr.

Appendix E

TEST1C

E.1 Free surface

Table E.1: Test 1c: Hourly free surface measurements during 13 hours.

test	**x (m)**	$\overline{\eta}$ **(m)**	σ_η **(m)**
1c.1	0	-0.008	0.138
	20	-0.009	0.143
	39	-0.010	0.153
1c.2	0	-0.009	0.137
	20	-0.009	0.142
	89	-0.012	0.156
1c.3	0	-0.006	0.137
	20	-0.007	0.141
	76	-0.012	0.156
1c.4	0	-0.007	0.138
	20	-0.007	0.143
	104	-0.011	0.155
1c.5	0	-0.006	0.138
	20	-0.007	0.143
	99	-0.045	0.160
1c.6	0	-0.008	0.138
	20	-0.009	0.143
	108	-0.008	0.154

test	**x (m)**	$\overline{\eta}$ **(m)**	σ_η **(m)**
1c.7	0	-0.006	0.138
	20	-0.006	0.142
	112	-0.010	0.161
1c.8	0	-0.008	0.138
	20	-0.008	0.143
	119	-0.018	0.152
1c.9	0	-0.006	0.136
	20	-0.007	0.140
	126	-0.003	0.126
1c.10	0	-0.007	0.138
	20	-0.007	0.142
	134	0.006	0.122
1c.11	0	-0.010	0.137
	20	-0.007	0.142
	144	0.011	0.097
1c.12	60	-0.009	0.152
	105	-0.010	0.156
	118	-0.019	0.159
1c.13	60	-0.008	0.151
	105	-0.010	0.155
	125	0.003	0.121

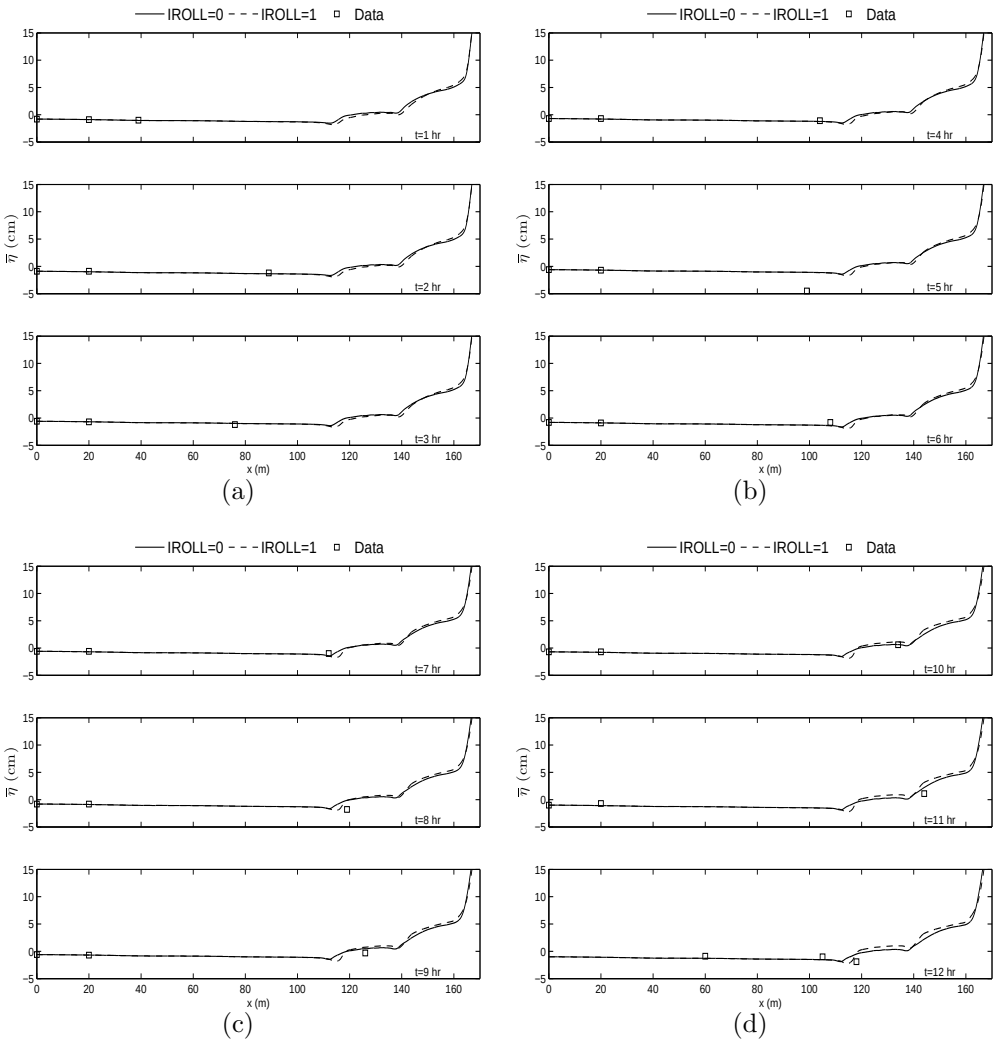

Figure E.1: Test 1c: Individual measured and predicted mean of free surface elevation, η, for (a) t=1 to 3 hr, (b) t=4 to 6 hr, (c) t=7 to 9 hr, and (d) t=10 to 12 hr.

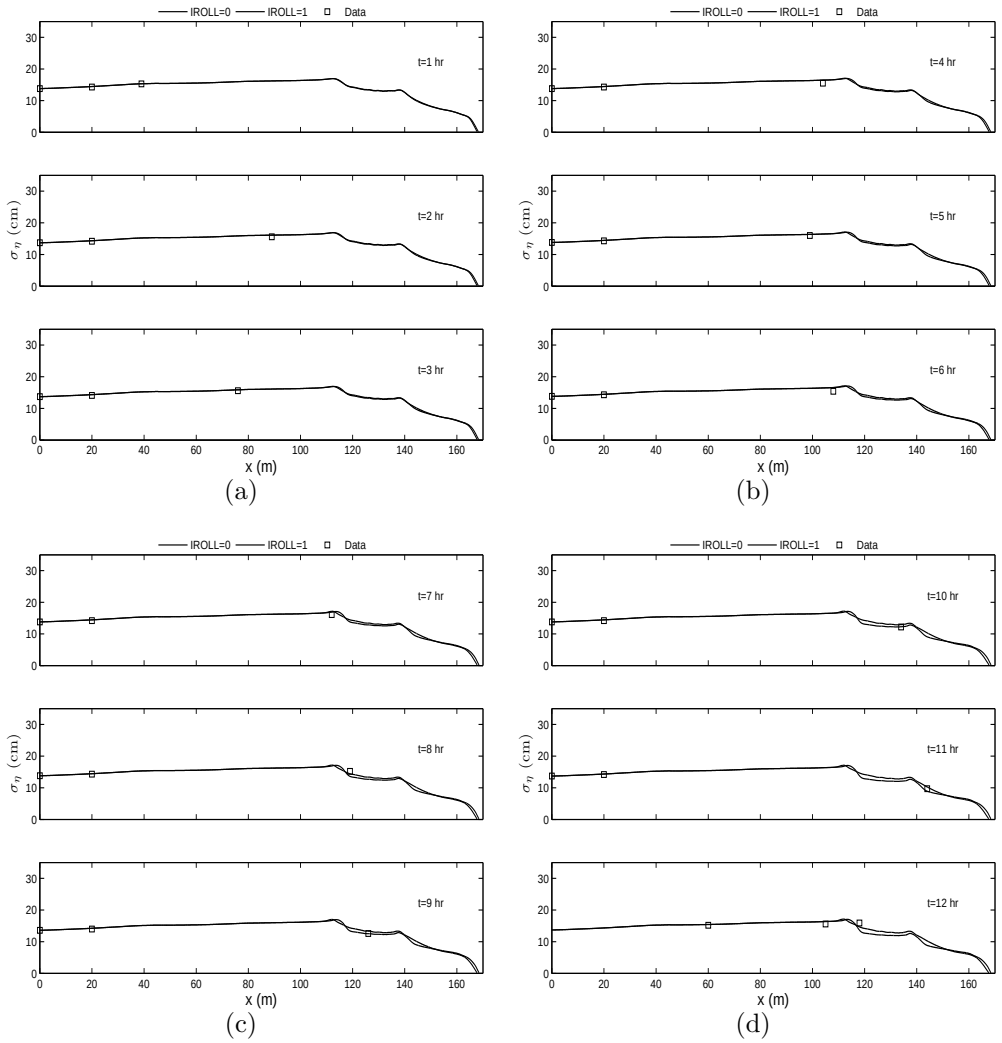

Figure E.2: Test 1c: Individual measured and predicted standard deviation of free surface elevation, η, for (a) t=1 to 3 hr, (b) t=4 to 6 hr, (c) t=7 to 9 hr, and (d) t=10 to 12 hr.

E.2 Velocity

Table E.2: Test 1c: Hourly horizontal velocity measurements during 13 hours.

test	**x** (m)	**z** (cm)	$\overline{U}$ (cm/s)	σ_U (cm/s)	$\overline{U_0}$ (cm/s)	**average** σ_U (cm/s)
1c.1	45	10	-1.2	27.5	-0.84	26.7
		20	-1.2	27.8		
		40	-0.8	28.0		
		70	-0.3	21.2		
		110	-0.7	29.1		
1c.2	95	10	-0.8	31.6	-1.4	31.3
		20	-0.4	32.1		
		40	-1.3	32.4		
		70	-1.1	25.3		
		110	-3.4	35.0		
1c.3	82	10	-0.5	30.5	-0.92	30.0
		20	-0.1	31.0		
		40	-0.8	31.4		
		70	-0.9	23.8		
		110	-2.3	33.4		
1c.4	110	10	-2.4	37.3	-3.10	36.3
		20	-3.1	38.0		
		40	-4.4	38.8		
		70	-3.7	31.0		
		110	NaN	NaN		

test	**x**	**z**	$\overline{U}$	σ_U	$\overline{U_0}$	**average** σ_U
	(m)	(cm)	(cm/s)	(cm/s)	(cm/s)	(cm/s)
1c.5	105	10	-2.1	34.2	-2.56	36.0
		20	-1.5	35.0		
		40	-2.4	35.6		
		70	-2.4	36.5		
		110	-4.4	38.7		
1c.6	114	10	-5.2	42.7	-6.10	44.1
		20	-6.1	43.5		
		40	-7.1	44.2		
		70	-7.3	46.1		
		110	NaN	NaN		
1c.7	118	10	-6.7	46.9	-8.22	49.9
		20	-9.6	47.4		
		40	-11.9	49.7		
		70	-3.7	55.5		
		110	NaN	NaN		
1c.8	125	10	-14.5	31.0	-11.10	31.4
		20	-14	31.2		
		40	-11.5	31.1		
		70	-4.8	32.3		
		110	NaN	NaN		
1c.9	132	10	-13.9	32.4	-9.10	32.6
		20	-13.3	32.6		
		40	-9.8	32.2		
		70	-3.0	33.2		
		110	NaN	NaN		
1c.10	140	10	-11.8	47.0	-9.17	50.2
		20	-11.8	47.4		
		40	-0.5	56.2		
		70	NaN	NaN		
		110	NaN	NaN		

test	**x** (m)	**z** (cm)	$\overline{U}$ (cm/s)	σ_U (cm/s)	$\overline{U_0}$ (cm/s)	**average** σ_U (cm/s)
1c.11	150	10	-11.7	33.6	-9.10	40.00
		20	-9.4	34.9		
		40	-6.2	51.5		
		70	NaN	NaN		
		110	NaN	NaN		
1c.12	NaN	10	NaN	NaN	NaN	NaN
		20	NaN	NaN		
		40	NaN	NaN		
		70	NaN	NaN		
		110	NaN	NaN		
1c.13	NaN	10	NaN	NaN	NaN	NaN
		20	NaN	NaN		
		40	NaN	NaN		
		70	NaN	NaN		
		110	NaN	NaN		

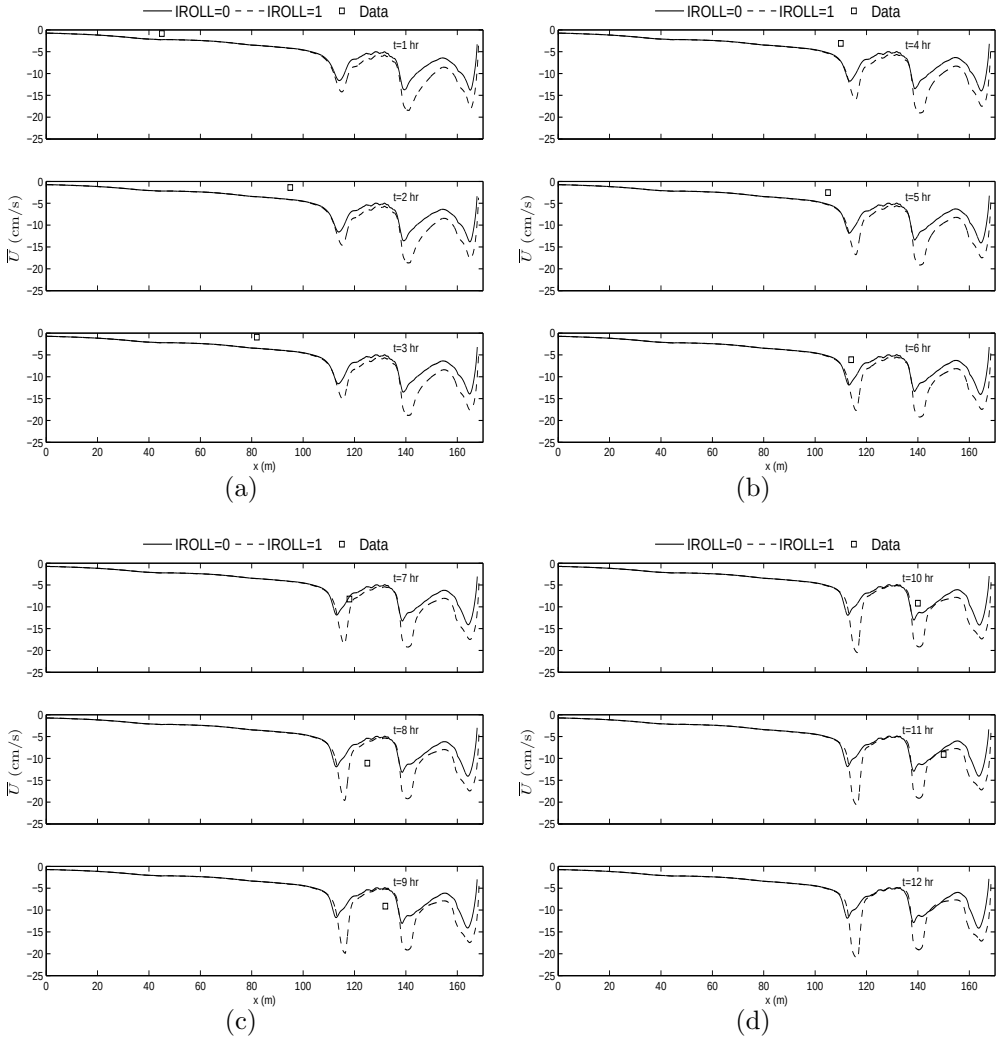

Figure E.3: Test 1c: Individual measured and predicted mean of the horizontal fluid velocity, U, for (a) t=1 to 3 hr, (b) t=4 to 6 hr, and (c) t=7 to 9 hr.

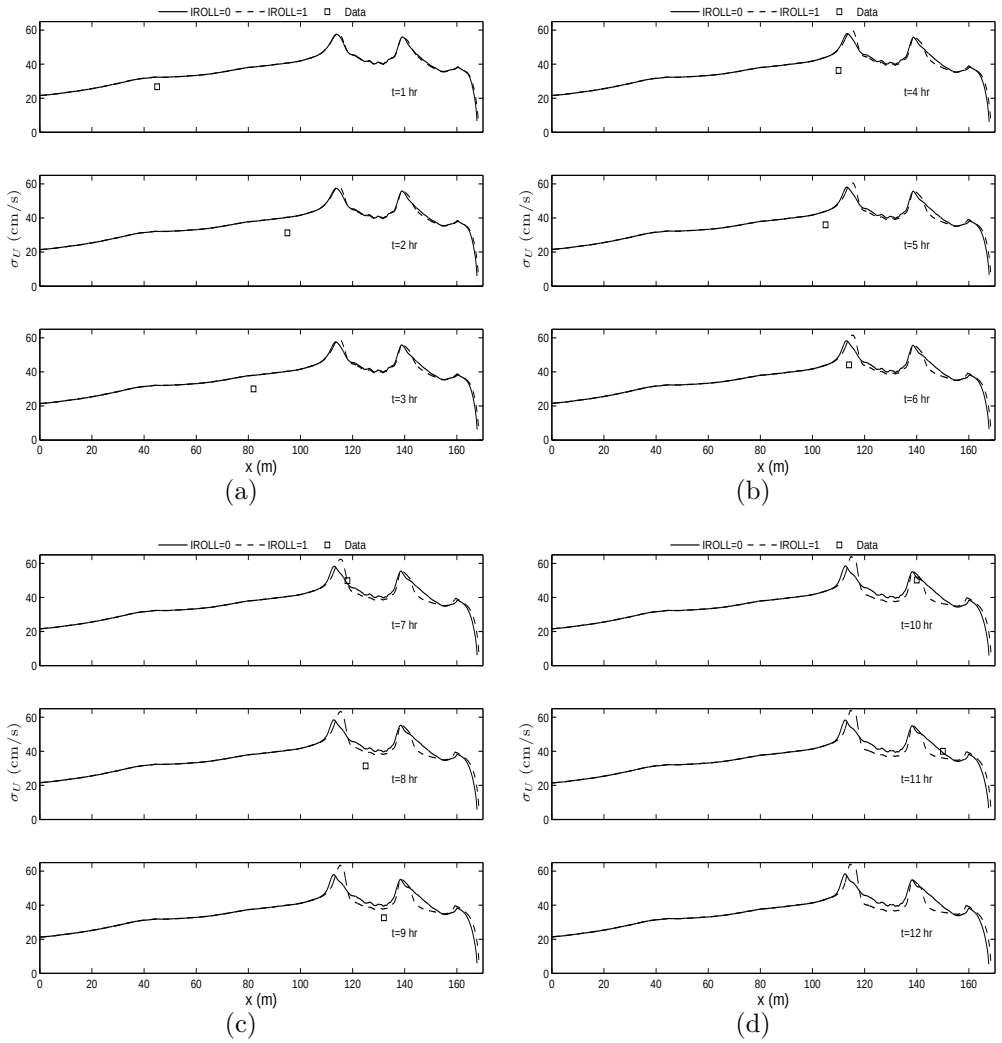

Figure E.4: Test 1c: Individual measured and predicted standard deviation of horizontal fluid velocity, U, for (a) t=1 to 3 hr, (b) t=4 to 6 hr, (c) t=7 to 9 hr, and (d) 10 to 12 hr.

E.3 Concentration

Table E.3: Test 1c: Hourly concentration measurements during 13 hours.

test	**x (m)**	**z (cm)**	$\overline{C}$
1c.1	45	5	0.0000411
		7.5	0.0000257
		10	0.0000223
		13	0.0000192
		18	0.0000136
		25.5	0.0000075
		40	0.0000075
		65	NaN
		105	NaN
		155	NaN
1c.2	95	5	0.0000830
		7.5	0.0000506
		10	0.0000166
		13	0.0000117
		18	0.0000049
		25.5	NaN
		40	NaN
		65	NaN
		105	NaN
		155	NaN

test	**x (m)**	**z (cm)**	$\overline{C}$
1c.3	82	5	0.0000321
		7.5	0.0000143
		10	0.0000068
		13	0.0000053
		18	0.0000057
		25.5	NaN
		40	NaN
		65	NaN
		105	NaN
		155	NaN
1c.4	110	5	0.0001204
		7.5	0.0000823
		10	0.0000774
		13	0.0000672
		18	0.0000581
		25.5	0.0000438
		40	0.0000377
		65	0.0000283
		105	0.0000328
		155	NaN

test	x (m)	z (cm)	$\overline{C}$
1c.5	105	5	0.0000547
		7.5	0.0000430
		10	0.0000257
		13	0.0000313
		18	0.0000268
		25.5	0.0000151
		40	0.0000166
		65	NaN
		105	NaN
		155	NaN
1c.6	114	5	0.0001849
		7.5	0.0001857
		10	0.0001826
		13	0.0001426
		18	0.0001102
		25.5	0.0001075
		40	0.0000781
		65	0.0000426
		105	NaN
		155	NaN
1c.7	118	5	NaN
		7.5	NaN
		10	NaN
		13	NaN
		18	NaN
		25.5	NaN
		40	NaN
		65	NaN
		105	NaN
		155	NaN

test	x (m)	z (cm)	$\overline{C}$
1c.8	125	5	NaN
		7.5	NaN
		10	NaN
		13	NaN
		18	NaN
		25.5	NaN
		40	NaN
		65	NaN
		105	NaN
		155	NaN
1c.9	132	5	0.0000860
		7.5	0.0000479
		10	0.0000517
		13	0.0000351
		18	0.0000313
		25.5	0.0000185
		40	0.0000128
		65	0.0000102
		105	NaN
		155	NaN
1c.10	140	5	0.0003094
		7.5	0.0002464
		10	0.0002449
		13	0.0002045
		18	0.0002079
		25.5	0.0001796
		40	0.0001332
		65	NaN
		105	NaN
		155	NaN

test	**x (m)**	**z (cm)**	$\overline{C}$
1c.11	150	5	0.0002060
		7.5	0.0001713
		10	0.0001502
		13	0.0001472
		18	0.0001279
		25.5	0.0000932
		40	0.0000721
		65	NaN
		105	NaN
		155	NaN
1c.12	NaN	5	NaN
		7.5	NaN
		10	NaN
		13	NaN
		18	NaN
		25.5	NaN
		40	NaN
		65	NaN
		105	NaN
		155	NaN
1c.13	NaN	5	NaN
		7.5	NaN
		10	NaN
		13	NaN
		18	NaN
		25.5	NaN
		40	NaN
		65	NaN
		105	NaN
		155	NaN

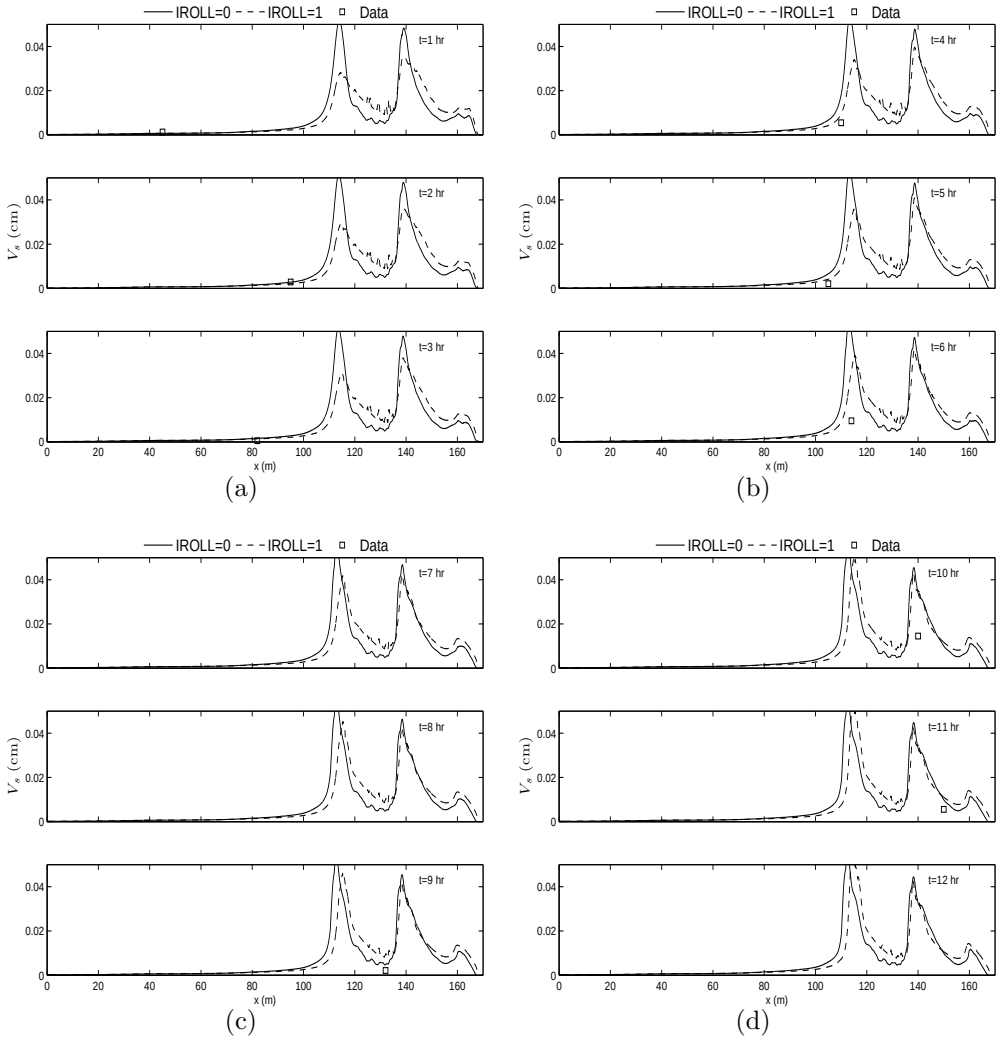

Figure E.5: Test 1c: Individual measured and predicted suspended sediment volume, V_s, per unit area for (a) t=1 to 3 hr, (b) t=4 to 6 hr, (c) t=7 to 9 hr, and (d) t=10 to 12 hr.

E.4 Profile change

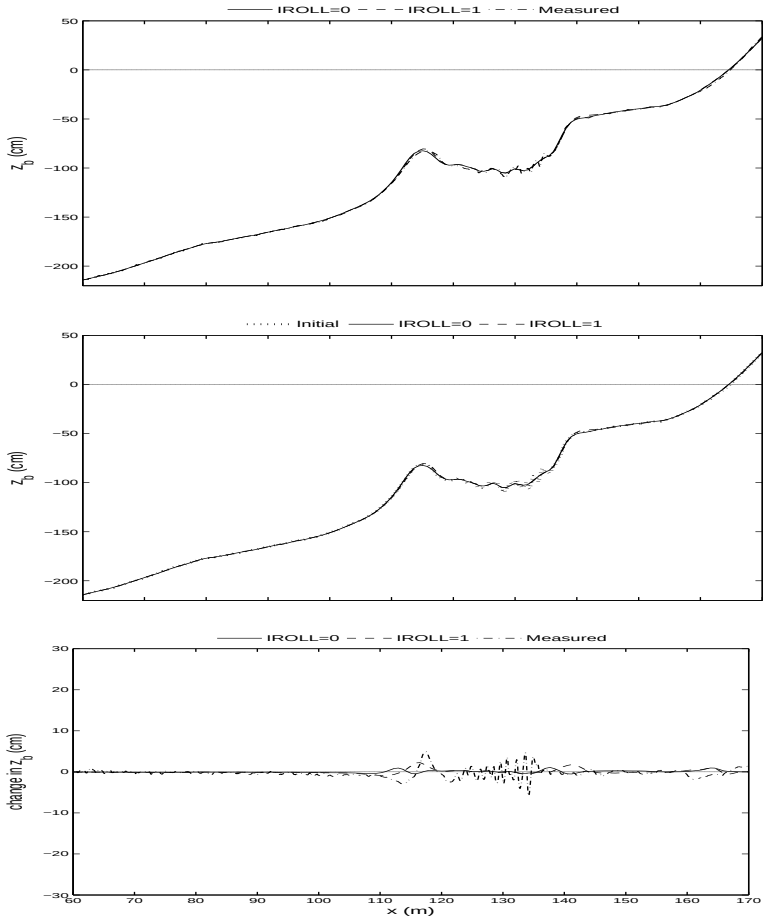

Figure E.6: LIP1c: (top) Computed and measured profiles for $t = 1$ hr, (middle) Computed and initial profile for $t = 1$ hr, (bottom) Computed change from the initial profile for $t = 1$ hr.

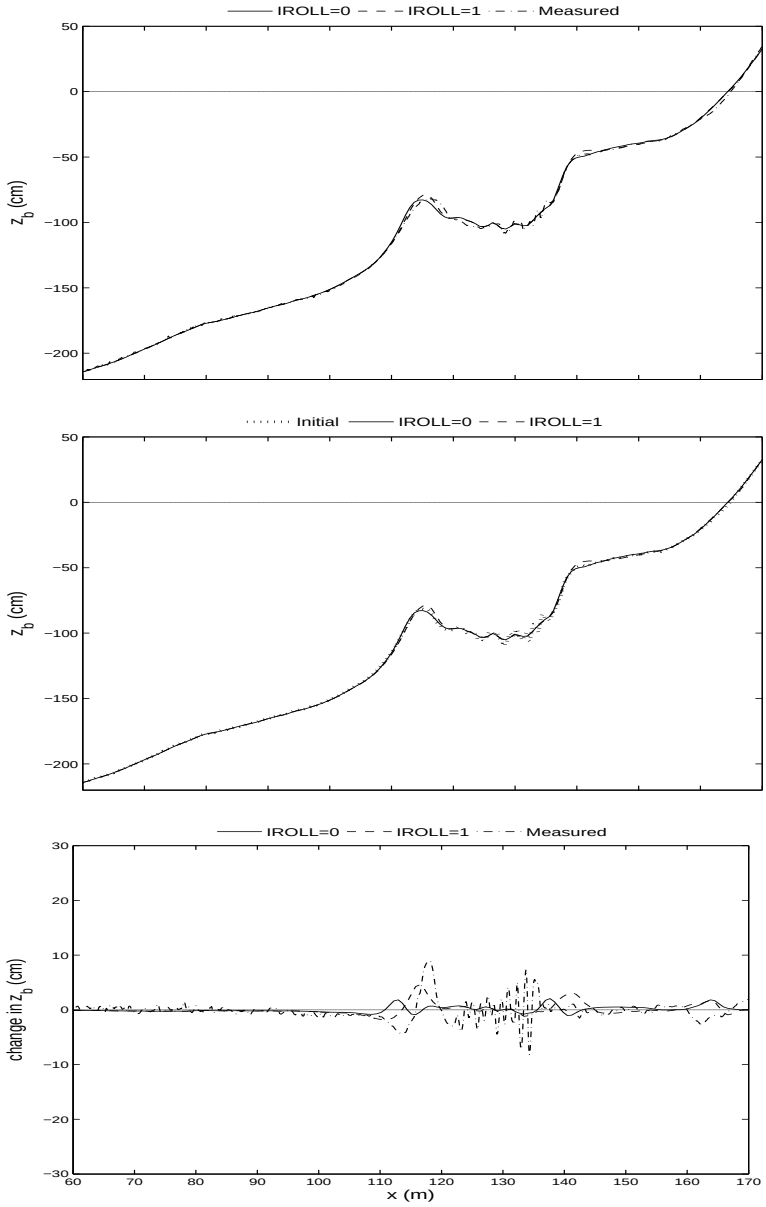

Figure E.7: LIP1c: (top) Computed and measured profiles for $t = 2$ hr, (middle) Computed and initial profile for $t = 2$ hr, (bottom) Computed change from the initial profile for $t = 2$ hr.

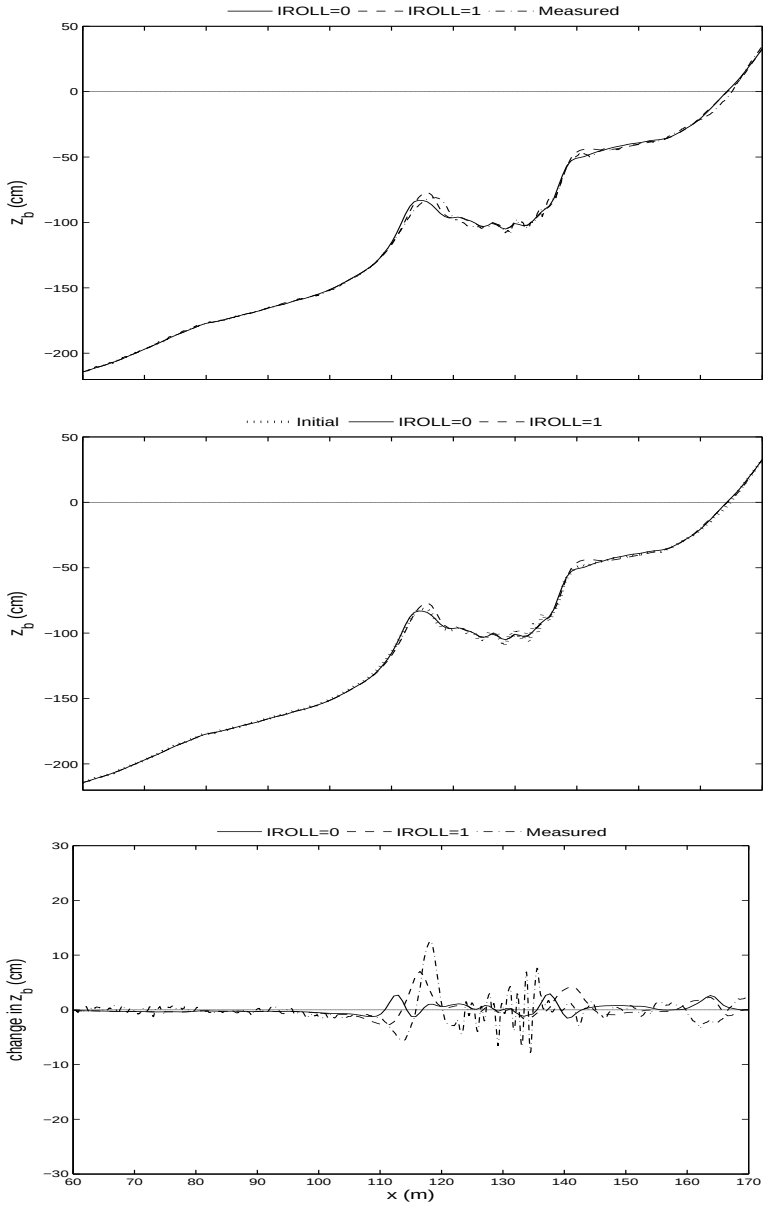

Figure E.8: LIP1c: (top) Computed and measured profiles for $t = 3$ hr, (middle) Computed and initial profile for $t = 3$ hr, (bottom) Computed change from the initial profile for $t = 3$ hr.

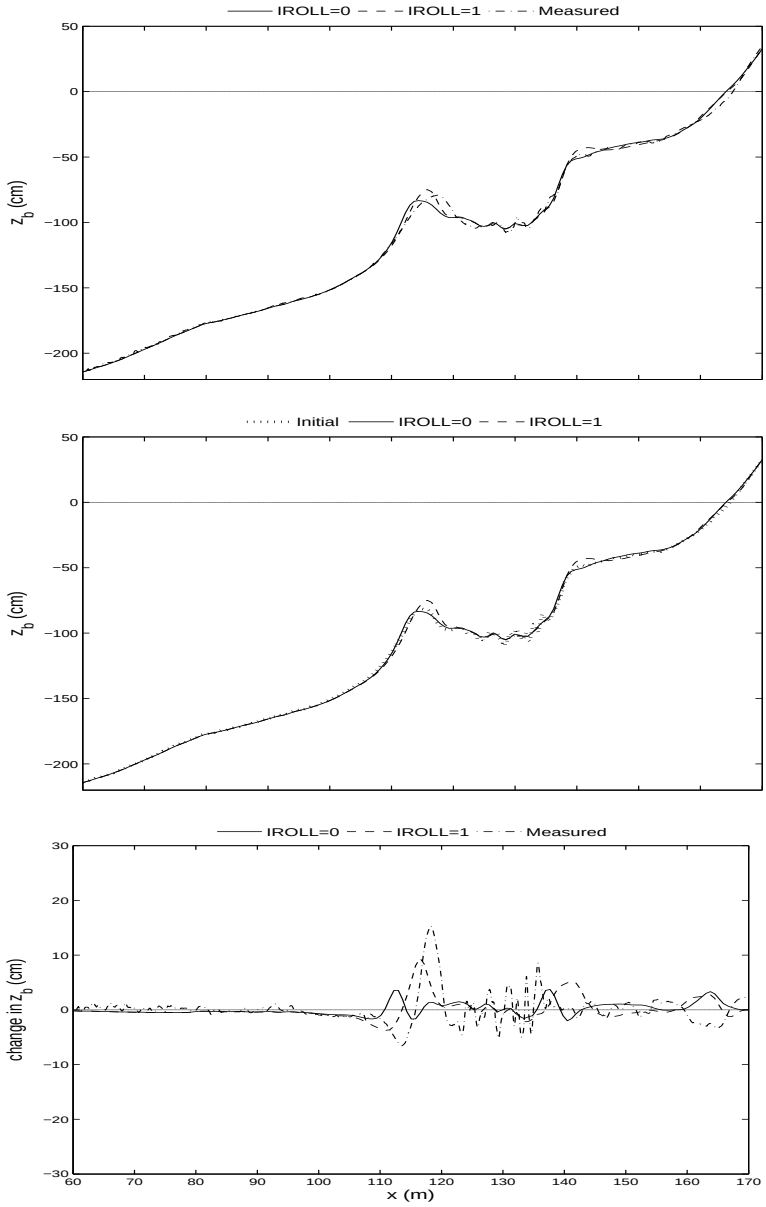

Figure E.9: LIP1c: (top) Computed and measured profiles for $t = 4$ hr, (middle) Computed and initial profile for $t = 4$ hr, (bottom) Computed change from the initial profile for $t = 4$ hr.

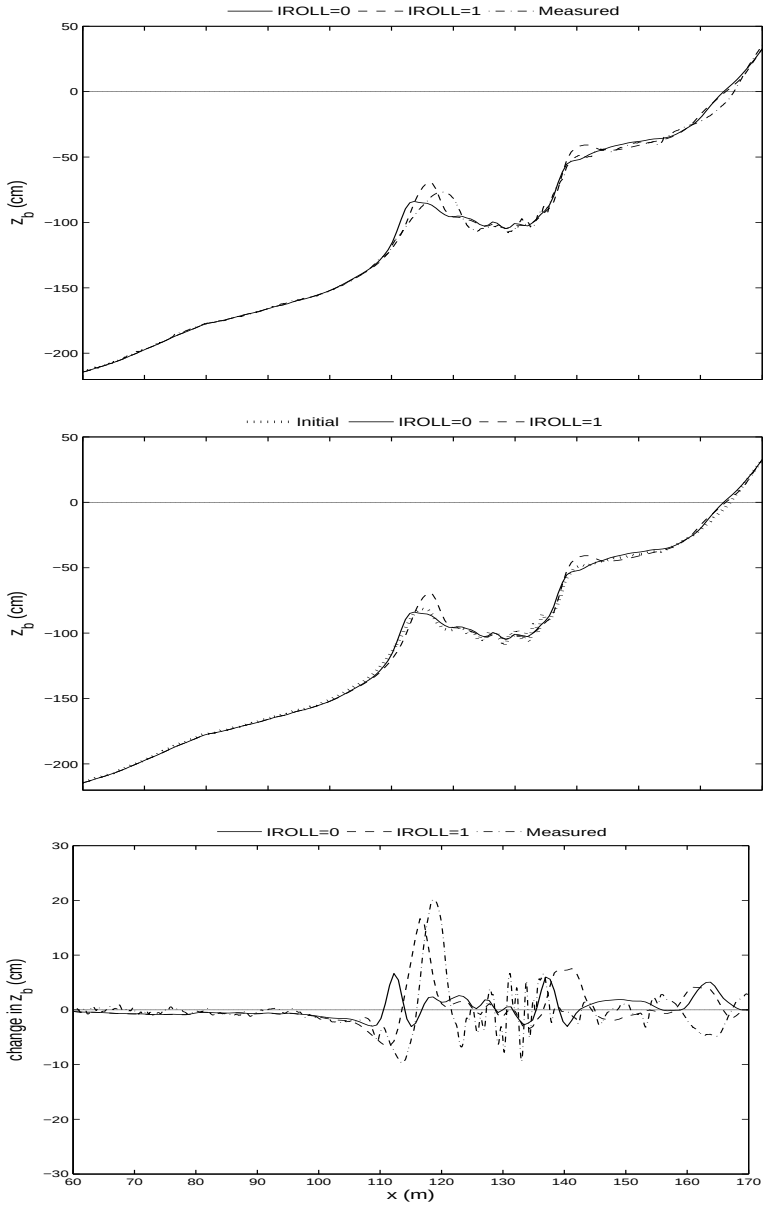

Figure E.10: LIP1c: (top) Computed and measured profiles for $t = 7$ hr, (middle) Computed and initial profile for $t = 7$ hr, (bottom) Computed change from the initial profile for $t = 7$ hr.

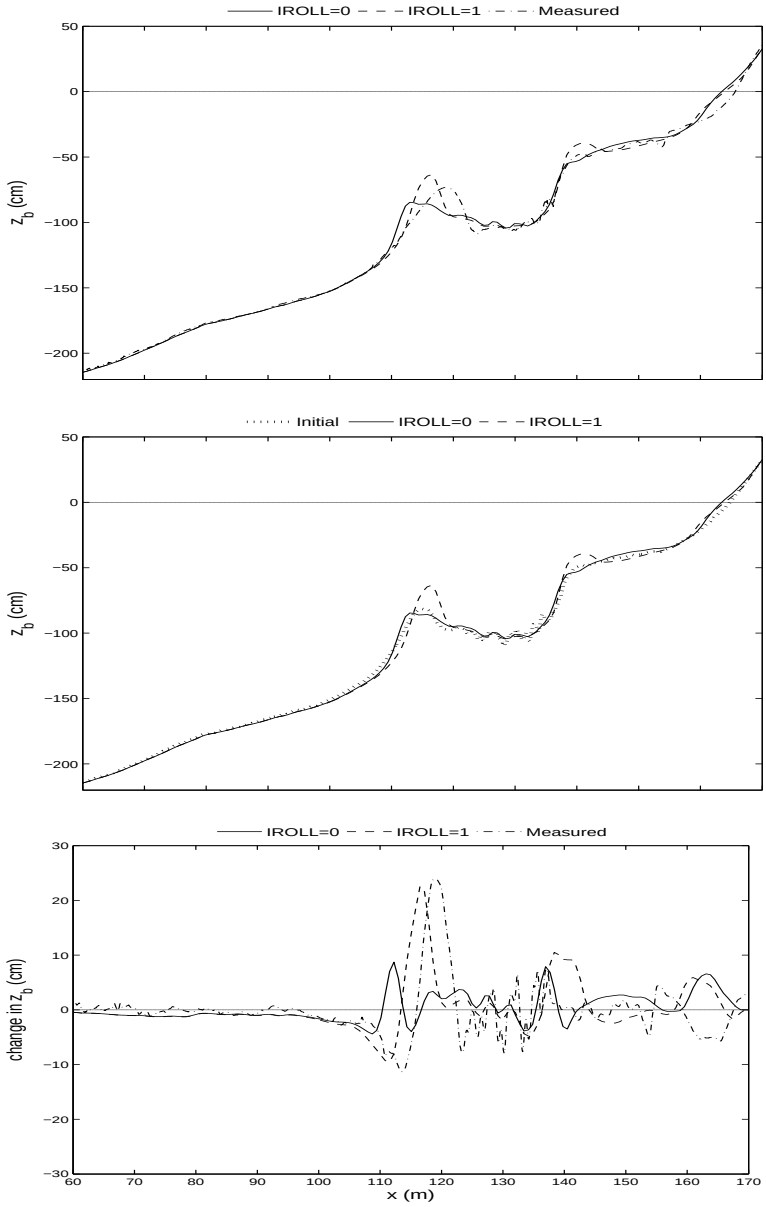

Figure E.11: LIP1c: (top) Computed and measured profiles for $t = 10$ hr, (middle) Computed and initial profile for $t = 10$ hr, (bottom) Computed change from the initial profile for $t = 10$ hr.

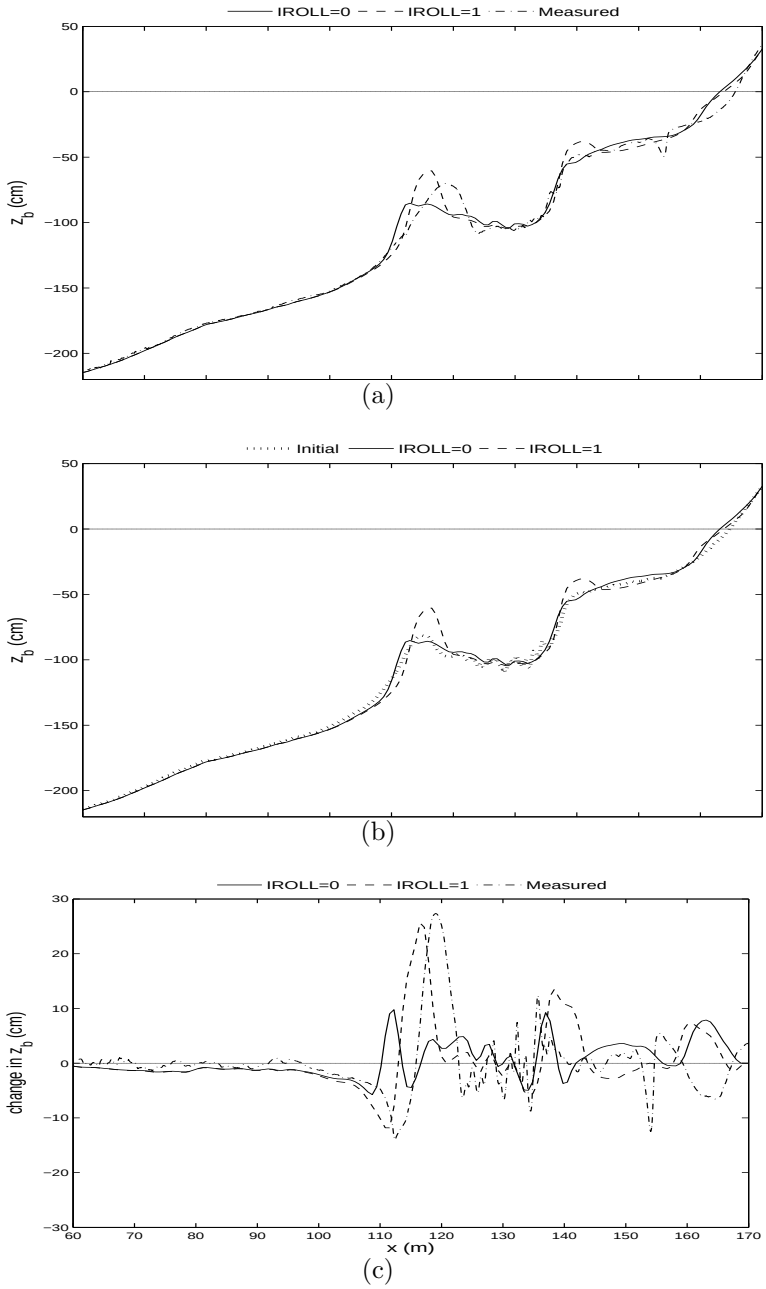

Figure E.12: Test 1c: (top) Computed and measured profiles for $t = 13$ hr, (middle) Computed and initial profile for $t = 13$ hr, (bottom) Computed change from the initial profile for $t = 13$ hr.

BIBLIOGRAPHY

Adams, A. E., Hinton, O. R., Valentine, E. M., and Tweedy, A. D. (1998). An acoustic imaging system for the concurrent measurement of suspended sediment concentration and particle velocity. *J. Acoust. Soc. Am.*, **104**(4), 2160–2166.

Bagnold, J. A. (1966). An approach to the sediment transport problem from general physics. Prof. Paper 422-I, U. S. Geol. Surv.

Bailard, J. A. and Inman, D. L. (1981). An energetics bedload model for a plane sloping beach:Local transport. *J. Geophys. Res.*.

Battjes, J. and Stive, M. J. F. (1985). Calibration and verification of a dissipation model for random breaking waves. *J. Geophys. Res.*, **90**, 9159–9167.

Battjes, J. A. (1988). Surf-zone dynamics. *Ann. Rev. Fluid Mech.*, **20**, 257–293.

Bowen, A. J. (1980). Simple models of nearshore sedimentation: beach profiles and longshore bars. In S. B. McCann, editor, *The Coastline of Canada*, pages 1–11. Geol. Surv. of Canada.

Brenninkmeyer, B. M. (1976). Sand fountains in the surf zone. In R. A. D. Jr and R. L. Ethington, editors, *Beach and Nearshore Sedimentation*, number 24. Society Economic Paleontologists and Minerologists.

Cox, D. T. and Kobayashi, N. (2000). Identification of intense, intermittent coherent motions under shoaling and breaking waves. *J. Geophys. Res.*, **105**(C6), 14223–14236.

Cox, D. T., Kobayashi, N., and Okayasu, A. (1996). Bottom shear stress in the surf zone. *J. Geophys. Res.*, **101**, 14337–14348.

Crawford, A. M. and Hay, A. E. (1998). A simple system for laser-illuminated video imaging of sediment suspension and bed topography. *IEEE J. Oceanic Eng.*, **22**(1), 12–19.

Dean, R. G. (1991). Equilibrium beach profiles: Characteristics and applications. *J. Coastal Res.*, **7**(1), 53–84.

Dean, R. G. and Dalrymple, R. A. (1984). *Water Wave Mechanics for Engineers and Scientists*. World Sci., New York.

Deigaard, R. and Fredsœ, J. (1989). Shear stress distribution in dissipative waver waves. *Coastal Eng.*, **13**, 357–378.

Dohmen-Janssen, C. M. and Hanes, D. M. (2002). Sheet flow dynamics under monochromatic nonbreaking waves. *J. Geophys. Res.*, **107**(C10).

Dohmen-Janssen, C. M., Kroekenstoel, D. F., Hassan, W. N., and Ribberink, J. S. (2002). Phase lags in oscillatory sheet flow: experiments and bed load modelling. *Coastal Eng.*, **46**, 62–87.

Downing, J. P., Sternber, R. W., and Lister, C. R. B. (1981). New instrumentation for the investigation of sediment suspension processes in the shallow marine environment. *Mar. Geol.*, **42**, 19–34.

Dunkley, E. C., Mocke, G. P., Diedericks, G. P. J., and Tanczos, I. (1999). Evaluation of bed shear, vertical mixing, and reference concentration formulations, *paper presented at Coastal Sediments '99 Conference*. Reston, Va. Am. Soc. of Civ. Eng.

Erikson, L. and Hanson, H. (2005). A method to extract wave tank data using video imagery and its comparison to conventional data collection techniques. *Comp. and Geosci.*, **31**, 371–384.

Foote, M., Horn, D., and Li, L. (2002). Measuring swash zone hydrodynamics and morphodynamic change - a high-resoultion laboratory system using digital video. *J. Coastal Res.*, **SI36**, 300–316.

Gallagher, E. L., Elgrar, S., and Guza, R. T. (1998). Observations of sand bar evolution on a natural beach. *J. Geophys. Res.*, **103**, 16999–17010.

Guza, R. T. and Thornton, E. B. (1980). Local and shoaled comparisons of sea surface elevations, pressure and velocities. *J. Geophys. Res.*, **85**, 1524–1530.

Guza, R. T. and Thornton, E. B. (1985). Velocity moments in nearshore. *J. Waterw. Port Coastal Ocean Eng.*, **111**, 235–256.

Hay, A. E. and Bowen, A. J. (1994). Coherence scales of wave-induced suspended sand concentration fluctuations. *J. Geophys. Res.*, **99**(C6), 12749–12765.

Henderson, S. M., Allen, J. S., and Newberger, P. A. (2004). Nearshore sandbar migration predicted by an eddy-diffusive boundary layer model. *J. Geophys. Res.*, **109**(C06024,doi:10.1029/2003JC002137).

Hoefel, F. and Elgar, S. (2003). Wave-induced sediment transport and sandbar migration. *Science*, **299**, 1885–1887.

Holland, K. T., Holman, R. A., Lippmann, T. C., Stanley, J., and Plant, N. (1997). Practical use of video imagery in nearshore oceanographic field studies. *IEEE J. Oceanic Eng.*, (1), 81–92.

Iverson, H. W. (1952). Waves and breakers in shoaling water. pages 1–12. University of California, Berkeley.

Jaffe, B. E. and Sallenger, A. H. (1992). The contribution of suspension events to sediment transport in the surf zone. pages 2680–2693, New York. Am. Soc. Civ. Eng.

Jiang, L., Perlin, M., and Schultz, W. (1998). Period tripling and energy dissipation of breaking standing waves. *J. Fluid Mech.*, **369**, 273–299.

Kobayashi, N. and Johnson, B. D. (2001). Sand suspension, storage, advection, and settling in surf and swash zones. *J. Geophys. Res.*, **106**(C5), 9363–9376.

Kobayashi, N. and Tega, Y. (2002). Sand suspension and transport on equilibrium eeach. *J. Waterw. Port Coastal Ocean Eng.*, **128**, 238–248.

Kobayashi, N., Cox, D. T., and Wurjanto, A. (1990). Irregular wave reflection and run-up on rough impermeable slopes. *J. Waterw. Port Coastal Ocean Eng.*, **116**, 708–726.

Kobayashi, N., Herrman, M. N., Johnson, B. D., and Orzech, M. D. (1998). Probabilistic distribution of surface elevation in surf and swash zones. *J. Waterw. Port Coastal Ocean Eng.*, **124**, 99–107.

Kobayashi, N., Zhao, H., and Tega, Y. (2005). Suspended sand transport in surf zones. *J. Geophys. Res.*, **110**(C12009,doi:10.1029/2004JC002853).

Kobayashi, N., Schmied, L., and Payo, A. (2006). Cross-shore suspended sand and bedload transport on beaches. *J. Geophys. Res.*. In press.

Kriebel, D. L., Kraus, N. C., and Larson, M. (1991). Engineering methods for cross-shore beach profile response, paper presented at *Coastal Sediments '91 Conference*. Reston, Va. Am. Soc. of Civ. Eng.

Lawrence, A. and Kobayashi, N. (2003). Experiments on cross-shore sediment transport under positive and negative solitary waves. Technical Report *Res. Rep. CACR-03-03*, Cent. for Appl. Coastal Res., Univ. of Delaware, Newark, Del.

Madsen, O. S. and Grant, W. D. (1976). Quantitative description of sediment transport by waves, paper presented at *15th Coastal Engineering Conference*. Reston, Va. Am. Soc. of Civ. Eng.

Miller, R. L. (1972). Study of air entrainment in breaker waves. *Am .Geophys. Union Trans.*.

Nadaoka, K., Hino, M., and Koyano, Y. (1989). Structure of the turbulent flow field under breaking waves in the surf zone. *J. Fluid Mech.*, **204**, 359–387.

Nairn, R. B. and Southgate, H. N. (1993). Deterministic profile modelling of nearshore processes. part 2. sediment transport and beach profile development. *Coastal Eng.*, **19**, 57–96.

Nielsen, P. (1992). *Coastal boundary layers and sediment transport*. World Scientific, Singapore.

Okayasu, A., Uno, Y., Kobayashi, T., and Shimaya, M. (2004). Laboratory measurement of suspended sediment concentration in surf zone with ct concentration meter. *Coast. Eng. J.*, **46**, 203–218.

Pedersen, C., Deigaard, R., Fredsœ, J., and Hansen, E. A. (1995). Simulations of sand in plunging breakers. *J. Waterw. Port Coastal Ocean Eng.*, **121**(2), 77–87.

Peregrine, D. H. (1983). Breaking waves on beaches. *Ann. Rev. Fluid Mech.*, **15**, 149–178.

Peters, K. and Dette, H. H. (1999). Sediment suspension in the surf zone, paper presented at *Coastal Sediments '99 Conference*. Reston, Va. Am. Soc. of Civ. Eng.

Puleo, J. A., Johnson, R., Butt, T., Kooney, A. N., and Holland, K. T. (2006). The effect of air bubbles on optical backscatter sensors. *Marine Geol.*, **230**, 87–97.

Raubenheimer, B., Guza, R. T., and Elgar, S. (1996). Wave transformation across the inner surf zone. *J. Geophys. Res.*, **101**, 25589–25597.

Raubenheimer, B., Guza, R. T., and Elgar, S. (2001). Field observations of wave-driven setdown and setup. *J. Geophys. Res.*, **106**, 4629–4638.

Ribberink, J. S. (1998). Bed-load transport for steady flows and unsteady oscillatory flows. *Coastal Eng.*, **34**, 59–82.

Ribberink, J. S. and Al-Salem, A. A. (1994). Sediment transport in oscillatory boundary layers in cases of rippled beds and sheet flow. *J. Geophys. Res.*, **99**(12), 707–727.

Roelvink, J. A. and Reniers, A. J. H. M. (1995). Lip 11d delta flume experiments. Technical Report *Data Rep. H2130*, Delft Hydraulics Institute.

Ruhl, C. A., Shoellhamer, R. P., Stumpf, R. P., and Lindsey, C. L. (2001). Combined use of remote sensing and continuous monitoring to analyse the variability of suspended sediment measurements in san fransisco bay, california. *Estuar. Coast. Shelf S.*, **53**, 801–812.

Schmied, L., Kobayashi, N., Puleo, J., and Zhao, H. (2006). Cross shore suspended sand transport on beaches. In press.

Simhadri, K. K., Iyengar, S. S., Holyer, R., Lybanon, M., and Jr., J. M. Z. (1998). Wavelet-based feature extraction from oceanographic images. *IEEE T. Geosci. Remote*.

Soille, P. and Pesaresi, M. (2002). Advances in mathematical morphology applied to geoscience and remote sensing. *IEEE Trans. on Geosci. Remote Sensing*, **40**(9), 2042–2055.

Stive, M. J. F. and DeVriend, H. J. (1994). Shear stresses and mean flow in shoaling and breaking waves presented at *24th Coastal Engineering Conference*. Reston, Va. Am. Soc. of Civ. Eng.

Svendsen, I. A. (1984). Mass flux and undertow in a surf zone. *Coastal Eng.*, **8**, 347–365.

Svendsen, I. A. (1987). Analysis of surf zone turbulence. *J. Geophys. Res.*, **92**, 5115–5124.

Tega, Y. and Kobayashi, N. (1999). Numerical modeling of overwashed dune profiles, paper presented at *Coastal Sediments '99 Conference*. Reston, Va. Am. Soc. of Civ. Eng.

Thornton, E., Humiston, R. T., and Birkemeier, W. (1996). Bar/trough generation on a natural beach. *J. Geophys. Res.*, **101**(C5), 12097 – 12110.

Trowbridge, J. and Young, D. (1989). Sand transport by unbroked water waves under sheet flow conditions. *J. Geophys. Res.*, **94**, 10971–10991.

van Rijn, L., Walstra, D. J. R., Gramsmejer, B., Sutherland, J., Pan, S., and Sierra, J. P. (2003). The predictibility of storms and seasons using process-based profile models. *Coastal Eng.*, **47**, 295–327.

Zhao, H. and Kobayashi, N. (2005). Suspended sand transport in surf zones on equilibrium beaches. Technical Report *Res. Rep. CACR-05-01*, Cent. for Appl. Coastal Res., Univ. of Delaware, Newark, Del.